Mitigation of atmospheric turbulence effects on optical links by integrated optics

Luca Rinaldi

université PARIS-SACLAY

Mitigation of atmospheric turbulence effects on optical links by integrated optics

Compensation des effets de la turbulence atmosphérique sur les liens optiques par optique intégrée

Thèse de doctorat de l'université Paris-Saclay

École doctorale n° 572, Ondes et matières, EDOM
Spécialité de doctorat: Physique
Graduate School : Physique, Référent : Faculté des sciences d'Orsay

Thèse préparée dans les unités de recherche **DOTA (Université Paris-Saclay, ONERA)**, **IPAG (Université Grenoble Alpes, CNRS, CNES)**, **FEMTO-ST (Université Bourgogne Franche-Comté, CNRS)**, sous la direction de **Vincent MICHAU**, Maître de recherche, et le co-encadrement de **Guillermo MARTIN**, Maître de Conférence

Thèse soutenue à Paris-Saclay, le 3 Février 2022, par

Luca RINALDI

Composition du jury

Marc OLLIVIER Astronome, IAS	Président du jury
Antonella D'ORAZIO Professeure, Politecnico di Bari	Rapporteur & Examinatrice
Jean-Philippe BERGER Astronome, IPAG	Rapporteur & Examinateur
Antonella BOGONI Professeure, Scuola Superiore Sant'Anna	Examinatrice
Guillermo MARTIN Maître de Conférence, IPAG	Examinateur
Vincent MICHAU Maître de recherche, ONERA	Directeur de thèse

THESE DE DOCTORAT
NNT : 2022UPASP013

université PARIS-SACLAY | ÉCOLE DOCTORALE Ondes et Matière (EDOM)

Titre: Compensation des effets de la turbulence atmosphérique sur les liens optiques par optique intégrée

Mots clés: Communications optiques en espace libre; Optique adaptative; Optique intégrée; Photonique

Résumé: La croissance des liaisons optiques en espace libre conduit à des systèmes dont les débits de données atteignent des dizaines de gigabits/s. Pour atteindre de tels débits, une des approches les plus fréquemment envisagées est de coupler le signal reçu dans une fibre optique monomode, et ainsi bénéficier des technologies développées pour les liaisons par fibre. Cependant, en raison des effets de la turbulence atmosphérique, une dégradation de l'efficacité du couplage est présente lorsque le faisceau se propage en espace libre.

Bien que les techniques d'atténuation des turbulences, telles que l'optique adaptative, soient largement utilisées à des angles d'élévation élevés, les liaisons satellite-sol en orbite basse doivent faire face à des angles d'élévation faibles et à une distance de propagation plus longue dans l'atmosphère. Cette propagation plus longue induit des fluctuations d'intensité qui rendent la mesure du front d'onde plus complexe. Dans ce contexte, une nouvelle alternative prometteuse aux miroirs déformables consiste à décomposer l'onde perturbée en un ensemble de modes de propagation associés à différents guides d'ondes, puis à combiner de manière cohérente ces modes guidés. La décomposition des modes est réalisée par un dispositif de multiplexage spatial. Une fois que le faisceau reçu est décomposé en un ensemble de modes, ils sont recombinés par un circuit photonique intégré. Les avantages de cette méthode sont l'absence de pièces mobiles, sa compacité et sa moindre sensibilité aux effets de scintillation.

Ce travail est dédié au développement d'un tel dispositif. Dans la première partie, une approche analytique est développée afin de décrire les effets moyens de la turbulence atmosphérique lorsqu'un faisceau est couplé à un ensemble de modes de propagation. Sur la base de cette analyse, la deuxième partie de cette thèse est consacrée à la combinaison cohérente de différents modes guidés sur un circuit photonique intégré. Dans le choix des matériaux pour les circuit photoniques, il y a un compromis entre la bande passante, la facilité de fabrication et le nombre de canaux. Les performances de ce dispositif en termes de marge de puissance globale, ainsi que son comportement statistique et temporel sont étudiés à travers des simulations *end-to-end*. Deux matériaux différents ont été étudiés: le nitrure de silicium (SiN) et le niobate de lithium ($LiNbO_3$). En particulier, la conception et la fabrication d'un circuit photonique à 8 canaux à base de $LiNbO_3$ sont analysées. Un circuit à base de SiN a également été caractérisé en termes de réponse temporelle et d'effets de couplage. Malgré ses principaux avantages, le dispositif présente toujours des pertes élevées. Pour remédier à ces pertes, nous proposons dans la dernière partie de ce manuscrit l'utilisation d'un dispositif de multiplexage spatial dans une approche d'optique adaptative dite *Sensorless*. Contrairement aux approches d'optique adaptative *Sensorless* classiques, qui n'utilisent qu'une seule fibre optique monomode, les multisorties du dispositif de multiplexage sont utilisées pour améliorer le temps de convergence de l'algorithme d'optimisation.

Title: Mitigation of atmospheric turbulence effects on optical links by integrated optics
Keywords: Free-space optical communications; Adaptive Optics; Integrated Optics; Photonics

Abstract: The growth of optical links in free space leads to systems with data rates of tens of gigabits/s. To reach such data rates, one of the most frequently considered approaches is to couple the received signal into an optical single-mode fiber and thus benefit from technologies developed for fiber links. However, due to atmospheric turbulence effects, a degradation of the coupling efficiency is present when the beam propagates in free space.

Although turbulence mitigation techniques such as adaptive optics are widely used at high elevation angles, low-Earth orbit satellite-to-ground links have to deal with low elevation angles and longer propagation distance in the atmosphere. Such longer propagation induces intensity fluctuations which results in a more complex wavefront measurement. In this context, a new promising alternative to deformable mirrors is to decompose the perturbed wave into a set of propagation modes associated with different waveguides, and then coherently combining these guided modes. The mode decomposition is performed by a space-division multiplexing device. Once the received beam is decomposed into a set of modes, they are recombined through a photonic integrated circuit. The advantages of this method include the absence of moving parts, its compactness, and its lower sensitivity to scintillation effects.

This work is dedicated to the development of such a device. In the first part, an analytical approach is derived in order to describe the average effects of atmospheric turbulence when a beam is coupled with a set of propagation modes. Based on this analysis, the second part of this thesis is devoted to the coherent combination of different guided modes on a photonic integrated circuit. In the selection of materials for such circuits, there is a trade-off between bandwidth, manufacturability and number of channels. The performance of this device in terms of overall power margin, as well as its statistical and temporal behavior are considered through end-to-end simulations. In this thesis, two different materials have been studied: silicon nitride (SiN) and lithium niobate ($LiNbO_3$). Particularly, the design and fabrication of a 8-channel $LiNbO_3$ based photonic circuit is analyzed. A SiN-based circuit has been also characterized in terms of time response and coupling effects. Despite its main advantages, the device still presents high losses. To tackle these losses, in the last part of this manuscript we propose the use of a space-division multiplexing device in a sensorless adaptive optics approach. In contrast to standard sensorless approaches, which use only one single-mode fiber, the multi-outputs of the space multiplexing device are used to improve the convergence time of the optimization algorithm.

Résumé en Français

Dans le contexte de la croissance des liaisons optiques en espace libre, des systèmes à haut débit de données sont nécessaires. Pour atteindre de tels débits de données, l'une des approches les plus courantes consiste à coupler le signal reçu dans une fibre optique monomode. Cependant, en raison des effets de la turbulence atmosphérique, une dégradation de l'efficacité du couplage est présente lorsque le faisceau se propage en espace libre.

Les techniques d'atténuation des turbulences, telles que l'optique adaptative, soient largement utilisées à des angles d'élévation élevés. Cependant, lorsqu'il s'agit de liaisons satellite-sol en orbite basse, nous devons faire face à de faibles angles d'élévation et à une plus grande distance de propagation dans l'atmosphère. Cette propagation plus longue induit des fluctuations d'intensité qui rendent la mesure du front d'onde plus complexe. Dans ce contexte, une nouvelle alternative proposé pour la première fois par N. Schwartz pour mesurer et corriger le front d'onde en régime de forte perturbation consiste à décomposer l'onde perturbée en un ensemble de modes de propagation associés à différents guides d'ondes, puis à combiner de manière cohérente ces modes guidés. La décomposition des modes est réalisée par un dispositif de multiplexage spatial. Une fois que le faisceau reçu est décomposé en un ensemble de modes, ils sont recombinés par un circuit photonique intégré. Les avantages de cette méthode sont l'absence de pièces mobiles, sa compacité et sa moindre sensibilité aux effets de scintillation.

Les travaux présentés dans ce manuscrit ont porté sur le développement d'un tel dispositif. Dans le Chapitre 1, un aperçu général des missions spatiales optiques satellite-sol a été proposé, mettant en évidence les méthodes d'atténuation des turbulences utilisées au fil du temps, à mesure que la demande de débits de données augmentait. Les paramètres clés décrivant le comportement de la turbulence ont également été présentés, ainsi que le logiciel interne utilisé afin de se débarrasser de l'hypothèse de la petite perturbation. Par la suite, nous avons fourni une description de la méthode de combinaison cohérente utilisée dans cette thèse. Sur cette base, différents dispositifs de multiplexage de mode utilisés pour réaliser l'étape de décomposition de mode sont décrits. Enfin, dans la dernière partie de ce chapitre, nous avons donné un aperçu sur les différentes plateformes de matériaux photoniques, en soulignant leurs principaux avantages et inconvénients.

Dans le Chapitre 2, nous analysons le premier bloc qui compose l'approche de combinaison cohérente : la décomposition des modes. On peut aussi voir cela comme une analyse spatiale, c'est-à-dire analyser l'efficacité moyenne du couplage en fonction du nombre de modes décomposés.

Pour ce faire, l'objectif de ce chapitre est de mettre en œuvre un outil de simulation analytique plus rapide que les outils conventionnels, afin de décrire les effets moyens de la turbulence atmosphérique lorsqu'un faisceau est couplé à un ensemble de modes de propagation. L'application de cette approche au cas des modes Hermite-Gaussiens tels que ceux utilisés dans un dispositif de multiplexage par répartition spatiale est également analysée dans ce document. La pertinence de telles études réside dans la capacité à bien décrire une onde perturbée par la turbulence atmosphérique avec un ensemble de modes de propagation. Nous avons également présenté comment, en utilisant une stabilisation rapide de l'image dans l'expression de l'efficacité du couplage, on peut obtenir une meilleure optimisation dans l'ensemble des modes considérés par rapport à celle obtenue avec l'approche des modes propres, quelles que soient les conditions de turbulence. Cette étude a mis en évidence l'impact potentiel d'un dispositif de correction de l'inclinaison en amont du multiplexeur, alors que le développement d'un multiplexeur avec des modes optimisés apportera un gain de l'ordre de quelques pourcents seulement.

En outre, afin d'étudier l'aspect instantané (c'est-à-dire les fluctuations de l'efficacité de couplage), une simulation de Monte-Carlo a été réalisée dans la dernière partie de ce chapitre. Une analyse du système de liaison satellite-sol est présentée, définissant un budget de liaison pour un scénario spécifique. Les efficacités de couplage moyennes obtenues à partir de l'approche MC sont très similaires à celles rapportées par l'analyse analytique, validant également les formules données. De plus, les fluctuations de l'efficacité de couplage sont fonction du nombre de modes utilisés dans la décomposition de mode, plutôt que fonction du type de correction (phase et amplitude ou phase seulement). En considérant le scénario d'intérêt, un télescope de 25 cm est trop petit pour atténuer les fluctuations de l'ensemble du flux collecté. Par conséquent, une pupille de télescope de 50 cm a été étudiée. Avec un tel diamètre, différents types de correction peuvent être envisagés (en considérant également la présence d'une correction d'inclinaison par rapport au type de correction précédent phase + amplitude et phase seule). Les résultats suggèrent que l'exigence ne dépend pas seulement dépend pas seulement de l'efficacité moyenne du couplage. En analysant la fonction de distribution cumulative (CDF), il semble que le nombre de modes doit être considéré séparément du type de mode. En fait, une étude de conception complète complète doit être réalisée en tenant compte des pertes induites par les effets temporels et en optimisant le diamètre du télescope récepteur. le diamètre du télescope récepteur.

Sur la base de cette analyse, la troisièm partie de cette thèse est consacrée à les aspects temporels de la boucle de correction. Il est maintenant nécessaire d'introduire ces problèmes dans la spécification d'un circuit intégré. Une nouvelle loi de contrôle a été proposée afin de faire face à une demande de bande passante élevée, bien adaptée aux applications PIC. D'autre part, malgré les avantages de l'utilisation des circuits photoniques pour corriger la turbulence atmosphérique, les pertes élevées sont toujours au cœur de leur construction. Cette solution alternative permet également de résoudre les problèmes de l'OA standard dans les fortes perturbations, sans attendre la maturité technologique des PICs. Contrairement aux approches d'optique adaptative *Sensorless* classiques, qui n'utilisent qu'une seule fibre optique monomode, les multi-sorties du dispositif de multiplexage sont utilisées pour améliorer le temps de convergence de l'algorithme d'optimisation.

Nous avons évalué la performance de notre approche. Dans ce cas, une proposition d'une modulation capable de créer une matrice inversible a également été détaillée, c'est-à-dire une somme de d'une inclinaison de la pointe à 45°et d'une aberration de défocalisation. Néanmoins, des analyses plus poussées ont été mises en évidence dans le cadre du stage de Yann Lucas à l'ONERA, et poursuivie au cours de sa thèse de doctorat. Dans notre montage expérimental, seules 8 sorties du dispositif MPLC sont équipées de photodiodes et 8 modes de déformation sont contrôlés sur le miroir déformable. Comme nous l'avons vu, une seule modulation est nécessaire lorsqu'on considère une approche multi-sorties, comparé aux 15 modulations obtenues lorsque l'algorithme SPGD est appliqué.

Enfin, dans la dernière partie de cette thèse, nous avons décrit la combinaison cohérente de différents modes guidés sur un circuit photonique intégré, et l'impact que les analyses spatiales et temporelles ont sur ce circuit. Dans le choix des matériaux pour les circuit photoniques, il y a un compromis entre la bande passante, la facilité de fabrication et le nombre de canaux. Deux matériaux différents ont été étudiés: le nitrure de silicium (SiN) et le niobate de lithium ($LiNbO_3$). En particulier, la conception et la fabrication d'un circuit photonique à 8 canaux à base de $LiNbO_3$ sont analysées. Toutefois, en raison de contraintes de temps, la phase d'encapsulation de ce composant a débuté en octobre 2021. Les premières caractérisations de ce PIC, notamment la réponse temporelle d'un déphaseur donné et la tension demi-onde ont été réalisées dans la dernière partie de cette thèse.Une valeur de perte d'insertion d'environ 12 dB et une valeur de tension demi-onde d'environ V 13 V ont été trouvées, et sont en accord avec ce qui est prédit théoriquement.

Un circuit à base de SiN a également été caractérisé en termes de réponse temporelle et d'effets de couplage. En effet, une réponse temporelle relativement lente d'environ 100 s a été évaluée et comparée à celles trouvées dans la littérature, lorsqu'un déphasage de 2 est appliqué à un déphaseur donné. Dans ce contexte, des méthodes alternatives doivent être trouvées pour gérer ces déphasages. La présence d'un couplage entre différents MZI a également été observée, ce qui ajoute aux pertes déjà importantes du circuit.

Cette étude a permis de tracer une voie à suivre concernant les spécifications à attribuer pour le développement d'un circuit intégré dans un scénario de télécommunication optique satellite-sol. Une analyse plus précise sur le choix de l'algorithme de contrôle et des tests supplémentaires sur des perturbations dynamiques sont prévus dans le cadre de la thèse de Yann Lucas, ainsi que le développement d'un circuit intégré photonique de plus de 8 canaux tout en considérant des de matériaux alternatifs pour sa construction, tels que l'InP déjà décrit dans la dernière partie du partie du Chapitre 1.

Acknowledgements/Remerciements

Je pense que le moment des remerciements est celui qui m'a fait le plus réaliser à quel point mon doctorat était fascinant. J'ai retracé les moments que j'ai vécus pendant mes trois années à Paris, au cours desquels j'ai rencontré des personnes qui sont devenues très importantes pour moi.

Tout d'abord, je tiens à remercier tous les membres du jury - Antonella D'Orazio, Antonella Bogoni, Marc Ollivier et Jean-Philippe Berger - pour avoir accepté d'être présents et pour l'intérêt qu'ils ont porté à mon travail. Je remercie tout particulièrement Guillermo Martin, Nadège Courjal et Mathieu Boutillier, pour leur disponibilité, les nombreuses discussions et l'incroyable enthousiasme qu'ils m'ont apporté au fil des ans. Merci beaucoup pour vos enseignements. Malgré la distance qui me sépare de lui, je tiens à remercier Guillermo pour son sourire et la chaleur qu'il m'a témoignée, surtout au cours de la dernière période. J'ai beaucoup apprécié cela et je te remercie beaucoup.

Je tiens à remercier la personne qui m'a le plus supporté pendant ces trois années : mon directeur de thèse Vincent Michau. Mon estime pour Vincent est sans égale, et je pense qu'après tout ce temps, je n'aurais pas pu souhaiter une meilleure personne pour travailler. Il a été disponible dès le début et a été à mes côtés jour après jour tout au long de mon parcours. Je lui dois mes plus grands remerciements. J'espère te revoir dans le futur, tu me manqueras beaucoup.

Comment oublier l'incroyable et fantastique HRAmbiance de ma fabuleuse équipe ! Laurie, Matthieu, Yann, Chloé, Caro, Antoine, Pablo, Alix, Hiyam, Perrine, Yann Lucas, Valentina, Emile, Léa, Pierre, François, Romain, Mehdi, Cyril, Hugo, Daniel, Antoine Guilmain, Eve, Iva, Keryann, Mahawa, Thibault, Nicolas et tous ceux que j'ai rencontrés au fil des ans. Je tiens à remercier Jean-Marc pour nos nombreuses discussions (en italien), Nicolas, Cyril, Serge pour son infinie disponibilité et son enthousiasme, Joseph, Aurélie, Laurent, Pedro, Béatrice, Clélia, Frédéric, Bruno, Thierry et Marie-Thèrese ! Un grand GRAZIE à vous tous ! Je n'oublierai jamais le soutien de Laurie ni les nombreuses sorties à Arkose avec Pablo et Yann. Vous avez fait de mon doctorat à l'Onera une expérience sans pareille, je vous en serai toujours reconnaissant. Et entre les discussions scientifiques et les pauses café, vous m'avez appris à ne pas abandonner, vous m'avez donné de la force quand j'en avais le plus besoin et ensemble, vous m'avez fait me sentir chez moi. Vous êtes une petite famille pour moi, j'espère vous voir encore et encore. Vous serez toujours dans mon cœur.

Je remercie ma famille pour le soutien et l'affection qu'elle me donne jour après jour, vous me manquez tous énormément. Vous êtes mon meilleur soutien. Merci à la famille élargie et surtout à Lalla!

Je tiens à remercier Pietro du fond du cœur pour l'amitié infinie qui nous lie, et je porterai toujours ton souvenir avec moi.

Je remercie mes amis de toujours, Gabriele, Giuliano, Andrea, Peppe, Danila, Giuseppe, Simone, Fabio, Giovanni e Petros. Ils m'ont toujours soutenu et seront toujours à mes côtés. Je vous aime, merci d'être toujours là.

Je voudrais terminer en remerciant la personne qui, jour après jour, pas après pas, m'a donné de la force, m'a fait rire, m'a soutenu et m'a supporté avec tant d'affection et d'amour. Ce dernier et immense merci, du fond du cœur, va à Francesca. Ai tuoi bellissimi abbracci.

Contents

List of Figures

List of Tables

List of Abbreviations and Acronyms

AO Adaptive Optics.

ATP Acquisition, tracking and pointing.

BPM Beam propagation method.

CDF Cumulative distribution function.

CNES Centre national d'études spatiales.

DM Deformable mirror.

DWDM Dense-wavelength division multiplexing.

EDFA Erbium Doped Fiber Amplifiers.

FCA Fiber collimator array.

FSO Free-space optical communications.

GEO Geostationary Orbit.

HG Hermite-Gaussian.

IPAG Institut de Planétologie et d'Astrophysique de Grenoble.

LEO Low-Earth Orbit.

LG Laguerre-Gaussian.

MMF Multi-mode fiber.

MPLC Multi-plane light conversion.

MZI Mach-Zehnder Interferometer.

OGS Optical ground station.

ONERA Office national d'études et de recherches aérospatiales.

OOK On-off keying.

PIC Photonic Integrated Circuit.

PILOT Propagation and Imaging, Laser and Optics through Turbulence.

PL Photonic lantern.

PM Polarization mantaining.

PS Phase shifter.

PSD Power spectral density.

RF Radio-frequency.

RTC Real time computer.

SDM Space-division multiplexing.

SHWS Shack-Hartmann wavefront sensor.

SMF Single mode fiber.

SNR Signal-to-noise ratio.

SOI Silicon-on-insulator.

SPGD Stochastic parallel gradient descent.

SVD Singular value decomposition.

SWaP Size, weight and power.

TURANDOT TURbulence simulator for spAce-grouND Optical Telecommunication.

WDM Wavelength-division multiplexing.

WFS Wavefront sensor.

Introduction

The growing interest in communication technologies for high-speed inter-satellite, satellite-to-ground links or Earth observation requires system to have data rates of tens of Terabits/s. Free-space optical communications technologies are presently under development to reach such data rates. In this context, the received signal is coupled into a single mode optical fiber, thus making it possible to take advantage of the technologies developed for the fiber communications. Unfortunately, the availability and the reliability of such links are still limited by turbulence-induced fading. The atmospheric turbulence effects degrade the spatial coherence of optical waves, and hence the coupling into the fiber.

Different methods have been proposed for the mitigation of atmospheric turbulence effects. They may be divided into Passive and Active methods. Considering passive methods, diversity techniques are usually employed, divided into time, frequency and space domain. Despite their advantages, such methods are based on complex transceivers and receivers, not compatible with low cost solutions [Khalighi et al. (2009); Kiasaleh (2017)]. On the other hand, active methods, such as Adaptive Optics (AO), are developed to correct the disturbances in the phase of the wave at each instant. In standard adaptive optics, the perturbations are measured with a wavefront sensor and corrected by a deformable mirror. However, adaptive optics is still a complex technology. Moreover, when considering low-elevation satellite-to-ground downlink, as the one studied in this thesis, wave amplitude fluctuations can no longer be ignored. Indeed, errors on the wavefront measurement appears, degrading the performance of AO [Primmerman et al. (1995); Barchers et al. (2002)].

A new promising approach for turbulence effect mitigation has been proposed in Noah Schwartz doctoral thesis [Schwartz (2009)]. The incoming perturbed beam is firstly coupled onto a set of propagation modes associated with different waveguides, and then the fields in the waveguides are coherently combined. The coupling between the incident beam and the propagation modes is achieved through a Space-Division Multiplexer (SDM) device. Such devices are developed to increase the capacity of multi-mode fibers. Different space-division multiplexer devices can be used, such as the fiber collimator array, the Multi-Plane Light Conversion device developed by Cailabs company, or the photonic lantern [Dikmelik and Davidson (2005); Labroille et al. (2014); Leon-Saval et al. (2017)]. To deal with high number of modes, the mode combining may be performed with a Photonic Integrated Circuit (PIC). The main advantages of this approach are its compactness, the absence of moving parts, and its lower sensitivity to scintillation effects.

Despite the concept of this method has been established and some experimental laboratory demonstrations of the principle have been carried out, its performances have never been characterized in detail for realistic conditions, either theoretically or experimentally.

This thesis is dedicated to the study of coherent recombination for the correction of atmospheric turbulence effects. In order to go beyond the proof of concept, this work is positioned in a concrete framework that goes from the definition of the use case to the technology of the photonic circuit.

For this purpose, in Chapter 1, I recall the context of satellite-to-ground optical links as well as the principle of the main techniques for atmospheric turbulence mitigation. I then detail the different components of the coherent combining approach, giving an overview on the main photonic material platforms. In Chapter 2, I propose an analytical formulation in order to describe the effects of atmospheric turbulence on the coupling with a set of propagation modes, as those representatives of a SDM device. In fact, a set of Hermite-Gaussian modes has been used throughout this thesis, although it is not the only available solution. A mode optimization has been also detailed, analyzing the most suitable set of modes with respect to the turbulence conditions. Once this stage validated, in Chapter 3 the performance of a PIC has been evaluated in terms of both overall power margin and coupling efficiency fluctuations. Moreover, through a Monte-Carlo analysis, I study the link between the previous performance metrics and two important development parameters: the number of modes and the type of correction. I also detailed the temporal analysis, assessing the performance of the circuit with respect to the phase shift experienced. Then, I consider two different material platforms for the PIC development: the silicon nitride and the lithium niobate, both presenting attractive but different properties. I describe the design of an 8-channel $LiNbO_3$ based PIC performed in collaboration with N. Courjal and G. Martin, highlighting the implementation constraints of each basic component that makes up this circuit. The encapsulation of the chip is currently in progress. Finally, I characterize a SiN based PIC in terms of time response and coupling effects.

Despite its main advantages, still high losses appear with the PIC development. In short term, a DM-based phase correction remains attractive. In Chapter 4 a new sensorless AO approach is proposed. In contrast with standard AO approaches, a SDM device is used for mode decomposition of the received beam. The DM is controlled from the multi-outputs of this device, using a multi-output control algorithm, gathering the advantages of the standard AO - quick convergence time - and those of sensorless AO - less sensitivity to scintillation, and lack of non-common path aberrations.

Chapter 1

Context

1.1 Introduction

The aim of this Chapter is to introduce briefly the context of free-space optical communications (FSO), focusing especially on space-to-ground optical links. The benefits and challenges addressed by FSO are firstly summarized, thus emphasizing the importance of atmospheric turbulence compensation techniques. Furthermore, the statistical properties of atmospheric turbulence and some associated key parameters are detailed in Section 1.3. With regard to this, the tool used to describe the turbulence effects on a beam propagation is also described.

Turbulence mitigation solutions will be shown in the final part of this Chapter. Indeed, various passive and active turbulence mitigation techniques already exist in order to overcome these limitations. In the Section 1.5.2 the most commonly used Adaptive Optics (AO) approach is presented as turbulence mitigation technique. Derived from its main limitations, in section 1.5.4, the coherent combining solution is reported, thus emphasizing the photonic integrated approach developed in this thesis.

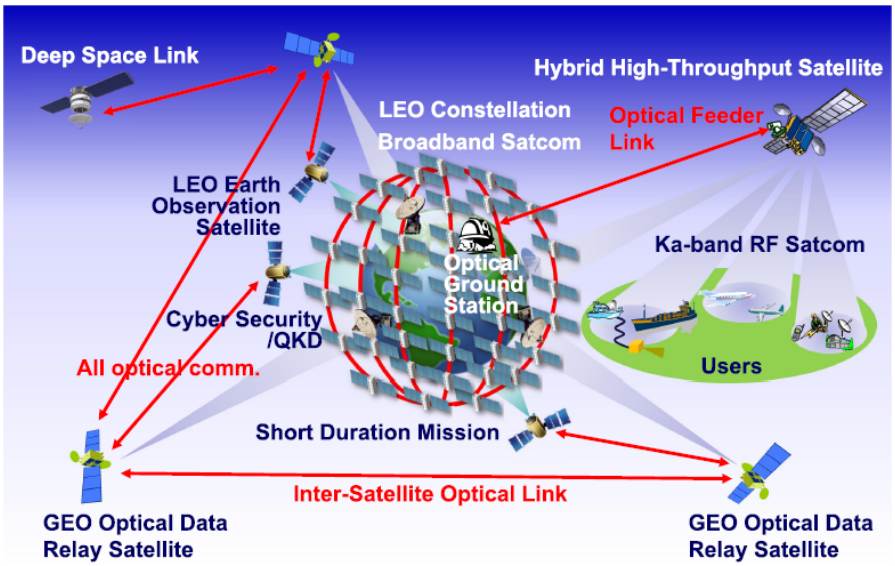

Figure 1.1: Major free-space laser links applications. From [Toyoshima (2021)]

1.2 Satellite-to-ground optical links

The growing interest in information and communications technology, with the increase in usage of high-speed internet and connectivity application such as 5G mobile communications etc., has focused much more attention on optical systems, now adopted in various different scenarios, as reported in Fig. 1.1. As a consequence of the progressive increase in the capacity of these systems, it is evident that conventional radio-frequency (RF) technologies reach their limitations. Higher frequencies are envisioned in order to meet the data rate requirements of next generation systems, which leads to an increasing of the available bandwidth. In this context, free-space optical communications are mainly considered, as they benefit most from the use of fiber technologies.

1.2.1 Benefits and challenges of FSO

Free-space optical communications refers to transmission in unguided media by employing optical carriers. In this sense, a source generates information waveforms which are subsequently modulated onto optical wavelengths. After propagation through the atmosphere, in the reverse direction, a receiver collects the light whilst a photo-detector convert the optical field in an electric signal. The gap between RF and optical communications leads to some interesting characteristics between the two systems, that are summarized in the following:

- ✓ **Large modulation bandwidth**: It is well known how increasing the carrier frequency will increase the amount of information available by the considered system. In optical frequency, even if a fraction of the bandwidth is taken, hundreds of THz are still allowable.

- ✓ **High directivity**: Due to the smaller wavelength, the directivity of a FSO system is remarkably higher than RF system. The gain brought by optical wavelengths in this case is proportional to λ/D_R, where λ represents the wavelength and D_R the transceiver diameter [Kaushal and Kaddoum (2017)]. However, despite these advantages, one of the main drawbacks over RF systems lies in the requirement of a very accurate acquisition, tracking and pointing (ATP) system due to the narrow beam divergence.

- ✓ **Reduction in SWaP requirements**: A typical dimension of an optical system is about ten times less than an RF-based one. This is mainly due to the high directivity, which allows small diameters to be used in optical communications, while also reducing optical losses. Moreover, the high intensity brought by a laser at the emitter and the very small weight achievable using optical components contribute to an overall reduction of the Size Weight and Power reduction.

- ✓ **High security**: Inherent security given by FSO through the narrow beam divergence used, thus reducing the probability of any kind of interception.

- ✓ **Unlicensed spectrum**: No restriction on the spectrum used for optical communications with respect to the RF spectrum availability: this is still due mainly to the high directivity of optical beams over RF, which suffer from interference of adjacent carriers, thus requiring a licensed spectrum.

Despite the major benefits of FSO and its wide field of applications, the feasibility of such a technique is compromised by atmospheric turbulence induced fading [Khalighi (2021); Jahid et al. (2020)]. Indeed, fading on the received signal are induced by fluctuations of the power collected by the receiver aperture, degrading the coupling efficiency of such a beam into the single mode fiber at the receiver output.

Achieving the expected data rate in the context of optical communications between satellite and earth also translates into improved link durability, and low elevation angles are investigated in this respect. Particularly, this thesis deals with the effects of atmospheric turbulence and their mitigation.

A chronological state-of-the art of space missions is proposed in the following subsection, with a focus on actual/future missions and applied technologies.

1.2.2 Roadmap of Space-based laser Communications

During the past years, various different space missions in order to demonstrate optical technologies have been performed, thus augmenting the feasibility of optical links. In Figure 1.2 trends in data rates, expressed in bits per second, are shown for past and future space programs. New technologies derived from the optical fiber domain are now involved in space laser communications, using dense-wavelength-division multiplexing (DWDM), space-division multiplexing (SDM) and multi-level modulation solutions (m-QAM) [Toyoshima et al. (2015); Toyoshima (2021)], while photonic payloads are designed by space agencies for telecom satellites [Anzalchi et al. (2019); Aveline et al. (2017)].

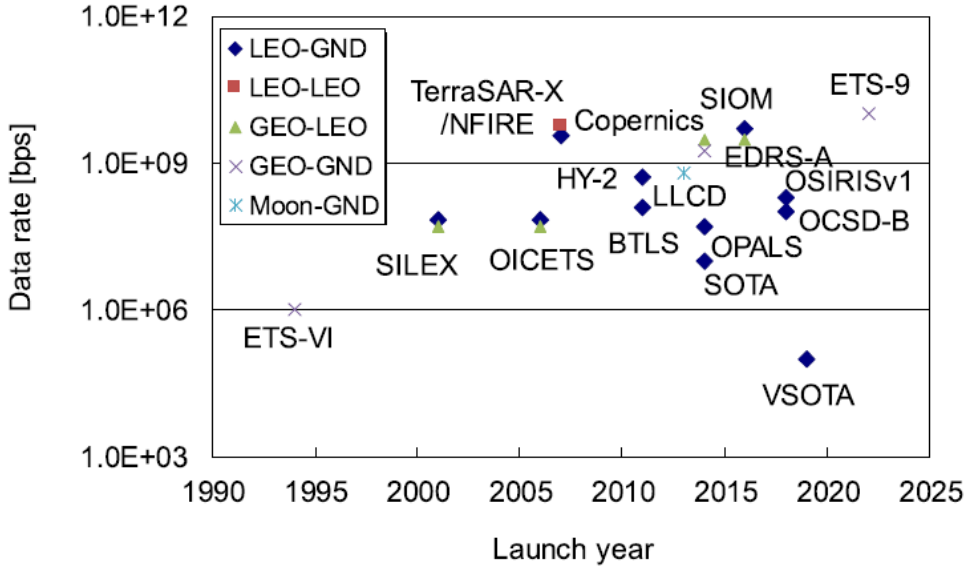

Figure 1.2: Data-rate trends of laser communications. From [Toyoshima (2021)]

Going back in time, the most important programs validating optical solutions on satellite-to-ground, ground-to-satellite or deep-space can be identified in the following:

1.2.2.1 Past optical-space missions

In order to better understand some of the challenges of lasercomm links, in early 1990 NASA JPL has performed the deep-space Galileo Optical Experiment (GOPEX [Wilson (1993)]). Here, optical transmissions were beamed to the Galileo spacecraft, in its way to Jupiter, from optical ground stations (OGS) mounted at both California and New Mexico. The results showed the **first demonstration of a laser communications uplink to a deep space vehicle**, validating the theoretical model developed to predict the performance of an optical link. Later, in 1994 and 1995 two space missions called Laser-Communication Experiment **(LCE)** and Ground/Orbiter Lasercomm Demonstration (**GOLD**) have been performed by the Communications Research Laboratory (CRL) and CRL with NASA/JPL respectively, using the Japanese Engineering Test

Satellite (**ETS-VI**). These missions constitute the **first demonstration of space-to-ground laser communication links**.

The goal of these missions was first of all to evaluate the basic technologies for a low data rate optical satellite communication system and to acquire technical data through scientific and engineering experiments using an on-board optical system [Arimoto et al. (1995)].

In particular, a laser diode with a wavelength of 0.83 μm and an argon ion laser at 0.5145 μm were used for the downlink and uplink transmission respectively. The initial performance of a coarse tracking subsystem was tested, while intensity modulation and direct detection techniques were used in the bidirectional links between ETS-VI and the ground station, achieving a data rate of approximately 1.024 Mbps in both up- and down-link. Furthermore, to understand the optical link performance under a variety of atmospheric turbulence conditions for future missions was also a major objective in this context [Wilson et al. (1997b)].

Considering Inter-Satellite Link (ISL), in 2001 the European Space Agency (ESA) launched a geostationary satellite called **ARTEMIS**, with one of its payloads being a laser communication terminal (LCT) and called Optical PAyload for Inter Satellite Link Experiment (**Opale**) [Kuzkov et al. (2012)]. In this context, the semi-conductor laser inter-satellite experiment (**SILEX**) combines both the aforementioned Opale terminal and the PASsanger TELecom (**Pastel**) one embarked in the French Earth observation satellite SPOT-4. Through this framework, optical communication links were performed, transmitting SPOT-4 imagery at a data rate of 50 Megabits per second (Mbps) to Artemis, which relay it to the ground via its Ka-band payload, and establishing the **world's first optical inter-satellite communication link**, with data rates of 50Mbps. Moreover, the **first bidirectional links between the ARTEMIS satellite and the ESA optical-ground station (OGS) in Tenerife** have been also established within this campaign, studying the effects of optical beam propagation through atmospheric turbulence [Alonso et al. (2004)].

Still considering the Artemis satellite, in 2006 the goal of the JAXA Optical Interorbit Communications Engineering Test Satellite **(OICETS)** was to conduct interorbit laser communications experiments with this latter. Moreover, with ESA cooperation, they also aimed to conduct experiments on new high-accuracy pointing, acquisition and tracking (ATP) technologies [Jono et al. (2006)]. The equipment used in this case is the so-called Jaxa (Japan Aerospace Exploration Agency) **LUCE**, or Laser Utilizing Communication Equipment. LUCE utilizes a semiconductor LD (Laser Diode) with a wavelength of $0.847\mu m$ as a transmission device and an APD (Avalanche Photo Diode) as detection device. The optical part of LUCE (LUCE-O) consists of three modules: an optical antenna, the optical system, and of two-axis gimbals. The OICETS-ARTEMIS link uses the 2PPM (2 Pulse Position Modulation) format at 2.048 Mbit/s, while the return link uses the NRZ (Non-return-to-zero) format at 49.3724 Mbit/s.

The previous achievements constituted an important technology milestone of inter-satellite and space-to-ground optical links. Moreover, a second generation of LCT has been developed by Tesat Spacecom and the German Space Agency (DLR), with a homodyne detection scheme and a binary phase-shift keying (BPSK) modulation format. A Nd:YAG laser operates in this case at 1.064 μm. Consequently, inter-satellite communication links at 5.6Gbps have been achieved between **TerraSAR-X** and American **NFIRE** satellites [Buckreuss and Roth (2008); Gregory et al. (2017)].

Future space to ground optical communications can benefit immensely from much higher data rates, in the range of hundreds of Gbps to Terabits per second. To achieve this benefits, fiber communication technologies are required at the optical ground station. Although small diameter telescope can be used here to focus on the SMF, the limitation on the minimum size will compromise the collection area or receiver gain, thus being unable to operational links.

As alternative, Adaptive Optics systems correcting turbulence perturbed phase has been already demonstrated in the literature as alternative to improve space-to-ground optical link, thus becoming critical to achieving the aforementioned data rates.

The **first atmosphere-compensated laser beam propagation using AO system** was performed through the Compensated Earth-Moon-Earth Retroreflector Laser Link (CEMERLL) experiment in 1994, thus showing a significant improvement on the received signal-to-noise ratio (SNR) [Wilson et al. (1997a)].

More recently, by combining adaptive optics with a laser communications technology aboard the International Space Station (ISS), NASA aimed to obtain advanced space communications with major benefits for data transmission needs. That is, through the Optical Payload for Lasercomm Science (**OPALS**) the proof of concept demonstration validates **Adaptive Optics correction of an optical signal from fast slewing low-Earth orbiting (LEO) spacecraft into a single-mode fiber** [Wright et al. (2015, 2016)].

In the same period,, after the successful lasercom demonstration carried out by the National Institute of Information and Communications Technology (NICT) using the LUCE equipment, new activities around the Small-Optical TrAnsponder (**SOTA**) instrument flying on the Low Earth Orbit satellite **SOCRATES** were implemented. The main goals of this mission were to experiment with Quantum Key Distribution (QKD) techniques and foster the new free-space optical technologies. In context of the Demonstration for Optical transMission at hIgh data rate iN Orbit (**DOMINO**) project, conducted between the French Space Agency (CNES), ONERA, Airbus Defence and Space, Thales Alenia Space and international partners as the NICT and NASA, an **AO system was performed with 976nm laser source provided by the SOTA** [Artaud et al. (2017)]. Here, the MeO telescope at the Observatoire de la Côte d'Azur (OCA) has been adapted to serve as ground station, while the AO bench -called **ODISEE**- was designed and developed at the Onera **to test injection into SMF** [Petit et al. (2016)].

Although feasibility of optical links have been already demonstrated, the **first relay communication system based on inter-satellite links**, the European Data Relay System (**EDRS**), is intent to provide almost full-time communications through GEO relay links, i.e. using low-Earth orbit (LEO), spacecraft and Earth stations that otherwise are not able to permanently transmit/receive data.

Furthermore, as part of the EDRS system it is worth noting the first commercially used optical data relay satellite (EDRS-A), designed to provide data rates up to 1.8 Gbit/s with high availability and is required to switch between different LEO satellites equipped with LCTs to acquire data during short links. This terminal is embarked on the commercial telecommunication satellite **Alphasat**, developed by Airbus Defence and Space in partnership with Inmarsat and ESA. Since 2014, various attempts have also been made to establish optical communication links

between the ground and the GEO Alphasat satellite using the Transportable Adaptive-Optics Ground Station (TAOGS) by Tesat Spacecom and the DLR. [Saathof et al. (2017); Heine et al. (2018)].

Another project contracted to Onera by ESA was the **FEEDELIO** experiment. Here, the **AO pre-compensation of atmospheric turbulence** on a 13km slat path in Tenerife has been employed for achieving very high throughput optical GEO feeder links [Bonnefois et al. (2019); Vedrenne et al. (2021)].

This experiment aimed at demonstrating a significant increase of the mean received power and decrease of the power fluctuations thanks to AO, as well as measuring the impact of the point-ahead angle (PAA) and turbulence strength on the overall performance of the link.

Finally, today optical inter-satellite and satellite to ground links are experimentally demonstrated, as is the possibility of using turbulence mitigation techniques such as adaptive optics on LEO-ground optical links.

1.2.2.2 Present and future optical-space missions

Following our conversation on the main optical space missions, new objectives are analyzed in the present and future lasercom missions. Among them, we can mention the increase in data rate, the mitigation of the atmospheric turbulence effects through AO on the uplink, and the operational character compared to the previous missions listed.

Regarding these future missions, a small summary table is presented below 1.1 for Europe, USA and Asia respectively. Various experiments has been conducted all over the world, such as the laser communication terminals using the Optical Space Infrared Downlink System (**OSIRIS**) developed by the German Aerospace Center (DLR) and planned in 2020, the Japanese Data Relay System (**JDRS**) by the JAXA transmitting at 1.8-Gbps in a GEO-ground link, or the Laser Communication Relay Demonstration (**LCDR**) satellite by the NASA in order to demonstrate 2.88-Gbps laser communication in GEO (2021). As previously stated, to obtain such data rates, Adaptive Optics system are employed in OSIRIS experiments, as well as in LCDR demonstration, in which the AO system uses two deformable mirrors, the first one correcting for low spatial frequencies aberrations with large amplitude and a second deformable mirror correcting for high spatial frequencies aberrations with small amplitude [Roberts et al. (2015)].

Optical feeder link are thus considered as the most advanced solution for the future Very-High Throughput Satellite (VHTS) system requirements. Another important framework in this case is **VERTIGO**, a three-year project funded by the European Commission and started in mid-2019. The ambition of this project is to implement and test the feasibility of various key techniques and technologies required for the development of high-capacity satellite systems based on optical feeder links [Kernec et al. (2019)]. These key building blocks range from the spectral and energy modulation formats and detection schemes (NRZ-On-off Keying "OOK" and NRZ-Differential Phase Shift Keying "DPSK" at 25 Gbps and NRZ-Differential Quadrature Phase Shift Keying "DQPSK" at 50 Gbps), high power wavelength multiplexing, high optical power amplification (10W and 50W will be developed, while optical power of 100W using power combining will be implemented), to coherent combining at both emitter and receiver sides (at

the reception performed by a Silicon Photonic Integrated Circuit, Si-PIC) as well as adaptive optics and multi-aperture optics for turbulence mitigation. Two different demonstrations will take place during this framework, firstly focusing on the impact of high and very high optical power on the integrity of the telecom signal, while also evaluating in representative conditions (53 km link through atmosphere) and both up/down-link, the feasibility of such very high throughput feeders links.

ESA has recently launched a new program called **Scy-Light**, that will bring unprecedented transmission rates, data security and resilience to meet the market demand.

The program will concentrate the efforts on new optical communication technologies also in the areas of Intra-Satellite Photonics/Optical Payloads and Quantum Cryptography [Hauschildt et al. (2017)]. Key elements (e.g. WDM, signal routing/switching etc) for high-throughput system (terabit per second, minimal 100 Gbps) are identified through the High thRoughput Optical Network (**HydRON**) program under ScyLight. In this framework, Airbus and the Netherlands Organisation for Applied Scientific Research (TNO) have launched a programme to develop a laser communication terminal demonstrator for aircraft, known as **UltraAir** [Air (2021)].

Europe			
Year	Program	Scenario and wavelength	Modulation and data rate
2020	**OSIRISv3-4** (DLR)	LEO-GND, $1.5\mu m$	IMDD, 10 Gbps
2021	**ScyLight#1** (ESA)	LEO/GEO-grond, inter-satellite links	
2021	**Moon Village** (ESA)	Moon-Earth	PPM, 7 Mbps
2024	**DOCS** (ESA)	Deep space-GND	16-PPM, 10 Mbps
USA			
2021	**LCRD** (NASA GSFC)	GEO-LEO/GND, $1.5\mu m$	DPSK/PPM, 2.8G/622 Mbps
2021	**DSOC** (NASA JPL)	Deep space-GND	PPM, 264 Mbps
2022	**LEMNOS**(NASA GSFC)	Moon-Earth	PPM, 311 Mbps
2025	**Gateway** (NASA)	Moon-Earth	
Asia			
2020	**JDRS** (JAXA)	GEO-GND,$1.5\mu m$	DPSK, 1.8 Gbps
2020	**CANON**		IMDD
2020	**ALOS-3** (JAXA)	LEO-GEO, $1.5\mu m$	DPSK, 1.8 Gbps
2021	**ALOS-4** (JAXA)	LEO-GEO , $1.5\mu m$	DPSK, 10 Gbps
2022	**ETS-9/HICALI** (NICT)	$1.5\mu m$	10 Gbps

Table 1.1: Future laser-communication space missions for Europe, USA and Asia respectively. Adapted from [Toyoshima (2021)]

Moreover, mega-constellation programs have been planned and launched by some space companies such as Space-X or Amazon in order to provide global satellite communications services by Non-GeoStationary Orbit (NGSO) systems.

In order to achieve high-capacity satellite-to ground systems, especially in low elevation angles, Adaptive Optics can be now considered as the most used system to mitigate the atmospheric turbulence distortion effects.

1.3 Atmospheric turbulence effects on optical propagation

This section is dedicated to the description of the optical propagation through atmospheric turbulence. Consequently, the main parameters characterizing the propagation are introduced.

In order to deal with high data rates, the optical signals at both transmitter and receiver are guided in single mode fibers (SMF). The coupling between the SMFs and the free space is performed by telescopes. In Figure 1.3, the schematic diagram of a free-space optical link is shown. In this context, atmospheric turbulence induces wave phase and amplitude perturbations. Indeed, while amplitude perturbations induce modulations of the flux collected by the receiver telescope, phase perturbation induce speckles in the focal plane of the receiver telescope, hence degrading the coupling of the wave in the SMF.

Particularly, fluctuations of the total flux captured in the pupil are represented in the left part of Figure 1.4, as a function of the time, while the effects of phase fluctuations onto the signal coupled in a single-mode fiber at the focal plane are described in the right part of the same figure.

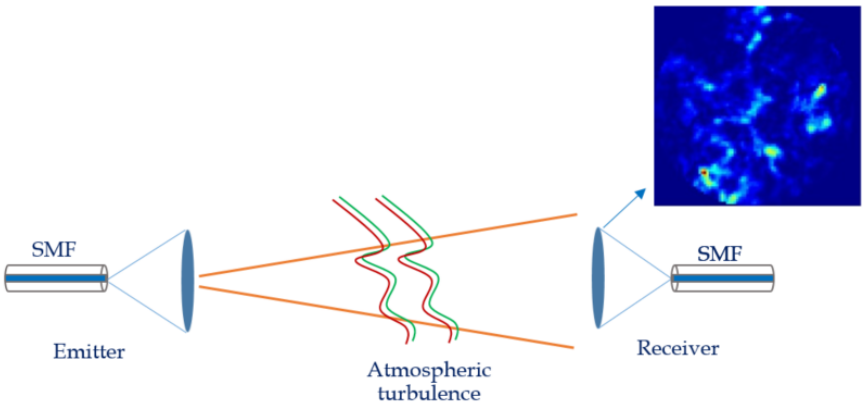

Figure 1.3: Schematic diagram of a propagation channel. In the top right-hand corner, the intensity distribution in the pupil plane is reported for a given turbulence condition.

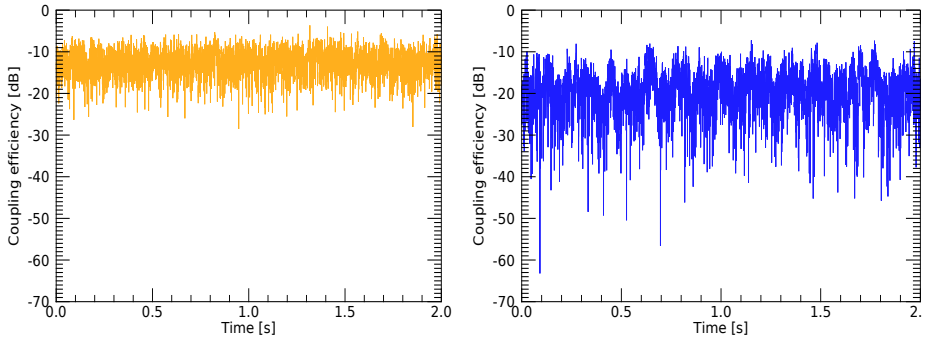

Figure 1.4: Power fluctuations as a consequence of amplitude and phase perturbations induced by atmospheric turbulence: (left) total power collected by the telescope, (right) power coupled in a SMF normalized by the total incident power.

1.3.1 Introduction to atmospheric turbulence

The complexity of the phenomena that characterize the Earth's atmosphere, related to the appearance of air masses of different density as well as to their motion due to the gravity and pressure gradient caused by this, has led scientists to adopt a phenomenological approach, thus describing it with its statistical properties.

The first description of atmospheric turbulence statistical properties was proposed by Kolmogorov [Kolmogorov (1941)]. The kinetic energy induced by large movements of air is injected within large eddies, and transmitted to smaller eddies until it is dissipated by friction. The larger scale of such eddies is called outer scale, and denoted by L_0, while the smallest scale by l_0. That is, below l_0, the kinetic energy is dissipated as heat due to friction, while L_0 results from macroscopic phenomena such as wind or meteorological perturbations.

The lengths of both inner and outer scale can range from a few millimeter near the ground to a few centimeter at the tropopause for the inner scale, and from one to hundreds of meters anywhere for L_0. The domain defined by these two scales is called inertial domain. In that domain, the turbulence is said to be fully developed. Moreover, all these phenomena lead to a fluctuations of the refractive index [Obukhov (1949)].

1.3.2 Main characteristics parameters

Refractive index fluctuations

Within the inertial domain and for an established turbulent regime (stationary in time and space), the variance of the difference in refractive index at two points in space, is given by [Obukhov (1949)]:

$$D_n(\boldsymbol{\rho}) = \langle |n(\boldsymbol{r}) - n(\boldsymbol{r}+\boldsymbol{\rho})|^2 \rangle = C_n^2 \rho^{\frac{2}{3}} \tag{1.1}$$

where the $\langle . \rangle$ represents the statistical average on time. $D_n(\boldsymbol{r})$ is the so called refractive index structure function, while C_n^2 the refractive index structure constant, which measures the magnitude of the refractive index fluctuations and is expressed as in $m^{-2/3}$.

In a first approximation, the C_n^2 profile can be seen as function of the altitude only, *h*. However, various models are available describing the C_n^2 profile.

Power spectral density of refractive index

Another way to characterize the fluctuations of the refractive index leads into the power spectral density. This quantity can be deduced from the structure function of the refractive index, thanks to a simple Fourier transform and to the Wiener-Khinchine theorem [Tatarski (1961)]. The spectrum, also called Kolmogorov spectrum, can be written as:

$$W_n(\mathbf{f}) = 0.033(2\pi)^{-2/3} C_n^2 f^{-11/3} \tag{1.2}$$

where f=|**f**| denotes the modulus of **f**, the spatial frequency, expressed in m^{-1}. This expression is valid in the inertial domain only. In order to take into account the influence of the inner and outer scales defined in the previous sections, von Karman proposed the following spectrum [McGlamery (1976)]:

$$W_n(\mathbf{f}) = 0.033(2\pi)^{-2/3} C_n^2 (f^2 + \frac{1}{L_0^2})^{-11/6} e^{\frac{-2\pi l_0 f^2}{5.91}} \tag{1.3}$$

Spatial coherence function

The spatial coherence function of the complex field Ψ, B_Ψ, is defined by:

$$B_\Psi(\boldsymbol{\rho}) = < \Psi(\mathbf{r}) \Psi^*(\mathbf{r} + \boldsymbol{\rho}) > \tag{1.4}$$

If the field perturbations are assimilated to those of a spherical or plane wave, B_Ψ is function of only ρ, and is given by the following formula [Fante (1975)]:

$$B_\Psi(\rho) = exp\Big[- (\frac{\rho}{\rho_0})^{5/3} \Big] \tag{1.5}$$

Furthermore, in case of plane wave:

$$\rho_0 = \Big[1.46 k_0^2 \int_0^L C_n^2(z) dz \Big]^{-3/5} \tag{1.6}$$

in which $\rho = |\rho|$, while z refers to the position along the optical path.

Fried parameter

Fried's parameter, denoted r_0, characterizes the effects of atmospheric turbulence on imaging. That is, λ / r_0 represent the average angular resolution of an infinite diameter telescope [Fried (1966)]. In this context, r_0 is given by the following expression, for a plane wave considering a Kolmogorov spectra:

$$r_0 = \Big[0.423 (\frac{2\pi}{\lambda})^2 \int_0^{z_{max}} C_n^2(z) dz \Big]^{-3/5} \tag{1.7}$$

Moreover, ρ_0 is also related to the Fried parameter by:

$$r_0 = 2.11 \rho_0 \tag{1.8}$$

1.3.3 Analytical resolution of the Helmholtz equation

As previously reported, distortions occur for a wave propagating through the atmosphere, due to refractive index fluctuations induced by atmospheric turbulence effects. In order to describe these distortions, several approaches already exist, relying on the resolution of the wave propagation equation.

We can consider a single component, E_i, of an electromagnetic wave that satisfies the *Helmholtz* equation:

$$(\nabla^2 + k^2)E_i = 0 \tag{1.9}$$

where k represents the wave number, also equal to $2\pi n(r)/\lambda$, and E_i any components of the electric field **E**. In this case k can be considered as a product between the refractive index, $n(\mathbf{r})$, and the wave number of the beam propagating through vacuum, k_0.

Weak perturbation regime: The Rytov approximation

In the particular case of small fluctuations, that is, assuming small amplitude of the perturbations induced by atmospheric turbulence, the Helmholtz equation 1.9 can be analytically solved. Following the approach used by Tatarski [Tatarski (1961)], an analytical solution of the Helmholtz equation can be found assuming the Rytov approximation, which considers the perturbations as multiplicative with respect to the unperturbed field. In this context, the turbulence impact on the field propagation is written as an exponential term, such as:

$$E_i = E_0 \Psi e^{-jkz} \text{ and } \Psi = e^{\chi + j\phi} \tag{1.10}$$

where E_0 is the non-perturbed term of the field, while χ and ϕ denotes the *log-amplitude* and the phase associated to the perturbation. Moreover, applying the parabolic approximation to the Eq. 1.10, one can also derive the expressions of χ and ϕ [Tatarski (1971)], which in turns lead to their power spectral densities. From the integral of this latter, the variance of χ and ϕ are given as following:

$$\sigma_\chi^2 = k_0^2 \int_0^L \int_0^\infty 2\pi f W_n(f) sin^2(\pi z \lambda f^2) df dz \tag{1.11}$$

$$\sigma_\phi^2 = k_0^2 \int_0^L \int_0^\infty 2\pi f W_n(f) cos^2(\pi z \lambda f^2) df dz \tag{1.12}$$

where $W_n(f)$ represents the index fluctuations spectra. Due to the term $sin^2(\pi z \lambda f^2)$ the integral 1.11 converges, whatever W_n (Kolmogorov or von Karman). In reverse, Eq. 1.12 converges only with the von Karman spectrum. For a Kolmogorov spectrum, σ_χ^2, called Rytov variance writes:

$$\sigma_{\chi_R}^2 = 0.5631 k^{7/6} \int_0^L C_n^2(z) z^{5/6} dz \tag{1.13}$$

It could be shown that the Rytov approximation remained valid as long as the expression of the variance of the log-amplitude, σ_χ^2, resulting from this approximation remained less than 0.3 [Fante (1975)].

The optical wave irradiance (sometimes called intensity), and denoted by I in the following, is given by the squared magnitude of the field: $(I = \Psi\Psi^* = I_0 e^{2\chi})$.

In Rytov regime, χ and Φ are considered as gaussian random variables, and σ_I^2, the normalized variance of the field intensity writes:

$$\sigma_I^2 = \frac{< I^2 >}{< I >^2} - 1 = exp(4\sigma_\chi^2) - 1 \tag{1.14}$$

In very weak perturbation regime ($\sigma_\chi^2 < 0.1$), the exponential term $e^{4\sigma_\chi^2}$ can be approximated by $1 + 4\sigma_\chi^2$, thus leading to:

$$\sigma_I^2 \simeq 4\sigma_\chi^2 \tag{1.15}$$

Beyond small perturbations

Considering a case of a satellite-to-ground downlink, as the elevation decreases, the amplitude of the perturbations as well as the scintillation effects increase, so that the expression of σ_χ^2 and therefore that of $\sigma_{\chi_R}^2$ increase without limit. It is possible to describe a moderate perturbation area, when $\sigma_{\chi_R}^2 \approx 1$, while a saturation zone can be defined close to the horizon, when $\sigma_{\chi_R}^2 \to \infty$.

In our case study, represented by a satellite-to ground optical link at 10 degrees elevation, the variance of the log-amplitude is about $\sigma_\chi^2 \approx 0.56$. In this context, intensity fluctuations limit the measurement on the wavefront sensor used in classical adaptive optics method [Primmerman et al. (1995)]. Moreover, since the Rytov approximation is no longer valid, another tool has to be used to analyze the perturbation. In the following, the description of such tool is reported.

1.3.4 In house propagation tool: TURANDOT

In order to avoid the assumption of small perturbations which reduces the validity range of the analytical expressions used in the previous sections, a numerical resolution of the propagation equation based on the phase-screen propagation modeling has been proposed by Martin and Flatté [Flatté et al. (1993)]. This is illustrated in the following Figure 1.5:

The split and step method used in this context consists of a piecewise solution of the propagation equation: considering a given volume, the principle is to solve the propagation equation by dissociating turbulence induced phase effects from diffraction effects induced by propagation. Moreover, the turbulence volume is discretized in several turbulent layers of thickness ∂h, numerically simulated by phase screens.

The thickness of the turbulent layers are large enough so that two successive phase screens can be considered decorrelated. Finally, the propagation of the optical wave between two screens takes place in a vacuum.

Within a layer, the impact of the refractive index heterogeneity is modeled by multiplying the field by a simple phase shift term, $e^{j\phi}$, corresponding to the path difference experienced by the optical wave through ∂h:

$$\phi(x, y, z + \partial h) = k_0 \int_h^{h+\partial h} \Delta_n(x, y, h) dh \tag{1.16}$$

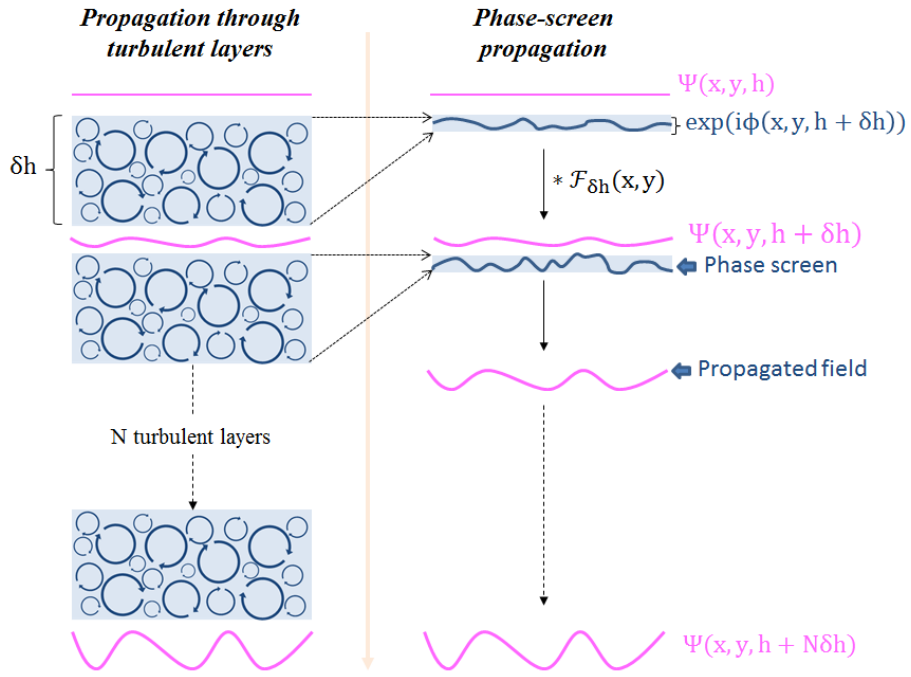

Figure 1.5: Principle of phase-screen propagation

where $k_0 = \frac{2\pi}{\lambda}$ denotes the wave number. Here, the field $\Psi(x, y, h + \partial h)$ at the output of a given layer of thickness ∂h, is written function of the input field $\Psi(x, y, h)$ as:

$$\Psi(x, y, h + \partial h) = \left[\Psi(x, y, h) e^{j\phi(x,y,h+\partial h)} * \mathcal{F}_{\partial h}(x, y)\right] \tag{1.17}$$

where $*$ denotes the convolution operator and $\mathcal{F}_{\partial h}(x, y)$ denotes the Fresnel propagator:

$$\mathcal{F}_{\partial h}(x, y) = \frac{e^{jk_0\partial h}}{j\lambda\partial h} e^{jk_0\left(\frac{x^2+y^2}{2\partial h}\right)} \tag{1.18}$$

The method described is then applied to the total sequence of phase screens representing the turbulence volume. The field propagation is described in this way as succession of both phase-perturbations added by the phase screens and propagation in the vacuum between each layers.

1.3.4.1 Temporal effects

In order to describe the temporal evolution of turbulence, the "frozen turbulence" hypothesis is used. Through this hypothesis, the effect of the translation of the turbulence due to the wind is considered as a major parameter with respect to the time evolution of the wavefront. In this way, at two different time instants only the translation due to the average transverse wind speed, denoted by V_T, is taken into account between two turbulent layers. The refractive index at an instant t can be thus written as $n(t) \approx n(\mathbf{r} - V_T(\mathbf{r})t$. That is, the temporal evolution is considered by translating the phase screens described in the last section transversely to the direction of propagation. The amplitude of this translation is determined as combination of

the apparent velocity, which is related to the angular displacement of the satellite, and the transverse wind velocity. It is so possible to write:

$$v(h) = h\Big(\frac{v_{sat}}{D_{sat}}\Big) + v_{wind}(h) \tag{1.19}$$

where h denotes the height of the considered layer ($h(z) = z\ sin(\theta)$), D_{sat} the distance between the satellite and the optical ground station, while the term $\frac{v_{sat}}{D_{sat}}$ represents the satellite angular velocity, also noted by ω_{sat}. In the previous equation v_{sat} denotes also the satellite velocity component orthogonal to the line of sight.

To describe the evolution of the wind function of the distance to the ground, a Bufton profile has been used throughout this thesis [Bufton (1973)]. It is defined as a function of the distance h by the wind speed at ground level v_G and the wind speed at the tropopause v_T as:

$$v_{wind}(h) = v_{ground} + v_T\ exp\Big(-\Big[\frac{(h-h_T)}{L_T}\Big]^2\Big) \tag{1.20}$$

where for the following, $L_T = 4800m$ represents the thickness of the tropopause, while $h_T = 12448m$ its height above the ground.

1.3.4.2 TURbulence simulator for spAce-grouND Optical Telecommunication

Such a modeling was firstly implemented in a propagation code called *PILOT* (Propagation and Imaging, Laser and Optics through Turbulence), developed at the French aerospace lab (ONERA). A version of PILOT was also developed at the ONERA, in which an automation of the input parameters is defined, such as turbulence and wind profile, C_n^2, satellite velocity etc. Each phase-screen is generated from a white noise, then colored in the Fourier domain by a von Karman turbulence spectrum. The latest version is also able to produce end-to-end simulations with tilt tracking, taking into account both point-ahead angle (PAA) and aperture mismatch while using downlink informations in order to pre-compensate the uplink. It can also deal with any type of wave forms, such as plane wave, spherical as well as Gaussian beams.

Despite these advantages, TURANDOT is a computationally intensive code, which results in a choice of analytical description of propagation phenomena. A reference case of a LEO-ground downlink at 10° will be presented in the Chapter 3.

1.3.5 Atmospheric turbulence effects on coupling into single-mode fibers

Fiber optical components, such as high-power Erbium Doped Fiber Amplifiers (EDFAs), coherent receivers, multiplexer units etc are key features for new future high data rates satellite ground downlinks, achieving thousands of Gbps.

In such a system, as reported in Figure 1.3, the optical signal is coupled into a SMF before being corrected and transmitted.

Mathematically, one can consider an incoming perturbed beam after the telescope pupil of diameter D as:

$$\Psi(\mathbf{r}) = \Psi_0 e^{\chi(\mathbf{r}) + j\phi(\mathbf{r})} \tag{1.21}$$

where Ψ_0 denotes the complex field amplitude without perturbation, ϕ represent the phase variations and χ the turbulence-induced log-amplitude fluctuations.

Furthermore, under paraxial propagation conditions, the matching of an unperturbed beam Ψ_0 and the SMF mode, M_0, can be characterized by the following overlap integral [Shaklan and Roddier (1988)]:

$$s^{pw} = \frac{\langle \Psi | M_0 \rangle}{(\langle \Psi | \Psi \rangle \langle M_0 | M_0 \rangle)^{1/2}} \tag{1.22}$$

where $\langle A|B\rangle = \int A(\mathbf{r}, z)B^*(\mathbf{r}, z)d^2\mathbf{z}$ is the scalar product associated with the norm defined by the power carried by the wave in its propagation direction. The SMF mode profile M_0 can be also approximated by a Gaussian mode, with its waist w_0 associated to the physical radius of the fiber.

The coupling efficiency corresponds then to the square modulus of the aforementioned overlap integral:

$$\eta = |s^{pw}|^2 \tag{1.23}$$

In the astronomical case, the maximum coupling efficiency with a SMF placed in the focal plane of the telescope is $\sim 80\%$. The effects of atmospheric turbulence on coupling with a single mode fiber were first described by [Shaklan and Roddier (1988)].

The compensation of turbulence-induced phase distortion can also be obtained using Adaptive Optics (AO) ahead of the SMF coupling. An analytical expression of the single mode coupling efficiency for partially-corrected light was obtained by Ruilier [Ruilier and Cassaing (2001)] in 2001, while a numerical evaluation of the SMF coupling efficiency for a laser light distorted by atmospheric turbulence was reported in [Dikmelik and Davidson (2005)], demonstrating how the SMF-coupling efficiency decreases rapidly with increasing turbulence strength and link distance.

1.4 Assessment of link performance

The effects of atmospheric turbulence presented in the previous sections are not the only factors to be considered when evaluating the performance of an optical link such as the one considered in this thesis. In this section, in order to establish a link budget for the performance assessment of the LEO-to-ground downlink at 10° elevation, we will first introduce the other main figures of merit to be considered, such as the gains related to the transmitter/receiver, the signal attenuation etc.

1.4.1 Link budget

The goal of this section is to give an overview on the main parameters used in a link budget of a LEO-to-ground optical communication link. Different factors affect the performance of the link, such as attenuation due to turbulence, pointing errors, the gain of antenna, emitted power etc. The establishment of a link budget allows the determination of the overall power margin defined as the difference between the allocated power, available at the ground receiver, and the power required on board to achieve a given performance.

Such received power, P_R, is estimated as a function of the emitted optical power, P_E, and is given by:

$$P_R = G_E P_E \underbrace{L_{atm} L_{fs} L_{turb}}_{L_{total}} G_R \tag{1.24}$$

where G_E and G_R denote the emitter and receiver gain respectively, while L_{total} represents the power losses related to different phenomena, such as free-space propagation losses (L_{fs}), atmospheric turbulence (L_{turb}), absorption and scattering effects, as well as attenuation due to clouds (L_{clouds}). Among them, free-space losses and both transmitter and receiver gains results as predominant effects on the budget link.

Furthermore, the information quality of a satellite-to-ground link is often specified through the bit error rate (BER), which represents the ratio between the incorrect detected bits (errors) on the number of transmitted bits. Assuming an on-off keying (OOK) modulation format with non-return to zero (NRZ) pulses, and that the probabilities to obtain a bit equal to 0 or 1 are the same, $(p(0) = p(1) = 1/2)$, the bit-error rate has been widely described by [Agrawal (2012)] as:

$$BER = \frac{1}{2} erfc\Big(\frac{Q}{\sqrt{2}}\Big) \approx \frac{exp(-Q^2/2)}{Q\sqrt{2\pi}} \tag{1.25}$$

In the same way, assuming that after the propagation through the atmosphere, the optical received signal is amplified by an Erbium-Doped Fiber Amplifier (shot noise predominant), the signal-to-noise ratio can be written as:

$$SNR \approx \frac{P_R}{4h\nu B_E} = Q^2 \tag{1.26}$$

where P_R denotes the received power expressed in W, $h\nu$, the photon energy, and B_E, the number of bits per second. In this context, the Q-factor represents the minimum signal-to-noise ratio (SNR) required to obtain a specific BER.

Antenna gains

As for radio frequency systems, it is possible to define the optical antenna gains for the transmitter and receiver modules. The transmitter gain reported in [Klein and Degnan (1974)] rely the transmitter diameter to a coefficient which depend on the optical losses related to the presence of a central obstruction, g_T. For a general pupil without central obstruction $g_T = 0.8145$, and the transmitter gain is thus given by:

$$G_E = 10log_{10}\Big(\Big(\frac{\pi D_{Tx}}{\lambda}\Big)^2 g_T\Big) \tag{1.27}$$

In the same way, the receiver gain writes:

$$G_R = 10log_{10}\Big(\frac{\pi D_{Rx}}{\lambda}\Big)^2 \tag{1.28}$$

where D_{Tx} and D_{Rx} denote the emitter and receiver diameter respectively.

Signal attenuation

The transmitted and received flux are attenuated by the transmission of the various optical components of both transmitter and receiver modules, denoted by L_{Tx} and L_{Rx}. Furthermore, other important attenuation rely on the pointing losses, L_p, due to the miss-pointing of the transmitted beam toward the ground station, as well as both absorption and scattering losses, L_{ab}, and clouds losses, denoted by L_{clouds}, which depends on their altitude, behavior etc.

Free-space losses

The free-space propagation losses are reported in [Friis (1946)], for a given satellite-to-ground distance, d_{sat-gr}, and are given by the following expression:

$$L_{fs} = \left(\frac{\lambda}{4\pi d_{sat-gr}}\right)^2 \tag{1.29}$$

Moreover, such losses are not even the only ones present. The losses due to molecular absorption in the atmosphere, L_{atmo}, as well as that one related to the clouds,L_{clouds}, have to be taken into account. All these terms are considered in the link budget as L_{total}, and removed from the overall transmitted power.

Link margin

The link margin corresponds to the difference, expressed in dB, between the allocated signal power and the minimal power required to achieve a given link performance.

$$Link\ margin = (P_E + G_E - L_{total} + G_R) - P_{total} \tag{1.30}$$

In the Chapter 3 an example of a link budget for a transmission between a LEO satellite and an optical ground station is presented.

1.5 Turbulence mitigation techniques

In the previous section, we presented the effects of atmospheric turbulence on optical propagation, thus defining the main characteristics parameters used in this context. Moreover, we noticed how this leads to random fluctuations in both the amplitude and phase of the received signal, and finally in signal fadings. The aim of this section is to present different mitigation techniques to improve efficiently channel fading. Two major approaches will be considered, based on *Passive* and *Active* turbulence mitigation methods. Regarding passive compensation methods, an overview of diversity techniques is shown in 1.5.1, while active methods, such as Adaptive Optics, are presented in subsection 1.5.2.

1.5.1 Passive methods

In order to mitigate atmospheric turbulence effects, *diversity* techniques are generally employed, operating in three different domain, such as time, frequency and space. The idea in both cases is to transmit the same data through different channels or in different time in order to average turbulence effects on uncorrelated beams.

1.5.1.1 Time diversity

Time diversity techniques are normally used for time selective fading channels, where data are transmitted multiple times, thus relying on the temporal decorrelation of the atmosphere. Indeed, the coherence time of the link is much higher than the one of symbol generation: 1 millisecond for atmospheric turbulence, compared to 1 nanosecond to generate a bit. In addition, the larger the aperture, the longer the correlation time. This technique is used in modern communication system through interleaving of the transmitted symbols and channel coding [Khalighi et al. (2009); Xu et al. (2008)]. However, time diversity techniques are often subject of long delay latencies, and large buffer memories are necessary. As a consequence, this technique is not applicable without combining it with other techniques, as it increases the overall system complexity.

1.5.1.2 Wavelength diversity

Besides the previous time diversity technique, where data are transmitted multiple times, the second way to reduce the overall fluctuations of the received signal is the transmission of the same modulated data through multiple beams with different wavelength: i.e. the case of wavelength diversity. As the refractive index variations are different for different wavelengths, the fading is not same for distinct wavelengths. The effects of atmospheric turbulence on wavelength were studied in different works [Giggenbach et al. (2006)]. However, the main limitation of this latter consists in a sufficient wavelength separation in order to obtain effective diversity. Only a small reduction of fadings is expected with this method [Kiasaleh (2017)].

1.5.1.3 Spatial diversity

Another approach to mitigate atmospheric turbulence effects is to use spatial diversity [Khalighi (2021)]. Aperture separation should be greater than the coherence length of the atmosphere, r_0, so that multiple beams may be considered as independent. Particularly, this technique can employ multiple apertures either at the transmitter - and called transmit diversity, or at the receiver - receive diversity, or also at both sides and called multiple input multiple output (MIMO). In this regard, transmit and receiver diversity require the use of multiple emitter and detection modules respectively. Finally, these advantages come at the expense of greater complexity [Khalighi et al. (2009)].

Moreover, at both receiver/transmitter, it is not always easy to ensure the required spacing between the apertures. The effective number of detectors as well as the number of transmitted beams are limited. Performance parameters such as complexity, cost, efficiency, accuracy of modulation times and availability of space, will in practice however limit the order of diversity to less than ten [Kaushal and Kaddoum (2017)].

Always considering the spatial diversity, another mitigation approach consists to use mode diversity reception with large telescope and multiple propagation modes of a multi-mode fiber (MMF) [Geisler et al. (2016); Arikawa and Ito (2018)]. The method is based on a complex modulation format, coherent detection and digital processing (DSP), which are not compatible with low cost solutions.

Same mitigation approach relying on mode division multiplexing is also proposed by the German Space Agency (DLR), using the Cailabs' Multi-Plane Ligh Conversion (MPLC) device in order to perform mode decomposition [Calvo et al. (2020)].

1.5.2 Introduction to active methods

In active methods servo-controlled optoelectronic systems are used, based on the measurement and correction of perturbation effects.

Compared to the passive methods seen in the previous section, we will consider here active turbulence mitigation systems, mainly divided into two categories, depending on the device employed to compensate the effects of turbulence: the deformable mirror -based and the coherent combining active methods.

In the Section 1.5.3, we will refer to the first category as the adaptive optics method, widely described in the following section, while in Section 1.5.4 the coherent combining method used in this thesis is presented.

1.5.3 DM based active methods

1.5.3.1 Introduction to adaptive optics systems

Although proposed by Babcock [Babcock (1953)] in 1953, the first research program started in the early 1970s pushed by the Defence Advanced Research Projects Administration (DARPA), while 1990s the Very-Large Telescope (VTL) agreement was signed between some European partners such as Paris-Meudon Observatory, ONERA, the European Southern Observatory (ESO) and the COME-ON project started. Within this framework a low-order system with 19-actuators deformable mirror (DM) and a 20 sub-aperture Shack-Hartmann (SH) wavefront sensor achieved the diffraction-limit of a 1.5m telescope in the NIR [Rousset et al. (1990)]. Nowadays, Adaptive Optics systems are used in several fields of interests. We will present here the operational principle of a standard AO method, as well as the challenges using it in the FSO context.

After propagating through the atmospheric turbulence, the incident perturbed beam is received at the OGS and can be therefore corrected by AO systems. The general principle and components of an AO system is presented in the following section [Michau and Petit (2021)], and a focus on the main challenges can be found in the subsection 1.5.3.4.

1.5.3.2 Principle

A general principle and a schematic diagram of an Adaptive Optics system is presented in Figure 1.6. Three main components can be distinguished:

- the *wavefront sensor* (WFS), which measures the instantaneous phase or the local slope of the incoming disrupted beam
- the *real-time computer* (RTC) that processes the measurement sent by the WFS, translating them into command for the deformable mirror

- the *deformable mirror* (DM), which introduces the associated deformations through the different actuators in order to compensate the phase measurements made by the WFS

More detailed review of the principles and characteristics regarding the main AO components is outlined as follows.

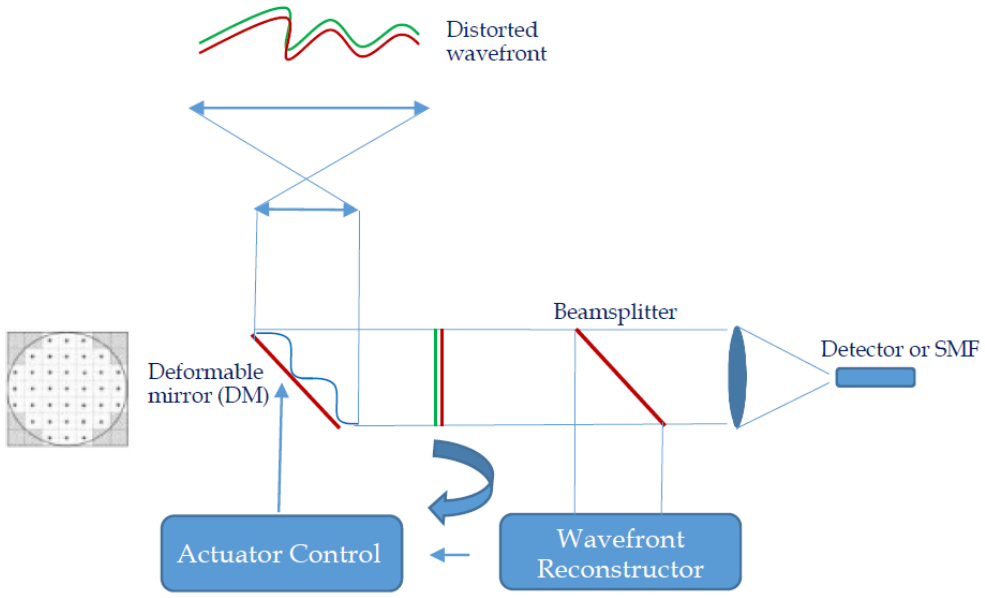

Figure 1.6: General working principle of a closed-loop Adaptive Optics system

1.5.3.3 Adaptive Optics components

Wavefront sensors

The most commonly wavefront sensor measures the local slope of the wavefront, sampling the total pupil by sub-apertures. An overview of this Shack-Hartmann wavefront sensor (SH-WFS) is given in Figure 1.7. Other types of wavefront sensors are used in order to measure the local slopes, such as the pyramidal, or the curvature WFS [Rousset (1993); Ragazzoni (1996); Roddier (1988)].

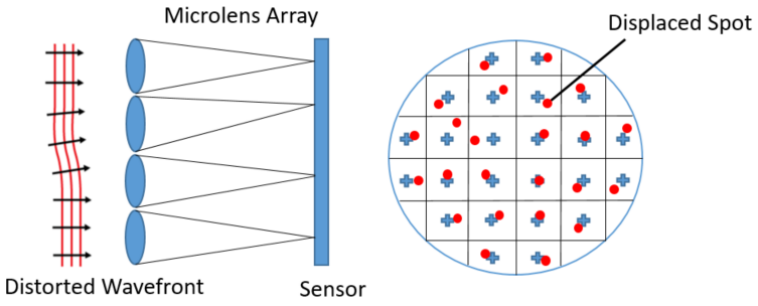

Figure 1.7: Principle diagram of a Shack-Hartmann wavefront sensor.

As reported in Figure 1.7, through the image spot at the focal plane of the sub-pupils the wavefront local-slopes are derived.

The local-slope information is carried out by a measurement of a center of gravity (right).

Being ϕ and $|\Psi(\mathbf{r})|$ the phase and the amplitude of the complex field in the pupil plane, the expression of the local-slope in a subaperture *p* in the *x* and *y* direction can be derived:

$$\alpha_x^p = \frac{\int\int_{S_p} \frac{\partial\phi(\mathbf{r})}{\partial x}|\Psi(\mathbf{r})|^2 d\mathbf{r}}{\int\int_{S_p}|\Psi(\mathbf{r})|^2 d\mathbf{r}} \tag{1.31}$$

$$\alpha_y^p = \frac{\int\int_{S_p} \frac{\partial\phi(\mathbf{r})}{\partial y}|\Psi(\mathbf{r})|^2 d\mathbf{r}}{\int\int_{S_p}|\Psi(\mathbf{r})|^2 d\mathbf{r}} \tag{1.32}$$

In weak perturbations, $|\Psi(\mathbf{r})|$ may be supposed constant on the pupil surface. Furthermore, the slope vector, α, is a linear function of the phase in the pupil, ϕ:

$$\alpha = M\phi \tag{1.33}$$

However, the measurement writes:

$$\tilde{\alpha} = M\phi + n \tag{1.34}$$

where n denotes the noise vector impacting the measurement, while *M* is a linear operator.

Deformable mirror

The deformable mirror (DM) consists of a finite set of actuators, thanks to which they can deform their shape. There is a wide variety of DM available on the market, depending on the pupil diameter, on the thickness of the reflective membrane or even on the technology concepts used to control the actuators. A first classification can be made depending on their surface, thus considering a *segmented* or a *continuous faceplate* concept.

Under the hypothesis of linearity of the DM, the corrected phase can be written as:

$$\phi_{corr} = \overline{\mathbf{M}}\mathbf{u} \tag{1.35}$$

where $\overline{\mathbf{M}}$ denotes the influence matrix of the DM and $\mathbf{u}$ the vector of commands applied to the deformable mirror actuators.

The phase description can be expressed in both a set of measurement points (or pixels), as well as a decomposition into a mode basis. Several mode basis exist, and the most commonly used is that of Zernike polynomials, which represents an orthonormal basis on a circular pupil [Noll (1976)].

Each Zernike polynomial has an analytical expression written as the product of a radial function, $\mathbb{R}_n^m(\mathbf{r})$, and an azimuthal function, $\mathbb{O}_n^m(\mathbf{r})$:

$$Z_i(\mathbf{r}) = \mathbb{R}_n^m(\mathbf{r})\mathbb{O}_n^m(\mathbf{r}) \tag{1.36}$$

where the *n* and *m* indexes denote respectively their radial and azimuthal degrees.

By defining ϕ_{turb} the phase degraded by turbulence, ϕ_{corr} the correction induced by the deformable mirror and ϕ_{res} such as:

$$\phi_{res}(\mathbf{r},t) = \phi_{turb}(\mathbf{r},t) - \phi_{corr}(\mathbf{r},t) \tag{1.37}$$

and considering a DM which perfectly corrects the first n radial orders of Zernike, the residual phase variance is given by [Fusco and Conan (2004)]:

$$\sigma^2_{res} \simeq 0.46(n+1)^{-5/3}(\frac{d}{r_0})^{5/3} \tag{1.38}$$

Feedback loop

A standard Adaptive Optics feedback closed-loop is shown in Figure 1.8. Considering α_{corr} the WFS measurements if $\phi_{turb} = 0$, the relation with the command voltages can be written as:

$$\alpha_{corr} = \overline{\mathbf{M}}_{int}\mathbf{u} \tag{1.39}$$

where $\mathbf{u}$ are the commands applied to the DM, and $\overline{\mathbf{M}}_{int}$ represents the interaction matrix which can be experimentally determined. The choice of a control law structure is based on a performance criterion. The most commonly used criterion is to minimize the measurement provided by the detector at each temporal instant: i.e. to find the commands minimizing at instant t the following relation:

$$\epsilon_t(\mathbf{u}) = \| \, m_t - \overline{M}_{int}u_t \, \|^2 \tag{1.40}$$

where m_t represents the available measurement. This approach leads quite naturally to an integrator. The least squares solution of the minimization problem is given by:

$$\partial\mathbf{u}_{t+1} = \overline{\mathbf{M}}^*_{int}\mathbf{m}_t \tag{1.41}$$

where $\overline{\mathbf{M}}^*_{int}$ is the inverse generalized of $\overline{\mathbf{M}}_{int}$: $\overline{\mathbf{M}}^*_{int} = \left(\overline{\mathbf{M}}^T_{int}\overline{\mathbf{M}}_{int}\right)^{\dagger}\overline{\mathbf{M}}^T_{int}$. The correction system can be written as:

$$\mathbf{u}_{t+1} = \mathbf{u}_t + g\partial\mathbf{u}_{t+1} \tag{1.42}$$

where g must to be chosen on the basis of a trade-off between accuracy and stability of the feedback loop.

Figure 1.8: Schematic of an Adaptive Optics feedback closed-loop

1.5.3.4 Challenges

As we stated in the previous paragraph, the Shack-Hartmann wavefront sensor (SHWS) is widely used. However, as the turbulence increases, amplitude fluctuations can no longer be ignored, and an error on the wavefront measurement appears. In this context, the adaptive optics performance is drastically degraded [Primmerman et al. (1995)]. These effects were also demonstrated on a SHWF, in case of strong perturbation regime, by Barchers [Barchers et al. (2002, 2003)]. Moreover, to limit the complexity of such a system (this approach requires complex, bulky and costly setup, using both deformable mirror and wavefront sensor), the investigation of complementary methods is addressed in the next part of this manuscript.

In the following sections we will present a second approach in order to mitigate the atmospheric turbulence effects, in the particular case of strong perturbation regime, as the one defined by a LEO-ground satellite at $10°$ of elevation.

1.5.3.5 Sensorless Adaptive Optics

In Sensorless adaptive optics the deformable mirror is controlled in order to maximize a criterion estimated from the measurements at the focal plane of the system, without the use of a wavefront sensor. In that case, the signal coupled in the SMF is the criterion to maximize. A schematic diagram of a Sensorless AO adapted to focusing in a single-mode fiber is proposed in Figure 1.9.

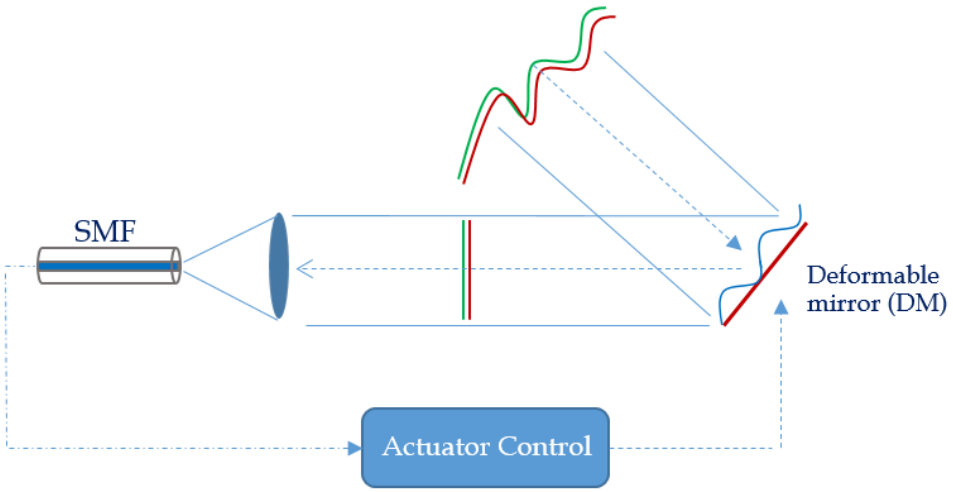

Figure 1.9: Sensorless Adaptive Optics for SMF focusing. Adapted from [Piscaer et al. (2019)]

In order to compensate phase distortion dynamically, various algorithms have been developed over time [Brignon (2013)]. Among them, it is worth mention the multidither principle reported in [O'Meara (1977)], or the most commonly used hill-climbing algorithm, the stochastic parallel gradient descent (SPGD) algorithm [Vorontsov et al. (1997); Vorontsov and Sivokon (1998)]. These algorithms, however, to obtain optimal solution require lots of iterations increasing with the number of actuators of the DM.

This technique has recently gained more attention, being employed in a wide range of applications and especially in free-space optical communications. In this context, iterative optimization of the signal of interest is performed. However, the number of iteration require a large bandwidth compared to that of the fluctuations.

Considering a typical case of a LEO-to-ground optical link, bandwidths of hundreds of kHz order are required, difficult to reach with enabling DM.

The implementation of the previous dithering techniques requires the adjustment of parameters such as the dithering amplitude, the loop gain factor etc. These adjustments are usually made empirically. Martin Booth proposes an approach called "model-based" in which a mathematical representation of the optical system is proposed to improve the optimization algorithm [Booth (2006)]. The speed of convergence is slightly improved. Nevertheless, the estimation of the parameters defining the model remains tricky.

A drastic way to accelerate the convergence is to treat a multidimensional criterion. Several authors propose to use the whole image at the focal plane to control the DM. Such an approach is close to the old phase retrieval problem [Fienup (1982)]. Carrizo proposed a sequential optimization increasing the brightness of a speckle in the focal plane [Carrizo et al. (2018)]. A linearization of the inverse problem is also proposed by Piscaer [Piscaer et al. (2019)]. Machine learning approaches have recently been applied in adaptive optics in order to further optimize the searching criterion: various model-based methods with an artificial or convolutional neural network have been implemented, as proposed by [Li and Zhao (2017); Paine and Fienup (2018); Tian et al. (2019); Vera et al. (2021)].

1.5.4 Coherent combining

1.5.4.1 Principle

In an adaptive optics system, the disturbed wave is reshaped in free space by a deformable mirror and then coupled with the mode of a SMF. Another approach, proposed in Noah Schwartz thesis [Schwartz (2009)], is to couple the perturbed wave with a set of propagation modes associated with different waveguides, and then coherently add these guided modes. The present approach is proposed in Figure 1.10.

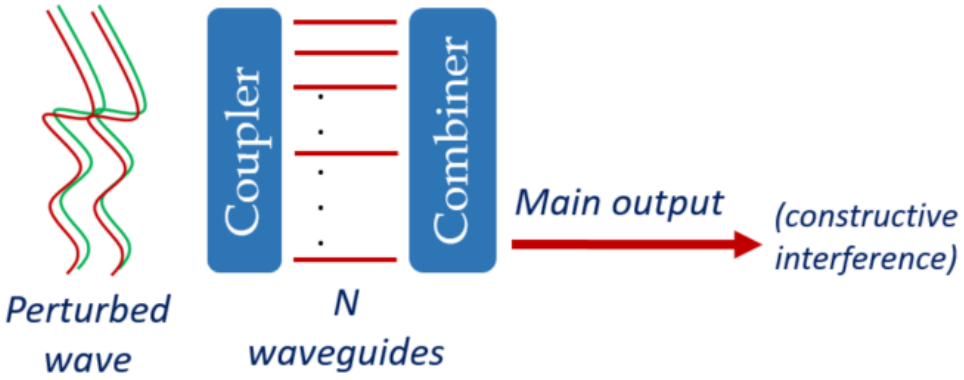

Figure 1.10: Principle of coherent combination

The coupling with guided modes can be achieved by a Space-Division Multiplexing (SDM), a device developed to increase the transport capacity of multimode fibers [Richardson (2016); Essiambre and Tkach (2012)]. Such devices are described in Section 1.5.4.2. On the other hand, the combining can be done with a photonic integrated circuit (PIC) when the number of modes considered is relatively high. Different concepts can be considered for this, such as using active Mach-Zehnder intereformeters (MZI) arranged in a tree-like manner (Figure 1.11). Furthermore, different photonic integrated circuit platforms will be introduced in the following Section 1.5.4.3.

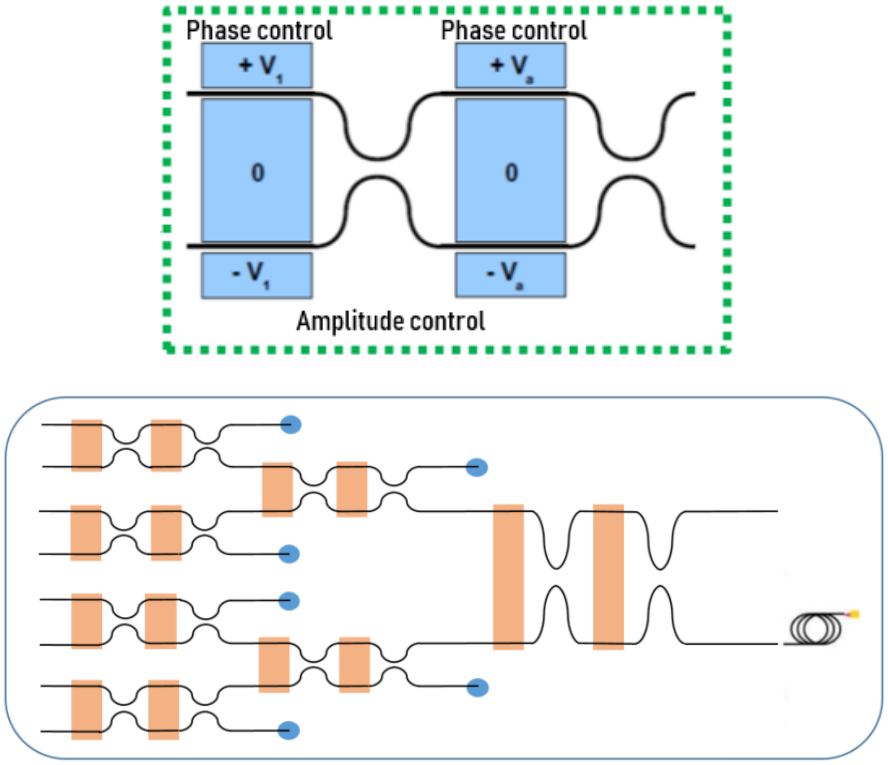

Figure 1.11: Integrated optical Mach-Zehnder: (Up) Principle of an integrated active MZI, (Down) cascade of MZI based PIC

1.5.4.2 Spatial-Division Multiplexing

1.5.4.2.1 Propagation modes

This paragraph is dedicated to the description of usual propagation modes used in spatial multiplexer devices. In this context, the concept of spatial mode decomposition is a central subject of this thesis.

From the Helmholtz equation reported in 1.3.3 and letting *z* the direction of propagation, it is also possible to rewrite the distribution of any components of the electric field as:

$$E_i(x,y,z) = \Psi(x,y,z)exp(-jkz) \tag{1.43}$$

where now $\Psi(x,y,z)$ represents a complex scalar function that will define the non-plane wave part of the field. The Helmholtz equation thus writes as:

$$\frac{\partial^2\Psi}{\partial^2 x} + \frac{\partial^2\Psi}{\partial^2 y} + \frac{\partial^2\Psi}{\partial^2 z} - 2jk\frac{\partial\Psi}{\partial z} = 0 \tag{1.44}$$

The paraxial approximation, which consists of assuming a small variation of the amplitude along the direction of propagation and a small axial variation compared to the perpendicular direction leads to the following expression:

$$\frac{\partial^2\Psi}{\partial^2 x} + \frac{\partial^2\Psi}{\partial^2 y} - 2jk\frac{\partial\Psi}{\partial z} = 0 \tag{1.45}$$

A solution of this equation is the Gaussian beam mode:

$$E(r,z) = \Big(\frac{w_0}{w(z)}\Big)exp\Big(\frac{-r^2}{w^2(z)} - jkz - \frac{j\pi r^2}{\lambda R(z)} + jarctan(\frac{z}{z_R})\Big) \tag{1.46}$$

where *w(z)* represents the so-called **beam radius**, which is the value of the radius at which the field falls to $1/e$ with respect to its on-axis value.

$$w(z) = w_0\Big[1 + \Big(\frac{\lambda z}{\pi w_0^2}\Big)^2\Big]^{1/2} \tag{1.47}$$

where w_0 denotes the beam radius at z=0, which is called **beam waist radius**, while *R* parameter represents the radius of curvature, given by:

$$R(z) = z + \frac{1}{z}\Big(\frac{\pi w_0^2}{\lambda}\Big)^2 \tag{1.48}$$

Finally, the Rayleigh distance, Z_R, is the distance at which the wavefront surface is twice the surface at w_0:

$$Z_R = \frac{\pi w_0^2}{\lambda} \tag{1.49}$$

In Figure 1.12 the evolution of the Gaussian mode following the *z* axis is presented.

We can also deal with solutions with a more complex transverse variation of the electric field, called **high-order Gaussian modes**.

Particularly, Hermite polynomials, $H_m(u)$, represent a solution of the differential equation $\frac{d^2H(u)}{du^2} - 2u\frac{dH(u)}{du} + 2mH(u) = 0$, with m positive integer.

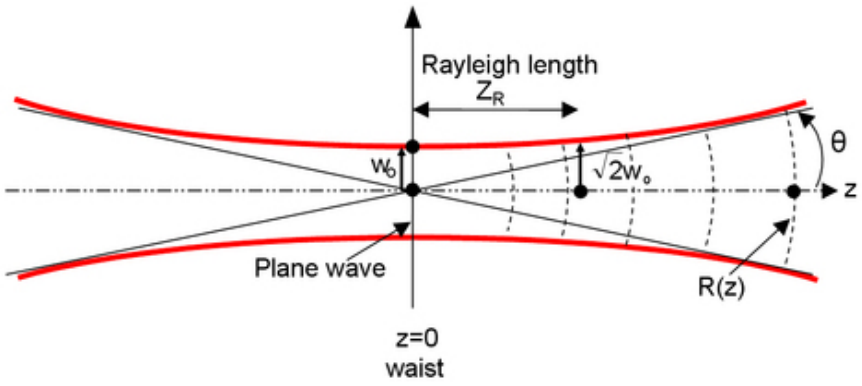

Figure 1.12: Gaussian beam propagation properties

The general expression for the Hermite-Gaussian family of index m in the x direction and n in the y direction is given by the following expression:

$$E_{mn}(x,y,z) = \Big(\frac{1}{\pi w^2 2^{m+n-1} m!n!}\Big)^{1/2} H_m\Big(\frac{\sqrt{2}x}{w}\Big) H_n\Big(\frac{\sqrt{2}y}{w}\Big) \cdot exp\Big[\frac{-(x^2+y^2)}{w^2} - jkZ - \frac{j\pi(x^2+y^2)}{\lambda R} + j(m+n+1)arctan(\frac{z}{z_R})\Big] \tag{1.50}$$

In a cylindrical coordinate system, a general solution with a field variation function of the polar angle ϕ is found. This solution defines the Laguerre-Gaussian modes family, with $L_{pl}(u)$ being the generalized Laguerre polynomials with *p* which represents the radial direction and *m* the angular index:

$$E_{pl}(r,\phi,z) = \Big[\frac{2p!}{\pi(p+m)!}\Big]^{1/2} \frac{1}{w(z)} \Big[\frac{\sqrt{2r}}{w(z)}\Big]^m L_{pm}\Big(\frac{2r^2}{w^2(z)}\Big) \cdot exp\Big[\frac{-r^2}{w^2(z)} - jkz - \frac{j\pi r^2}{\lambda R(z)} - j(2p+m+1)arctan(\frac{z}{z_R})\Big] \tag{1.51}$$

Figure 1.13 presents the spatial profile (intensity: left, phase: right) of both 16 first Hermite-Gaussian modes (a) and (b) 16 Laguerre-Gaussian modes.

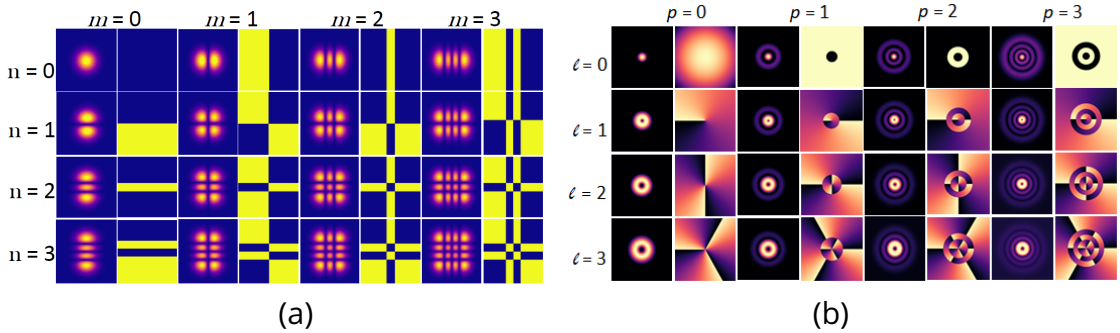

(a) (b)

Figure 1.13: Spatial profile (intensity: left, phase: right) of both first 16 Hermite-Gaussian modes (a) and (b) 16 Laguerre-Gaussian modes.

Since each Hermite-Gaussian mode can be expressed as a linear combination of Laguerre-Gaussian modes, and vice versa, the Hermite-Gaussian mode basis will be applied throughout this manuscript [Abramochkin and Volostnikov (1991); Kimel and Elias (1993)]. Moreover, for common single-mode step-index fibers with cylindrical symmetry it is possible to approximate the fiber modes by suitable free-space modes. In the case of a weakly guiding in such step-index fiber, the fiber modes are given by the so-called Linearly Polarized (LP) modes, and the field distribution is given by the solution of the Helmholtz equation. An approximation of LP modes by free-space Laguerre-Gaussian modes is reported in [Brüning et al. (2015)], shownig the overlap relation between both mode sets as a function of a scale parameter for the free space as well as the fiber parameters.

1.5.4.2.2 Mode demultiplexer devices

This section aims to give an overview of the most promising devices realizing first step used in the latter presented approach: the mode demultiplexer device.

Fiber Collimator Array (FCA)

Fiber collimator array is a promising alternative to conventional adaptive optics systems, and multi-aperture receiver with optical combining architecture are reported in various works [Lao et al. (2020); Dikmelik and Davidson (2005); Bruesselbach et al. (2004); Vorontsov and Lachinova (2008); Wu et al. (2010)] as turbulence mitigation technique. An example of FCA with 37 subapertures is presented in Figure 1.14 [Vorontsov and Lachinova (2008)].

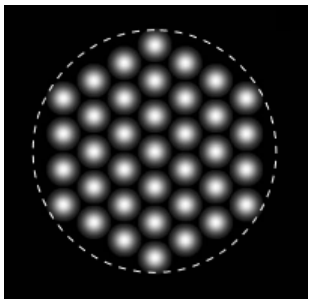

Figure 1.14: Focus on the geometry of a circular aperture -dashed circle-, with a set of 37 subapertures. From [Vorontsov and Lachinova (2008)].

An architecture based on collective active phase control of a large number of fiber has been presented by Bourderionnet [Bourderionnet et al. (2011)], that involves a microlens array of 64-polarization maintaining (PM) fibers on a silicon wafer placed in an 8x8 matrix square arrangement. In this case, PM fibers are inserted in each hole, polarization oriented, glued and polished in the holder, thus resulting in a fiber array that is well positioned in front of the microlens array. The limit on the number of fibers has recenlty reached 100, resulting in a fiber array of 127 fibers configured as a hexagon distribution, which is the largest fiber laser array for coherent beam combining (CBC) [Chang et al. (2020)]. Despite this large number, the positioning of the fibers in front of the microlens array requires precise control of the structure

and the manufacturing process, resulting in an expensive and complex technique. To overcome these drawbacks, other multiplexing solutions are described in the following section.

Photonic Lantern

First used in astrophotonics and space photonics, photonic lanterns are now used as multiplexing devices in the context of free-space optical communications [Leon-Saval et al. (2017)]. Despite their investigation in astronomy and the use of large-core multimode fibers since 1980s, only a few years ago more complex forms of light manipulation have been considered [Leon-Saval et al. (2014); Birks et al. (2015); Diab and Minardi (2019)]. A photonic lantern represents the interface between a multi-mode fiber and a set of N single-mode waveguides.

A schematic of a Photonic Lantern is shown in Figure 1.15, with a cross-section in different positions of the taper. The transition between the multi-core and the single mode fibers is well described in [Leon-Saval et al. (2010); Birks et al. (2015)]. Such transition can be realized by using different techniques: firstly, using an all solid standard optical fiber splitter/combiner, in which a bundle of SMFs was inserted into a low index glass capillary then fused and tapered down to form a solid MMF at the other end. Moreover, another interesting approach consists in using a multimode fiber with an array of identical SMFs. In this case, the multimode core is tapered, while placing a low refractive index jacket around the fibers to form the cladding of the MMF. A practical guide to filament tapering is also recently reported by Davenport et al. [Davenport et al. (2021)], in which SMFs were stacked inside a low refractive index, which was then heated and tapered to produce a transition from single-mode to multi-mode.

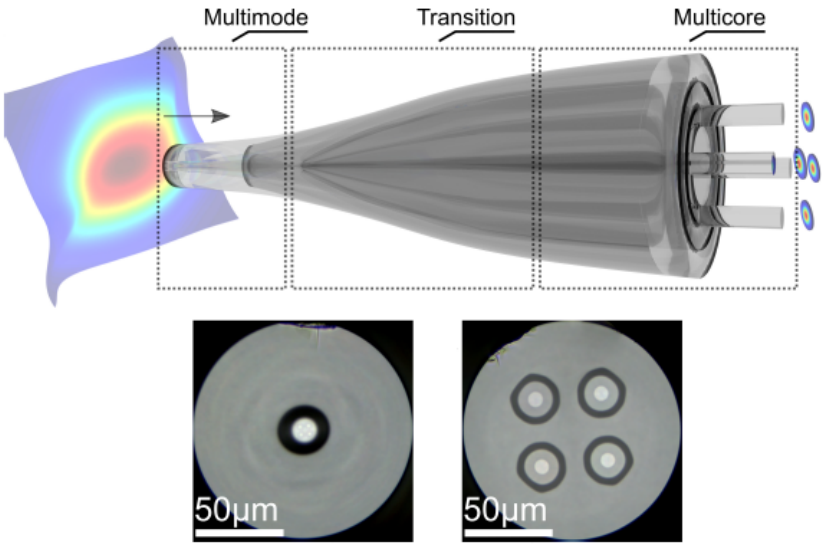

Figure 1.15: Schematic of a Photonic Lantern device (up), and microscope images of a fiber cross-section at the input and output of the taper (down). From [Cruz-Delgado et al. (2021)]

Nowadays PLs are being used in several fields, such as astronomy, collecting light from a telescope with a 1 x 7 PL [Diab et al. (2020)], wavefront sensing (19 single-mode outputs of the PL) [Norris et al. (2020); Cruz-Delgado et al. (2021)], spectroscopy (61-modes photonic

lantern) [Noordegraaf et al. (2010)], optics communications [Zhang et al. (2020a)], as well as bio imaging applications (121 PL outputs) [Choudhury et al. (2020)].

However, it is worth noting that the fabrication complexity of PLs increases as the number of modes increases, and lack of study about response of parameters are still unsolved problem. That is, the higher order PL-modes are more affected to perturbations, thus being vulnerable to minor imperfections that may arise during the fabrication process.

Multi-Plane Light Conversion

Another spatial-multiplexer device has recently been proposed: the so-called Multi-Plane Light Conversion (MPLC) device. The compactness and ease of integration of this device makes it one of the most suitable device for spatial division multiplexing. The working principle is presented in Figure 1.16 (left), as well as a photograph of the final realization (right) [Labroille et al. (2014)]. Basically, it is based on a succession of phase-screens that, separated by optical Fourier transforms, allows to convert any modal distribution into another selected one. That is, this device can take an input beam consisting on N orthogonal spatial components and transform them into N spatially separate beams which will form the output array. In Figure 1.16 (right), the produced device is reported:

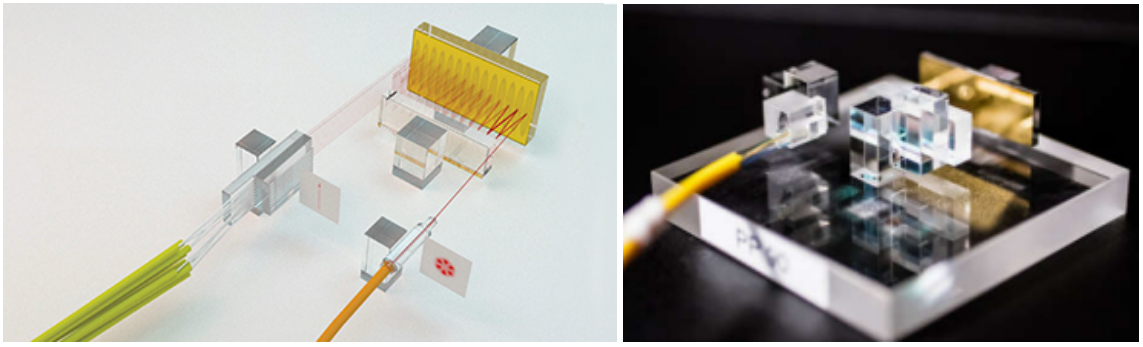

Figure 1.16: Multi-Plane Light Conversion techniques (left), and photo of the device (right). From [Labroille et al. (2014)]

Furthermore, Laguerre-Gaussian or Hermite-Gaussian mode basis are the most common propagation modes, typically employed in as modes of a phase plate multiplexer [Bade et al. (2018)]. Mainly in lasercom domain, numerous applications using MPLC technology are now emerging. Here, to achieve terabit/s throughput, we already mentioned as wavelength division multiplexing is a key technique in this sense. Multi-Plane Light Conversion for high-power optical beam combining can provide high beam quality whilst preserving the consumed power [Billaud et al. (2019)]. Other applications relate to inter-satellite communications using the Hermite-Gaussian modes based-MPLC for pointing error compensation [Billaud et al. (2020)], and high-data rates optical transmission systems.

With this robust and compact device, MPLC up to 45-single mode fibers are already available on Cailabs web site, thus providing a fully integrated module for free-space optical communications also improving the reliability in presence of atmospheric turbulence.

1.5.4.3 Overview of photonic integrated circuits platforms

As second step in the coherent combining approach reported in Figure 1.10, an overview of the main photonic platforms is given below, highlighting their main advantages and drawbacks.

1.5.4.3.1 The opportunity of Photonic Integration

The drive to continue augmenting the amount of data rates collected for satellite communication, military surveillance and environmental sensing has created a strong demand for the convergence of electronics and photonics systems.

Over the past decades, several research programs on photonic integrated circuits (PICs) have been commissioned, mainly driven by the needs of high-speed links for telecommunication, datacenters, cloud computing, while encouraging new applications in space, sensing and biophotonics, light detection and ranging (LiDAR), machine learning, quantum telecommunications and many more [Boes et al. (2018); Rahim et al. (2018); Thylen (2006); Rickman (2014)]. PICs are now emerging as a mature, industrial platform, enabling more reliable, simple and cost-effective broadband communications.

1.5.4.3.2 Trends evolution

While the first application of silicon photonics were for sensing application, developed and commercialized by Bookham Technologies in 1997/1998, an increasing number of development started in the last five to ten years. Google, Amazon, Facebook and Cisco will triple their data centers energy consumption reaching billions of terabytes/yr. ESA's roadmap on new technologies also includes photonic distribution of the radio-frequency, photonic-based microwave frequency generation, conversion, filtering, routing and beamforming, as well as optical interconnects at 25Gbps and 56Gbps. Such systems, or part thereof, can be integrated on a PIC, thus leading on new opportunities for decreasing cost, weight, size and power reduction.

This rapid development of silicon photonics technology is mainly due to the continuously evolving technology platforms, also thanks to the open-access model that overcomes the economic barriers to fabless companies. In Europe, silicon photonics pilot line was based on the previous model built for the well-established *Complementary Metal-Oxide Semiconductor* (CMOS). The main European open access platforms can be seen in the initiative of Imec and CEA-LETI who developed the ePIXfab, with a mission to promote silicon photonics science, technology and applications. Similar activities can be found in the Federal and State Engineering Technology Consortium, also called AIM, dedicated to advancing technology and manufacturing of integrated silicon photonics devices.

Moreover, through the Multiproject Wafer (MPW) approach, different companies can split the expensive maskset cost sharing the design areas with various other users [Rahim et al. (2017)]. Different Si-Ph platforms are also offered by various European fabs. To mention a few, we can found LioniX, which offers the SiN-based platform called TriPleX [Roeloffzen et al. (2018)], Ligentec's thick SiN platform offering its all-nitride core technology in MPWs, VTT's thick-SOI platfotm based on $3\mu m$ thick SOI where light is almost confined into the Si core and Cornestone

[Littlejohns et al. (2019)], which is an open access silicon photonics rapid prototyping foundry based in the UK that offers industrially-compatible tools (e.g., deep-UV lithography), to enable seamless scaling-up of production volumes, whilst achieving TRL5 technology platform.

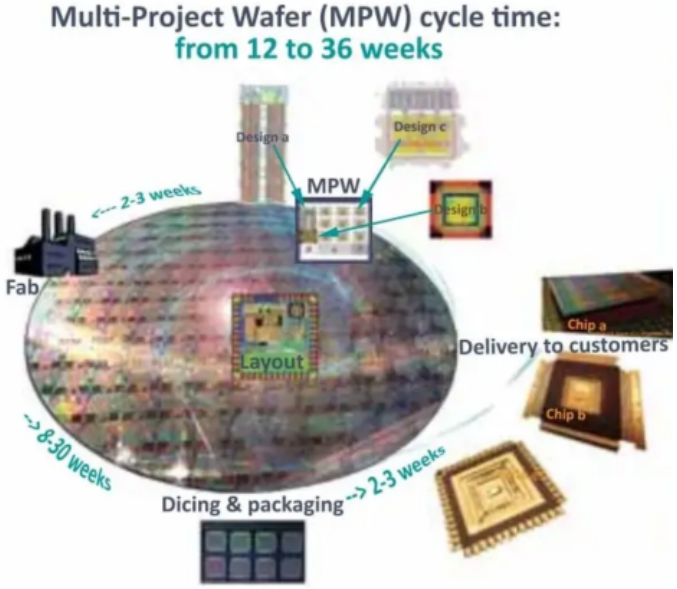

Figure 1.17: Multi-Project Wafer cycle time: from layout to packaged chips

Photonic technologies have changed considerably the astronomic instrumentation. Particularly for interferometry, advanced photonic chips performing different tasks are now adopted, such as beam splitting and combining (i.e. GRAVITY, SPICA etc.), phase delay control, nulling, as well as mode conversion [Cvetojevic (2020)]. For free-space-optical communications, optical phased arrays (OPA) on a PIC are a prime candidate as new photonic applied technology, achieving a widely steerable and low-divergence output beam [McManamon et al. (1996); Heck (2017); Fatemi et al. (2018); Miller et al. (2020)]. On the other hand, an alternative approach for multi-channel FSO receiver and wavefront correction for high rate free-space optical communications, has been already presented in section 1.5.4. Electro-optical components are integrated on this PIC, offering the possibility to extend the operation range to lower elevations, while having strong advantages compared to deformable mirrors, such as the absence of mobile mechanical parts (making them very robust) and higher bandwidth with respect to a deformable mirror.

The main objective of this thesis is to design and implement an innovative PIC suitable for a high performance compensation of quickly varying atmospheric turbulence effects on a space-ground laser link at 1.55 µm.

1.5.4.3.3 Photonic Integrated Circuits Platforms

As already mentioned, a variety of material platforms exist and can be considered for photonic integrated circuits (PICs), each with their own advantages and disadvantages.

Here, the main materials available for Ph-IC fabrication will be discussed, most of them are developed for telecommunication applications and are in the wavelength range of 1300 and 1600nm.

The key performance parameters for the photonic circuit designed and implemented in this thesis are briefly summarized as following:

- a dozen or more waveguides
- low propagation losses
- operation at the telecommunications wavelength (1550 nm)
- moderate/high modulation bandwidth
- possibility to moderate/high bending radii
- polarization independent

For this reason, an overview of the main photonic integrated circuit platforms is presented in this section, in relation to previous key performances.

- **Silicon-on-Insulator** (SOI)

  The high index contrast of this material, defined in the telecom window as $(n_{core}^2 - n_{clad}^2)/(2 \cdot n_{core}^2)$, makes this platform the most mature silicon-photonic material. In a SOI wafer, the device is fabricated with a thin silicon layer (core layer, with $n_1 \approx 3.5$) sitting on a insulating material (cladding layer, with $n_2 \approx 1.45$), typically silicon dioxide, also called buried oxide (BOX). The thickness of the silicon layer is generally in the range of a few ten of nanometers to several micrometers, while dioxide layer between 50nm and 1µm [Roelkens et al. (2015)]. Finally, a silicon substrate ends the whole structure. Furthermore, with the compatibility with the CMOS technology and the well-established industrialization process, monolithic integration of Si-Ph with electronics was so far implemented. However, due to the indirect band-gap of this material, an integrated laser is missing from this platform. Although a large wafer topography can be achieved with this technology, with high density integrated components, a critical drawback for our optical link application can be found in a **lower modulation bandwidth** compared to other technology platforms [Rahim et al. (2018)]. With respect to other technology platform, in which high modulation can be achieved by Kerr and Franz-Keldysh (FK) effects for phase and amplitude modulation respectively, high-refractive index change in Si can be also obtained with plasma-dispersion effect [Rahim et al. (2021)].

  Through this electro-refractive effect, a phase modulation occurs with the change of free carrier concentration by the movement of charge carriers into or out of the waveguide. Intensity modulation can be subsequently obtained embedding phase modulator into a MZI, Michelson interferometer, Bragg reflector etc. Finally, although the possibility of large integration of this platform, due to its **high index contrast** ($\Delta n \approx 2$) it is also very sensitive to manufacturing variations. Moreover, the need for waveguides with low propagation losses (typically less than 3dB/cm), as in telecommunication applications, is in contrast with the high Δn reported, which makes the guides much more sensitive to roughness at the interface with the oxide, also causing high propagation losses due to diffraction effects. The mode size is another factor of interest, as it is closely dependent

on the index contrast present in the waveguides. The larger the Δn, the smaller the mode size ($\approx 100nm$), causing problems in interfacing with standard fiber injection.

Silicon photonics devices are not only sensitive to geometric variations and material composition, but also to thermal effects. Moreover, silicon has a high thermo-optic coefficient ($1.86 \cdot 10^{-4} K^{-1}$), which makes this platform a good candidate for thermo-optical phase shifter. In this sense, such temperature sensitivity can be used to actively compensate by locally heating or cooling the chip. In order to tune the behavior of this circuit, a current is driven through the heater, which results in a temperature variation in the waveguide, thus leading to a thermally induced phase shift. However, the generated heat needs to be dissipated, requiring electronics or algorithms for the control mechanism [Bogaerts and Chrostowski (2018)]. In [Tu et al. (2019)] and [Harris et al. (2014)], various MZI switches are reported, showing a thermo-optic (T-O) MZI with a deep etched cavity surrounding the heater and the waveguide in order to improve the T-O phase modulation efficiency, as well as ultra-low power of 50μW T-O switches. Phase-shifting efficiency of about 24.77 mW/pi are demonstrated, with an insertion loss measured of only 0.23 dB in a 8-inch SOI wafer.

The large-scale integration of SiPh with new materials provides high-modulation performance while at the same time preserving all the benefits derived from Si technology. A complete state-of-the art of new-materials on Silicon for high-speed modulator can be also found in [Bogaerts et al. (2014); Thomson et al. (2016)].

- **Silicon Nitride** (SiN)

  As mentioned above, SOI photonic platform is the mainstream and most used platform for silicon photonic devices, and its high-index contrast makes it a challenging material platform. However, inspired by its success, plenty of high-index contrast materials has been investigated in order to extend the wavelength range of silicon photonics. Among them, silicon nitride (SiN) is an emerging candidate, with a **large transparency window** that goes from $\sim 0.4\mu m$ up to mid-IR wavalengths of $4\mu m$ and which is also CMOS compatible to enable **high density photonic integration** [Muñoz et al. (2017)]. A state of the art of silicon nitride photonic integration platform is reported in [Rahim et al. (2017)]. Here, we present a brief comparison between the SOI and the SiN, highlighting the main andvatanges and drawbacks of these two material platforms [Baets et al. (2016)].

  Whereas in SOI the core layer material is composed by silicon, here the guiding layer is performed by SiN, deposited by either Low Pressure Chemical Vapour Deposition (LPCVD) or Plasma Enhanced Chemical Vapour Deposition (PECVD). For applications wavelength of 1.55µm, such as telecommunications, LPCVD is commonly used as it exhibits lower waveguide losses compared to the PECVD. Furthermore, SiN provides also moderately low index contrast, or $\Delta n \approx 0.5$, that is $\sim$ 3.5 to 4.5 times less than SOI in telecom wavelength range, thus leading to a reduced losses while having larger bending radius $\sim 75\mu m$ for a $1.2\mu m$ wide SiN waveguide at $1.55\mu m$ [Baets et al. (2016)]. As a result of its low Δn, we will have more voluminous waveguides, but almost free of propagation losses and manufacturing variations. Another term of comparison with SOI platforms is the lower temperature sensitivity of SiN ($\sim$5 times lower). Moreover, silicon

third-order non-linearity is useless in the telecom wavelength due to two-photon absorption effect (TPA) that induces extra waveguide losses [Khurgin et al. (2015)]. Silicon nitride has a lower Kerr effect while providing a TPA virtually zero, realizing frequency comb generation or wavelength conversion. Finally, both material platforms possess negligible second-order non-linearity due to their centrosymmetry. Therefore, electro-optic modulation is impossible. Nonetheless, as shown in [Baets et al. (2016)], recent research reported a strong electro-refraction effect in SOI, induced by a strained silicon nitride layer and leading to SiN-based Pockels modulator. Other phase-modulators based on stress-optic effects and geometric deformations have been reported [Hosseinnia et al. (2015)], using piezoelectric and zirconate titanate (PZT) thin films, or co-integration of PZT and SiN.

- **Lithium Niobate** $(LiNbO_3)$

  The growth of this material can be explained by its interesting properties for integrated photonics, such as the **low loss and broad transparency window** and **high second-order optical nonlinearity**, enabling wavelength conversion and optical signal generation. This optical nonlinearity is absent in centrosymmetric materials, as silicon or amorphous glasses, and allows also the lithium niobate to control the refractive index via electro-optics (EO) effect. High-speed telecommunications is one of the main applications using fast lithium niobate electro-optic modulators, as they provide **high modulation frequencies** with both low propagation losses ($\sim 0.1dB/cm$) and a wide transparency band (from $400nm$ to $4.5\mu m$), which also enable applications from visible to mid-infrared [Courjal et al. (2018)]. These properties are fundamental in order to have a high-compact device with low energy consumption. Conventional EO modulators are formed by low-index contrast waveguides and weak optical confinement, with the electrodes that must be placed far away from the waveguide in order to minimize the absorption losses, wich leads to an increased drive voltage. As a result, LN modulators have low modulation efficiency ($V_\pi L > 10V$cm) [Rabiei et al. (2013)]. Furthermore, another drawbacks of LN-based components rely in their polarization-dependent operation. Many integrated optical elements can be found in literature to be polarization-dependent, so that their response changes as a function of the polarization state in the waveguides. Usually, for integrated circuits based on an isotropic material, the coupling between the two polarized modes is very weak, and can therefore be neglected. Unfortunately, for anisotropic materials such as $LiNbO_3$, due to its strong material birefringence, the coupling between the two polarized modes cannot be ignored anymore, leading to a device that can be affected by the mode properties [Courjal et al. (2018); Zhang et al. (2020b)].

  Another limitation of this material concerns the small difference of its optical waveguides. They are generally bulky and cannot be bent sharply. [Rabiei et al. (2013)]. Furthermore, a LN device must be a few centimeters longer compared to other materials, due to the low intensity of the pump in the cross-section of the waveguide [Tanzilli et al. (2000)]. A state of the art of the EO-Mach Zehnder modulators (MZM) performance metrics is also reported by He. and al [He et al. (2019)], comparing silicon-organic-hybrid (SOH) MZMs, SOH plasmonic MZMs, and barium-titanate (BTO)/Si plasmonic MZMs.

Different approaches have recently been proposed to overcome these limitations [Boes et al. (2018)], such thin-film lithium niobate on-insulator (LNOI), providing LN modulators with a low-drive voltage and ultra-high EO bandwidth [He et al. (2019)], or hybrid LN membranes integration on SOI PICs [Weigel et al. (2018)], that combines silicon material properties (i.e. scalability) with the outstanding modulation performance of LN. Compared to conventional LN waveguides, LNOI waveguides exhibit high refractive index difference between LN and SiO_2, which results in a strong optical confinement. More compact components can be also obtained in this way, so that the length is reduced and the electrodes are closer together (higher electro-optical efficiency). Besides these renowned solutions, in the past two decades ridge waveguides in periodically poled $LiNbO_3$ (PPLN) mainly used for wavelength conversion have also attracted a lot of attention because of their less sensitivity to photo-refraction, thus operating at higher optical power levels without any degradation [Wang et al. (2018)]

The goal of integrating many LN optical components on a single IC is to achieve low-loss waveguides with a strong optical confinement in order to have also tight waveguide bending radii. In the next networks generation, high-scalable devices are required, and present $LiNbO_3$ modulators are not be able to meet this demand, even though they can achieve ultra-high modulation bandwidth due to the strong electro-optic effect.

- **Indium Phosphide** (InP)

  InP monolithic integration and silicon photonics are considered today the most prominent platforms in photonics [Smit et al. (2014)]. Furthermore, although the PIC literature has been dominated by silicon photonics, indium-phosphide-based solutions are still at the top of the PIC sales [Arafin and Coldren (2018)]. Around this platform, Europe's key players in InP photonic integration are reunited in the JePPIX-platform [Leijtens (2010)], including many different players, as PIC designers, packaging and test partners, software developers and PIC foundries. InP offers also a variety of optoelectronic devices with **passive and active functions**, while operating in a limited wavelength range between 1300-1700nm. In this context, an overview of recent development has been proposed in the Journal of Selected Topics in Quantum Electronics [Williams (2017)]. Concerning the refractive index modulation, the low mass of electrons in these materials allows an electron induced refractive index change 5 or 10 times larger than Si in the O and C bands, and **high-bandwidth** Mach-Zehnder modulator with InP-on-Si capacitive phase shifters are reported in [Thiessen et al. (2019)], showing a BW up to 30GHz for a phase modulation length of 250µm. However, the alternative to a pure monolithic integration is to use some hybrid or heterogeneous integration with electronics, even if it requires three layers of integration: a silicon electronics layer, a Si-Ph layer and an InP layer [Smit et al. (2019)].

  Another approach in which the full photonic circuit is being manufactured in an InP based stack is the InP Membrane on Silicon (IMOS) approach, shown in [Hiraki et al. (2020)]. InP PICs were first developed for telecommunications, although today's applications area covers microwave photonics, free-space laser communications, sensing and Lidar [Arafin and Coldren (2018); Zhao et al. (2018)].

Here, the integration between silicon photonics and InP can be required, by heteroepitaxy, co-packaging or heterogeneous approaches as described above. A comparison between SiPh and InP can be also found in [Doerr (2015)], and reported in the following table. Despite the rarity of In compared to Si and the high index contrast waveguides (larger bend radii in InP), in large-scale low-cost and short-reach wafer products silicon photonics suffers of not having integrated laser, such as vertical cavity surface-emitting lasers (VCSELs) or directly modulated lasers (DMLs). Direct modulation avoids the additional loss induced by a separate optical modulator. On the other hand, silicon's wafer are much larger (300mm compared to 75mm), and a lower temperature sensitivity compared to InP.

Table 1.2 summarises a comparison of the different integrated photonic material platforms, describing the different properties of each.

Property	*InP*	*SOI*	SiN	$LiNbO_3$
Chips per wafer	Medium	High	Medium/High	Low
Complexity	High	Medium	Medium	High
Foundries	Several	Several	Few	None
MPW	Yes	Yes	Yes	No
Laser	Yes	Hybrid/Heter.	Hybrid	No
Modulation BW	Medium/High	Low	Low	High
Propagation loss	Low/Medium	Low	Low	Low/Medium

Table 1.2: Main properties of previous mentioned photonic material platforms

1.5.4.4 System

Having introduced in the previous sections the principle and the different devices that constitute the coherent combining approach, in this section a description of the system as a whole is given, providing an overview of the systems already implemented. Theoretical analysis and experimental demonstrations of optical coherent combining have been investigated over time as a means for mitigating atmospheric turbulence effects.

In 2005 Dikmelik and Davidson [Dikmelik and Davidson (2005)] investigated the use of a coherent fiber array as a receiver structure. Particularly, a 7-elements coherent fiber array was employed, with each subapertures arranged in an hexagonal close-packed configuration. The outputs of the single-mode fibers were combined coherently, and fiber phase modulators in the form of piezoelectric stretchers have been used to obtain the required phase adjustment in the receiver array. For its simplicity in presence of a small number of subapertures, a multidither system was chosen to achieve the feedback control of the fiber phase. The coupling efficiency for the coherent fiber array system was found significant larger with respect to a single-aperture receiver, with its effectiveness decreasing as the turbulence increases.

Other all-fiber coherent beam combining systems have been reported in [Yang et al. (2017)]. In this case, four input beams are combined using cascaded of fiber couplers, and a piezoelectric-ring fiber-optic phase compensator was employed in the input paths to compensate the phase differences among the input beams. Furthermore, an SPGD algorithm was used to maximize the cost function. Again, the effectiveness of the combining module decreases as the turbulence increases, and about 27 iterations of SPGD are required to enhanced the average combining efficiency, defined as the ratio between the output constructive signal and all other ports, to be 97.83%, while 14 iterations to be about 96%. An experimental validation of the previous coherent combining approach is described in [Lao et al. (2020)], over a 1km urban link.

Billault et al. recently proposed a multichannel FSO receiver architecture with an MPLC as mode demultiplexer device [Billault et al. (2021)]. The Hermite-Gaussian mode basis is used for the MPLC device, while a Nelder-Mead algorithm was chosen for PIC optimization. A 15-channel silicon on insulator photonic circuit has been developed, with active Mach-Zehnder interferometers arranged in a tree-like manner. Compared to a SMF receiver, with this spatial demultiplexer and PIC receiver, the coupling efficiency remains almost constant over turbulence conditions, showing a much more resilient system than classical FSO receivers to phase and amplitude perturbations. However, high losses about 16dB are reported for the PIC, and no information on the convergence time is available.

The demonstrations presented above validate the concept of coherent combining applied to the correction of turbulence perturbations. On the other hand, many questions remain still open. The theoretical performances accessible with this type of device and therefore its contribution to a classical adaptive optics system are not well known. Moreover, these demonstrations involve a very small number of degrees of correction. In future correction systems, a larger number of degrees of correction is expected. The answer to these questions on current components (multiplexers and PICs) is awaited, but also finding control laws better suited to large numbers of corrections.

1.6 Conclusion

The first chapter of this thesis can be seen as a useful introductory tool for the reader approaching the topics discussed here for the first time.

In the first part of this chapter a general overview on satellite-to-ground optical space missions has been proposed, highlighting the turbulence mitigation methods used over time as the demand for data rates increased. The key parameters describing the turbulence behavior have been also presented, as well as the in-house software used in order to get rid of the hypothesis of the small perturbation.

Turbulence mitigation methods have been presented, and divided into passive and active methods. Regarding the first category, only spatial diversity at the reception can be found as real effective technique. However, a complex modulation format and a signal processing are required, as well as an adequate spacing between the apertures at both transmitters/receivers, which is incompatible with low-cost solutions. Regarding the active mitigation approaches,

adaptive optics has been shown to be as one of the main and most widely used methods for wavefront correction. Its principle has been described in this chapter, as well as the main components used in this case. Notably, as the satellite elevation decreases, the greater the distance to be covered between the satellite and the ground station, resulting in undesirable scintillation and phase dislocation effects, which make the wavefront measurement difficult.

Sensorless adaptive optics approach makes it possible to circumvent Shack-Hartmann issues on wavefront measurement. With the dithering approach, we noticed how this results in a limitation of the deformable mirror bandwidth. The use of efficient optimization algorithms as well as alternative methods based on deep learning are reported in the literature in order to drastically reduce the overall system bandwidth.

Another approach, firstly proposed by N. Schwartz for measure and correct the wavefront in strong perturbation regime, is to couple the incoming perturbed beam with a set of propagation modes associated with different waveguides, and then coherently recombine this guided modes. Indeed, a mode decomposition follows a coherent combining block, thus optimizing the signal of interest. Based on this, different mode multiplexer devices used to perform the mode decomposition stage are described. Finally, in the last part of this Chapter we gave an overview on different photonic material platforms, highlighting their main advantages and drawbacks.

This thesis is dedicated to the study of coherent recombination for the correction of atmospheric turbulence effects. In order to go beyond the proof of concept, this work is positioned in a concrete framework that goes from the definition of the use case to the technology of the PIC. The analysis developed in this manuscript can be divided into three main objectives, listed in detail below:

- **Chapter II: Spatial analysis**

  In this Chapter we analyze the first block that composes the coherent combining approach: the mode decomposition. We are primarily interested here in comparing the effectiveness of different space-division multiplexing devices. This can be seen also as a *spatial analysis*, thus analyzing the average coupling efficiency as function to the number of decomposed modes. To do this, the aim of this Chapter is to implement a simulation tool that is faster than conventional end-to-end simulations. Furthermore, in order to study the instantaneous aspect (i.e. the fluctuations of the coupling efficiency), a Monte-Carlo simulation has been performed in the last part of this Chapter. An analysis of the satellite-to-ground link system is given, defining a link budget for a specific scenario of interest.

- **Chapter III: Temporal analysis of the correction loop**

  Once the study of the number of modes required to achieve a given coupling efficiency as a function of turbulence conditions has been validated, we introduce in this Chapter the temporal aspects of the correction loop. The need now becomes to introduce such problems into the specification of an integrated circuit. A new control law has been proposed in order to deal with a high bandwidth demand, well suited for PIC applications. Moreover, despite the advantages of using photonic circuits to correct atmospheric turbulence, large losses are still at the heart of their construction. The aim of this Chapter is also to propose an alternative solution to solve the problems of standard AO in strong perturbations, without waiting for the technological maturity of PICs.

- **Chapter IV: Impact on photonic integrated circuit technology**

  In the last part of this thesis, the impact of the previous spatial and temporal analysis on the PIC technology has been addressed. Two different PIC material platforms have been considered. The design and the first test on a lithium-niobate circuit and the characterization of a silicon-nitride PIC will form the first and the second part respectively of this study.

Chapter 2

Spatial analysis

2.1 Introduction

As reported in Chapter 1, before being collected by the telescope, the incoming wave undergoes random perturbations of phase and amplitude, leading to both modulations of the collected optical flux and speckles in the receiver focal plane respectively. In addition to this, high data rate in satellite-to-ground optical links imposes the coupling of the optical signal with a single-mode fiber. We have presented in Chapter 1 several methods that attempt to mitigate the effects of atmospheric turbulence, employing AO, sensorless AO, as well as the coherent combining approach.

In this latter, a space-division multiplexing device is employed to couple the incident wave to a set of propagation modes, increasing at the same time the capacity of multi-mode fibers. The use of such devices, shown in Section 1.5.4.2 of Chapter 1, is spreading in the field of optical communications in free space as well as in astronomy. In both cases, the aim is to collect the received flux in the most efficient way possible, either to send it to several detectors or to recombine it in a coherent way. Nevertheless, the SDM coupling efficiency for free-space beams in the presence of atmospheric turbulence has not been investigated untill now.

The aim of this Chapter is to evaluate the atmospheric turbulence effects when coupling a beam in free-space with a SDM device, i.e. with a set of propagation modes. In this way, through the so called *spatial analysis*, the limitation on the coupling efficiency induced by the number of modes is analyzed. The first part is an adaptation of a paper published during this thesis. In this context, Figure 2.1 describes the schematic modeling of a mode decomposition through a SDM device. After propagation through turbulence, the disrupted beam is focused into a SDM device using a telescope. Subsequently, such beam is decomposed onto a set of propagation modes.

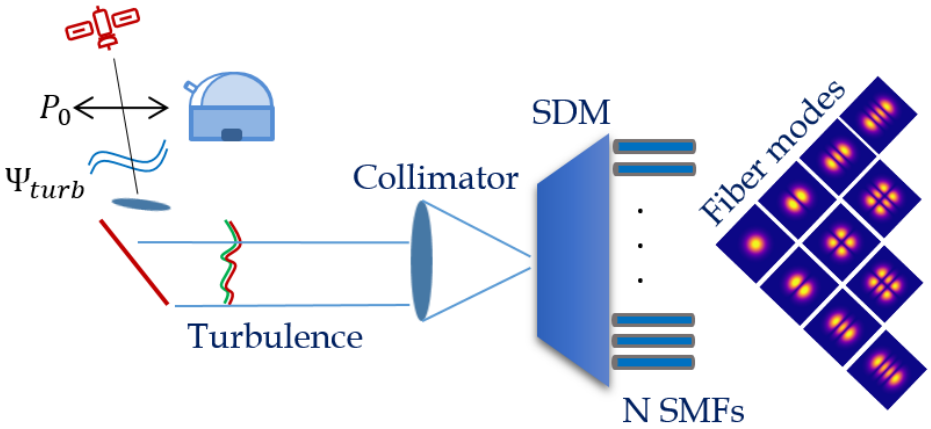

Figure 2.1: Schematic diagram of free-space propagation and modal decomposition through a SDM device

Considering the first part of this Chapter, a general formulation of the coupling efficiency estimator is given, validating its evaluation with a fiber collimator array as SDM device. Furthermore, the average coupling efficiency in case of a plane wave, for a set of Hermite-Gaussian modes of growing number has been numerically estimated, and a telescope central occultation

is also considered, for a given set of modes.

The presence of turbulence is then introduced, reporting the coupling efficiency as function of ratio between the telescope diameter and the Fried parameter, D/r_0.

It is also possible to go further and evaluate whether the HG set of modes is the most suitable for describing atmospheric turbulence perturbations on optical waves. As a consequence, a modal optimization is also taken into account for a given set of modes and different turbulence conditions. The covariance matrix of a given set is reported, while the derived optimization is compared to the possibility of a tip-tilt correction before the SDM device, highlighting the gain brought by its use.

In the second part of this Chapter another parameter of interest is analyzed: the fluctuations of the coupling efficiency. In order to analyze the performance of this system and build specifications for a photonic integrated circuit as beam recombiner after a SDM device, a given scenario is defined for the case of a satellite-to-ground downlink. Such case of study is based on one hand, on a link budget, providing the performance in terms of overall power margin, and on the other hand, on an end-to-end simulation to perform a statistical as well as a temporal analysis. The cumulative distribution function is also used to study the behavior of fluctuations in coupling efficiency, both in the case of amplitude and phase, and phase-only correction performed by the PIC.

2.2 Coupling efficiency estimator for a SDM device

In this section, a general expression to evaluate the coupling efficiency between a perturbed incoming beam and a set of propagation modes as those representative of a SDM device is presented. The overlap integral reported in Chapter 1, Section 1.3.5, that characterize the matching between an unperturbed beam and a SMF mode, can be adapted for a set of N^2 orthonormal propagation modes, M_i, thus writing:

$$s_i = \frac{\langle \Psi | M_i \rangle}{(\langle \Psi | \Psi \rangle \langle M_i | M_i \rangle)^{1/2}} \tag{2.1}$$

Moreover, the part of the field Ψ coupled with a set of propagation modes, M_i, can be also described as:

$$\Psi_{coupled} = \sum_{i=0}^{N^2-1} s_i M_i \tag{2.2}$$

In order to take into account pupil truncation, $\Psi = P\Psi_{turb}$, the coupling efficiency is calculated in the pupil plane [Shaklan and Roddier (1988)]:

$$\overline{|s_i|^2} = \int d^2\mathbf{r} \int d^2\mathbf{r}' M_i(\mathbf{r}) M_i^*(\mathbf{r}') P(\mathbf{r}) P(\mathbf{r}') \overline{\Psi_{turb}(\mathbf{r}) \Psi_{turb}^*(\mathbf{r}')} \tag{2.3}$$

where P denotes the transmission of the pupil and Ψ_{turb} the incident field.

We are interested here at the ratio of the average coupled power to the average incident power, given by:

$$\eta \triangleq \frac{\overline{\langle \Psi_{coupled} | \Psi_{coupled} \rangle}}{\overline{\langle \Psi | \Psi \rangle}} \tag{2.4}$$

Substituting the expression of the coupled field from Eq. 2.2, the coupling efficiency can be written in the following form as well:

$$\eta = \frac{\sum_{i=0}^{N^2-1} \overline{|s_i|^2}}{\overline{\langle \Psi | \Psi \rangle}} \tag{2.5}$$

According to Roddier [Roddier (1981)], the second order moment $B_{\Psi_{turb}}(|\mathbf{r} - \mathbf{r}'|) \triangleq \frac{\overline{\Psi_{turb}(\mathbf{r})\Psi^*_{turb}(\mathbf{r}')}}{\overline{\Psi_{turb}(\mathbf{r})\Psi^*_{turb}(\mathbf{r})}}$, denotes the spatial coherence function of the field, also called atmospheric transfer function.

Furthermore, in the case of the field perturbations are assimilated to those of a spherical or plane wave, one can taking into account the second order moment in the Eq. 2.3, thus writing:

$$\eta = \frac{1}{\langle P|P \rangle} \int d^2\mathbf{r} B_{\Psi_{turb}}(r) \Big\{ \sum_{i=0}^{N^2-1} [PM_i \otimes PM_i](\mathbf{r}) \Big\} \tag{2.6}$$

where $\otimes$ represent the correlation product. Following Fried [Fried (1966)], the coherence function in the previous equation is also given by:

$$B_{\Psi_{turb}}(r) = \exp\left\{ -3.44 \left(\frac{r}{r_0} \right)^{5/3} \right\}, \tag{2.7}$$

The latter, in case of short-exposure or rapid image stabilization becomes [Fried (1966)]:

$$B_{\Psi_{turb_{se}}}(r) = \exp\left\{ -3.44 \left(\frac{r}{r_0} \right)^{5/3} \left[1 - \left(\frac{r}{D} \right)^{1/3} \right] \right\}. \tag{2.8}$$

In the following sections we will first apply the previous formulation of the coupling efficiency to a fiber-collimator array, as it corresponds to the well known problem of coupling evaluation of a wave perturbed by propagation in turbulence and a SMF. Subsequently, the application to a set of propagation modes is reported, thus giving the number of modes required for a given turbulence strength condition. Through this study we wish to investigate whether the modes set used in the SDM device design we implemented are optimal or not. This optimization criterion varies according to the turbulence conditions. However, the tool we developed in the last section can be well used for this purpose.

2.3 Decomposition through a Fiber Collimator Array

A basic solution for spatial decomposition of the incoming beam can be found in the fiber collimator array. With such a device, as mentioned in Chapter 1, section 1.4.4.1, each mode is defined by a lenslet coupled with a single-mode fiber.

Paving the pupil, the fiber array samples the complex amplitude of the wave [Dikmelik and Davidson (2005)]. We choose this solution as the first implementation the formalism developed in the previous Section. The central idea of this Chapter is, however, to apply it with regards to more elaborate set of modes. The subpupils are defined by the lenslets to avoid artifacts related to the filling of the pupil support.

For sake of simplicity, the support of the pupil is restricted to the set of the subpupils, here denoted by *p*. Under these assumptions, we can rewrite the Eq. 2.6, that simplifies:

$$\eta_{FCA} = \frac{1}{\langle p|p\rangle} \int d^2\mathbf{r} B_{\Psi_{turb}}(r)[pG \otimes pG](\mathbf{r}) \tag{2.9}$$

where G denotes the SMF mode propagated in the lenslet. In the following, G will be approximate by a Gaussian mode. It is also worth noting that the total coupling efficiency equals the coupling efficiency of a single lenslet. An example of a hexagonal fiber collimator array is presented in Figure 2.2.

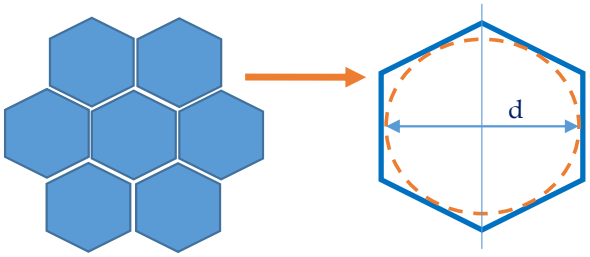

Figure 2.2: Hexagonal fiber collimator array arrangement.

2.3.1 Waist optimization

Furthermore, the numerical aperture of the lenslet was chosen to maximize the coupling efficiency between an incident plane wave and the Gaussian-SMF mode. In Figure 2.3 the coupling efficiency is reported for the Gaussian mode only, as function of $d/2w$. Two different curves are reported in such Figure, for a circular (black) and hexagonal (red) pupil, thus showing a slight variation between both configurations.

The maximum value of the coupling efficiency is $\eta_{FCA_0} = 0.81$. Particularly, η_{FCA_0} is obtained with $d/2w_0 = 1.25$. Here, w_0 represents the waist size of the Gaussian mode in the plane of the fiber array as defined by Kogelnik [Kogelnik and Li (1966)], while d represents the diameter of the hexagon inscribed in the circle.

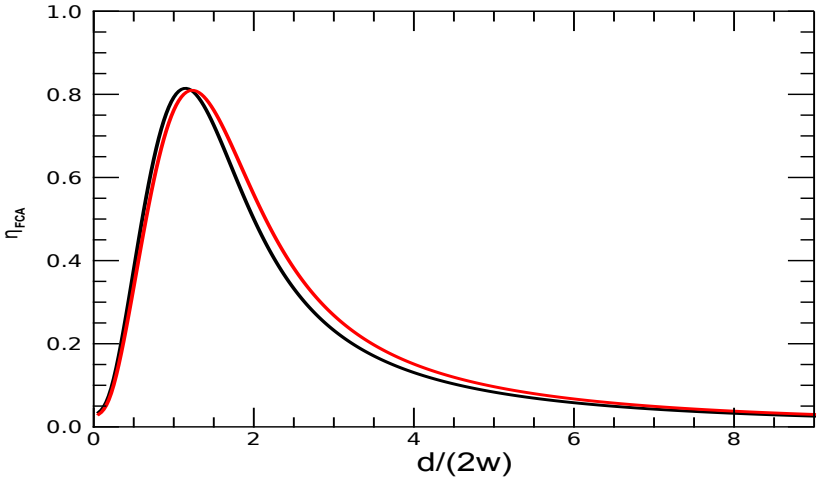

Figure 2.3: Plane wave truncated by (a) a circular pupil (black line) and (b) hexagonal pupil (red line): coupling efficiency obtained from Eq. 2.6 and Eq. 2.9 respectively as a function of $d/2\omega$ for the Gaussian mode only. d : diameter of the hexagon inscribed in the circle; w : beam waist at the pupil plane.

2.3.2 Presence of turbulence

In Figure 2.4, the coupling efficiency normalized by its maximum value, η_{FCA_0}, is shown, for a hexagonal fiber collimator array as function of the d/r_0. As we can see, when *d* is large with respect to r_0 (large values of d/r_0), the autocorrelation of the Gaussian mode (Eq. 2.9) is constant on the B_Ψ support, thus leading to the coupling efficiency to be proportional to the B_Ψ integral, i.e. to $(d/r_0)^{-2}$.

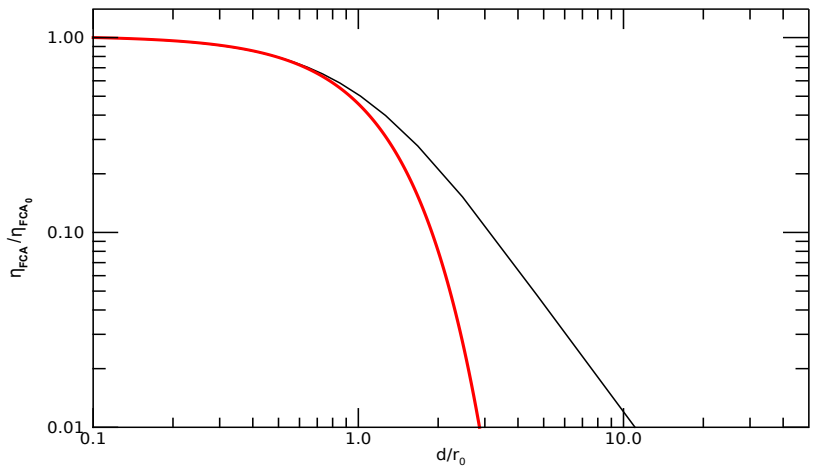

Figure 2.4: Relative coupling efficiency, $\frac{\eta_{FCA}}{\eta_{FCA_0}}$,of an hexagonal collimator array, as function of turbulence perturbations (d/r_0). Black line: results obtained with Eq. 2.9; Red line: fit for small d/r_0 with the expression obtained in 2.10. d : diameter of the hexagon inscribed in the circle; r_0 : Fried parameter.

On the other hand, when *d* is small compared to r_0, the relative coupling efficiency can be approximated by the following formula, also reported in Figure 2.4 with a red line:

$$\frac{\eta_{FCA}}{\eta_{FCA_0}} \approx e^{-0.8\left(\frac{d}{r_0}\right)^{5/3}} \tag{2.10}$$

Ruilier and Shaklan [Ruilier and Cassaing (2001); Shaklan and Roddier (1988)] provided a similar expression to the previous Eq. 2.10, neglecting the field module perturbations and assuming phase perturbations of mean variance equal to that given by Noll [Noll (1976)]. However, here module and phase perturbations have been taken into account to obtain Eq. 2.10. Hence, scintillation effects are then reported in the figure below.

2.4 Decomposition over a set of propagation modes

We evaluate in this section the coupling efficiency for two different mode basis: the Laguerre-Gaussian basis and the Hermite-Gaussian one. As described in the Chapter 1, in the paraxial approximation, both modes family are approximate solutions of the wave equation and are typical modes of a phase plate multiplexer [Bade et al. (2018)]. Thus, rectangular geometry leads to Hermite-Gaussian (HG) modes, while in a circular-cylinder or polar coordinate system Laguerre-Gaussian (LG) modes are more appropriate. Although LG modes are largely used in various applications focused on their orbital-angular momentum (OAM) [Li et al. (2017)], such as quantum mechanics and telecommunications [Arikawa and Ito (2018)], usually the transverse amplitude of a laser light is described in terms of product of HG modes, $H_n(x)H_m(y)$, associated with the transverse electro-magnetic (TEM_{nm}) modes. A laser with a slight angle components will breaks the typical circular symmetry of LG beams, thus making HG modes better suited to the description of laser beams.

2.4.1 Optimization of waist size in the absence of turbulence

Before computing the coupling efficiency for a set of Hermite-Gaussian modes, we aim in this section to characterize the optimization of the waist with respect to the chosen set of modes. According to the conventions, *w* is the second parameter defining the set of HG modes. In the case of a plane wave at the pupil of the telescope, in Figure 2.5 the coupling efficiency is reported,$\eta^N_{HG_{pw}}$, for different sets of modes, as function of $D/2w$. Considering a circular pupil, *P*, we denotes *D* the pupil diameter.

Given the symmetries of Hermite-Gaussian modes, one can see from the figure below that $\eta^N_{HG_{pw}} = \eta^{N-1}_{HG_{pw}}$, if N is even. Furthermore, the maximum value of the coupling efficiency will be denoted as $\eta^N_{HG_0}$.

Considering also $N = 1$ (Gaussian mode), $\eta_{HG_0} = 0.82$, while for a set of increasing number of modes the pupil is better fitted, such that: $\eta^N_{HG_0} \geq 0.9$ if $N^2 \geq 9$.
For the following sections, the HG mode waist, *w*, will be always chosen such that the coupling efficiency value equals the maximum coupling efficiency in case of plane wave, as: $\eta^N_{HG_{pw}} = \eta^N_{HG_0}$, whatever *N* or *D*. As an example, for the only Gaussian mode, $w_{HG_{00}} \approx \frac{D}{2 \cdot 1.1}$.

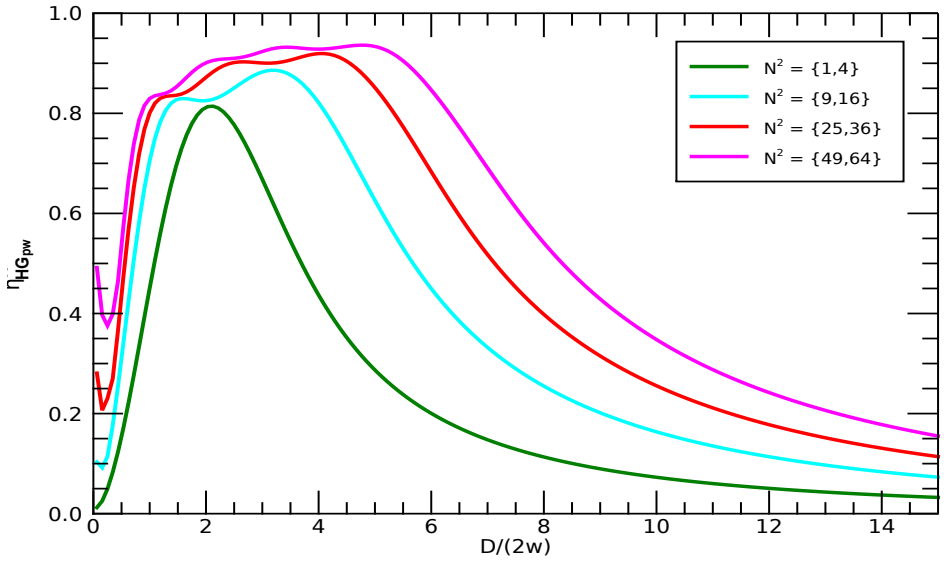

Figure 2.5: Plane wave truncated by a circular pupil: coupling efficiency, $\eta_{HG_{pw}}$, obtained from Eq. 2.6 as function of $D/2\omega$ for different sets of Hermite-Gaussian modes. Each set is denoted by N^2, the number of modes in the set. D : pupil diameter, w : beam waist.

In the following we evaluate the effect of a central obstruction in the pupil receiver, here noticed by T. The coupling efficiency is defined as reported in [Ruilier and Cassaing (2001)] with the overlap integral between a plane-wave and Gaussian mode representative on the SMF mode. As shown in the Figure 2.6, central occultations from 0% to 50% are considered.

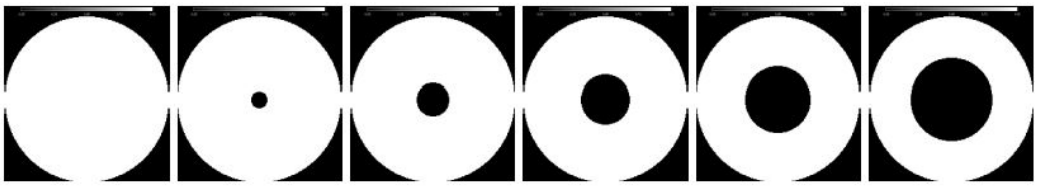

Figure 2.6: Pupil with different central obstruction. Rate of obstruction from left to right: 0, 0.1 ,0.2, 0.3, 0.4, 0.5.

The coupling efficiency varies according to the set of modes considered. For the sake of simplicity, we reported only three different sets of modes: the Gaussian only SMF mode ($N = 1$), a set of 16 HG modes ($N = 4$) and a set of 64 HG modes ($N = 8$).

In Figure 2.7 the coupling efficiency for the only-Gaussian mode is shown. As one can see, for the Gaussian mode case, the maximum value of η is obtained for $D/(2w) \approx 1.1$. This value shifts slightly in the case of a central occultation, thus having a $D/(2w) = 1$ for a T = 50%. Moreover, increasing the number of modes, the effect of a central obstruction is less significant as long as the occultation rate is less than 40%. In Figure 2.8 set of 16 Hermite-Gaussian and 64 HG modes are presented, thus showing no significant central obstruction effect for a set of 64 HG modes.

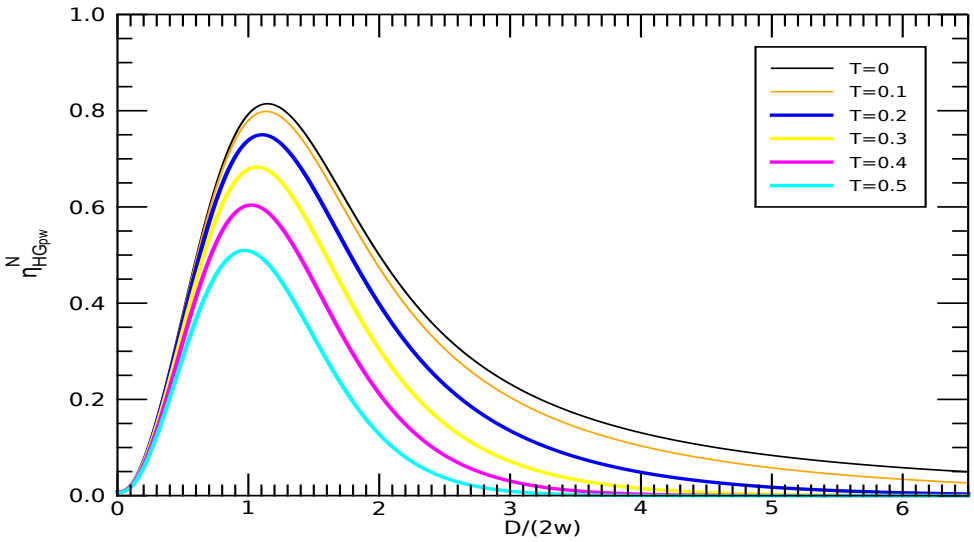

Figure 2.7: Coupling efficiency $\eta^N_{HG_{pw}}$ (obtained from Eq. 2.6), as function of the pupil diameter normalized by the waist, for different rate of central obstruction and considering the only-Gaussian mode. T : obstruction rate, D : pupil diameter, w : beam waist.

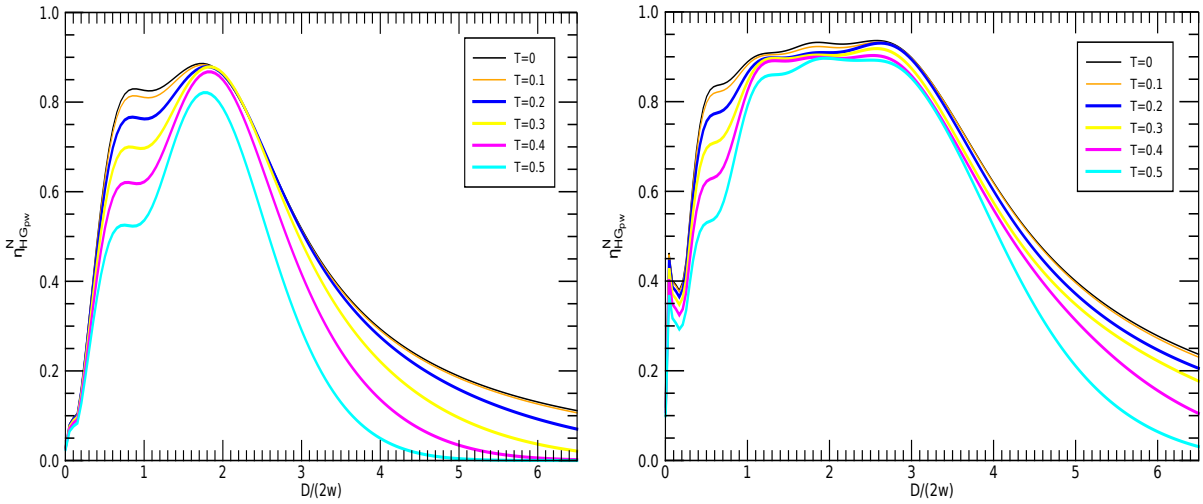

Figure 2.8: Coupling efficiency $\eta^N_{HG_{pw}}$ (obtained from Eq. 2.6), as function of the pupil diameter normalized by the waist, for different rate of central obstruction. Left: Set of 16 HG modes; Right: Set of 64 HG modes. T : obstruction rate, D : pupil diameter, w : beam waist.

2.4.2 Presence of turbulence on HG modes decomposition

The ratio between the average coupling efficiency defined in Eq. 2.6 and the correspondent value in case of plane wave, $\eta^N_{HG_{pw}}$, is numerically estimated in this section, as function of turbulence conditions (D/r_0), for different sets of Hermite-Gaussian modes.

In Figure 2.9, the average coupling efficiency is first shown as function of D/Nr_0. It appears that η^N/η_0^N depends mainly on D/Nr_0. η_0^N, or $\eta_{HG_0}^N$, represent the maximum coupling efficiency value obtained in case of a plane wave. We can consider two different operating zones depending on this value: a first with $D/Nr_0 \gg 1$ and the second with $D/Nr_0 < 1$. For $D/Nr_0 \gg 1$ the different curves are almost superimposed. The slight differences between them can be explained considering the method used for waist optimization.

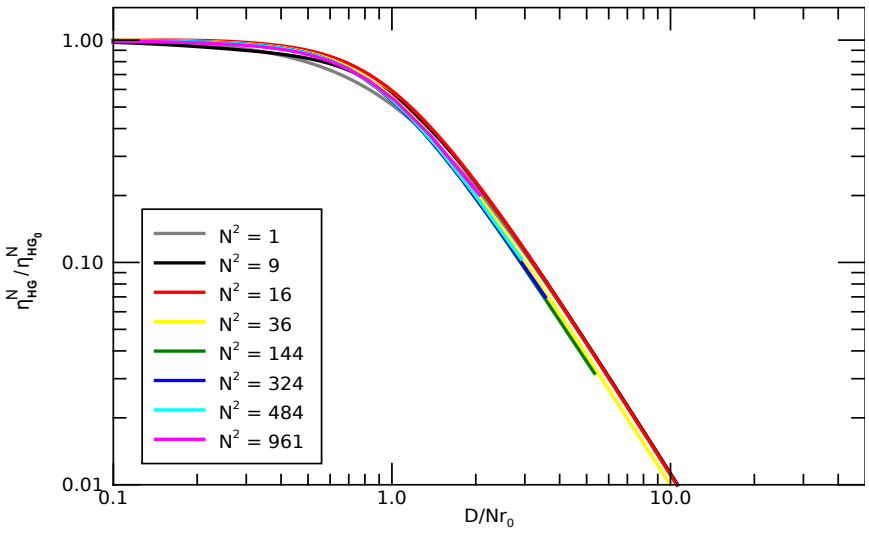

Figure 2.9: Atmospheric turbulence perturbations: coupling efficiency normalized by its maximum plane-wave value, $\eta_{HG}^N/\eta_{HG_0}^N$, as function of D/Nr_0 for different set of Hermite-Gaussian modes. Each of them is denoted by N^2, the total number of modes in the set. D : pupil diameter; r_0 : Fried parameter.

For $D/Nr_0 < 1$ the behavior is different according to the value of N. In Figure 2.10 the relative coupling efficiency is reported, for different set of modes. Concerning the Gaussian mode (left plot of Figure 2.10), the average coupling efficiency is the same as the one obtained with a hexagonal fiber collimator array and described with Eq. 2.10. Indeed, for $N > 1$ (right plot of Figure 2.10), a different approximation can be derived: $\sum_{i=0}^{N^2-1}[PM_i \otimes PM_i](\mathbf{r})$ is roughly approximated by a Gaussian function.

Furthermore, a Taylor expansion of Eq. 2.6 gives: $\eta_{HG}^N/\eta_{HG_0}^N \approx 1 - \alpha_N\left(\frac{D}{Nr_0}\right)^2$, where α_N is a parameter slightly varying according to N. In Figure 2.10 a zoom of the average coupling efficiency obtained in the previous Figure 2.9 is reported. It also confirm the validity of the approximation, and gives an estimate of α_N:

$$\frac{\eta_{HG}^N}{\eta_{HG_0}^N} \approx 1 - 0.5\left(\frac{D}{Nr_0}\right)^2 \tag{2.11}$$

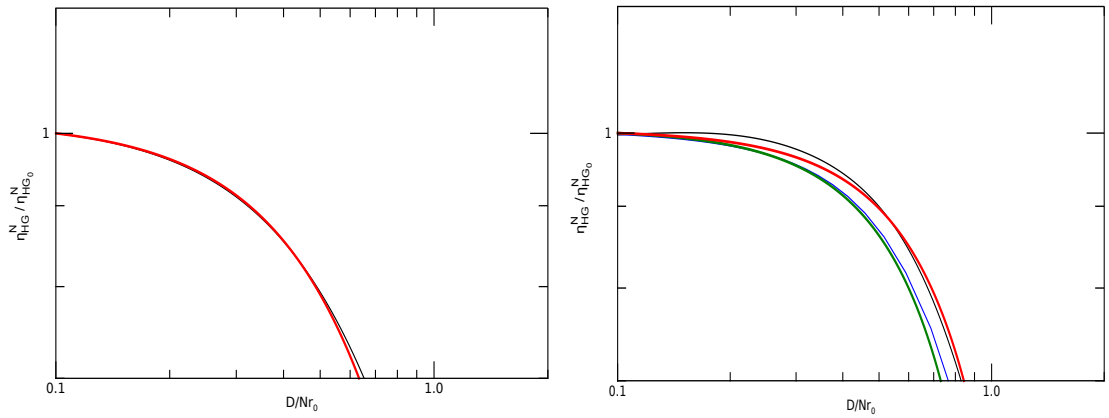

Figure 2.10: Atmospheric turbulence perturbations: zoom of average coupling efficiency normalized by its maximum plane-wave value, $\eta^N_{HG}/\eta^N_{HG_0}$, for different sets of Hermite-Gaussian modes and considering $D/Nr_0 < 1$. Left: Gaussian mode only (black line), and fit obtained with Eq. 2.10 (red line). Right: Result obtained with $N^2 = 16$ (black line), and $N^2 = 961$ (blue line) HG modes, and plot of $1 - \alpha_N \left(\frac{D}{Nr_0}\right)^2$, for $\alpha_N = 0.43$ (red line) and $\alpha_N = 0.57$ (green line). D : pupil diameter; r_0 : Fried parameter.

Moreover, in Figure 2.11 the average coupling efficiency of Eq. 2.6 normalized by its plane-wave value is reported as function of D/r_0, for different set of HG modes.

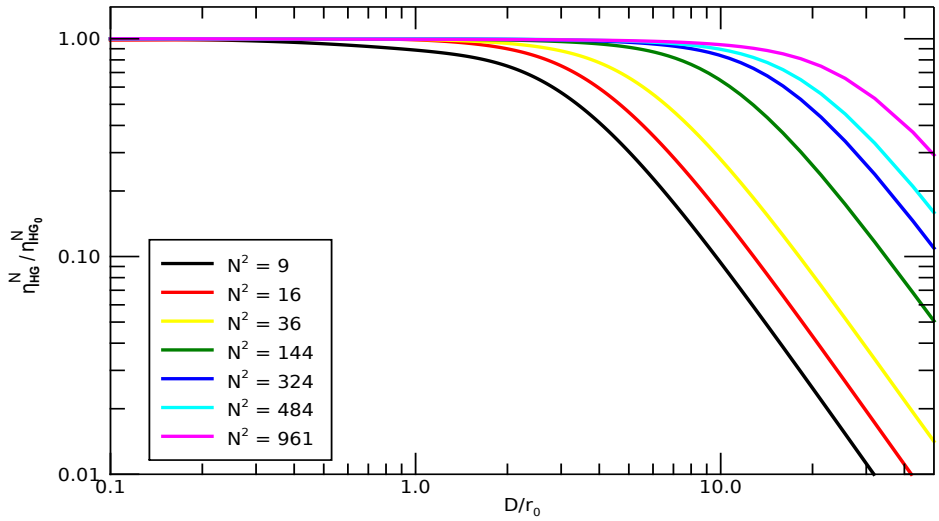

Figure 2.11: Atmospheric turbulence perturbations: coupling efficiency normalized by its maximum plane-wave value, $\eta^N_{HG}/\eta^N_{HG_0}$, as function of D/r_0 for different set of Hermite-Gaussian modes. Each of them is denoted by N^2, the total number of modes in the set. Spatial coherence function, B_Ψ, obtained with Eq. 2.7. D : pupil diameter; r_0 : Fried parameter.

As stated in section 2.3, for large values of D compared to r_0, the coupling efficiency decreases proportionally with $(D/r_0)^{-2}$. It is worth comparing the performance of the Hermite-Gaussian mode decomposition and the one used for a hexagonal fiber array. Under the conditions where the number of modes is identical, i.e. for $N^2 \approx \frac{\pi D^2}{4d^2}$ or $d \approx \frac{\sqrt{\pi}D}{2N}$, the relative coupling efficiency of the Hermite-Gaussian mode set is nearly identical to that of a hexagonal lenslet array, such that: $\frac{\eta^N_{HG}\left(\frac{D}{Nr_0}=1\right)}{\eta^N_{HG_0}} \approx \frac{\eta_{FCA}\left(\frac{d}{r_0}=\sqrt{\pi}/2\right)}{\eta_{FCA_0}} \approx 0.6$. Nevertheless, the maximum coupling efficiency achieved with the fiber collimator array is always equal to 0.82, while a maximum value close to 1 can be obtained with a set of Hermite-Gaussian modes, as soon as its number is important.

Indeed, the main gain brought by HG modes lies in their ability to optimize the coupling with a plane wave. Through the previous figure, we may able to answer to the number of modes needed for a given turbulence condition. Hence, the performance of such a system can be compared to those of an Adaptive Optics system. Considering a case of good-correction, the Strehl ratio obtained with AO is given by: $1 - \sigma^2_\phi$. From the theoretical expression of the variance for each radial order given by Noll [Noll (1976)], the istantaneous Strehl ratio can be deduced [Fusco and Conan (2004)], equal to:

$$\langle ISR_0 \rangle \simeq (1 - \sigma^2_\phi) \simeq \left[1 - 0.458(n_0 + 1)^{-5/3}\left(\frac{D}{r_0}\right)^{-5/3}\right] \tag{2.12}$$

where n represent the largest radial degree of the set of Zernike polynomials used for describing the phase. Once again, the performance of both AO and mode-decomposition device are closed considering the same number of modes. Nevertheless, the complex coefficients of Hermite-Gaussian mode decomposition leads to a number of degrees of freedom multiplied by a factor of 2 compared to the AO one, which coefficients are real. Indeed, with Hermite-Gaussian modes, and particularly with Eq. 2.11 we are taking into account also the scintillation effects, while these are assumed to be negligible in case of adaptive optics.

2.4.3 Phase tip-tilt correction

The relative coupling efficiency has been estimated until now using the expression of the coherence function of the field as given by Eq. 2.7.

In this case, all the perturbations induced by atmospheric turbulence are taken into account. In this subsection we aim to evaluate the effect of a simple tip-tilt implementation through image stabilization on the average coupling efficiency previously shown. The results presented in this section are obtained substituting in Eq. 2.6 the expression of Eq. 2.7 with the short-exposure coherence function of Eq. 2.8, still in the considered case of Hermite-Gaussian mode decomposition.

In Figure 2.12 we reported the relative coupling efficiency as function of D/r_0 for different sets of modes, using the expression of the coherence function given by Eq. 2.8. Furthermore, according to Figure 2.13, the gain brought by tip-tilt compensation is very different with D/Nr_0. Hence, the coupling efficiency curves are not superimposable as shown in Figure 2.9. The gain is large for $N = 1$, almost five times the coupling efficiency value obtained without image stabilization. Nevertheless, it decreases with the increase of N, since tip-tilt aberrations may be described by high-order modes. Despite this, the gain is still significant even with several hundreds of modes, thus having a gain of almost 1.5 times for $N^2 = 324$ modes.

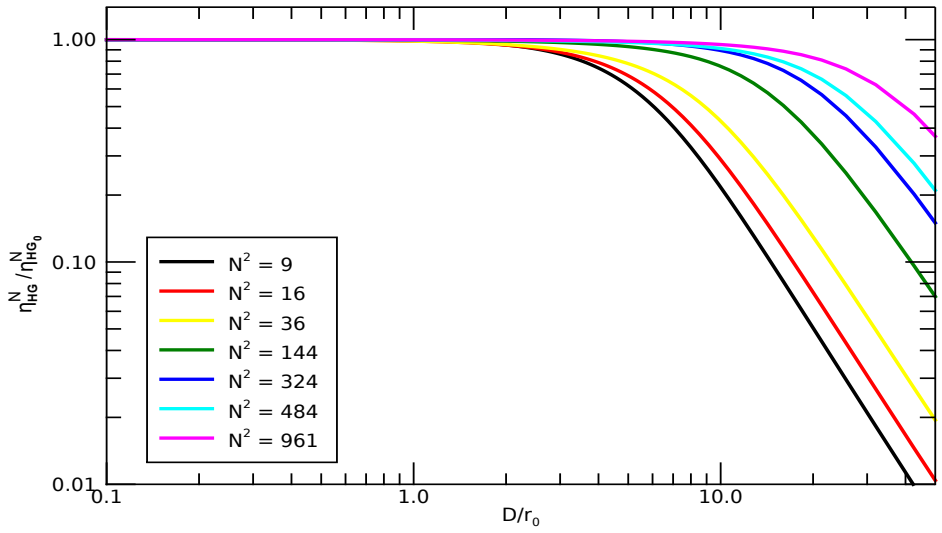

Figure 2.12: Atmospheric turbulence perturbations: coupling efficiency normalized by its maximum plane-wave value, $\eta^N_{HG}/\eta^N_{HG_0}$, as function of D/r_0 for different sets of Hermite-Gaussian modes. Each of them is denoted by N^2, the total number of modes in the set. Spatial coherence function, $B_{\Psi_{se}}$, obtained with Eq. 2.8. D : pupil diameter; r_0 : Fried parameter.

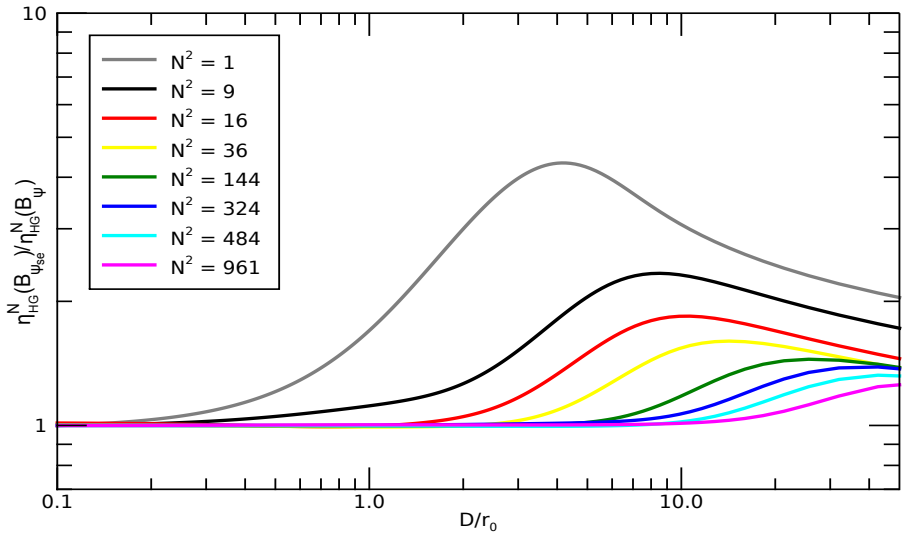

Figure 2.13: Atmospheric turbulence perturbations: ratio between the average coupling efficiency with and without image stabilization, $(\eta^N_{HG}(B_{\Psi_{se}})/\eta^N_{HG}(B_\Psi))$, as function of D/r_0, for different sets of HG modes. B_Ψ: spatial coherence function of the field, as obtained in Eq. 2.8; $B_{\Psi_{se}}$: spatial coherence function of the field obtained in case of rapid image stabilization, Eq. 2.7; D : pupil diameter; r_0 : Fried parameter.

2.4.4 Comparison between Laguerre-Gaussian and Hermite-Gaussian beams

In the previous sections we chose the Hermite-Gauss as modal basis. However, several other bases exist as solution of the wave propagation equation, and the same development as before can be applied to them. In this section, the Laguerre-Gaussian modes are taken into account, which does not restrict the generality of our study since any mode of a given mode family may be expressed as a linear combination of elements of the other family [Kimel (2021)]. Moreover, we consider a set of N^2 LG, characterized by their radial and azimuthal degrees, *p* and *l*, such that $0 \leq p \leq N-1$ and $0 \leq l \leq N-1$.

In Figure 2.14 we evaluate the coupling efficiency (Eq. 2.6) with both sets of LG and HG modes, for four different turbulence conditions. For instance, given a square set of HG modes, described with their m and n indices in the x and y direction respectively, it would take twice LG modes to achieve the same coupling efficiency.

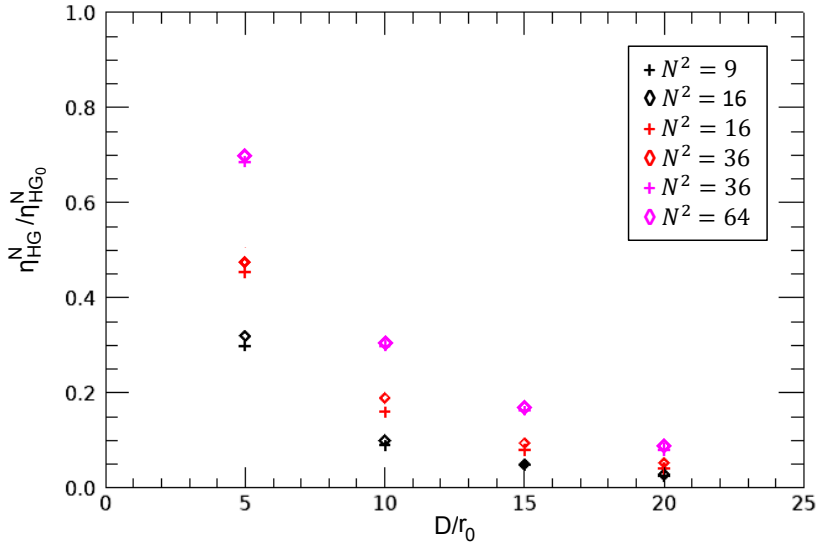

Figure 2.14: Atmospheric perturbations: coupling efficiency normalized by its maximum plane-wave value, $\eta^N_{HG}/\eta^N_{HG_0}$, as function of D/r_0 for different sets of Hermite-Gaussian (here denoted with the symbol '+') and Laguerre-Gaussian modes (symbol '◇'). Each of them is denoted by N^2, the total number of modes in the set. D : pupil diameter; r_0 : Fried parameter.

Indeed, we compared 9 HG modes with $\approx 2 \cdot 9$ LG modes, as well as 36 HG modes with ≈ 72 LG modes, always obtaining the same coupling efficiency. We think that one possible reason lies into the in the inherent optimized geometry of the Hermite-Gaussian modes with respect to the Laguerre-Gaussian one. The radial and azimuthal shape of the LG modes does not allow in fact a precise description in the case of the presence of speckles due to different turbulence conditions (as well as due to the different coherence lengths, or r_0), which is easy to do for the HG modes, given their particular geometry in the x and y directions.

The question now being addressed is a direct consequence from the previous analysis: given the set of N modes, does it represent the set of the most suitable modes with respect to the

different atmospheric turbulence conditions? We wish to study how a mode optimization can affect the analysis of the previous sections, and which gain we can obtain compared to the image stabilization already mentioned. In the following sections, we will use the only set of HG modes, due to their easy separability in the x and y axis of a Cartesian system, which makes them especially suited for the modal analysis.

2.4.5 Mode optimization

We have so far considered two distinct spatial division multiplexer devices, and shown that for the same number of modes, N^2, the coupling efficiency was slightly better using Hermite-Gaussian modes than with a fiber collimator array. Furthermore, as we stated beforehand, the problem we aim to tackle is that of the number of degrees taken by such a system, or number of modes, compared to a classical adaptive optics system. Nevertheless, it is legitimate to ask whether another set of modes would not be more efficient with regards to field perturbations induced by atmospheric turbulence. From a practical point of view, if some multiplexer is associated with particular modes, it is theoretically possible to have access to any set of modes with dedicated phase plates.

In this section, we are searching to study the mode optimization as function of different atmospheric turbulence conditions. Particularly, given a number of modes, N^2, we may be able to evaluate the covariance matrix of the field decomposition on the Hermite-Gaussian modes. The set of modes that maximize the coupling efficiency is the set of the N^2 first eigenmodes of the covariance matrix. Also, the coupling efficiency of each eigenmode is given by its associated eigenvalue.

It is possible to generalize the Eq. 2.3 for the evaluation of the covariances of these coefficients:

$$\overline{s_i s_j^*} = \frac{1}{\langle P|P\rangle} \int\int d^2\mathbf{r} d^2\mathbf{r}' M_i(\mathbf{r}) M_j^*(\mathbf{r}') P(\mathbf{r}) P(\mathbf{r}') \overline{\Psi_{turb}(\mathbf{r}) \Psi_{turb}^*(\mathbf{r}')} \tag{2.13}$$

In Figure 2.15 we compute the covariace matrix of a 144 Hermite-Gaussian set of modes. One can see that it is nearly diagonal but not completely null, thus inducing some correlation among the orthonormal coefficients. The latter is nevertheless relatively weak and can be neglected in a first approximation: the diagonal coefficients are predominant compared to the others.

Unfortunately, unlike phase perturbations correlation matrices, the coefficient of the previous matrix are not linearly dependent of a coefficient related to D/r_0. In Figure 2.16 we reported the eigenvalues of the covariance matrix for two different atmospheric turbulence conditions: a first case of moderate turbulence, with a $D/r_0 = 5$, and a second case of strong turbulence, with a $D/r_0 = 10$.

Both are analyzed in a space defined by a set of $N^2 = 961$ HG modes. The corresponding matrices were estimated for both perturbation conditions.

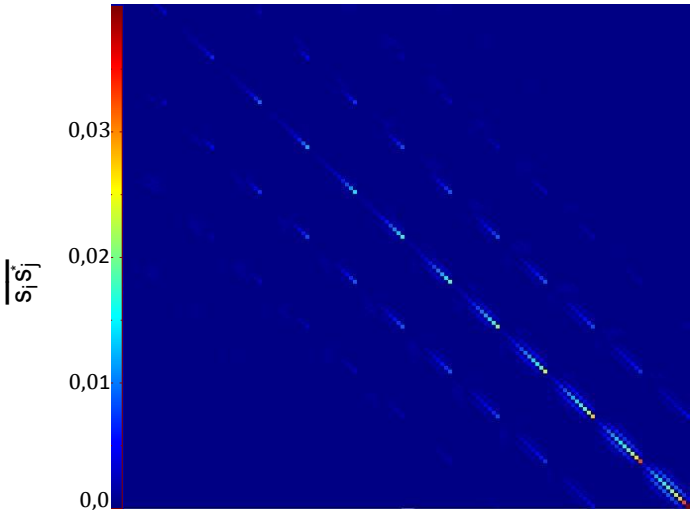

Figure 2.15: Covariance matrix of a 144 Hermite-Gaussian set of modes.

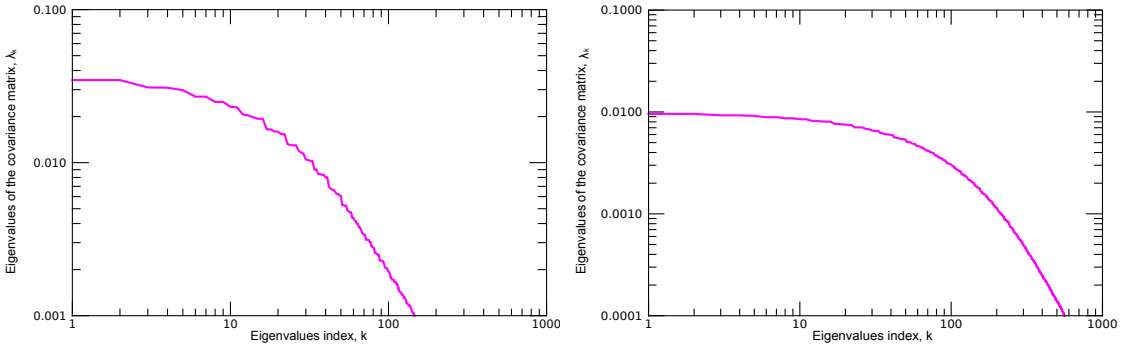

Figure 2.16: Atmospheric turbulence perturbations. Eigenvalues of the covariance matrix, λ_k, as a function of the eigenvalues index (here denoted by *k*), for: (left) $D/r_o = 5$, and (right) $D/r_o = 10$. D : pupil diameter; r_0 : Fried parameter; N^2 : number of modes = 961.

In both perturbation conditions of the Figure above, two distinct regimes can be distinguished: a first regime characterized with a slow decay of the first $\left(\frac{D}{r_0}\right)^2$ eigenvalues, and a second one with a fast decay of the next ones. Indeed, a slow decay of the first ≈ 20 eigenmodes is represented in Figure 2.16 (left), while ≈ 80 eigenmodes for the case of D/r_0 equal to 10 (right). The cutoff can be also defined as the dimension of the coherence area of the field perturbations: the first eigenvalues correspond to the eigenmodes with spatial modulations of size larger than r_0, probably nearly to low degree of HG modes. At f_{cut}, the eigenmodes are considered having the same size as the r_0.

For comparison, in Figure 2.17 the average coupling efficiency per Hermite-Gaussian mode is shown, for a set of 16 HG modes and a $D/r_0 = 5$. The collection for this set of modes confirm the slow decay of these eigenvalues. Moreover, the cumulative sums of the first *K* eigenvalues of the covariance matrix are presented in Figure 2.18, always for both turbulence perturbation levels: $D/r_0 = 5$ and $D/r_0 = 10$.

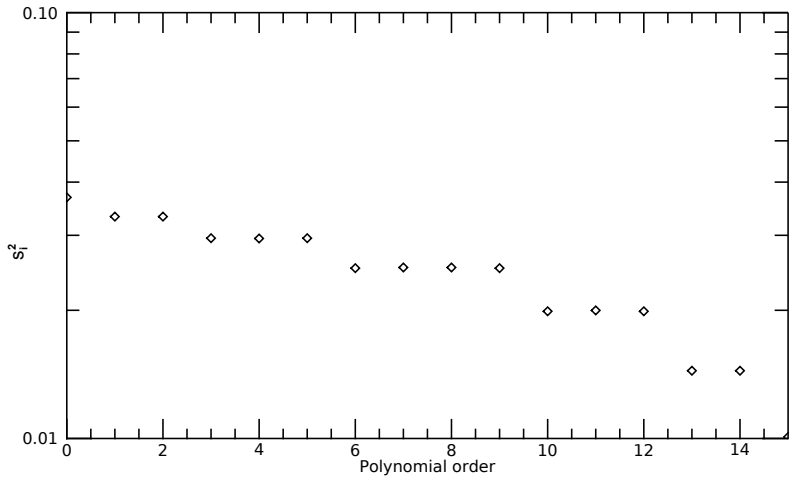

Figure 2.17: Atmospheric turbulence perturbations. Turbulent energy distribution per Hermite-Gaussian mode for a set of 16 modes and $D/r_o = 5$. Coupling coefficients, s_i^2, as function of the polynomial order. D : pupil diameter; r_0 : Fried parameter.

The sum of 961 eigenvalues, i.e. the coupling efficiency with 961 modes, will allow us to achieve a value of $\eta \approx 0.95$ and $\eta \approx 0.9$ for $D/r_0 = 5$ and $D/r_0 = 10$ respectively. One can also see that the coupling efficiency obtained from these eigenmodes is close to the one given with the Hermite-Gaussian set of modes.

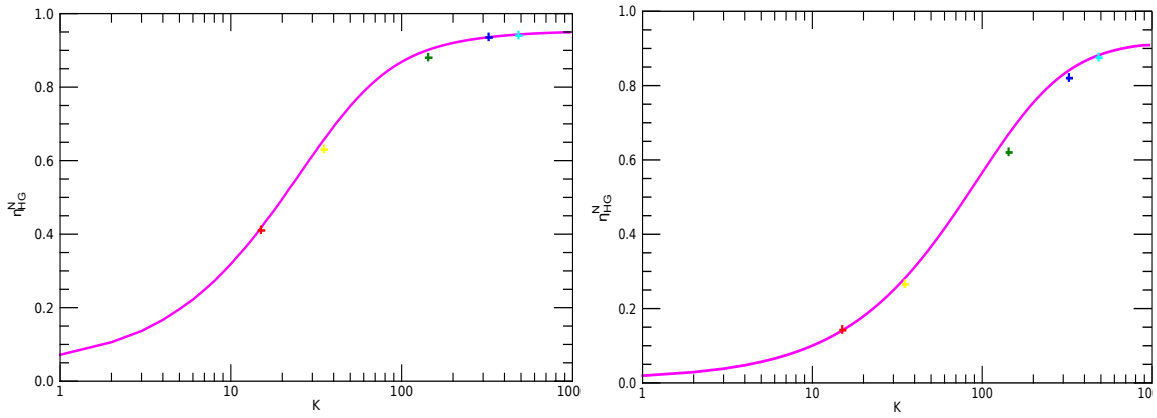

Figure 2.18: Atmospheric turbulence perturbations: cumulative sum of the first K eigenvalues of the covariance matrix (magenta line), and coupling efficiency (η_{HG}^N) for different sets of N^2 Hermite-Gaussian modes (crosses). Spatial coherence function B_Ψ obtained with Eq. 2.7. Left: $D/r_0 = 5$. Right: $D/r_0 = 10$. D : pupil diameter; r_0 : Fried parameter.

In the same figure, we reported also the coupling efficiency derived with an identical number of HG modes, each of them denoted with a cross of different color, such as 16 HG modes (red), 36 HG (yellow), 144 HG (green), 324 HG (blue), and 484 (light blue) Hermite-Gaussian modes. The gain in the coupling efficiency at a constant number of modes is of the order of few percent in the most favorable part of the curves, i.e. when the slope of the curve is more important. Namely, this result in a reduction of a few number of modes with the same coupling

efficiency, compared with the Hermite-Gaussian mode set.

We also evaluated the performance obtained with mode optimization in presence of rapid image stabilization. That is, will constitute the last part of this Chapter. In this case, as previously mentioned, the covariance matrix is computed with the coherence function derived with Eq. 2.8, and the results are shown in Figure 2.19. The gain brought by eigenmodes optimization is still a few percent whether for $D/r_0 = 5$ or $D/r_0 = 5$, as observed without image stabilization.

Moreover, as the performance obtained with mode optimization is similar to that derived without mode optimization, we can state that image stabilization brings a gain close to the gain reported in Figure 2.13. Indeed, image stabilization improves the coupling efficiency much more than mode optimization. The implemented optimization cannot provide a set of modes able to compensate the tip-tilt aberration: phase tip-tilt can not be described by just a few number of propagation modes.

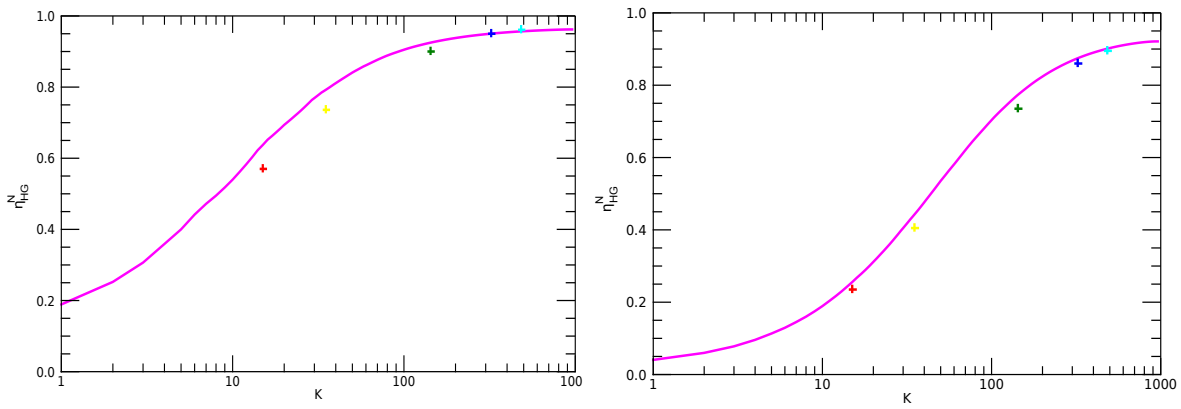

Figure 2.19: Atmospheric turbulence perturbations: cumulative sum of the first K eigenvalues of the covariance matrix (magenta line), and coupling efficiency (η^N_{HG}) for different sets of N^2 Hermite-Gaussian modes (crosses). Case of rapid image stabilization (spatial coherence function $B_{\Psi_{se}}$ obtained with Eq. 2.8). Left: $D/r_0 = 5$. Right: $D/r_0 = 10$. D : pupil diameter; r_0 : Fried parameter.

2.5 Impact of phase-only correction on coupling efficiency evaluation

We have so far analyzed the coupling between a beam in free space and an SDM device. The effects of atmospheric turbulence on this coupling have been taken into account. However, it is important to assess the difference in coupling efficiency obtained by recombining these modes without correction of both amplitude and phase.

In this section we are interested at the impact of phase-only correction on the coupling efficiency. In the following, we will consider a hierarchical tree structure, as the one presented in Figure 2.20 (left). Indeed, the previous Eq. 2.5 reported in Section 2.2, can be now rewritten assuming that after modal decomposition the output beams are recombined after compensation of the only-phase of the waves. The ratio of the flux carried by the wave after recombination to the input flux writes in average:

$$\overline{\eta}_{po} = \frac{\frac{1}{N^2}\overline{\left[\sum_{i=0}^{N^2-1}|s_i|\right]^2}}{\sum_{i=0}^{N^2-1}\overline{|s_i|^2}} \tag{2.14}$$

Through this architecture, the signal at the output communication channel is derived by considering the sum of the input signals: $A_{comm} = \left(\frac{\sqrt{2}}{2}\right)^n \sum_{i=1}^{N^2} A_i = \left(\frac{1}{2^{n/2}}\right)^n \sum_{i=1}^{N^2} A_i$, in which i denotes the number of channels. Here, the term $\sum_{i=0}^{N^2-1}\overline{|s_i|^2}$ represent the input intensity on the telescope pupil, while the numerator denote the square of the output complex amplitude. 0n the other hand, assuming the architecture of Figure 2.20 (right), a slightly different sum is obtained at the communication channel with respect to the one reported in Eq. 2.14. Considering a 8-channel base circuit, the signal at the output communication channel is now given by: $A_{comm} = \left(\frac{\sqrt{2}}{2}\right)^4 (A_1 + A_8) + \left(\frac{\sqrt{2}}{2}\right)^3 (A_2 + A_7) + \left(\frac{\sqrt{2}}{2}\right)^2 (A_3 + A_6) + \left(\frac{\sqrt{2}}{2}\right)(A_4 + A_5)$.

To go beyond this analysis, we can assume that $|s_i|$ and $|s_j|$ are independent random variables: $\overline{|s_i| \cdot |s_j|} = \overline{|s_i|} \cdot \overline{|s_j|}$. This assumption is justified by the spatial decorrelation of B_Ψ, i.e. considering a lenslet array, we can write that $r_0 < d$, where d represents the diameter of each microlens. This is also evident through the covariance matrix obtained for the Hermite-Gaussian modes and shown in Figure 2.15. Indeed, for the particular case of hierarchic couplers with n stages of couplers, such as $N^2 = 2^n$, and with amplitude coupling coefficients of $\frac{\sqrt{2}}{2}$, each input amplitude is divided by $\left(\frac{\sqrt{2}}{2}\right)^n = \frac{1}{N}$.

By developing the numerator of the Equation 2.14, we obtain:

$$\overline{\left[\sum_{i=0}^{N^2-1}|s_i|\right]^2} = \sum_{i=0}^{N^2-1}\overline{|s_i|^2} + \sum_{i=0}^{N^2-1}\sum_{j\neq i}^{N^2-1}\overline{|s_i|}\cdot\overline{|s_j|} \tag{2.15}$$

Furthermore, we can also assume that the previous $|s_i|$ and $|s_j|$ variables follow the same distribution, i.e. a Rayleigh distribution, for which the intensity statistics are described by the decreasing exponential law. This is one of the models used to describe intensity fluctuations in the established saturation regime [Saab (2017)]. Such an assumption is still justified considering a lenslet array. Moreover, as reported in Figure 2.16, the first eigenvalues of the covariance

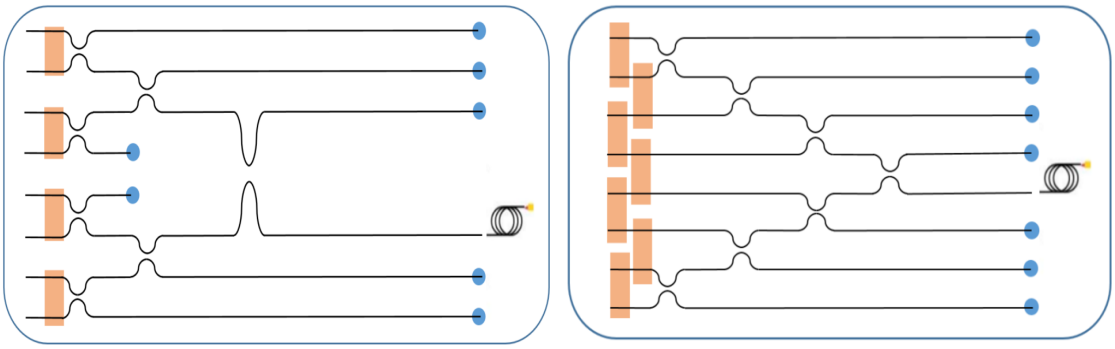

Figure 2.20: Different architecture for beam combining: (left) the input beams are arranged in a hierarchical tree structure, (right) recombination architecture proposed by K. Saab [Saab (2017)].

matrix are characterized by a slow decay (approximately the same value), thus respecting the previous hypothesis. As reported by Hu [Hu and Beaulieu (2005)], a closed-form expression does not exist for the sum distribution and consequently, it is often evaluated numerically or approximated. In this context, it is possible to describe the fluctuations of the field in the focal plane with a Rayleigh's law:

$$f(x,\sigma) = \frac{x}{\sigma^2} exp\Big(-\frac{x^2}{2\sigma^2}\Big) \tag{2.16}$$

Considering the previous Rayleigh distribution, the raw moments are given by:

$$\mu_j = \sigma^j 2^{j/2} \Gamma(1+\frac{j}{2}) \tag{2.17}$$

In this context, the first order moment is written as $\mu_1 = \overline{|s_i|} = \sigma\sqrt{\frac{\pi}{2}}$, while the second order moment, $\mu_2 = \overline{|s_i|^2} = 2\sigma^2$. Hence, $\sigma = \Big(\frac{\overline{|s_i|^2}}{2}\Big)^{\frac{1}{2}} = \frac{\overline{|s_i|}}{\sqrt{\frac{\pi}{2}}}$, that leads to:

$$\overline{|s_i|} = \Big[\frac{\pi}{4}\overline{|s_i|^2}\Big]^{\frac{1}{2}} \tag{2.18}$$

Therefore, substituting previous Equation 2.18 in Eq. 2.15, the numerator of Eq. 2.14 writes:

$$\overline{\Big[\sum_{i=0}^{N^2-1}|s_i|\Big]^2} = \sum_{i=0}^{N^2-1}\overline{|s_i|^2} + \frac{\pi}{4}\sum_{i=0}^{N^2-1}\sum_{j\neq i}^{N^2-1}\Big[\overline{|s_i|^2}\cdot\overline{|s_j|^2}\Big]^{1/2} \tag{2.19}$$

Considering a number of cross terms far larger than the number of diagonal terms:

$$\overline{\Big[\sum_{i=0}^{N^2-1}|s_i|\Big]^2} \approx \frac{\pi}{4}\sum_{i=0}^{N^2-1}\sum_{j\neq i}^{N^2-1}\Big[\overline{|s_i|^2}\cdot\overline{|s_j|^2}\Big]^{1/2} \tag{2.20}$$

Finally, the average coupling efficiency normalized by the input flux in the case of phase-only correction is given by:

$$\overline{\eta}_{po} \approx \frac{\frac{1}{N^2}\frac{\pi}{4}\sum_{i=0}^{N^2-1}\sum_{j\neq i}^{N^2-1}\Big[\overline{|s_i|^2}\cdot\overline{|s_j|^2}\Big]^{1/2}}{\sum_{i=0}^{N^2-1}\overline{|s_i|^2}} \tag{2.21}$$

Since all s_i follow the same law (same σ), $\sum_{i=0}^{N^2-1} \overline{|s_i|^2} = 1$ and $\overline{\eta}_{po} = \frac{\pi}{4}$. In this context, the previous Eq. 2.21 is considered to be in the worst case (saturation regime). On the other hand, if we are not in the saturation regime, $\overline{|s_i|} \geqslant \left[\frac{\pi}{4}\overline{|s_i|^2}\right]^{\frac{1}{2}}$, and we tend towards a log-normal distribution for weak disturbances. The impact of the phase-only correction over the phase and amplitude correction on a PIC is also analyzed through a Monte-Carlo (MC) simulation in the following part, considering a given scenario of LEO-to-ground downlink at 10° elevation.

2.6 High level specifications

In this section the fluctuations of the coupling efficiency are analyzed, as a function of the number of modes. An end-to-end simulation is used to perform a coherent combining system, starting from the definition of a link budget through the high level specifications. Such specifications depend on the conditions under which the photonic integrated circuit is operated. As a consequence, the scenario defining the LEO-to-ground link is firstly detailed.

The performance of the present approach composed by the MPLC + PIC may be analyzed in a way similar to the one used with AO. In this context, one important metric is represented by the coupling between an optical received signal and the SMF mode, M_0. Such overlap integral is defined in Chapter 1, Section 1.3.5, by Equation 1.22 [Shaklan and Roddier (1988)]. Through this expression the coupling efficiency is derived (Eq. 1.23). Indeed, the coupling efficiency is limited both by the number of modes used for the field decomposition, and by the phase correction errors induced by noisy measurements and temporal effects, such as the delay in the control loop. As already stated, the limitation induced by the number of modes is called spatial error. Otherwise, the errors induced by noise measurement have not been considered in this work: the available power being quite large, it may be neglected in a first analysis. Finally, the temporal error has not been studied in detail since it depends on the control law.

Only the requirement on the phase control has been detailed with respect to the performance of the envisioned materials.

2.6.1 Scenario and Link Budget

In order to establish a link budget, we introduce the main parameters of the considered scenario. Each of these parameters is linked to the various modules of which the link is composed (emitter and receiver characteristics, attenuation, etc). Finally, a first specification in terms of overall power margin and average coupling efficiency is derived at the end of this section.

2.6.1.1 Link geometry

We refer here to a LEO-to-ground downlink at 10° elevation, with a wavelength of $\lambda = 1.55\ \mu m$. The height of the satellite considered is $H = 550\ km$, and its velocity is equal to $v_{sat} = 7.5\ km/s$. A distance of $D_{sat} = 3168\ km$ is therefore considered at $\theta = 10°$. Finally, the free-space propagation losses, which measure the power losses of an electromagnetic wave propagating in free-space over a distance L, are obtained through the Eq. 1.29: $L_{fs} = -268.19\ dB$.

2.6.1.2 Atmospheric attenuation

As already stated in Chapter 1, Earth's atmosphere attenuates the optical beam propagation through absorption and scattering effects. A transmittance, T_{atm} is defined in [Hemmati (2009)] as the ratio of the intensity of a beam after a propagation over a distance L, over the intensity of the same collimated emitted beam:

$$T_{atm} = I(L)/I(L_0) = exp\Big(-\frac{L}{L_0}\Big) \tag{2.22}$$

Such transmittance can be also expressed in dB: $L_{atm} = -\frac{L}{L_0}\frac{1}{ln(10)}$. Assuming a transmission of $T_{atm} = 0.9$ at the zenith and substituting in the previous equation the propagation distance L with $L = H/sin(\theta)$, the previous transmittance writes: $L_{atm} = \frac{-0.46}{sin(\theta)} = -2.64dB$. Similar values are also reported in [Artaud et al. (2019)] for a LEO-to-ground satellite at 20° elevation. In the further hypothesis of thin clouds in clear sky, $L_{clouds} \approx 3dB$ is also taken into account in the following link budget.

2.6.1.3 Emitter module characteristics

The power dedicated to the on-board source is about $P_E = 2\,W$, which in turns implies an output power per channel equal to $33\,dBm$. Furthermore, the transmitter diameter is equal to $D_{Tx} = 80\,mm$. From the link performance assessment presented in the Chapter 1, Section 1.4, antenna gains can be easily calculated, thus following Eq. 1.27. Indeed, assuming a coefficient $g_T \approx 1$, the transmitter gain is equal to $G_E = 104.2\,dB$.

Transmitter optical losses, denoted by L_{Tx}, have been also considered in our case of interest. In [Hemmati (2009)] such optical losses are about $\approx 3\,dB$. Another important attenuation rely on the pointing losses, or L_p. Small pointing losses due to misalignment of the narrow emitted beam are considered here of $\approx 3\,dB$ in this context, as reported in Toyoshima [Toyoshima (2005)].

2.6.1.4 Receiver module characteristics

Regarding the receiver module, its diameter is larger with respect to the emitter one: $D_{Rx} = 250\,mm$. Moreover, as for the emitter case, the receiver gain can be obtained with Eq. 1.28, reporting a gain of $G_R = 114.1\,dB$.

The optical receiver losses summarized in the Table 2.1 amount to $6\,dB$, which is the sum of the term related to optical losses ($3\,dB$) and a term corresponding to the mean attenuation due to atmospheric turbulence after correction by adaptive optics ($\approx 3dB$). Similar values of optical receiver losses are reported in [Calvo et al. (2019)], with a margin of $6\,dB$ for a ground-to-LEO link. In this context, it is worth noting that optical losses of $3dB$ is a very ambitious goal nowadays.

2.6.1.5 Link budget

Therefore, setting an objective on the bit error rate, we are able to determine the received power, which in turns will give us the link margin, as reported in Chapter 1, Section 1.4.1. Indeed, a BER lower than 10^{-3} implies a value of $Q \geqslant 3$. Hence, for a 10 Gbps capacity channel, the minimum received power is $P_R \approx -45dBm$. This leads to approximately 36 photons per bit. Following the link budget presented in Table 2.1, a link margin of $-8.72dB$ is thus derived.

Parameters	Value	Commentary
Link parameters		
Wavelength, λ	1550 nm	
Satellite altitude, h_{sat}	550 km	Hypothesis of a satellite distance of 3168 km at 10° elevation
Elevation angle, θ	10 deg	
Vertical attenuation	-0.46 dB	Considering a transmission of $\tau = 0.9$
Transmitter diameter, D_{Tx}	80 mm	
Receiver diameter, D_{Rx}	250 mm	
Transmitter		
Booster output power per λ, P_E	33 dBm	Power of 2W employed
Optical transmission losses, T_{Tx}	-3.2 dB	From [Hemmati (2009)]
Pointing error, L_p	-3.0 dB	From [Toyoshima (2005)]
Transmitter gain, G_E	104.2 dB	Depends on the beam divergence, Eq. 1.27
Propagation		
Absorption and scattering losses, L_{atm}	-2,64 dB	From the vertical attenuation, considering $sin(\theta)$
Cloud attenuation, L_{clouds}	-3 dB	Hypothesis of thin clouds in clear sky
Free-space attenuation, L_{fs}	-268,19 dB	From Eq. 1.29
Receiver (OGS)		
Receiver gain, G_R	114,1 dB	Depends on the Eq. 1.28
Optical reception losses, T_{Rx}	-3 dB	From [Hemmati (2009)]
AO correction losses, T_{AO}	-3 dB	Due to the imperfection of the AO correction
Total power without SMF coupling	-34.73 dBm	
Losses on SMF coupling efficiency, L_{AO}	-1.55 dB	Considering a transmission of 0.7
Total power	-45 dBm	BER lower than 10^{-3},
Power margin	-8.72 dB	

Table 2.1: Link budget: LEO-to-ground downlink

2.6.2 Performance analysis

In this section the performance of a coherent combining approach is analyzed, based on numerical simulations. The atmospheric turbulence parameters are first introduced, as well as the parameters used in the TURANDOT tool and the parameters describing the propagation (mentioned in Section 1.3.4 of Chapter 1). The results obtained in term of coupling efficiency are described, as well as the spatial and temporal analysis.

2.6.2.1 Atmospheric turbulence

The following Hufnagel-Valley based $C_n^2(h)$ profile has been used [Valley (1980)], as recommended by the International Telecommunication Union (ITU-RP.1621-1):

$$C_n^2(h) = 8.148 \cdot 10^{-56} v_{rms}^2 h^{10} exp(\frac{-h}{1000}) + 2.7 \cdot 10^{-16} exp(\frac{-h}{1500}) + C_0 exp(\frac{-h}{100}) \quad (2.23)$$

where h is the altitude expressed in m, while v_{rms} denotes the wind velocity fluctuations at the upper layers of the atmosphere, and C_0 the value of $C_n^2(h)$ at the ground level. Such value at the ground is $C_0 = 5.410^{-14} m^{-2/3}$ while the wind velocity fluctuations at the upper layers of the atmosphere is: $v_{rms} = 21 m/s$. Based on the previous profile, Eq. 1.7 results in a vertical Fried parameter $r_0 = 15cm$, equal to $r_0 = 5.25cm$ at 10° elevation, at $\lambda = 1.55\ \mu m$.

A Bufton profile has been used to describe the wind as function of the distance to the ground, as expressed in Eq. 1.20. A wind speed at the ground of $v_G = 10 m/s$ is taken into account, as well as the wind speed of $v_T = 20 m/s$. It should be noted that, as reported in Section 1.3.4.1 of Chapter 1, the satellite velocity denotes also the satellite velocity component orthogonal to the line of sight. Indeed, these values are briefly summarized in the Table 2.2. They are in good agreement with the ones considered in literature for the dimensioning of adaptive optics systems dedicated to satellite-ground optical links [Gregory et al. (2013); Wilson and Roberts (2014); Calvo et al. (2014)].

Refractive index structure constant at the ground, C_0:	5.4 $10^{-14}\ m^{-2/3}$
Wind velocity fluctuations$_h$, v_{RMS}:	21 m/s
Fried parameter, r_0 @1.55 μm:	5.25 cm
Log-amplitude variance, σ_χ^2 @1.55 μm:	0.56
Wind speed at the ground, v_G:	10 m/s
Wind speed$_h$, v_T:	20 m/s
Satellite velocity, v_{sat}:	7.5 km/s

Table 2.2: Propagation conditions of a LEO-to-ground downlink at 10° elevation.

2.6.2.2 Numerical simulations

As presented in Figure 2.21, different simulation modules have been used or implemented during this thesis, and employed in order to address the performance of a coherent combining system in a representative case of LEO-to-ground optical link.

For the sake of simplicity, such modules are briefly summarized below:

- optical beam propagation through the atmosphere: use of an end-to-end simulation tools: TURANDOT;
- tip-tilt correction as optional step: a simple system that senses only the centroid of the image;
- demultiplexer device for mode decomposition: as the Multi-Plane Light Conversion device developed by Cailbas, through the evaluation described in Chapter 2;
- coherent combining: sum of the coefficients of the previous modal decomposition;
- coupling efficiency estimator for both correction types: analysis of the requirements on link margin and coupling efficiency derived from the previous link budget.

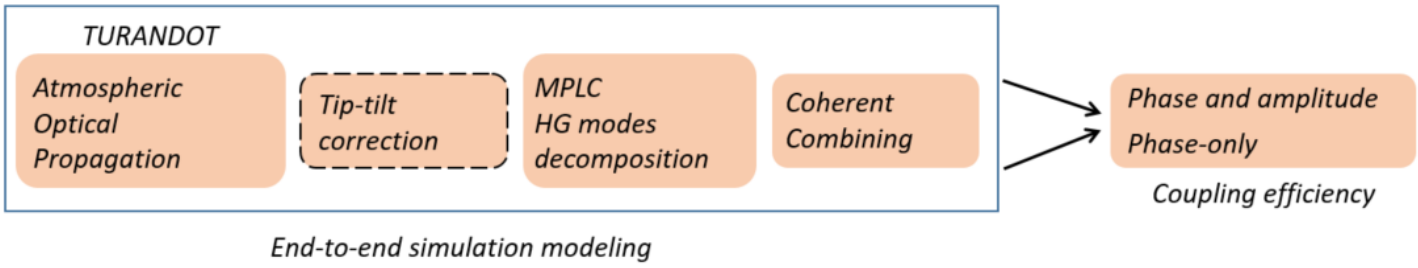

Figure 2.21: Architecture of the numerical simulation developed to model the coupling efficiency of a MPLC + PIC device.

2.6.2.3 Case of $D/r_0 = 4.76$

The coupling efficiency is shown in Figure 2.22, in our case of reference, i.e.: $D/r_0 = 4.76$ ($D = 25cm$ and $r_0 = 5.25cm$), for both correction types. In this context, 4000 temporal occurrences have been considered, while the time step between 2 occurrences is: $t = 0.5\,ms$. The red line represents here the average coupling efficiency value, denoted by μ. As one can see, the link budget requirement of a correction about $3dB$ is achieved with 16 HG modes for phase and amplitude correction, and 25 modes for phase-only correction type. It should be noted that the intensity fluctuations effects on the pupil are not taken into account in the following results.

For the sake of completeness, the influence of a phase-only correction is also presented in Figure 2.23, for a set of 16 Hermite-Gaussian modes. As stated in Chapter 2, an average coupling efficiency of $\eta = 0.5 \cdot \pi/4 \approx 0.36$ is obtained in this case.

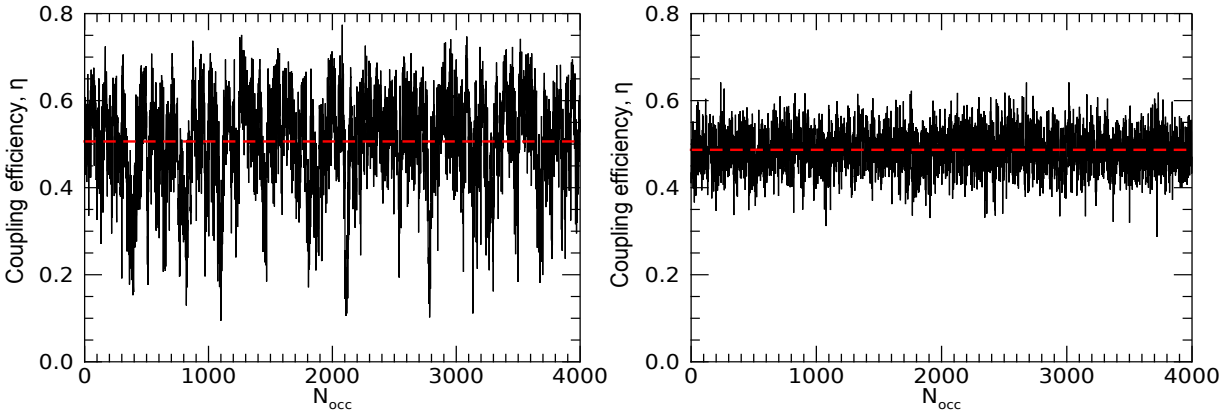

Figure 2.22: Coupling efficiency (Eq. 2.4) function of time, for (left): phase and amplitude correction and (right) phase-only correction. Values obtained with a set of 16 and 25 HG modes respectively, considering $D/r_0 = 4.76$, $\sigma_\chi^2 = 0.56$ and without tip-tilt correction. D : pupil diameter; r_0 : Fried parameter; σ_χ^2 : log-amplitude variance.

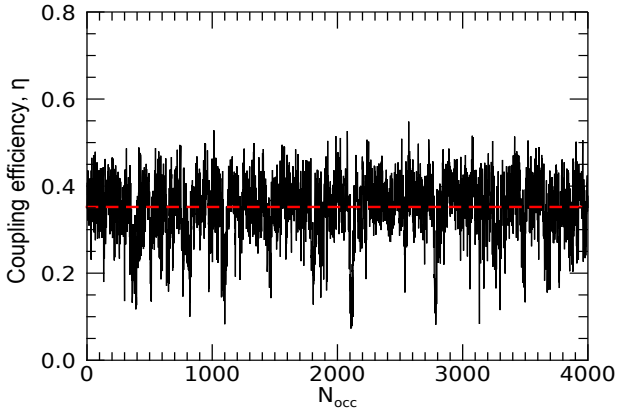

Figure 2.23: Coupling efficiency (Eq. 2.4) function of time, for the phase-only correction type. Values obtained with a set of 16 HG modes, also considering $D/r_0 = 4.76$, $\sigma_\chi^2 = 0.56$ and without a tip-tilt correction. D : pupil diameter; r_0 : Fried parameter; σ_χ^2 : log-amplitude variance.

In Table 2.3 the main statistical results corresponding to Figure 2.22 are summarized. The analytical value of the mean coupling efficiency found in Chapter 2 has also been reported in this table, and denoted by μ_{av}, as the value derived from the analytical analysis.

As observed in Figure 2.22, as well as on Table 2.3, the standard deviation in the case of phase-only correction is lower than the one obtained with phase and amplitude control. Indeed, small fading can be observed considering an higher number of modes and a phase-only control, compared to a case in which less modes are employed with a both phase and amplitude correction type. Hence, the question we address is: is better having a demultiplexer device with a high number of modes, while correcting the only phase, than fewer modes and correcting the amplitude and phase on our PIC?

	Phase and amplitude correction	Phase-only correction
Number of modes, N^2	16	25
Mean, μ	0.506	0.486
Standard deviation, σ	0.112	0.045
Variance, σ^2	0.013	0.002
Analytical mean value, μ_{av}	0.514	

Table 2.3: Statistical parameters for both correction types and different set of HG modes, considering 4000 temporal occurrences. Values obtained with $D/r_0 = 4.76$ and $\sigma_\chi^2 = 0.56$, without the presence of a tip-tilt correction.

Tip-tilt correction

It is worth noting that usually, a tip-tilt correction is often applied before the feedback loop, thus leading to higher values of the coupling efficiency when the same number of modes is considered. In this section, we aim to consider a tip-tilt correction before our coherent combining system. That is, considering Figure 2.24, the average coupling efficiency for the amplitude and phase control type can be compared with the one obtained in Figure 2.12, Chapter 2.

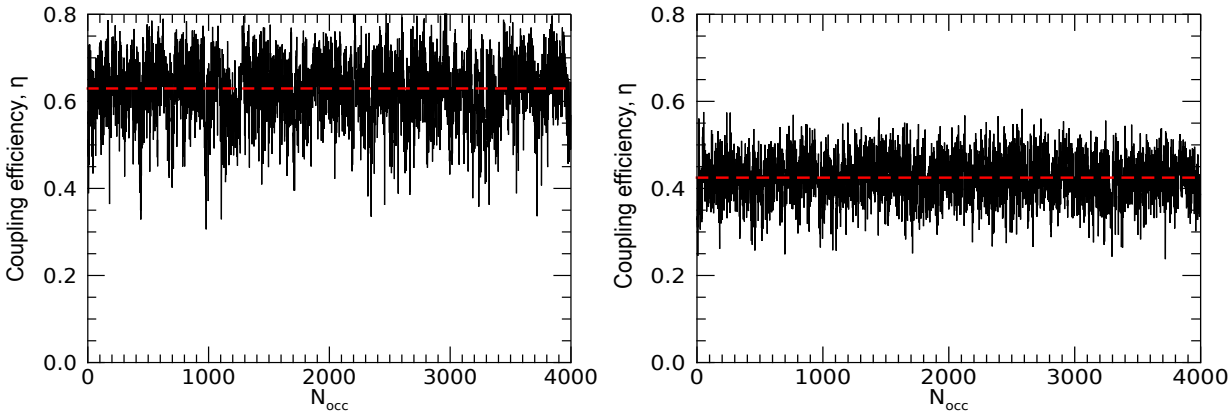

Figure 2.24: Coupling efficiency (Eq. 2.4) function of time, for (left): phase and amplitude correction and (right) phase-only correction. Values obtained with a set of 16 HG modes, $D/r_0 = 4.76$, $\sigma_\chi^2 = 0.56$ and with the presence of a tip-tilt correction. D : pupil diameter; r_0 : Fried parameter; σ_χ^2 : log-amplitude variance.

The case of reference is still the one reported in the budget link, corresponding to a $D/r_0 = 4.76$. In order to fulfill the link budget requirements on the coupling efficiency, an overall number of modes of $9 < N^2 < 16$ needs to be taken into account for the amplitude and phase correction, while $N^2 \approx 16$ for the phase-only correction type, thus resulting in a coupling efficiency of 0.63 and 0.43 for the two reported cases respectively, if a set of modes $N^2 = 16$ is considered for both correction types. In Table 2.4 such values are briefly reported. As previously stated, also in the case of a tip-tilt correction, a slightly lower standard deviation is shown if a phase-only correction type is applied, with respect to the phase and amplitude one.

	Phase and amplitude correction	Phase-only correction
Number of modes, N^2	16	16
Mean, μ	0.667	0.456
Standard deviation, σ	0.006	0.003
Variance, σ^2	0.08	0.055
Analytical mean value, μ_{av}	0.696	

Table 2.4: Statistical parameters for both correction types and a set of 16 HG modes, considering 4000 temporal occurrences. Values obtained with $D/r_0 = 4.76$, $\sigma_\chi^2 = 0.56$ and with the presence of a tip-tilt correction.

Until now, we have been interested in the coupling efficiency normalized by the incident flux. In order to assess the ability of the device to meet the specifications, fluctuations in the total flux collected through the pupil must be taken into account. In the following, this term has been taken into account through the study of the cumulative distribution function (CDF), reported for the same D/r_0, also considering the presence of a tip-tilt correction. On the y-axis, $P(I < I_t)$ denotes the probability that a given random value of coupling efficiency is less than a threshold value.

Indeed, in Figure 2.25, the cumulative distribution function is presented when a perfect correction is applied (i.e.: considering flux collected by the pupil of the telescope), thus highlighting a link margin value of $-8.67\ dB$ when a $P(I < I_t)$ of 10^{-3} is considered. This case shows that although a perfect correction is applied, the limit set in the budget link is already reached. In practice, this corresponds to a configuration that cannot be implemented in a real telecommunications system.

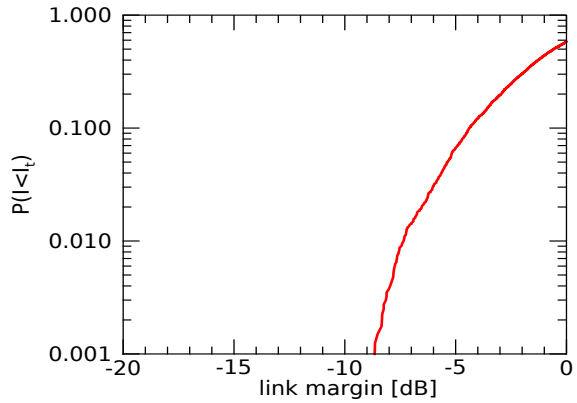

Figure 2.25: Cumulative distribution function (CDF) as function of the link margin, for a perfect applied correction. Values obtained with $D/r_0 = 4.76$ and $\sigma_\chi^2 = 0.56$.

On the left hand-part of the Figure 2.26, the CDF without tip-tilt correction is presented for the case of 16 HG modes, referring to an amplitude and phase control type, while on the right-hand part the only-phase correction is shown for the previous set of 25 HG modes.

Finally, the last CDF when correcting the only phase with a set of 16 HG modes is reported in Figure 2.27. In this context, as reported in Table 2.1, we consider $-3\ dB$ as fixed value for AO correction losses. Specifically, the threshold value of $-45\ dBm$ corresponds the value $-11.72\ dB$ ($-8.72\ dB - 3\ dB$). Hence, all considered values are less than $-11.72\ dB$, never fulfilling the link-budget requirement.

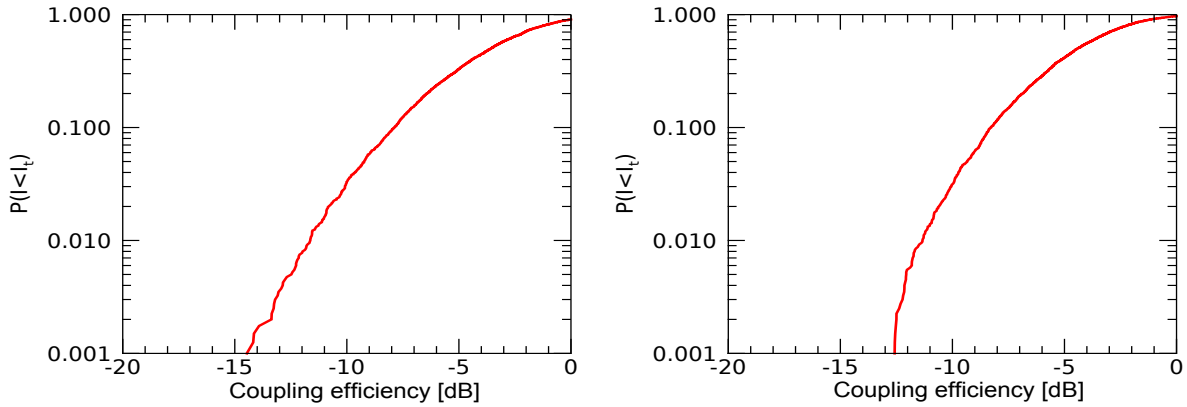

Figure 2.26: Cumulative distribution function (CDF) as function of the coupling efficiency, for (left) phase and amplitude control with 16 HG modes, and (right) phase-only control type with 25 HG modes. Values obtained with $D/r_0 = 4.76$ and $\sigma_\chi^2 = 0.56$, without the presence of a tip-tilt correction.

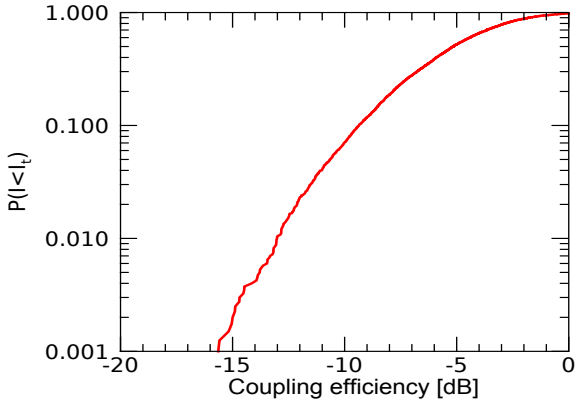

Figure 2.27: Cumulative distribution function (CDF) as function of the coupling efficiency and considering the phase-only correction type, for a set of 16 HG modes. Values obtained with $D/r_0 = 4.76$ and $\sigma_\chi^2 = 0.56$, without the presence of a tip-tilt correction.

Tip-tilt correction

The cumulative distribution function is also shown in Figure 2.28, when a tip-tilt correction is applied. Although applying a tip-tilt correction before the mode demultiplexer device results in an increasing on the coupling efficiency value for both correction types, the previous considerations on the coupling efficiency requirement remains valid. A coupling efficiency value for a set of 16 Hermite-Gaussian modes, of $\approx 11\ dB$ and $\approx 13\ dB$ is obtained when an amplitude and phase or a phase-only correction is applied to the circuit.

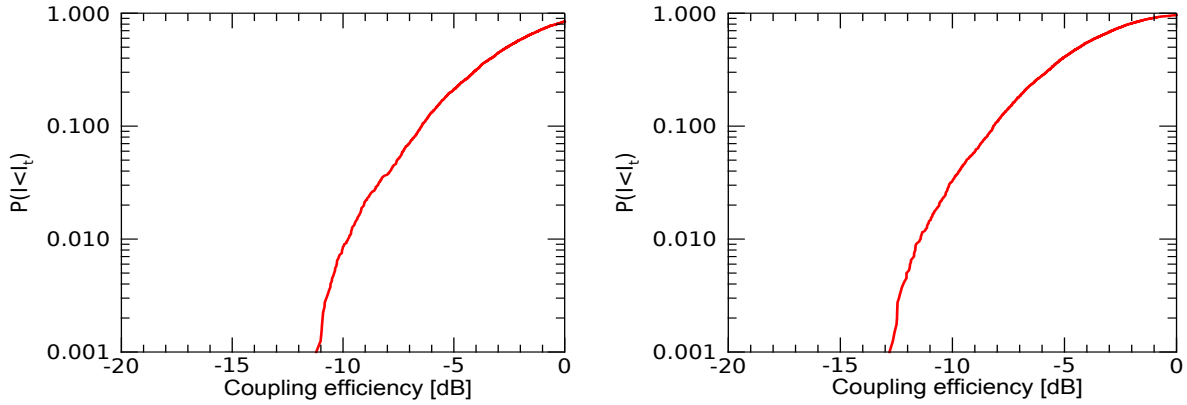

Figure 2.28: Cumulative distribution function (CDF), as function of the coupling efficiency, for (left) amplitude and phase control, and (right) phase-only control. Values obtained with a set of 16 HG modes, $D/r_0 = 4.76$, $\sigma_\chi^2 = 0.56$ and with the presence of a tip-tilt correction.

2.6.2.4 Case of $D/r_0 = 9.5$

In order to reduce the fluctuations of the collected flux, we consider here the case of D/r_0. It should be noted that when considering a diameter twice as large as the case presented in the budget link, a factor of $6\ dB$ is to be added on the total coupling efficiency, thus achieving a coupling efficiency of $\approx -17.72\ dB$. This section follows the same analysis procedure as above, providing again the information about the spatial effects on the PIC performance.

The coupling efficiency has been evaluated again for different set of modes. In Figure 2.29 the average coupling efficiency η is shown, as function of time, for both phase and amplitude and phase-only correction type. As introduced in Section **??**, a set of $N^2 = 49$ and $N^2 = 121$ modes are used to fulfill the link budget requirement in term of average correction for the case of amplitude + phase and phase-only correction respectively.

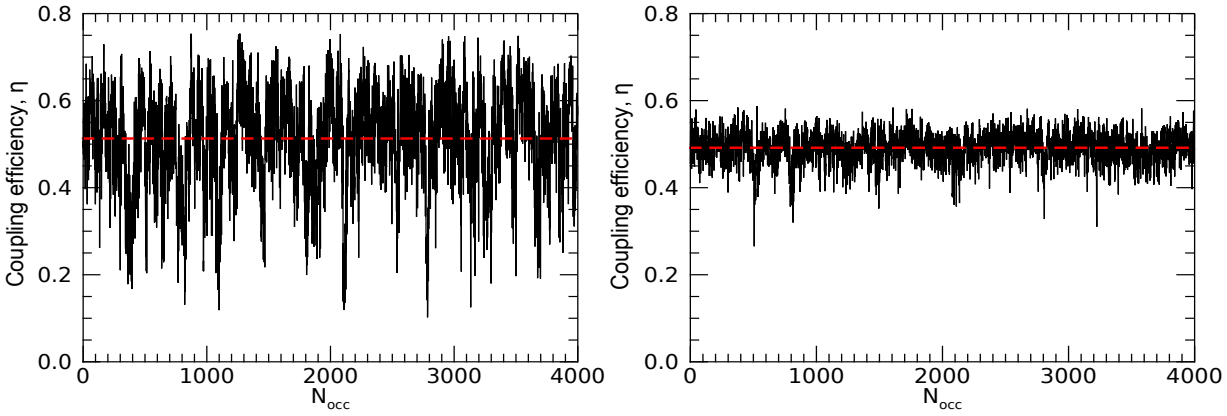

Figure 2.29: Coupling efficiency (Eq. 2.4) function of time, for (left): phase and amplitude correction, and (right) phase-only correction. Values obtained with a set of 49 and 121 HG modes respectively, considering $D/r_0 = 9.5$ and $\sigma_\chi^2 = 0.56$, without the presence of a tip-tilt correction. D : pupil diameter; r_0 : Fried parameter; σ_χ^2 : log-amplitude variance.

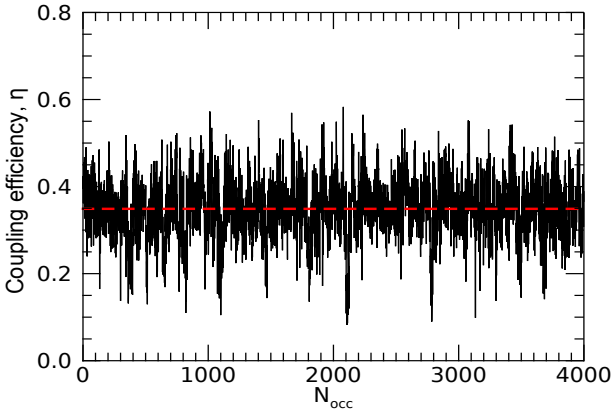

Figure 2.30: Coupling efficiency (Eq. 2.4) function of time, for the phase-only correction type. Values obtained with a set of 49 HG modes, also considering $D/r_0 = 9.5$, $\sigma_\chi^2 = 0.56$ and without the presence of a tip-tilt correction. D : pupil diameter; r_0 : Fried parameter; σ_χ^2 : log-amplitude variance.

For the sake of completeness, the influence of a phase-only correction is also presented in Figure 2.30, for a set of 49 Hermite-Gaussian modes. As previously stated for the case of $D/r_0 = 4.76$, an average coupling efficiency of $\eta = 0.5 \cdot \pi/4 \approx 0.355$ is obtained in this case. In Table 2.5 the main statistical parameters derived in this case are presented. As already reported in previous sections, in Figure 2.29 a lower standard deviation is shown for a phase-only correction with respect to the amplitude and phase correction type, hence highlighting again the trade-off between the control type and the considered number of modes, i.e.: having a large number of modes and a phase-only correction leads to a better system with respect to the fading specification.

The average coupling efficiency is also found in agreement with the value reported in the Chapter 2 (Section 2.4.2) for the considered value of D/r_0.

It is also worth noting that the waist size of each set of modes has been optimized following the evaluation reported in the Chapter 2, Section 2.4.1.

	Phase and amplitude correction	Phase-only correction
Number of modes, N^2	49	121
Mean, μ	0.51	0.492
Standard deviation, σ	0.11	0.03
Variance, σ^2	0.013	0.001
Analytical mean value, μ_{av}	0.526	

Table 2.5: Statistical parameters for both correction types and different set of HG modes, considering 4000 temporal occurrences. Values obtained with $D/r_0 = 9.5$ and $\sigma_\chi^2 = 0.56$, without the presence of a tip-tilt correction.

Tip-tilt correction

A tip-tilt correction has been also analyzed in Figure 2.31. In order to fulfill the requirements of the link budget, an overall number of modes of $N^2 \approx 36$ needs to be taken into account for amplitude and phase correction, while $N^2 \approx 64$ for the phase-only correction type. The trade-off between the number of modes and the type of correction is still valid here, although less pronounced than reported so far. In Table 2.6 the main statistical parameters of such results are summarized.

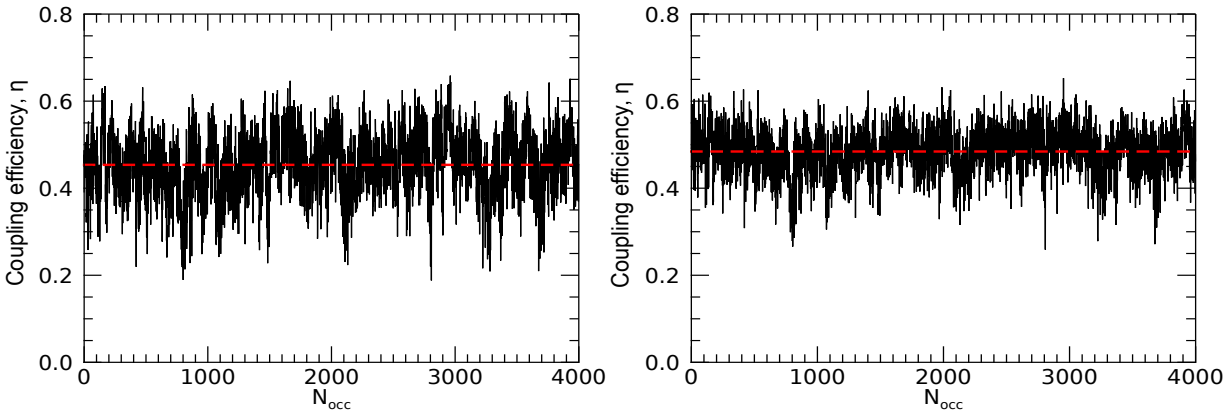

Figure 2.31: Coupling efficiency (Eq. 2.4) function of time, for (left): phase and amplitude correction, and (right) phase-only correction. Values obtained with a set of 36 and 64 HG modes respectively, also considering a tip-tilt correction, $D/r_0 = 9.5$ and $\sigma_\chi^2 = 0.56$. D : pupil diameter; r_0 : Fried parameter; σ_χ^2 : log-amplitude variance.

Following the same analysis reported above ($D/r_0 = 4.76$), in Figure 2.32 the CDF is shown when a perfect correction is applied, i.e.: considering the flux collected by the telescope pupil. A margin value of $\approx -7\,dB$ is obtained in this case when a pupil diameter is doubled. With such a diameter, the fluctuations of the collected flux are weak with regards to the link margin. Undoubtedly, further analyses must be carried out to determine the optimum diameter to be used, i.e.: between 25 and $50\,cm$.

	Phase and amplitude correction	Phase-only correction
Number of modes, N^2	36	64
Mean, μ	0.454	0.476
Standard deviation, σ	0.075	0.052
Variance, σ^2	0.006	0.003
Analytical mean value, μ_{av}	0.467	

Table 2.6: Statistical parameters for both correction types and different set of HG modes, considering 4000 temporal occurrences. Values obtained with $D/r_0 = 9.5$, $\sigma_\chi^2 = 0.56$ and with the presence of a tip-tilt correction.

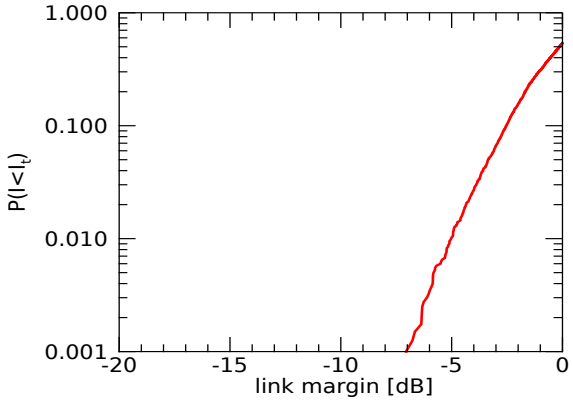

Figure 2.32: Cumulative distribution function (CDF) as function of the link margin, for a perfect applied correction. Values obtained with $D/r_0 = 9.5$ and $\sigma_\chi^2 = 0.56$, without the presence of a tip-tilt correction.

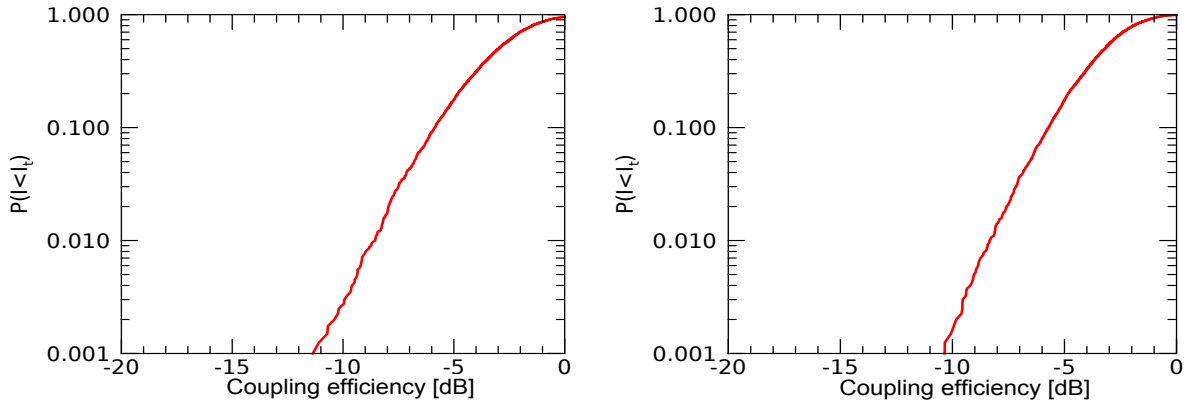

Figure 2.33: Cumulative distribution function (CDF) as function of the coupling efficiency, for (left) amplitude and phase control with 49 HG modes, and (right) phase-only control with 121 HG modes. Values obtained with $D/r_0 = 9.5$ and $\sigma_\chi^2 = 0.56$, without the presence of a tip-tilt correction.

Figure 2.33 presents the corresponding cumulative distribution function taking into account the collected flux fluctuations. In the left-hand part of this Figure, the CDF is shown when a set of 49 HG modes is considered, applying an amplitude and phase correction type, while in

the right-part of Figure 2.33, a set of 121 HG with a phase-only correction is presented.

The CDF illustrating the phase-only correction type for a set of 49 Hermite-Gaussian modes is also shown in Figure 2.34. As expected, comparing the phase and amplitude correction with respect to the phase-only one, a lower coupling efficiency value is derived when this latter is considered (same conclusion for the case of $D/r_0 = 4.76$).

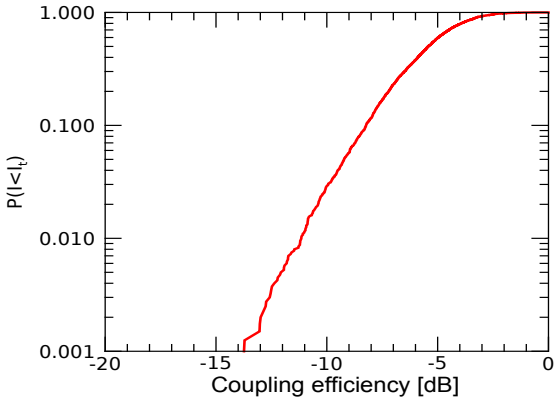

Figure 2.34: Cumulative distribution function (CDF) as function of the coupling efficiency, for a phase-only correction type while considering a set of 49 HG modes. Values obtained with $D/r_0 = 9.5$ and $\sigma_\chi^2 = 0.56$, without the presence of a tip-tilt correction.

Tip-tilt correction

A tip-tilt correction is finally considered also in the case of $D/r_0 = 9.5$. In this context, we obtain a power coupling efficiency of $\approx 11.5\,dB$ and $\approx 11.3\,dB$ for the case of amplitude + phase with a set of 36 HG modes, and phase-only correction with a set of 64 HG modes respectively.

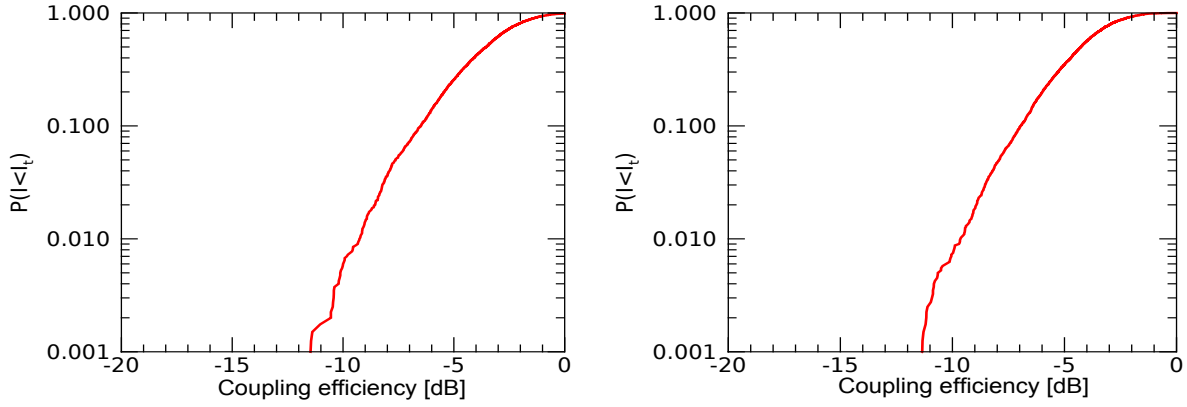

Figure 2.35: Cumulative distribution function (CDF), as function of the coupling efficiency, for (left) amplitude and phase control with 36 HG modes, and (right) phase-only control with 64 HG modes. Values obtained with $D/r_0 = 9.5$, $\sigma_\chi^2 = 0.56$ and with the presence of a tip-tilt correction.

No substantial improvement is noted compared to the absence of tip-tilt correction, as instead obtained for $D/r_0 = 4.76$. This can be explained by considering the different number of modes used to estimate the coupling efficiency.

2.7 Summary and conclusions

In the first part of this chapter we established an analytical formulation for the average coupling efficiency of an optical wave perturbed by propagation through atmospheric turbulence with a set of propagation modes. The application of this expression to the case of Hermite-Gaussian modes as those used in a spatial-division multiplexer device constitutes the second part of this chapter. In this context, we derived the optimum beam size, also called waist, for different sets of modes. A central obstruction was also considered, showing how its effect is less significant increasing the number of modes.

The relevance of such studies lies in the ability to well describe a wave perturbed by atmospheric turbulence with a set of propagation modes. In addition, the presence of atmospheric turbulence was taken into account in the second part of this chapter. The coupling efficiency has been evaluated function of both turbulence conditions, represented through the parameter D/r_0, and the set of modes. As expected, the normalized coupling efficiency depends mainly on D/Nr_0. Moreover, an approximation for the particular case of $D/Nr_0 < 1$ is given, where the behavior of each curve is different according to N. Finally, from these results and a given turbulence condition, one may be able to find the number of modes required for coupling efficiency specifications. Such performance are in good agreement with the instantaneous Strehl ratio obtained with adaptive optics in case of good correction, even though it is worth noting that the complex nature of the Hermite-Gaussian modes leads to a double number of the degrees of freedom compared to the AO one.

We also presented how, using a rapid image stabilization in the expression of the coupling efficiency, one may obtain a better optimization in the considered set of modes with respect to that derived with the eigenmodes approach, whatever the turbulence conditions. This study highlighted the potential impact of a tip-tilt correction device before the multiplexer, while the development of a multiplexer with optimized modes will bring a gain of the order of few percent only.

In the second part of this Chapter we used a Monte Carlo approach in order to validate the results obtained from the analytical analysis derived in the first part of the present Chapter. Indeed, the mean coupling efficiencies obtained from the MC approach are very similar to the ones reported from the analytical analysis, also validating the given formulas. Moreover, the coupling efficiency fluctuations are function of the number of modes used in the mode decomposition, rather than function of the correction type (phase and amplitude or phase-only correction).

By considering the scenario of interest, a $25\ cm$ telescope is too small to attenuate the fluctuations of the whole collected flux. Consequently, a $50\ cm$ telescope pupil has been studied. With such a diameter, different types of correction may be envisioned (considering also the presence of a tip-tilt correction to the previous phase + amplitude and phase-only correction type).

Tables ranging from 2.3 to 2.6 presents the number of modes required for each configuration, giving an insight of the requirement. The results suggest that the requirement does not only depend on the average coupling efficiency. Analyzing the CDF, it seems that the number of modes should be considered separately from the type of correction. In fact, a complete design study has to performed taking into account losses induced by temporal effects, and optimizing the diameter of the receiver telescope.

Chapter 3

Temporal analysis of the correction loop

3.1 Introduction

The description of the limitation of the coupling efficiency given by the number of decomposition modes has been introduced in Chapter 2. Furthermore, an end-to-end simulation of the coupling efficiency has been presented, using the parameters derived in Section 2.6. On the other hand, it is necessary to determine the amplitude of the phase to be corrected through the PIC and its temporal dynamics, thus investigating another important parameter for the PIC development, closely linked to the type of material to be used. This parameter will give us a first condition for both modulation bandwidth and the capability of the material platform to overcome such shift by its refractive index changes.

In the first part of this Chapter, the temporal analysis of the scenario of interest is presented, highlighting the impact of a limited phase correction performed by a photonic integrated circuit. Such analysis is reported for both cases of a telescope diameter of 25 cm and 50 cm, also considering a tip-tilt correction before the SDM device.

On the other hand, due to the limitations on the bandwidth of a PIC, as well as the high losses commonly present in such a device, a new control law is proposed in the second part of this chapter. In this way, an SDM device is employed without a PIC but using instead a deformable mirror, thus accelerating the feedback loop and developing a new sensorless adaptive optics approach.

3.2 Temporal analysis: case of $D/r_0 = 4.76$

In a first approach, the phases of the coefficients of the overlap integral defined as $s_i =< \Psi | HG_i >$ are studied.

The unwrapped phase, or full-phase, for both first and last (s_{15}) coefficient is reported in the top part of the Figure 3.1, where a zoom on 50 ms (100 temporal occurrences) is considered. In this case, as demonstrated in Chapter 2, we do not expect the full-phase of the last mode to be different from that of the first, since all HGs possess the same energy. In the bottom part, the power spectral density (PSD) of such phase sequences is also presented, always for both coefficients of the used set of modes (i.e.: s_0 and s_{15}). These spectra are defined by a relatively constant part at low frequencies, and a subsequent decreasing part in high frequencies domain. In this context, it is possible to define a cut-off frequency, denoted by f_c, as the intersection between the low frequencies fit of this spectrum and the high frequencies fit.

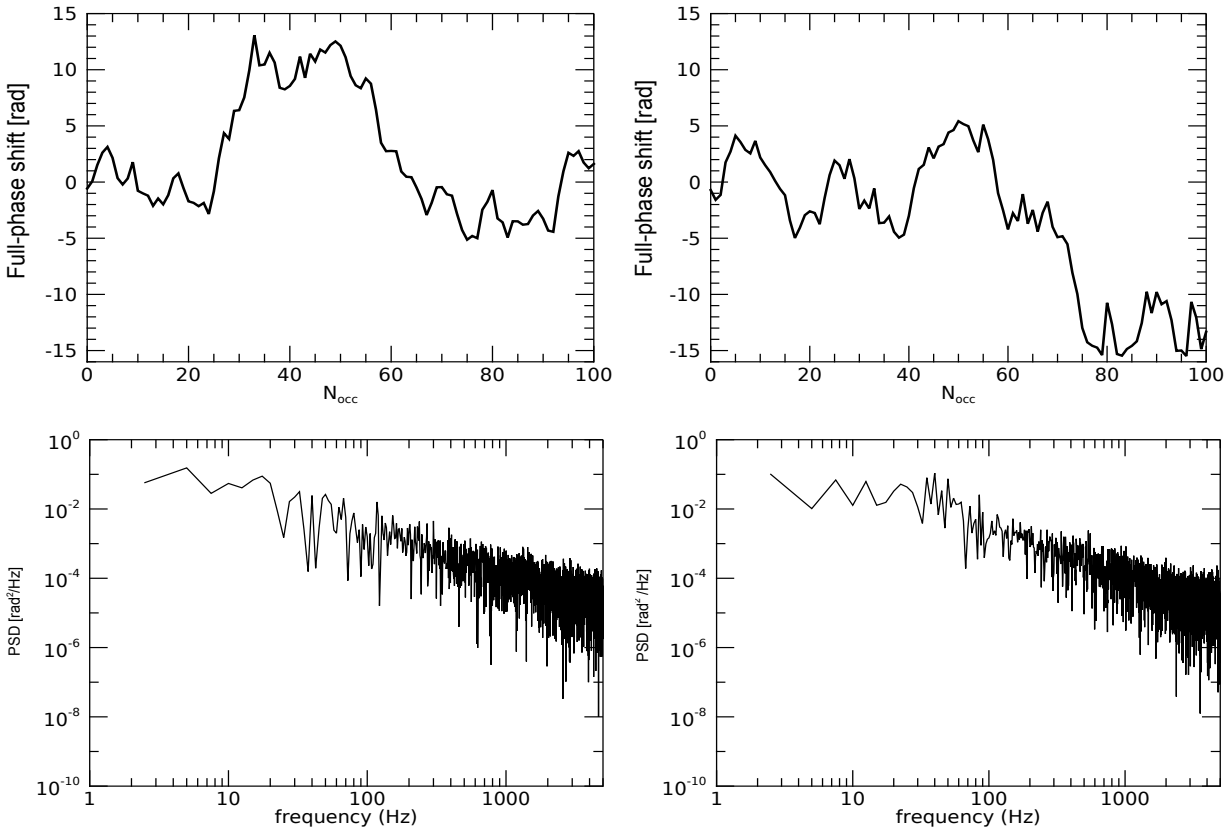

Figure 3.1: Top: full-phase shift for (left) first coefficient s_0 and (right) last coefficient s_{15} considering a set of 16 HG modes; Bottom: associated power spectral density for the s_0 and s_{15} coefficients respectively. Figures obtained without tip-tilt correction, considering $D/r_0 = 4.76$ and $\sigma_\chi^2 = 0.56$. D : pupil diameter; r_0 : Fried parameter; σ_χ^2 : log-amplitude variance.

As one can notice, the slower evolution of the full-phase shift leads to a cut-off frequency of the order of a hundred hertz. As in adaptive optics, these spectra should allow us to specify the temporal parameters of the phase correction loop with the PICs, assuming that they allow phase shifts of more than tens of radians. In practice, this is not the case, as a 2π phase shift is usually derived when considering a real PIC, thus considering higher cut-off frequencies, which in turns implies higher required bandwidths.

2 π phase correction

In the previous section, the full-phase shift is shown. In practice, PICs do not allow such high phase shifts. They are limited to phase shifts of a few π. In the following, we will take the example of a PIC allowing phase shifts of 2π. We therefore assume that the phase is corrected modulo 2π, i.e.: wrapped.

In this case, it appears that the content of the high-frequency spectrum of the wrapped phase is imposed more by the amplitude of the unwrapped phase than by its spectral content. Considering the PSD of a wrapped and an unwrapped signal, it is possible to see how the fundamental peak of the unwrapped signal is proportional to the amplitude of the signal.

On the other hand, when considering the wrapped signal, its fundamental peak does not depend on its amplitude, contrary to what happens with its harmonics.

In the following Figure 3.2 a nearly flat spectrum is obtained when considering a wrapped phase, with a higher cut-off frequencies compared to the one considered in Figure 3.1. That is, with a device not capable of an infinite phase shift, large bandwidth must to be taken into account in the PIC development.

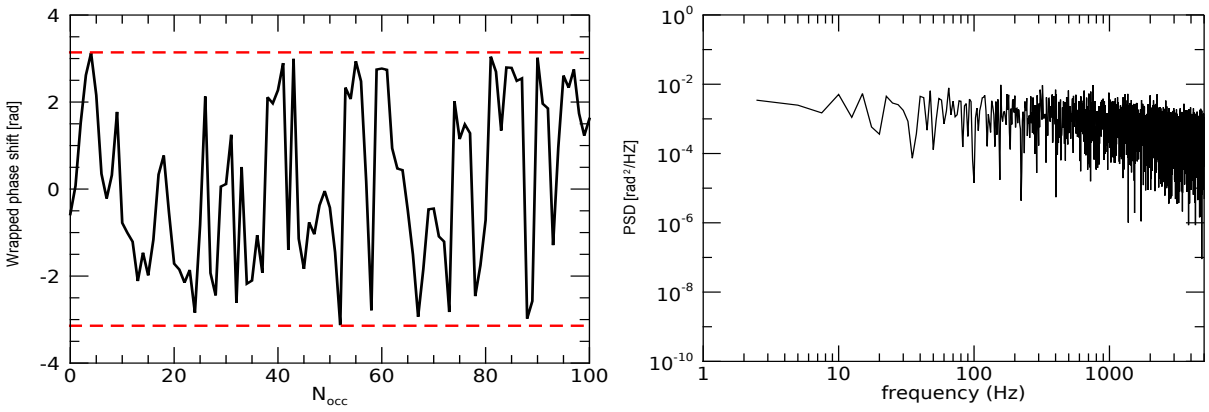

Figure 3.2: Left: wrapped phase shift evolution for the first coefficient s_0; Right: associated PSD for the same coefficient. Figures obtained without tip-tilt correction, considering $D/r_0 = 4.76$. D : pupil diameter; r_0 : Fried parameter.

The rapid evolution of the wrapped phase shift results in cut-off frequencies of the order of a thousand hertz. Such frequency f_c therefore implies a bandwidth of the order of tens of thousands hertz. Consequently, even for a small number of modes, a high bandwidth seems to be required for a photonic circuit used in the coherent combining approach as a beam combiner block. Nevertheless, the study of the effect of a finite temporal bandwidth on the coupling efficiency has to be performed to quantify this specification.

Following this consideration, lithium niobate-based components are widely used in this context due to their properties that guarantee high available bandwidths, which is also the main reason why this component is developed within the framework of this thesis. Nevertheless, circuits with numerous waveguides are difficult to realize with such a material, and silicon-based circuits are preferred for a high number of modes, provided the bandwidth requirements are met.

Tip-tilt correction

Regarding the full-phase correction and 2π correction analysis, a slightly lower spectrum was found in the case of tip-tilt correction compared to the results obtained so far. In the left-part of Figure 3.3 the full-phase spectrum is shown, while on the right part the associated power spectral density is reported, thus leading again to a cut-off frequency of the order of hundreds hertz.
Such results has been obtained for the first coefficient, s_0. On the other hand, in Figure 3.4 the full-phase spectrum for the s_{15} coefficient is presented, although no substantial difference is noted with respect to the absence of a tip-tilt correction.

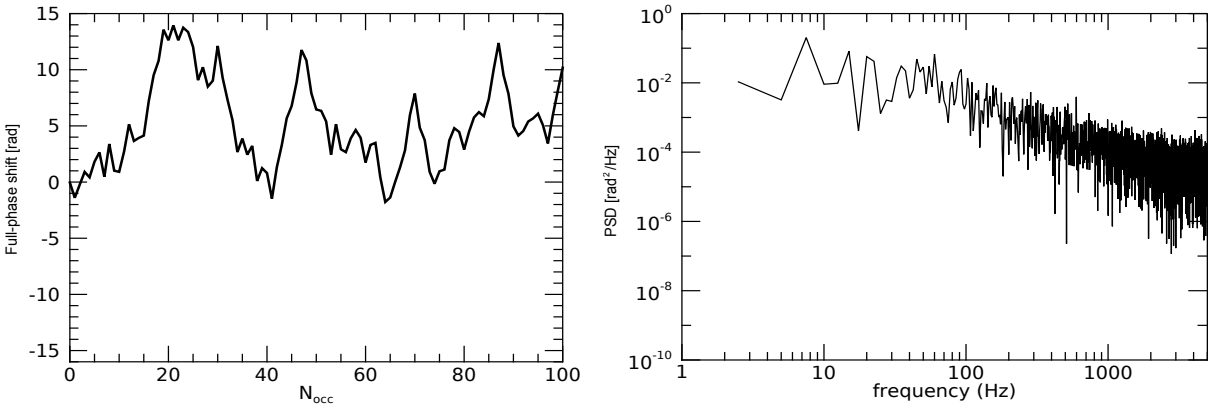

Figure 3.3: Left: full-phase shift evolution for the first coefficient s_0; Right: associated PSD for the same coefficient. Case of tip-tilt correction, considering $D/r_0 = 4.76$. D : pupil diameter; r_0 : Fried parameter.

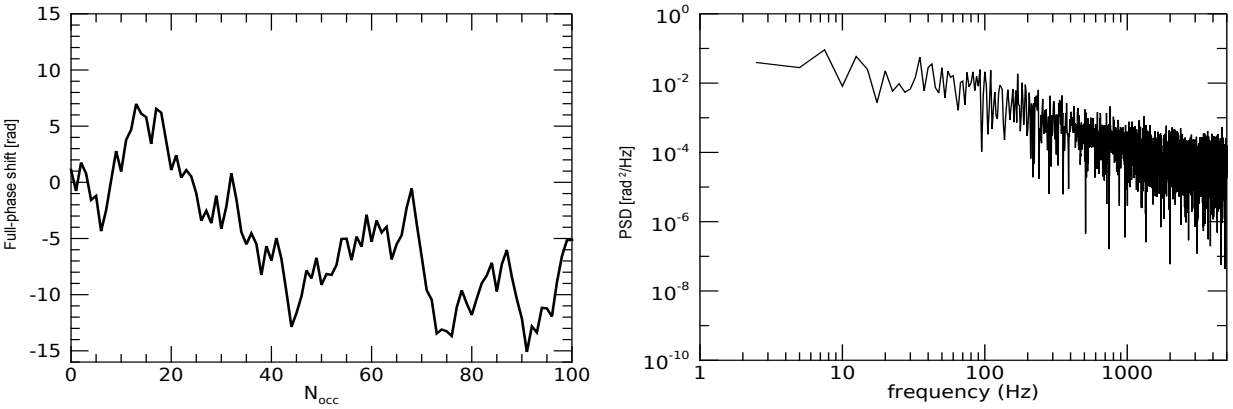

Figure 3.4: Left: full-phase shift evolution for the last coefficient s_{15}; Right: associated PSD for the same coefficient. Case of tip-tilt correction, considering $D/r_0 = 4.76$. D : pupil diameter; r_0 : Fried parameter.

Higher cut-off frequencies are also obtained for the case of a 2π spectrum, as the one given in Figure 3.5, in which large bandwidth needs to be considered for a PIC development.

3.2.1 Temporal analysis: case of $D/r_0 = 9.5$

As previously reported for the case of $D/r_0 = 4.76$, the temporal analysis is derived in the following when considering a receiver diameter of $50\,cm$. In Figure 3.6 the full phase shift is presented, with the associated PSD, for the first coefficient of the HG modes set, s_0. For the sake of completeness, the same full phase spectrum is also reported in Figure 3.7 for the last coefficient, s_{48} (set of 49 HG modes). Furthermore, in Figure 3.8 the wrapped phase shift and its PSD are shown.

Finally, in case of a tip-tilt correction, the full-phase spectrum for the first (s_0) and last (s_{35}) coefficient, as well as their associated PSD are presented in Figure 3.9, and Figure 3.10. At the same way, in Figure 3.11 the 2π phase spectrum has been analyzed, also considering a rapid image stabilization.

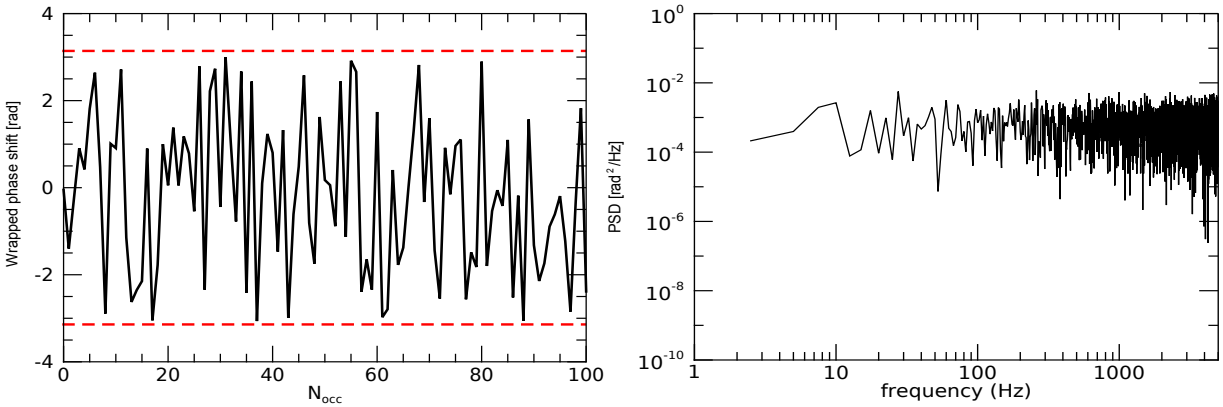

Figure 3.5: Left: wrapped phase shift evolution for the first coefficient s_0; Right: associated PSD for the same coefficient. Case of tip-tilt correction, considering $D/r_0 = 4.76$. D : pupil diameter; r_0 : Fried parameter.

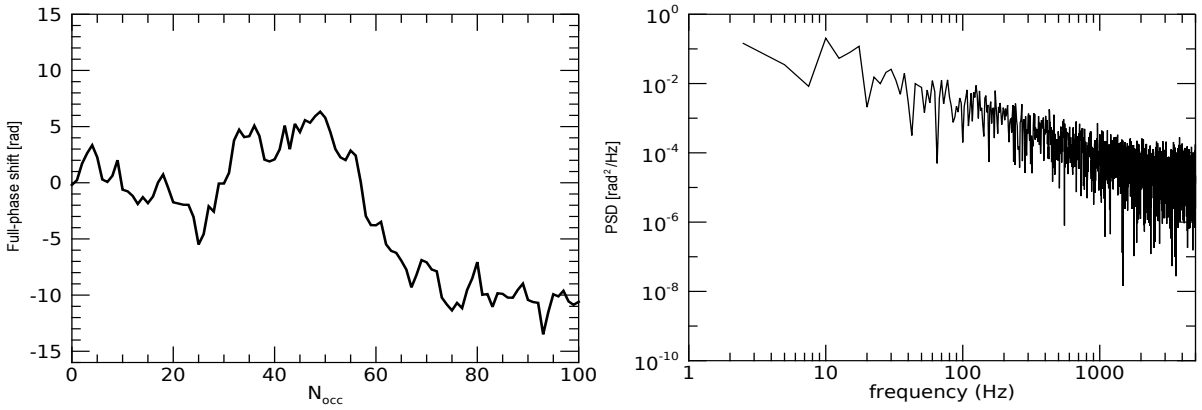

Figure 3.6: Left: full-phase shift evolution for the first coefficient s_0; Right: associated PSD for the same coefficient. Case of $D/r_0 = 9.5$. D : pupil diameter; r_0 : Fried parameter. No tip-tilt correction applied.

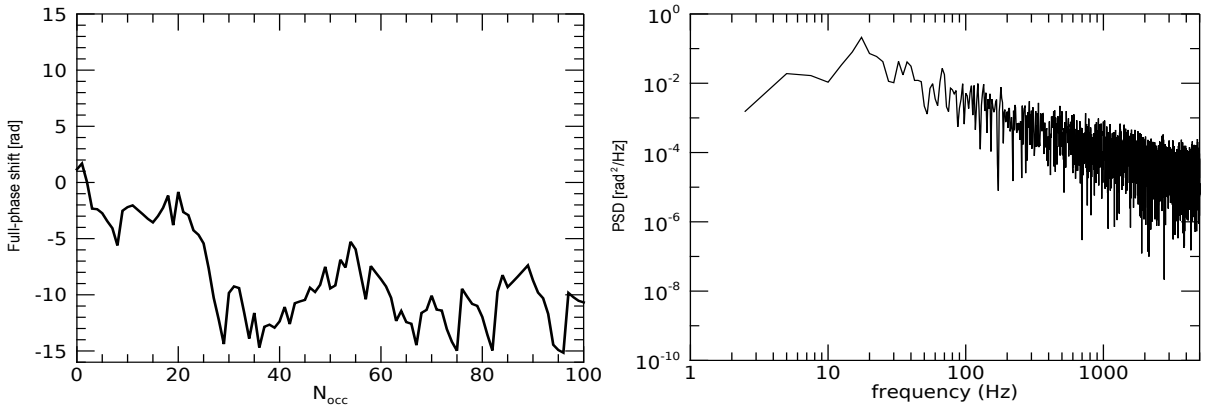

Figure 3.7: Left: full-phase shift evolution for the last coefficient s_{48}; Right: associated PSD for the same coefficient. Case of $D/r_0 = 9.5$. D : pupil diameter; r_0 : Fried parameter. No tip-tilt correction applied.

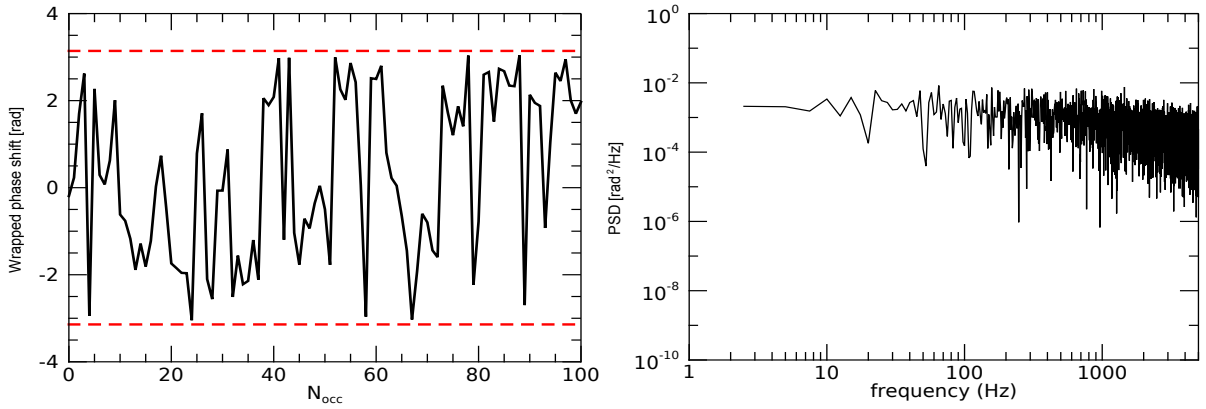

Figure 3.8: Left: wrapped phase shift evolution for the first coefficient s_0; Right: associated PSD for the same coefficient. Case of $D/r_0 = 9.5$. D : pupil diameter; r_0 : Fried parameter. No tip-tilt correction applied.

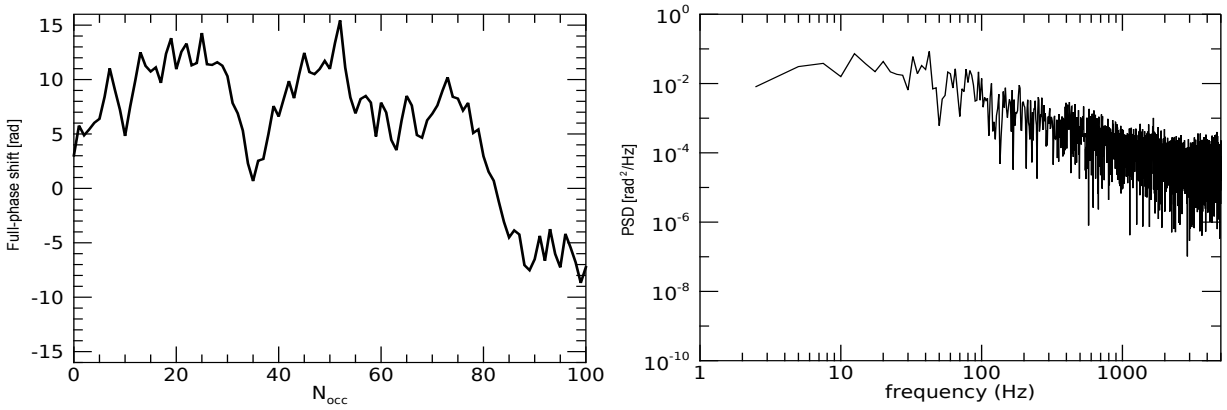

Figure 3.9: Left: full-phase shift evolution for the first coefficient s_0; Right: associated PSD for the same coefficient. Case of $D/r_0 = 9.5$, considering a tip-tilt correction. D : pupil diameter; r_0 : Fried parameter.

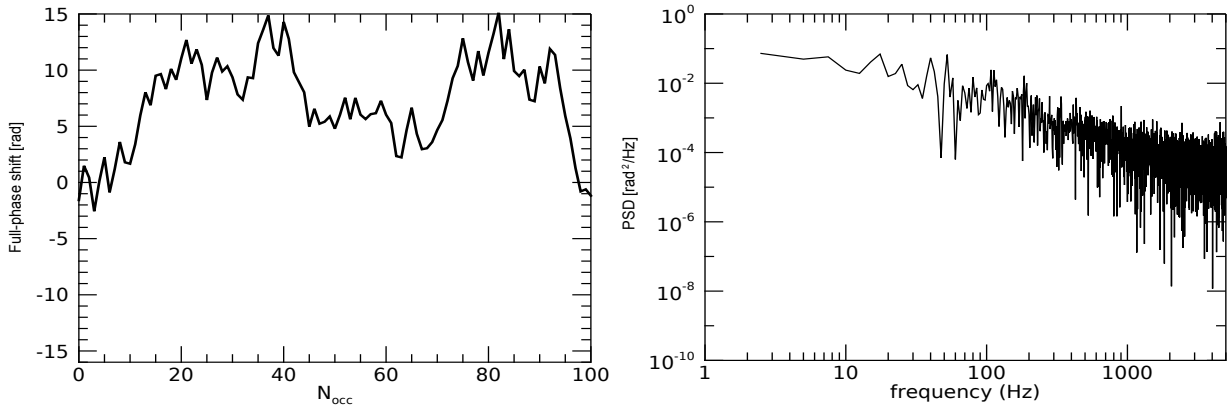

Figure 3.10: Left: full-phase shift evolution for the last coefficient s_{35}; Right: associated PSD for the same coefficient. Case of $D/r_0 = 9.5$, considering a tip-tilt correction. D : pupil diameter; r_0 : Fried parameter.

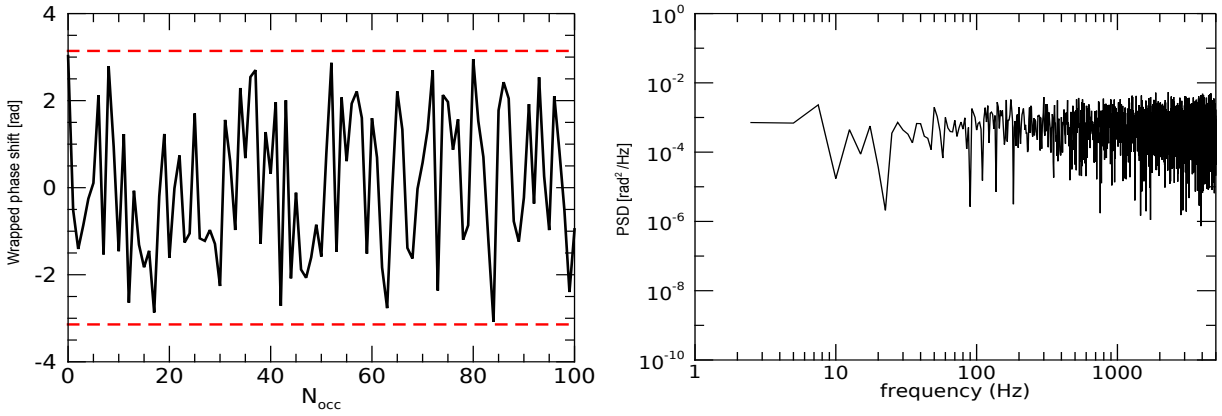

Figure 3.11: Left: wrapped phase shift evolution for the first coefficient s_0; Right: associated PSD for the same coefficient. Case of $D/r_0 = 9.5$, considering a tip-tilt correction. D : pupil diameter; r_0 : Fried parameter.

3.2.2 Conclusion of the specification study

A Monte Carlo approach has been developed for this study and described in the last part of Chapter 2, also validating the proposed analytical approach. Moreover, the fluctuations of the coupling efficiency, as obtained from the MC approach, appear to depend from the number of modes rather than from the type of correction (phase and amplitude or phase-only correction).

In the scenario of interest, the scintillation is strong: a $25\ cm$ telescope is not large enough for mitigating the fluctuations of the collected flux, and an higher pupil diameter is required. In this context, we considered a $50\ cm$ telescope. With such diameter, different type of correction may be envisioned, a few tens of modes being required.

Finally, a preliminary study of the temporal characterization of the correction phase has been performed. The need of phase correction induces nearly flat temporal spectrum until a few kHz, whatever the modes, even with a $D/r_0 = 4.7$ or a tip-tilt correction. In order to accelerate the feedback loop, in the next section a new command law has been proposed and detailed, which employs an SDM device and a DM, without using a photonic integrated circuit.

3.3 Accelerating the feedback loop

The maximum frequency of the feedback loop is mainly due to the number of modulations used and the response time of the PIC. In order to increase this frequency, we can act both on the total number of modulations to be applied and on the response time of the PIC. Furthermore, despite its main advantages, high losses still characterize this device today, with large propagation and coupling losses of $\approx 16dB$ reported in [Billault et al. (2021)] for a 16-channel bases PIC fabricated within a Silicon On Insulator (SOI) foundry. This property is not compatible with the link budget reported in Section 2.6.1, for a telecommunication FSO link.

Adaptive optics constitute the most commonly used approach for turbulence mitigation, limiting the fading of coupled signal. As stated in Chapter 1, most existing adaptive optics systems include a dedicated wavefront sensor to evaluate the corrections to be applied.

In Sensorless adaptive optics the deformable mirror is not controlled by using the measurement delivered by the wavefront sensor, but directly optimizing the signal of interest. Therefore, in order to distinguish the modes of mirror deformation in the individual signal, each mode is always associated with a different time modulation. Various algorithms have been developed over time, as reported in Section 1.5.3.5, [O'Meara (1977); Vorontsov et al. (1997); Vorontsov and Sivokon (1998); Booth (2006)]. To speed up the convergence time of this method, several developments have been proposed in literature. A first part of such approaches involve the optimization of the modulation, thus using a sequential optimization as well as the linearization of the inverse problem. [Carrizo et al. (2018); Piscaer et al. (2019)]. On the other hand, artificial intelligence (AI) may be used in order to determine the correction to be applied, without any modulation [Li and Zhao (2017); Paine and Fienup (2018); Tian et al. (2019); Vera et al. (2021)]. Nevertheless, for the first group of techniques described above, limitations on the available DM bandwidth occur when dealing with atmospheric turbulence. Each DM-mode is associated with different frequency/time modulations to distinguish the modes of mirror deformation, thus being restricted by the mechanical bandwidth of the DM. Indeed, considering a typical case of a LEO-to-ground optical link as the one introduced in this thesis, bandwidth of hundreds of kHz order are required, difficult to reach with standard DMs. On the contrary, when considering approaches using AI, high computing power is required, raising questions about the embedding capacity of such systems.

The onset of spatial multiplexers, as the ones reported in Section 1.5.4.2 [Noordegraaf et al. (2010); Labroille et al. (2014)], makes it possible to envisage a solution combining sensorless adaptive optics advantages without high frequency DM modulation. In this Chapter, we propose the use of a spatial multiplexer device in a standard sensorless approach, thus circumvent the limitations of high frequency DM modulation. Similar concepts have been recently proposed [Noordegraaf et al. (2010); Labroille et al. (2014); Corrigan et al. (2016); Norris et al. (2020)], implementing a wavefront sensor based on a photonic lantern fiber-mode-converter. In this context, the spatial mux device can be seen as a wavefront sensor, and only one modulation is applied on all DM actuators at the same time.

The general principle is presented in the first part of the present section, adapted from a conference paper published during this thesis, [Rinaldi et al. (2021)]. Furthermore, its performance is described in the second part, thus detailing the implemented numerical simulations. Finally, in the last part, the laboratory bench used in this application is analyzed, illustrating the experimental results obtained.

3.4 Spatial multiplexer wavefront sensor

By employing a spatial multiplexer as wavefront sensor, placed behind the DM, the incoming perturbed beam is first decomposed into a set of propagation modes, each of them being transformed in a gaussian mode and coupled in an array of SMFs, as reported in Figure 3.12. The spatial multiplexer device used in this context is the Multi-Plane Light Conversion (MPLC) developed by Cailabs. Moreover, each intensity information derived from this device is used to control the shape of the deformable mirror, optimizing the coupling of the optical beam in a privileged mode called "communication mode". Our aim here is to use these multi-outputs to reduce the complexity of time modulation, not compatible with the capacity of the deformable mirror.

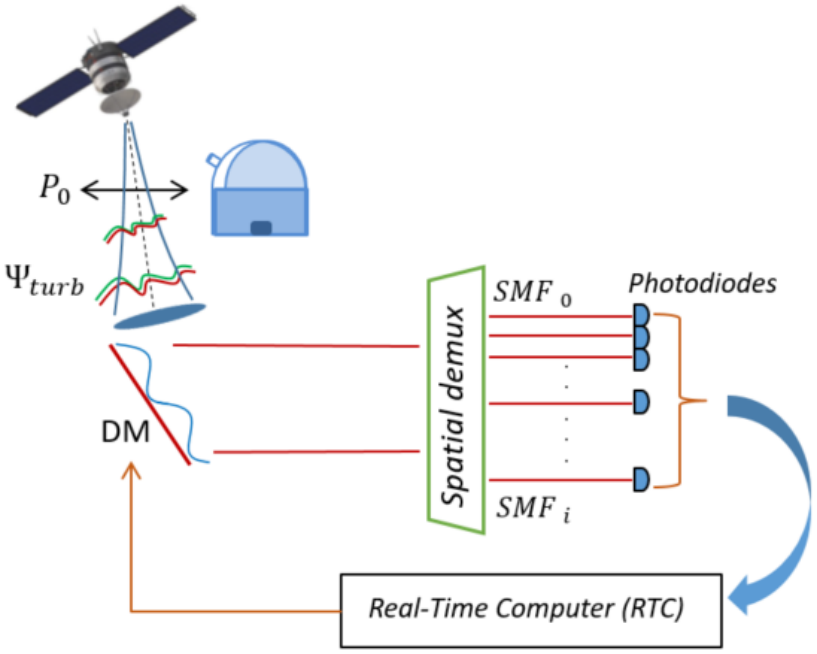

Figure 3.12: Spatial multiplexer wavefront sensor applied to a Sensorless AO system for free-space optical communications.

It is worth noting that the proposed method (Figure 3.12) is adapted to weak phase perturbations, i.e. to the measurement of phase residuals after correction by DM. In the following, this latter method will have to be completed by an alternative technique used to lock the feedback loop.

3.4.1 Multiple detector-based control algorithm

The incoming wave Ψ, that is reflected by the deformable mirror, can be easily written as:

$$\Psi = e^{i\varphi}P, \tag{3.1}$$

where P represents the truncation of the pupil, and φ the wavefront on the DM. It should be noted that in the previous equation, the scintillation is not taken into account, i.e. the log-amplitude term e^{χ}, as reported in Eq. 1.10 of Chapter 1. Hence, the optical power at the output of the fiber associated with the mode i and denoted by s_i is expressed by the present formulation:

$$s_i(\varphi) = |<\Psi|HG_i>|^2 \tag{3.2}$$

where now HG_i represents the Hermite-Gaussian modes basis in which the incident beam is decomposed. Assuming φ small with respect to 1, it is possible to have a Taylor expansion of Ψ following φ at order 2:

$$\Psi = \Big(1 + i\varphi - \frac{\varphi^2}{2}\Big)P + o(\varphi^2) \tag{3.3}$$

Indeed, the optical power associated with the mode i writes as:

$$\begin{aligned} s_i(\varphi) &= |<\Big(1 + i\varphi - \frac{\varphi^2}{2}\Big)P|HG_i>|^2 + o(\varphi^2) \\ &= |<P|HG_i> - (<\frac{\varphi^2}{2}P|HG_i>|^2 - |<\varphi P|HG_i>|^2) + o(\varphi^2) \\ &= <P|HG_i>^2 - <\varphi^2 P|HG_i><P|HG_i> + <\varphi P|HG_i>^2 + o(\varphi^2) \end{aligned} \tag{3.4}$$

Moreover, the phase on the deformable mirror, φ, can be written as sum of two different components:

$$\varphi = \varphi^{\parallel} + \varphi^{\perp}, \tag{3.5}$$

where $\varphi^{\parallel}$ is the part of the phase corrected by the DM. In the case of a small fitting error:

$$\varphi^{\perp} \approx 0$$

i.e.:

$$s_i(\varphi) \approx s_i(\varphi^{\parallel}).$$

Furthermore, denoting F_k the influence function of the actuator k, and a_k its amplitude, the phase on the DM is obtained by:

$$\varphi^{\parallel}(A) = \Sigma_k a_k F_k. \tag{3.6}$$

with $A = (a_k)$. The Taylor expansion of $\varphi^{\parallel}$, following A, near the optimal correction, $A = 0$, writes:

$$s_i(\varphi^{\parallel}(A)) = s_i(A = 0) + \frac{1}{2}\Sigma_k\Sigma_l a_k a_l \frac{\partial^2 s_i}{\partial a_k \partial a_l}(A = 0)$$

Finally, the optical power at the output of the fiber associated with the mode i can be written as:

$$s_i(\varphi) \approx s_i(\varphi = 0) + \frac{1}{2}\Sigma_k\Sigma_l a_k a_l \frac{\partial^2 s_i}{\partial a_k \partial a_l}(\varphi = 0) + o(\varphi^2) \tag{3.7}$$

By adding a modulation $M = (m_k)$ to the previous expression:

$$s_i(A+M) = s_i(\varphi = 0) + \frac{1}{2}\Sigma_k\Sigma_l(a_k + m_k)(a_l + m_l)\frac{\partial^2 s_i}{\partial a_k \partial a_l}(\varphi = 0) \tag{3.8}$$

Finally, the difference quotient, or rate of change of the function evaluated by applying the difference of the signals obtained with the same modulation of opposite signs, writes:

$$S_M(A) = s_i(A+M) - s_i(A-M) = \Sigma_k\Sigma_l a_k m_l \frac{\partial^2 s_i}{\partial a_k \partial a_l}(\varphi = 0) \tag{3.9}$$

Either, by using a matrix notation:

$$S_M(A) = \mathbf{B_M} A \tag{3.10}$$

In this way, by applying a given modulation, we are able to linearize the problem, thus resulting in a bilinear system with respect to a_k and a_l. By inverting the previous relationship, it is possible to obtain an estimate of A, $\tilde{A}$, from the measurements, s_i, in the presence of a modulation M.

$$\tilde{A} = \mathbf{B}_M^{\dagger} S_M \tag{3.11}$$

where $\mathbf{B}_M^{\dagger}$ denotes the pseudo-inverse of $\mathbf{B}_M$. In that sense, the spatial multiplexer plays the role of a wavefront sensor.

3.5 Performance analysis

The implementation of the approach described in the previous section raises several questions. Firstly, in order to be able to correct the wavefront aberrations, the choice of a modulation capable of creating an invertible matrix is the first aspect to consider. Therefore, we are also interested on the dynamic of this method with respect to the amplitude of such aberrations.

In this context, we are not interested in finding a general solution, but have studied a particular case through numerical simulations, namely that of a Gaussian mode perturbed by atmospheric turbulence. Indeed, in this case $P = HG_0$ (HG_0 denotes the Gaussian mode associated with the Hermite-Gaussian mode basis), and two distinct case can be distinguished: a first case in which $i = 0$, that following Eq. 3.4 translate onto $< P|HG_i >=$
$< HG_0|HG_0 >= 1$, while the s_i can be written as:

$$s_0(\varphi) = 1 - \Big(< \varphi^2 HG_0|HG_0 > - < \varphi HG_0|HG_0 >^2 \Big) + o(\varphi^2) \tag{3.12}$$

Furthermore, it is possible to demonstrate how:

$$< \varphi^2 HG_0|HG_0 > - < \varphi HG_0|HG_0 >^2 = < \Big[\varphi - < \varphi HG_0|HG_0 > \Big]^2 HG_0|HG_0 > \tag{3.13}$$

so that s_0 is less than 1, or equal to 1 when $\varphi = 0$ (case of a plane surface on the deformable mirror).

On the other hand, when $i \neq 0, < P|HG_i >=< HG_0|HG_i >= 0$, and the output of the i-fiber, s_i, is now written by the following expression:

$$s_i(\varphi) =< \varphi HG_0|HG_i >^2 + o(\varphi^2) \tag{3.14}$$

In this way, substituting the Eq. 3.6 in Eq. 3.14, yields to:

$$s_i = \sum_k \sum_l a_k a_l < F_k HG_0|HG_i >< F_l HG_0|HG_i > \tag{3.15}$$

Therefore, by adding a modulation, the previous Equation 3.8 lies to:

$$s_i(A+M) = s_i(\varphi = 0) + \frac{1}{2}\Sigma_k \Sigma_l (a_k + m_k)(a_l + m_l) < F_k HG_0|HG_i >< F_l HG_0|HG_i > \tag{3.16}$$

while Equation 3.9 gives:

$$S_M(A) = \Sigma_k \Sigma_l 2 a_k m_l (\ < F_k HG_0|HG_i >< F_l HG_0|HG_i >\ ) \tag{3.17}$$

Particularly, in our simulation we consider a deformable mirror described by a set of 8 by 8 actuators arranged on a Cartesian coordinate system. The intensity distribution in the plane of the deformable mirror is uniform. In this system, 52 actuators are considered valid. Moreover, the spatial demultiplexer decomposes the incoming wave over a set of 45 Hermite-Gaussian modes, as reported by Bade & al [Bade et al. (2018)]. As a consequence, with those modes we are able to control almost all the available actuators.

Figure 3.13 illustrates the performance evaluation process of a Sensorless AO approach. For the sake of completeness, such process is described below:

- the modeling of the Hermite-Gaussian mode basis;
- the construction of a DM influence functions, denoted as F_k;
- the definition of the signal second derivative over the 2D grid of actuators;
- the application of a modulation, m_l;
- the application of a perturbation, a_k;
- the estimation of outputs signals, S_i;
- the DM-phase estimation: analysis of the system performance.

3.5.1 Proposal of a spatial modulation

In the present section we try to answer the first of the questions we asked earlier, i.e. the choice of the optimal modulation capable of creating an invertible matrix, previously denoted as B_M. Therefore, given the shape of the Hermite-Gaussian modes considered in this particular case, we have chosen a modulation given by the sum of a 45° tilt and a defocus aberration. Indeed, with a X-tilt aberration we can excite the modes oriented according to the x-direction, as the modes HG_{0i} reported in the right part of Figure 3.14.

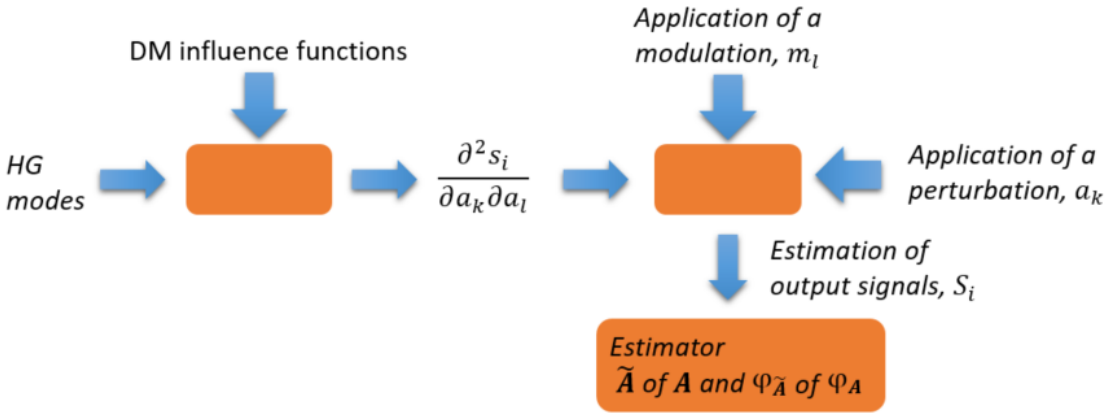

Figure 3.13: Architecture of the numerical simulation developed to model the performance of a Sensorless AO approach with an MPLC as mode demultiplexer device. Example of bilinear model.

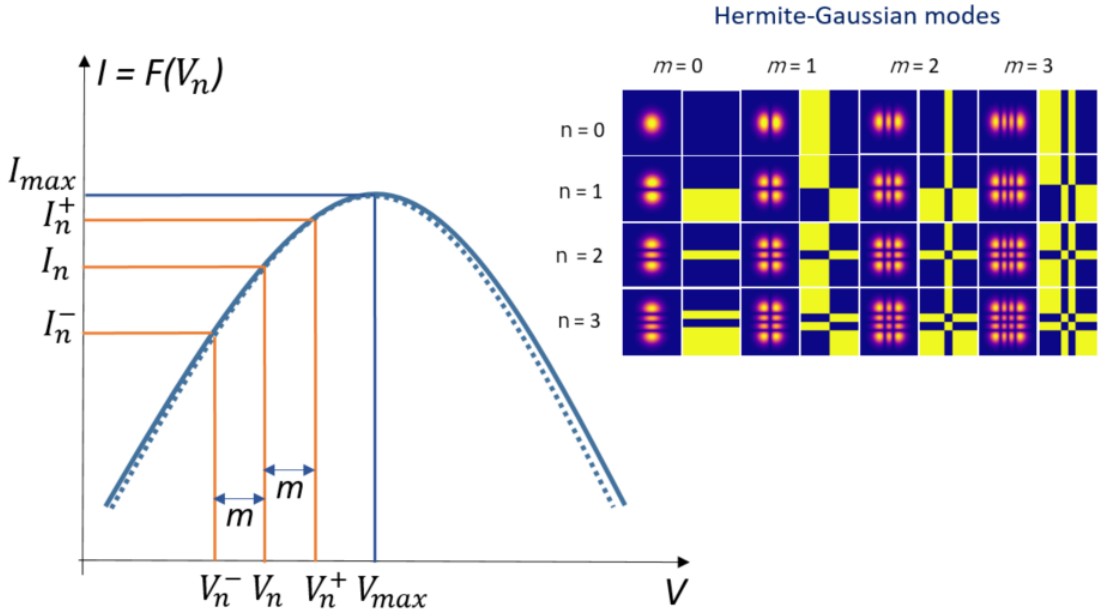

Figure 3.14: Left: Principle of parabolic estimation, from K. Saab doctoral thesis [Saab (2017)], Right: Hermite-Gaussian mode basis.

In the same way, with a Y-tilt aberration we can excite the modes oriented according to the y-direction, as the modes HG_{i0}, while with a defocus aberration all the centrosymmetric modes are excited. With such modulation applied, we can move around the different lobes of each mode, thus finding the maximum for each of them, as shown in the left part of Figure 3.14. A representation of the modulation applied is also reported in Figure 3.15.

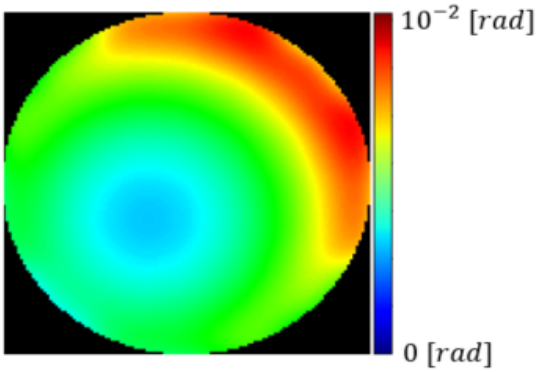

Figure 3.15: Modulation applied: sum of a 45° tilt and defocus aberration.

It is worth noting that this modulation is only a first raw modulation we derived. In this context, the effectiveness of the modulation was evaluated by means of the eigenvalues obtained through the singular value decomposition (SVD) of the control matrix. Indeed, the modulation applied must be able to act within a maximum number of Hermite-Gaussian modes.

In Figure 3.16 we present the eigenvalues of the B_M matrix, denoted by K, when the modulation we chose is applied. As we can quantify, the eigenvalues are rapidly decreasing. In the absence of measurement noise, this behavior is not a handicap to reverse the problem. In the real case, the measurement noise does not allow all eigenvectors for the phase estimation, i.e. for the estimation of the voltages on the deformable mirror actuators. In the following, we study the validity of the limited expansion to the order of 2, as reported on Eq. 3.3, by numerical simulation. For this purpose, we assume the BM matrix is calculated under the assumption of very low phases. The associated generalized inverse is obtained by filtering out all except the 10 highest eigenvalues. This choice of filtering is justified by the conditions encountered in the experiment.

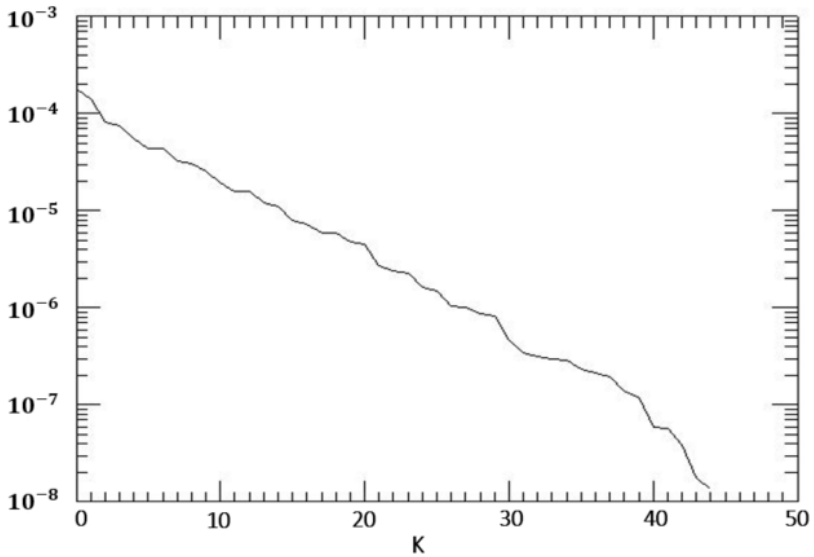

Figure 3.16: Eigenvalues K of the B_M matrix as function of the number of modes, when the modulation of Figure 3.15 is applied to the system.

Further modulations have been analyzed through Yann Lucas' internship at ONERA and continued during his doctoral thesis. These results were presented by Yann Lucas during the workshop 'WAVEFRONT SENSING IN THE VLT/ELT ERA VII', held on 1-3 December 2021. Through this study, several modulations have been compared. The best solution was derived by verifying all the actuators combinations. It is noteworthy that each actuator can only take on two values in this case, 0 and 1. Such modulation, presented in Figure 3.17, is not far from being a tilt and defocus modulation, with which we are able to act with almost all the modes considered.

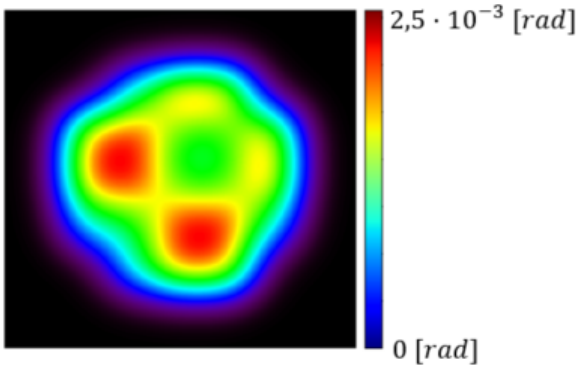

Figure 3.17: Optimized modulation obtained by verifying all the actuators combinations.

3.5.2 Estimate of the DM phase

Aiming at defining the overall performance of such sensorless adaptive optics approach, the linearity domain and the estimate of the deformable mirror's phase can prove to be important performance metrics, and useful for simple understanding and characterizing the system. The first metric we present is the estimate of the deformable mirror phase, $\varphi_{\tilde{A}}$. The demultiplexer outputs after applying modulation mentioned above, m_l, and the perturbation, denoted by φ_p, can be written as:

$$S_i = |\int e^{j(\varphi_p+\varphi_m)} HG_i|^2 - |\int e^{j(\varphi_p-\varphi_m)} HG_i|^2 \tag{3.18}$$

In this context, φ_p represents a tilted phase on the DM plane, while φ_m the modulation consisting of the sum of a $45°$ tilt and a defocus aberrations, as reported in Figure 3.15. In the following, the amplitude of this modulation is considered small ($\approx 10^{-2}$ rad), as well as the amplitude of the applied perturbation, thus remaining in the linearity regime of the system. Furthermore, from the previous section we have seen how about ten modes can be reconstructed with such modulation. The question which is addressed is however slightly different: what does such modulation mean when applied to common aberrations such as tilt and defocus?

Substituting the Eq. 3.18 in Eq. 3.11, the estimate of A, denoted by $\tilde{A}$, is shown in Figure 3.18. On the other hand, with the same derived modulation, considering a defocus perturbation on the DM, the estimate of the DM-phase is reported in Figure 3.19.

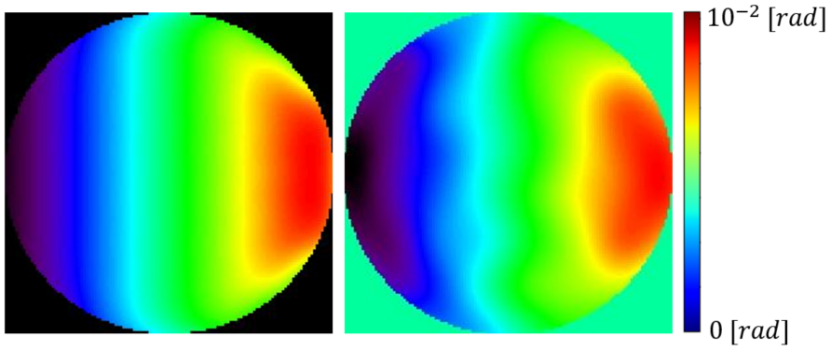

Figure 3.18: Left: Tip-tilt perturbation on the DM phase; Right: estimate of such perturbation obtained with Eq. 3.11 and Eq. 3.18.

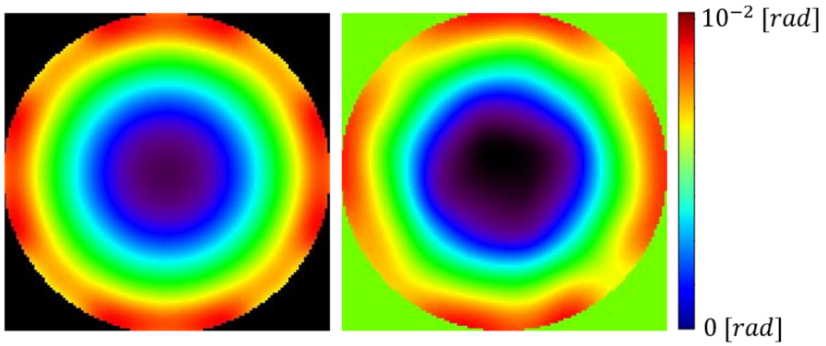

Figure 3.19: Left: Defocus perturbation on the DM phase; Right: estimate of such perturbation obtained with Eq. 3.11 and Eq. 3.18.

As we can see, in both cases the phase is not perfectly reconstructed, and its estimate is slightly different from the phase on the deformable mirror. This is due to the fact that 52 degrees of freedom are available through the DM actuators, while only about ten modes are controlled through our approach.

3.5.3 Linearity domain

Another way to study the performance of the system described in this chapter leads to the observation of the communication signal after correction. This signal is associated with the first output fiber of the demultiplexer device, also referred to as $s_0(A-\tilde{A})$. Here, $\tilde{A}$ represents the estimate of A obtained by least square inversion of the Eq. 3.10.

Two different cases have been considered: the application of voltage to the deformable mirror actuators following a tilted plane and following a parabola. In this context, the output signal after correction of the DM phase can be written as:

$$s_0(A-\tilde{A}) = |\int HG_0 e^{j\left(\varphi_A - \varphi_{\tilde{A}}\right)} HG_0|^2 \tag{3.19}$$

This is illustrated in Figure 3.20, in which the signal after correction is reported, as function of the Root-Mean Square (RMS) amplitude of the phase perturbation.

As already mentioned, this perturbation represents a defocus aberration. It is worth noting that the amplitude modulation is still considered small ($\approx 10^{-2}$ rad). In the same way, in Figure 3.21 the same output signal is derived for a tip-tilt aberration. In both cases, the greater the amplitude of the perturbations, the further we move away from the linearity regime of the equation 3.11, showing a decrease in the signal $s_0(A - \tilde{A})$ that tends towards 0 when the RMS amplitude reaches around 1. In this context, for an amplitude perturbation of about 40% of the signal amplitude, the linearity hypothesis remains valid.

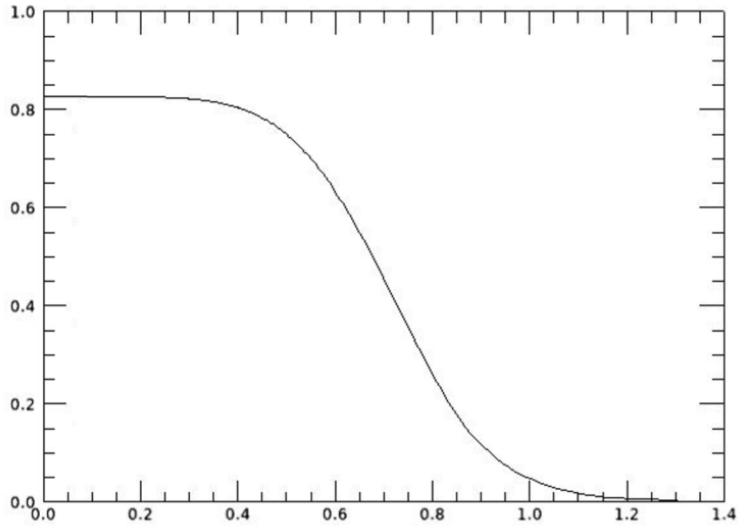

Figure 3.20: Communication signal after correction, $s_0(A - \tilde{A})$, function of the rms amplitude of the phase perturbation (case of defocus perturbation).

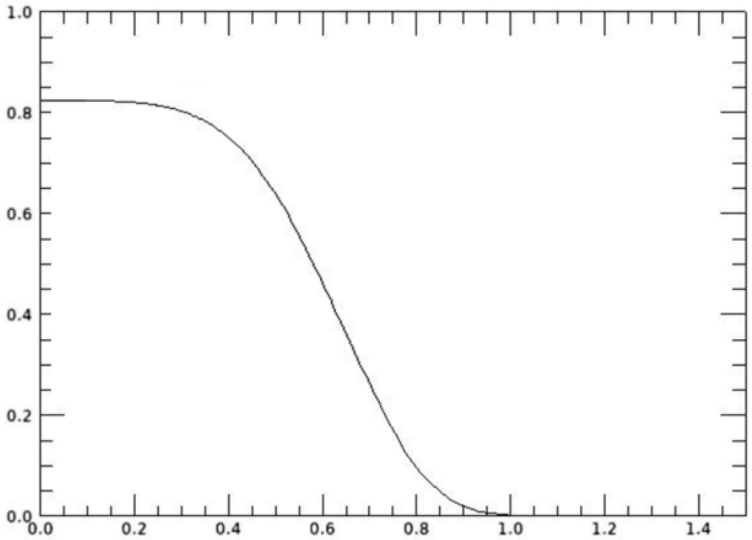

Figure 3.21: Communication signal after correction, $s_0(A - \tilde{A})$, function of the rms amplitude of the phase perturbation (case of tilted plane perturbation).

3.6 Experimental validation

In this section, we describe the experimental setup of this Sensorless AO approach. The in-house software employed in this case is firstly introduced. In the second part, the misalignment on focusing into the MPLC device are reported, thus measuring the cross-talk terms between the different modes. Finally, the first results on the closed-feedback loop are shown. The performance of such approach are derived applying a perturbation and measuring the time, or number of iterations, in which the system is able to compensate them.

3.6.1 Experimental setup

In Figure 3.22, we present the experimental setup we built to test and validate our numerical analysis. In order to have a precise control of the input beam, a fiber optic collimator (Thorlabs TC25FC-1550, Triplet Collimator) is injected with a $1.5\ \mu m$ laser diode. In this case we make the assumption of a strong received flux. A static Gaussian beam is incident on the deformable mirror, with a waist of $w_0 = 2.35\ mm$. After reflection on the DM, the beam is sent to a Multi-Plane Light Conversion device and decomposed into a set of 15 Hermite-Gaussian modes. It is worth noting that, although the MPLC is able to decompose the incoming beam into a set of 15 HG modes, in our system only 8 outputs out of 15 are equipped with photodiodes. Hence, using only 8 actuators in the sub-pupil reported in the DM layout of Figure 3.23, 8 modes of deformation are controlled onto the DM. Moreover, the lenses L_2 and L_3 constitute an afocal system that adapts the size of the Gaussian beam at the input fiber collimator to the size of the Gaussian mode at the input of the MPLC device, conjugating the DM plane with the MPLC input one.

The DM employed in this experiment is an ALPAO deformable mirror with 88 actuators on a 10 x 10 regular grid. Its inter-actuator distance, or pitch, is $p = 2.5\ mm$. Through the previous beam waist radius w_0, the beam illuminates a number of actuators $n_{act} \approx 9$. In Figure 3.23 the geometric layout of the DM88 is reported, with the pupil d illuminated by the Gaussian beam.

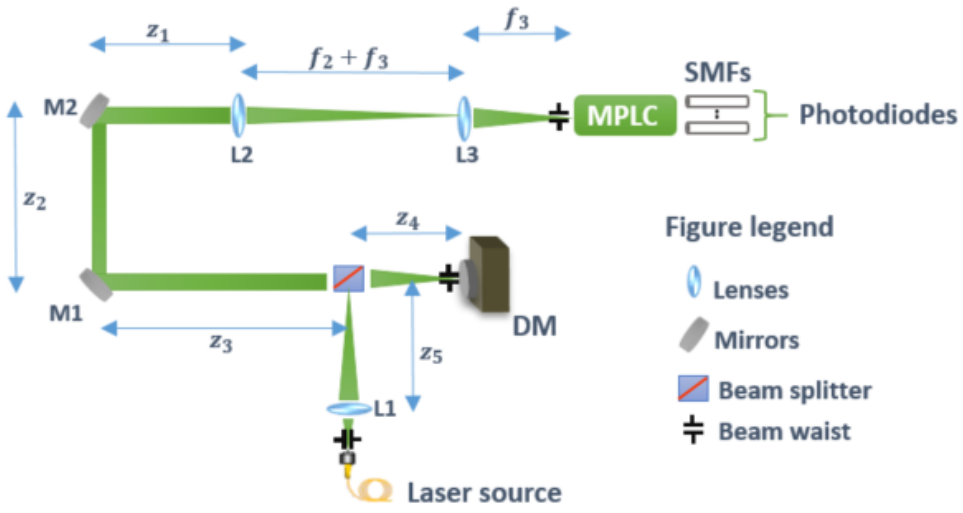

Figure 3.22: Experimental setup: Schematic representation

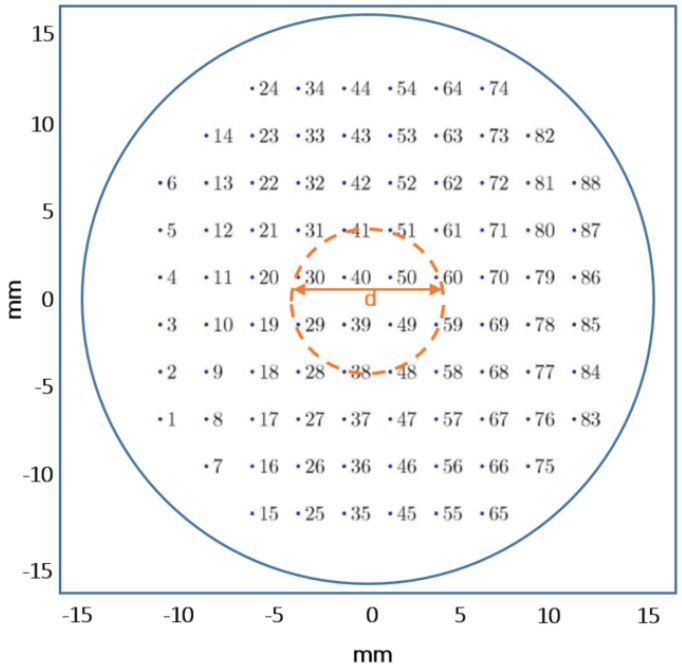

Figure 3.23: Geometric layout and numbering of the ALPAO DM88 actuators. Detail of the pupil d illuminated by the Gaussian beam.

In this way, we mode-match the input waist, w_0, to the waist radius used by the MPLC device, defined as $w_{mplc} = 300\ \mu m$. The ratio between the L_2 and L_3 is chosen such that the magnification factor is: $L_2/L_3 = 2350\ \mu m/300\ \mu m \approx 7.8$. As a consequence, considering the first L_2 lenses with focal length of $f_2 = 40\ cm$ and the L_3 with $f_3 = 5\ cm$, a ratio of 8 can be obtained, so that $f_2 + f_3 \approx 45cm$, and $z_1 + z_2 + z_3 + z_4 = f_2 = 40\ cm$. The focal length of the fiber collimator is $f_{fc} = 25.49\ mm$, so that $z_4 + z_5 = f_{fc}$. In this system, the z axis is defined by the direction of light propagation, while the x and y axes are respectively the horizontal and vertical directions perpendicular to the z axis (Figure 3.24).

Moreover, an in-house software performs the digitization of the output signals from the photodiodes, the signal processing, the control of the DM amplifier board and the graphic user interface (GUI).

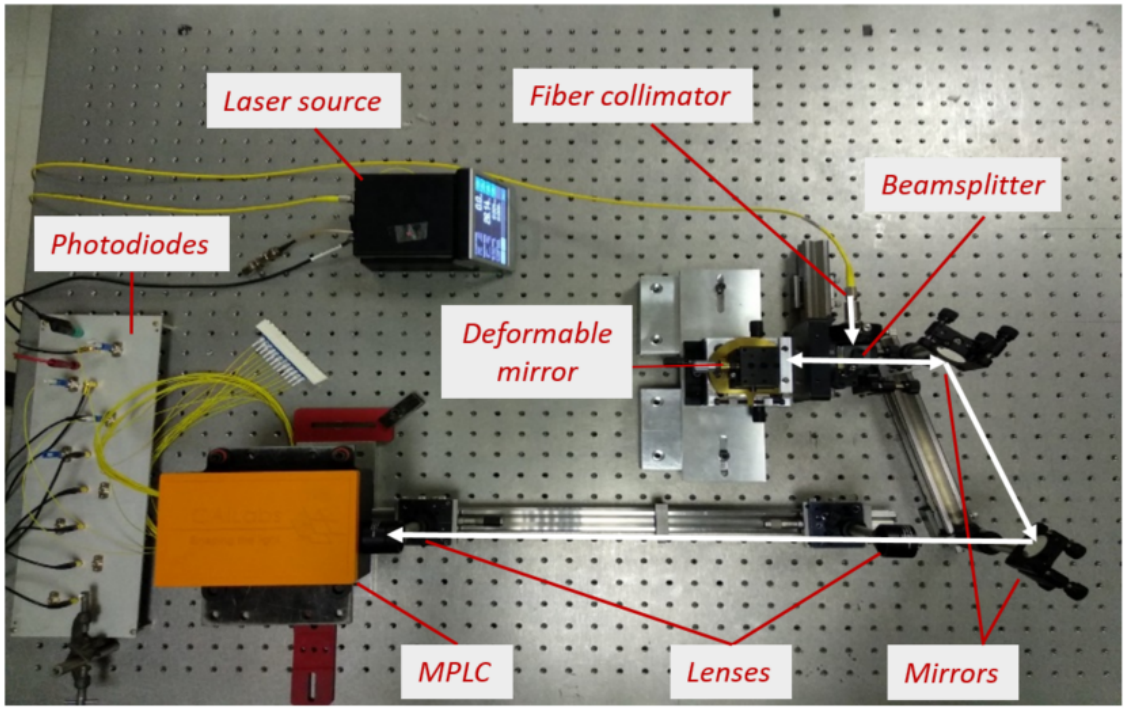

Figure 3.24: Experimental setup: Optical bench developed at the ONERA. After the fiber collimator the beam is reflected by the deformable mirror and goes to the MPLC demultiplexer device.

3.6.2 Misalignment on focusing into the MPLC

In our implementation of the present setup, the footprint of the optical elements leads to a small shift of the beam in the x direction, which in turn results in a waist-size mismatch between the optical injected beam and the beam used by the MPLC device. Such mismatch reduces the overlap integral between the input beam and the HG mode basis used for the MPLC device. In the following we will analyze the misalignment on focusing into the MPLC, thus evaluating the cross-talk between the output modes, for a given injected beam. The realized experimental configuration is reported in Figure 3.24.

We first measure the cross-talk between the Hermite-Gaussian modes introduced by the system reported in Figure 3.24. To do so, the light injected is optimized through the system lenses and mirrors such that the injection is performed in only one mode, the HG_{00}. That is, when the system is perfectly aligned, we assess the amount of energy that is leaked to the higher-order modes, since the intensity on these modes. The intensity of all other modes are reported in Table 3.1. These measurements were made during the first construction of the optical bench. The optical power measured in one high-order mode, denoted by HG_{mn}, can be defined by P_{mn}, thus leading to the cross-talk definition between the HG_{00} as: $10 \cdot log_{10}(P_{mn}/P_{00})$. It should be noted that a triangular set of 15 HG modes has been taken into account in this case.

$Mode$	HG_{01}	HG_{02}	HG_{03}	HG_{04}	HG_{10}	HG_{11}	HG_{12}
dB	-14.82	-19.59	-32.6	-29.59	-26.58	-26.58	-32.6

$Mode$	HG_{13}	HG_{20}	HG_{21}	HG_{22}	HG_{30}	HG_{31}	HG_{40}
dB	-32.6	-32.6	-32.6	-32.6	-21.81	-32.6	-32.6

Table 3.1: Experimental cross-talk values from mode HG_{00}, for a triangular set of 15 HG-modes

From the previous table, we can first note that the quality of the alignment is globally satisfactory. However, a slight difference is evident on the values of the mode HG_{01}. We think that this is due to the difficulty of alignment related to the quality of the adjustment of mirrors (Thorlabs).

3.6.3 Performance analysis: experimental results

The performance of our system has been analyzed in this section by implementing the SPGD algorithm using the only fundamental output, here denoted s_0, as first signal output. The results are shown in Figure 3.25. As one can see, a disturbance was added to the deformable mirror control voltages, in the form of a voltage step.

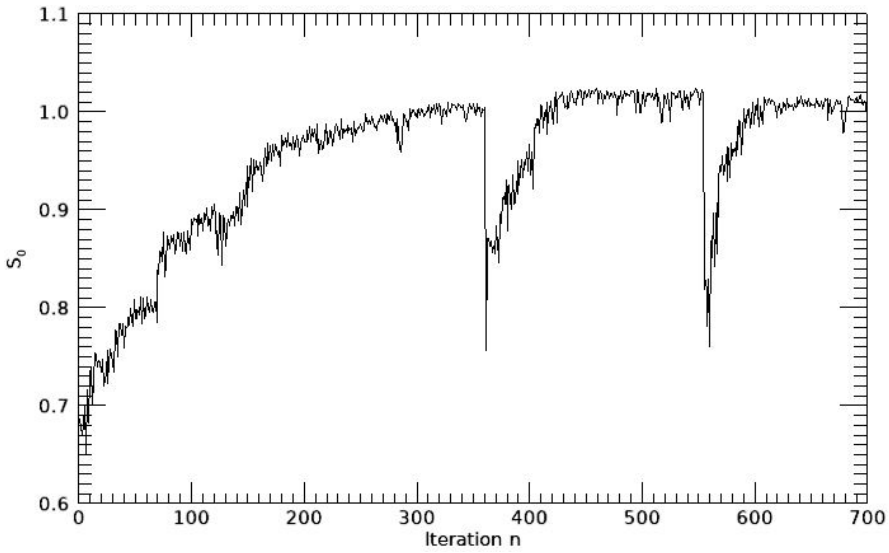

Figure 3.25: Response to an induced perturbation: single output SPGD based-control.

The modulation used in this case is the one reported in Section 3.5.1, Figure 3.15. Regarding the perturbation, we consider now a defocus aberration. Such perturbation results in a decrease of the s_0 signal of about 20% of its convergence value. It should be noted that while one iteration corresponds to the application of a set of voltages to the DM, a modulation is completed after two iterations. That is, the system takes about 15 modulations to return to the previously

found convergence value, a number close to the number of controlled modes (MPLC mode decomposition). Similar work has been carried out by Weyrauch & al. [Weyrauch et al. (2002)], in which hundreds of iterations are required to achieve the maximum value.

Contrarily, using the MPLC 8-output control matrix, as described in the previous section, only one modulation is required for the system to return to its convergence value when a disturbance in the form of a voltage step is applied. This is reported in the Figure 3.26, in which the coupling efficiency of the telecommunication signal is presented as function of the number of iterations. The used close-loop gain is $g = 0.5$. This value, chosen rather high, explain the slight oscillations on the Figure below.

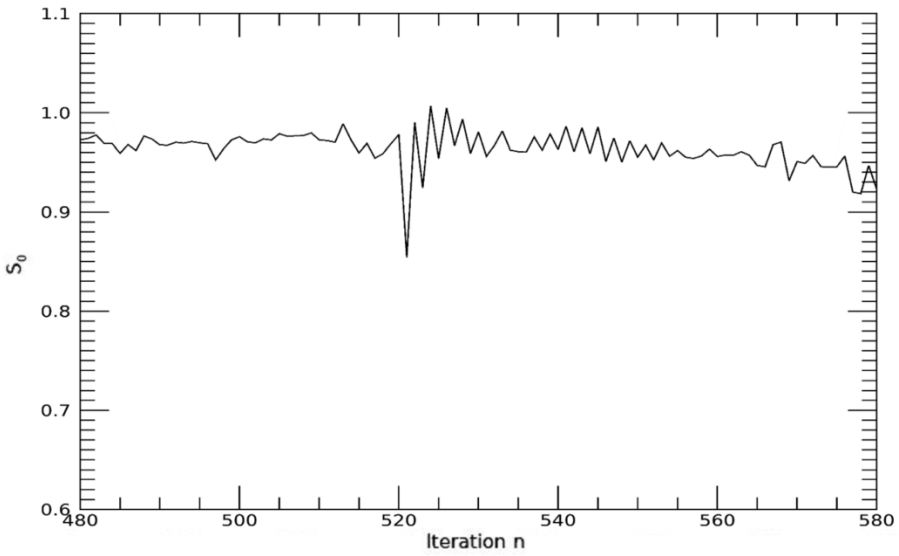

Figure 3.26: Response to an induced perturbation: multi-output based-control with a gain of $g = 0.5$.

3.7 Conclusion

In this Chapter, our aim was to study a new Sensorless adaptive optics approach using a Multi-Plane Light conversion as mode demultiplexer device. Indeed, we used a multi-detector based control algorithm in order to optimize the signal in only one SMF output: the communication mode, or HG_{00}. This algorithm is introduced in the first part of this Chapter. Only one modulation is applied in the linear domain with respect to a standard Sensorless method, employing all the MPLC outputs as signal metrics.

In the second part of this Chapter we analyze the performance of our approach. In this case, the architecture of the numerical simulations developed for this purpose is introduced. A proposal of a modulation capable to create an invertible matrix has been also detailed, i.e. a sum of a tip-tilt at 45° and a defocus aberration. Considering the eigenvalues associated with this modulation, about ten modes can be reconstructed, out of a total of 45. Nevertheless, further analysis has been highlighted in the framework of Yann Lucas' internship at the ONERA, and continued during his PhD thesis.

Furthermore, we derived the dynamic of this method with respect to the amplitude of the applied perturbation. Based on this, the linearity domain, as well as the estimate of a DM phase when applying two different perturbations have been studied: a tip-tilt and a defocus aberrations. In the last part, our laboratory bench has been described, and the first results are presented comparing the SPGD method with our multi-output approach.

In this context, only 8 outputs of the MPLC device are equipped with photodiodes, and 8 modes of deformation are controlled onto the deformable mirror. As we have seen, only one modulation is required when considering a multi-output approach, compared to 15 modulations obtained when the SPGD algorithm is applied.

As a perspective, further analysis needs to be focused on an algorithm capable to lock the feedback loop, which will complete our proposed method. Furthermore, more sensitive photodiodes can be employed in new experimental measurements. Finally, the development of a dedicated RTC is required in order to upgrade the device for on-sky demonstration. Control parameters such as the loop bandwidth, the number of modes of correction and measurement and the sensitivity of the detection stage will be adapted for this purpose.

Chapter 4

Impact on photonic integrated circuit technology

4.1 Introduction

We have introduced in the Section 1.5.4 of Chapter 1 the principle of a coherent combining system as an alternative technique to the conventional adaptive optics approach for mitigating the effects of atmospheric turbulence, and what components such a system consists of. In the coherent combining approach, the phase and the amplitude of the optical beam are actively controlled in order to maximize the signal. After the modal decomposition of the incoming perturbed beam previously described in Chapter 2, the present Chapter is dedicated to the combination of guided modes. We are particularly interested here in a combination performed by a photonic integrated circuit to prepare a solution suited to high number of modes.

As stated in Chapter 1, the basic components of the proposed combiner circuit are a phase modulator and a directional coupler. A trade-off has to be considered between SiN, which offers large scale integration and a mature material platform, and the $LiNbO_3$ platform, which on the contrary shows its attractiveness with high-modulation bandwidth through its electro-optic (EO) effect. In the first part of this chapter, both material platforms are studied. Indeed, both offer attractive properties in separate fields, each of them leading to different implementation constraints. The first studied platform is lithium niobate. Its design was directed by Guillermo Martin at the Institute for Planetary sciences and Astrophysics (IPAG) in Grenoble, and its development was carried out at the FEMTO-ST Institute in Besançon, supervised by Nadège Courjal. Such PIC has been received during the last part of this thesis, and the first characterization of the half-wave voltage and insertion losses is reported, thus comparing the experimental values with the theoretical ones.

Furthermore, in the framework of a CNES-funded research project, a SiN-based PIC was developed by Cailabs and provided to ONERA. Its characterization is presented in the last part of this Chapter. Through its time response (i.e. the maximum frequency of the feedback loop), we want to highlight the impact on the PIC of the previous spatial and temporal analysis.

4.2 Lithium-niobate based PIC

In the first chapter of this thesis we have reported different material platforms for the implementation of photonic integrated circuits as beam combiners. Among these, the main properties of lithium-niobate (also named $LiNbO_3$) PICs make them suitable when the realization of fast phase shifters is required. Based on this technology, photonic circuits have been developed by FEMTO ST for several years, in particular for astronomy applications, in collaboration with the Institute for Planetary sciences and Astrophysics of Grenoble (IPAG). We have chosen to have a dedicated component developed for the application of this technology to recombination for the correction of atmospheric turbulence effects in optical communications. I participated in the dimensioning of the component alongside Guillermo Martin and Nadège Courjal. The component was produced by Nadège Courjal at FEMTO ST and it is currently being tested and encapsulated.

This paragraph describes the work carried out to define the component. Such work focused on optimizing the parameters of the elementary components (directional coupler and phase modulator) as well as on the choice of the general architecture of the recombiner and its geometric definition.

An example of a schematic diagram applying a phase and amplitude control of n complex fields has been proposed in Noah Schwartz thesis [Schwartz (2009)], and reported in Figure 4.1 for completeness. In the case of a phase-only correction, the blue rectangles are reduced to simple directional couplers with electrodes in order to control the phase. These latter are placed at the beginning of the circuit, while the couplers are at the next stages. The main strengths of this architecture lie in the possibility of having one output for each active MZI considered, so that each MZI can be driven independently while having a control law that is simple to implement. The functions of a basic component presented in the architecture in Figure 4.1 can be summarized in the description of a directional coupler and a phase shifter, which have been modeled to get an idea of their dimensioning.

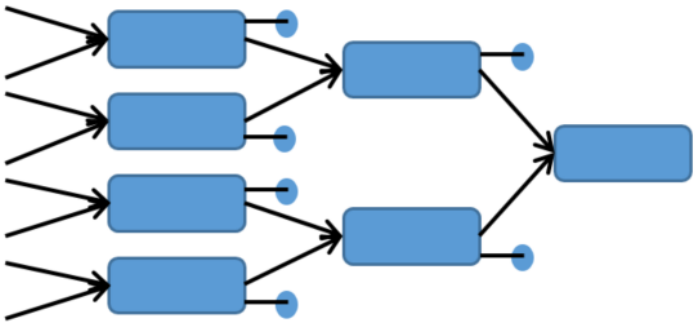

Figure 4.1: Schematic diagram of phase and amplitude control of n complex field [Schwartz (2009)].

A modeling tool based on the Beam Propagation Method (BPM) has been used, simulating wave propagation in guiding structures with small index variations along the propagation direction. Based on these simulations a correct geometry has been defined, before making the lithographic mask and the subsequent technological steps.

4.2.1 Modeling of basic components

The beam propagation method is a mathematical procedure used to study the propagation of electromagnetic fields in slowly varying optical waveguides. It is generally based on the resolution of the Helmholtz equation, following a slowly varying approximation. The accuracy and applicability have been studied extensively by Roey & all and Thylen [Roey et al. (1981); Thylén (1983)]. In this context, we need to apply this method over one time period, thus visualizing the fields along the propagation direction, or on the waveguide cross section.

A diversity of directional couplers with a wide variation of coupling parameters has been studied in the framework of Kassem Saab doctoral thesis [Saab (2017)].

Indeed, the parameters involved are:

- the waveguide width, L_{width}
- the gap between the waveguides at the coupling point, Δ
- the waveguide length at the coupling point, $L_{coupler}$

To go further, other fundamental parameters must be defined for the PIC development, such as:

- the bending radii
- the overall device size limited by the size of the wafer
- the polarization control

Regarding the polarization control, due to the material polarization dependent operation, which in turns derives from the intrinsic birefringence of such material, thus allowing only one polarization to propagate and avoiding any problems associated with the coupling of the two polarization.

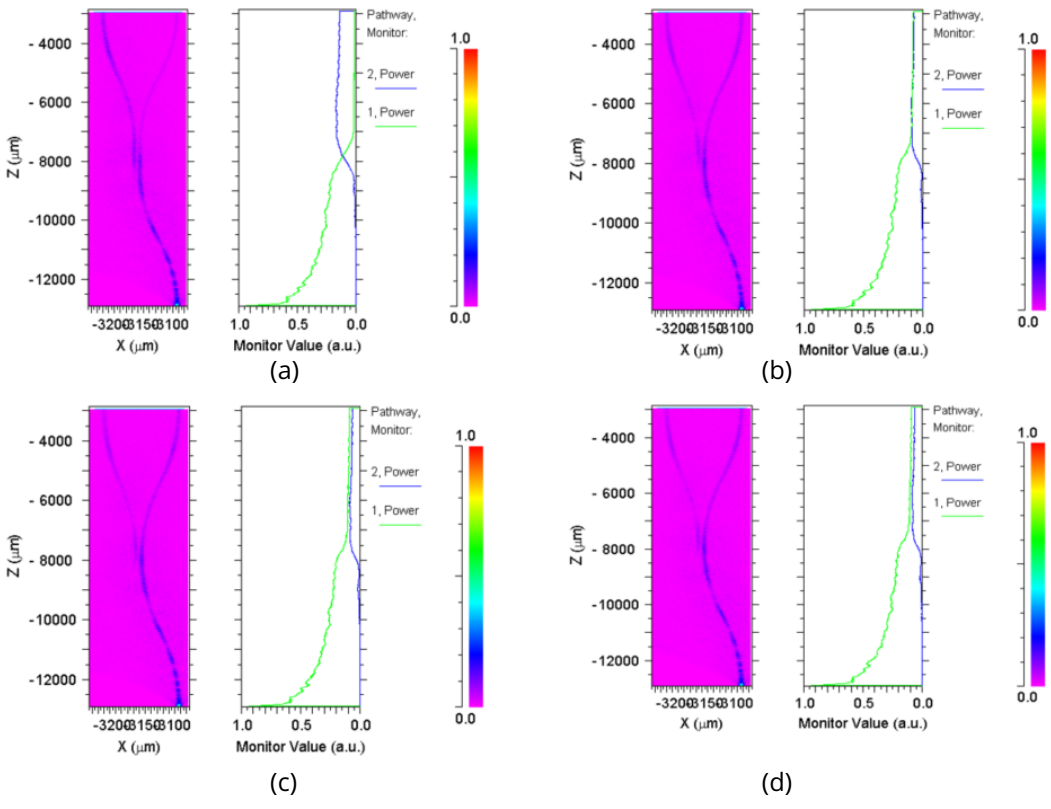

Figure 4.2: BPM simulation of the directional coupler described in Figure 4.3 with same $\Delta = 6\mu m$ and for different coupling length values: L_c = (a): 1000 μm (b): 100 μm (c): 10 μm (d): 1 μm

Many simulations were carried out to evaluate the energy output from each arm, defined as the integral of the electric field intensity over the cross-section of the waveguide, by varying Δ or $L_{coupler}$. Indeed, as example of the coupler parameters optimization, in Figure 4.2, different values of $L_{coupler}$ are considered for the same Δ, showing that an ideal 50/50 amplitude distribution is obtained for a coupling length of (b) $100\mu m$.

A simple 50/50 coupler has been defined throughout this thesis using BeamPROP software (Rsoft, Inc.), a tool based on the BPM for the design and simulation of integrated and fiber-optic waveguide devices. Indeed, the main optimized coupler parameters are shown in Figure 4.3.

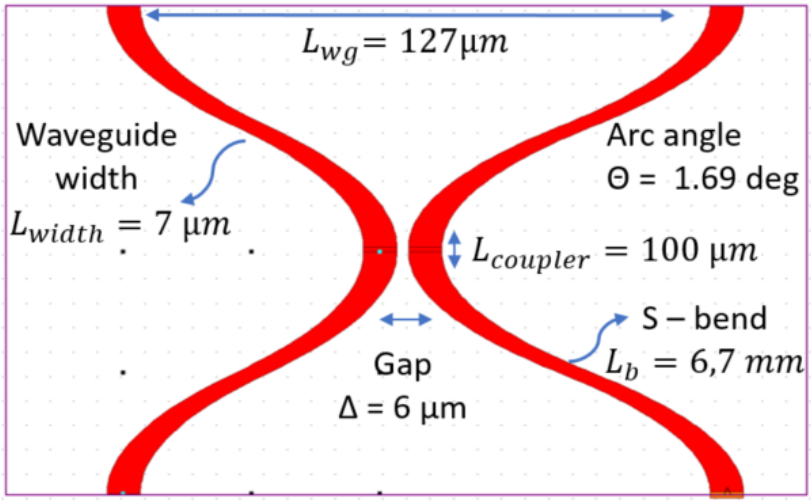

Figure 4.3: Schema of a 50/50 coupler. The most important parameters are listed and can be varied to obtain different coupling ratios

4.2.2 Phase shifters

In this section we introduce the optimization of a phase shifter for a basic module presented in Figure 4.1.

We first detail the electrodes design, derived as a trade-off between the electrodes length, denoted by L_{elec}, the modulation bandwidth, and the propagation losses. Indeed, due to our low modulation frequencies ($<MHz$), we can first of all consider the modulation bandwidth as negligible. Furthermore, regarding the separation between electrodes, they need to be close enough to interact with the guided mode, but not too close to avoid short circuits and manufacturing defects. Typically, such separation is the same as the width of the guide, here about $7.5\ \mu m$. In addition, further optimizations in the choice of the distance between the electrodes can be carried out using any field simulation software. In this way, the distance between the electrodes and the guided mode gives us the possibility to know the field seen by the latter, as shown in Figure 4.4 [Thi Bich and Le (2018)].

In this context, large electrodes length make it possible to reduce the control voltage, for the same given electro-optic (EO) efficiency ($V_\pi L_{elec}$). On the contrary, they increase the intrinsic

losses in the circuit. Finally, these size must always be compatible with the maximum wafer length of $L_{total} = 84\ mm$. In this way, the EO efficiency for our circuit is $V_\pi L_{elec} \approx 9\ V \cdot cm$, which in turns gives a maximum V_π value that ranges from 10 to $22.5\ V$, considering the length of the electrodes fixed to $L_{elec} \approx 9.5\ mm$. The width of such electrodes is $L_{width} \approx 120\ \mu m$.

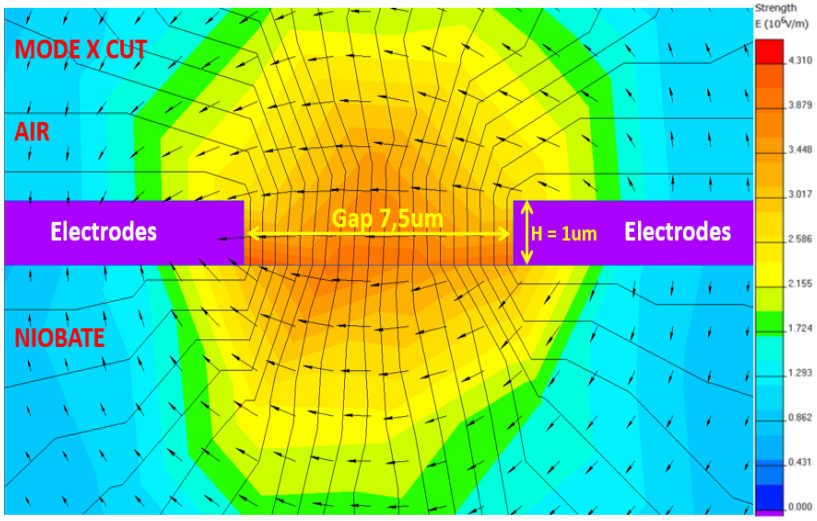

Figure 4.4: Example of electrodes separation optimization using QuickField simulation software.

4.2.3 PIC architecture design

Given the need for a simple architecture allowing an output for each MZI, which is necessary for its easy control, we have considered an architecture based on the recombination principle proposed by K Saab, and shown for simplicity in the following Figure 4.5.

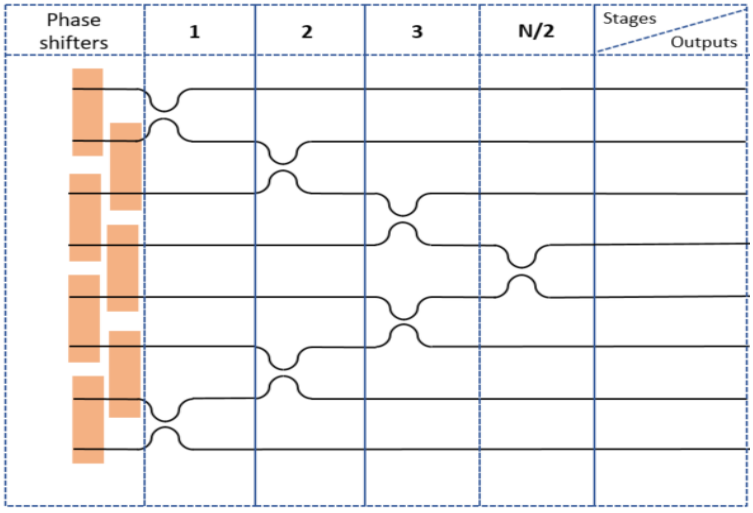

Figure 4.5: Recombination architecture proposed by K. Saab [Saab (2017)].

As one can see, such architecture differs from the one proposed in Figure 4.1. Indeed, it ensures that the waveguides do not intersect each other, so that any measurement signal can easily be taken at the output of each MZI. On the other hand, $N/2$ recombination stages are needed for a $N-channel$ device. It should be noted that in the case of an architecture such as the one shown in Figure 4.1, $log_2(N)$ recombination stages are required for the same $N-channel$ device. Through this architecture, the number of inputs/outputs, as well as the number of recombination stages, is function of both the total wafer length, the length of the electrodes, the separation between the inputs/outputs channels and the length of an elementary coupler.

Moreover, the waveguide bending radii are strictly related to the waveguide separation and the total length of the circuit: larger curvatures mean greater chip and electrode length, also increasing propagation losses. Indeed, a large gap leads the circuit to be insensitive to the variation of the coupling length. It is also worth noting that the coupling ratio is wavelength dependent, which means that further optimization are required for broadband applications.

It should be noted that the architecture reported in Figure 4.5 differs slightly from that simulated in this paragraph. In fact, through this last architecture, it is easy to derive the signal in the communication channel as the sum of the input signals. In this way, assuming the input signals are numbered from $i = 1$ to $N = 8$, where N is the total number of inputs, the telecommunication signal can be written as:

$$A_{comm} = (\frac{\sqrt{2}}{2})^{\frac{N}{2}}(A_i+A_N+A_{i+1}+A_{N-1})+(\frac{\sqrt{2}}{2})^{(\frac{N}{2}-1)}(A_{i+2}+A_{N-2})+(\frac{\sqrt{2}}{2})^{(\frac{N}{2}-2)}(A_{i+3}+A_{N-3})$$

Assuming the same amplitude in all channels, $A_i = A$, the previous formula writes:

$$A_{comm} = 2A[2(\frac{\sqrt{2}}{2})^{\frac{N}{2}} + (\frac{\sqrt{2}}{2})^{(\frac{N}{2}-1)} + (\frac{\sqrt{2}}{2})^{(\frac{N}{2}-2)}]$$

which in turns gives a total output intensity of $7.32\ A^2$, differing from $I_{comm} = \sum_{i=1}^{N} I_i$.

Due to the difficulty of having inter-guide separations of less than $L_{wg} = 127\mu m$ (which is a common pitch available for telecommunication fiber arrays) and taking into account the maximum curvature of the directional couplers, which is $L_{S-bend} = 6.7mm$, we have been limited to the construction of a circuit with 8 inputs/outputs. It is noteworthy that if we had chosen a tree architecture like the one proposed in Noah's thesis (Figure 4.1), we could have had a PIC with more inputs but fewer outputs, which would have resulted in a more complex phase control law.

Through the previous consideratons, the final realized architecture of a 8-channel lithium-niobate photonic integrated circuit is shown in Figure 4.6.

The wafer developed is divided into seven different architectures, each defining a different combiner system. The dimensions of each circuit are $5mm \times 84mm \times 500\mu m$ for width, length and thickness respectively.

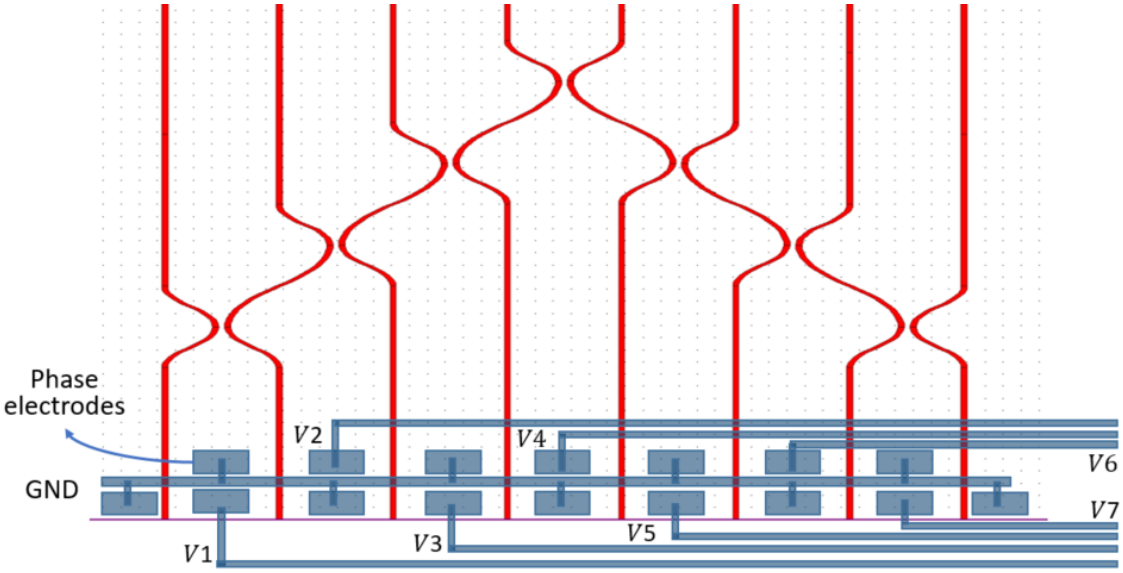

Figure 4.6: Example of a 8-channel lithium-niobate PIC architecture.

4.2.4 PIC fabrication

In Figure 4.7 the final wafer mask is presented. In the right part of this Figure we reported a zoom on the phase modulation electrodes placed at the beginning of the circuit. The waveguides realized in the context of this thesis follow the Ti-indiffusion technique.

The wafer construction was completed in July 2021 by Nadège Courjal (Femto-ST), while its encapsulation began in October. The next step concerns the an in-depth characterization of these components, already planned within the framework of Yann Lucas's doctoral thesis, which started last October.

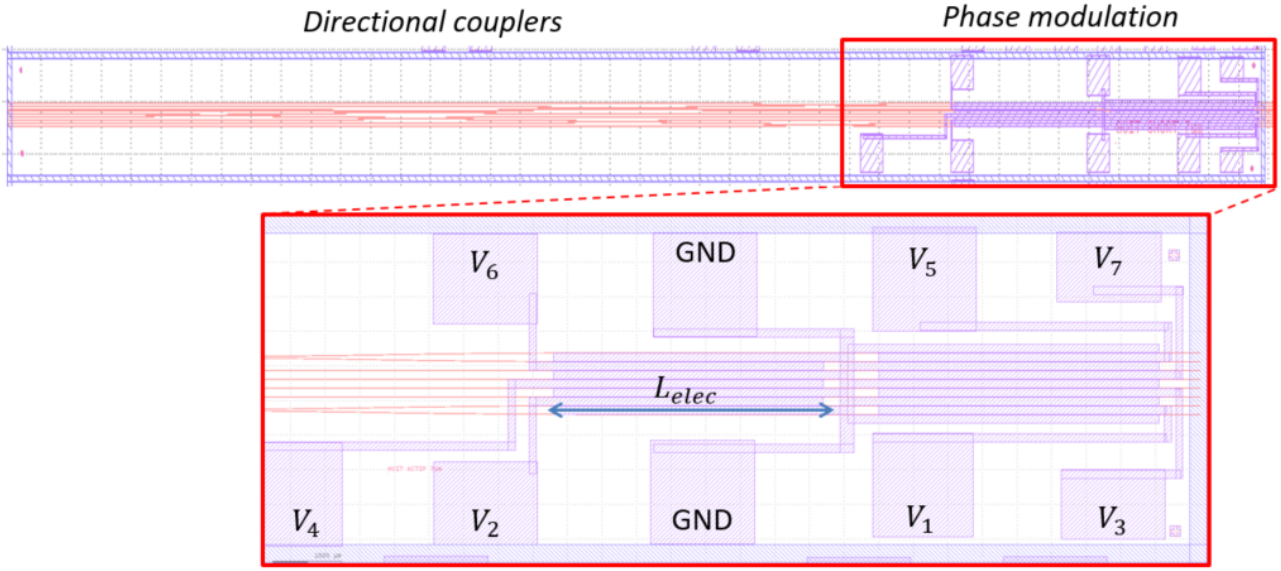

Figure 4.7: Mask design of the 8-channel lithium niobate circuit reported in Figure 4.6.

4.2.5 PIC characterization

Despite delays in the manufacture of the circuit caused by the Covid-19 pandemic, the integrated circuit has been received during the last week of January 2022. The final 8-channel lithium niobate photonic circuit is shown in Figure 4.8. In the following, the first measurements of the insertion losses and the half-wave voltage of the PIC.

Indeed, measurements of the intensity distributions at the output of each waveguides have been made. In this way, the average propagation loss of our PIC is about $12\,dB$. This value is not far from the expected value of $\approx 9\,dB$ due to the sum of coupling losses at the interfaces, propagation losses and losses due to bending radii in the circuit. Further measurements should be made to improve this value. Furthermore, the experimental half-wave voltage is approximately $V_\pi \approx 13\,V$, which is in accordance with Section 4.2.2 ($9\,V \leqslant V_\pi \leqslant 22\,V$).

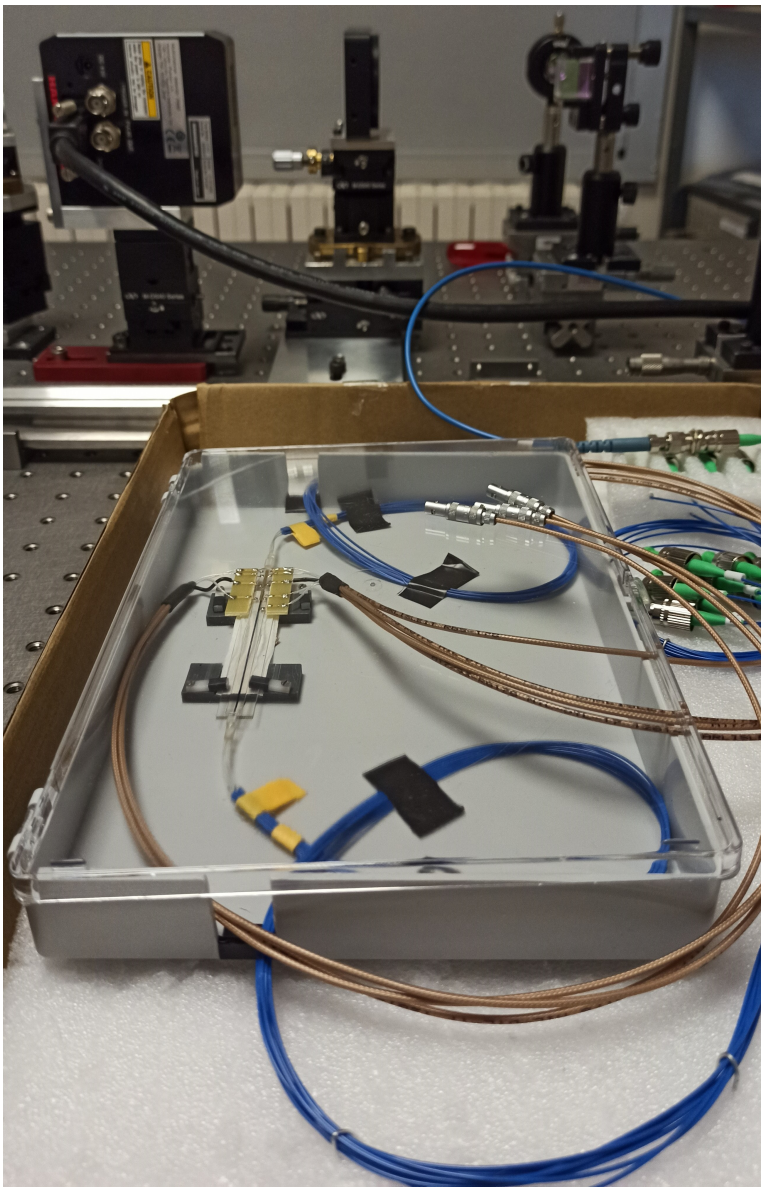

Figure 4.8: Final lithium niobate PIC with control electrodes.

4.2.6 Conclusion on $LiNbO_3$-based PIC

Based on a numerical simulation (BPM) and on the optical properties of the lithium niobate waveguides realized by FemtoST, we optimized the parameters of the elementary components (directional coupler and phase shifter). We also proposed a recombination architecture as well as a layout for a 8-channels recombiner. The masks were designed by G. Martin, while the component by N. Courjal. Because of Covid, this project was delayed. The encapsulation was performed by teem Teem Photonics during January 2022. Finally, its implementation, planned in the framework of my thesis, should finally be carried out in the framework of Yann Luca's thesis.

4.3 Characterization of a SiN-based PIC

In parallel with the work on lithium niobate, I was fortunate to have access to a SiN photonic integrated circuit developed by Cailabs and supplied by Cnes. This circuit allows the recombination of 8 channels with control of both phase and the amplitude [Billault et al. (2021)]. Due to lack of time, we limited ourselves to the characterization of a single MZI. The first step was its implementation and static testing with a dedicated amplifier.

Having highlighted that the temporal response of the phase shifters was a dimensioning parameter, I then set out to characterize it, particularly in the case of 2π phase shifts. This paragraph presents the results obtained.

4.3.1 Modeling of an active Mach-Zehnder

In order to constructively recombine two incident fields, a device composed of a phase shifter and a simple coupler can be used. However, with such configuration, the intensity cannot be optimized in a single output arm if the incident fields do not have the same amplitude. In an active MZI, two stages of phase shifters and couplers are combined: the first stage combine the two incident fields of different amplitude to obtain two resulting fields of equal amplitude on both output arms, while the second stage allows the two equal-amplitude fields to constructively interfere, thus optimizing the total intensity in one output arm of the device [Saab (2017)]. In Figure 4.9 such device is reported, with two different phase shifts applied on each arm. Such an active MZI corresponds to a single MZI used by Cailabs, whose characterization is detailed in the following. As reported in Chapter 1, it is noteworthy to recall that in a $LiNbO_3$ PIC each phase shifter on the circuit is controlled by an electro-optic effect, whereby on SiN the phase is controlled through a thermo-optic effect. As a consequence, a linear relation with the applied voltage can be found with lithium niobate phase shifter, while a quadratic relation with respect to the applied voltage is given when considering silicon nitride components.

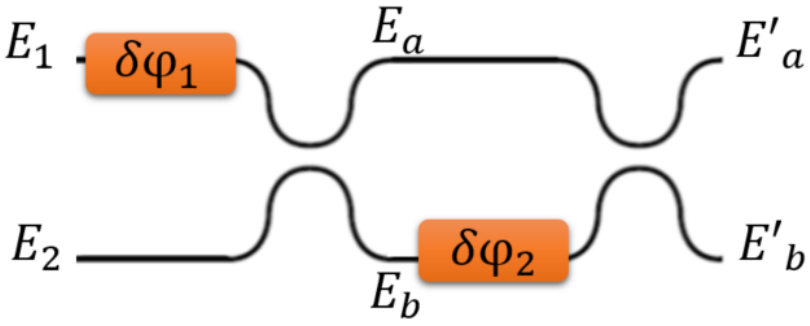

Figure 4.9: Principle of an active Mach-Zehnder interferometer

4.3.2 Phase shifter characterization

As already stated, each phase shifter is voltage-controlled, while a phase change is addressed inside each stages. Indeed, a quadratic relationship between the applied voltage and the desired phase can be written as:

$$\varphi = \alpha \frac{V^2}{R} \tag{4.1}$$

where α denotes a coefficient of proportionality, while R represents the equivalent resistance of a phase shifter ($R = 850\Omega$). It should be noted that the previous constant α depend on the considered phase shifter (PS), as well as R, and the following experiments are based on the given PS and R. In order to compute the voltage to be applied to achieve a desired phase shift (Eq. 4.1), we applied through the digital-analog converted (DAC) a square root voltage to one phase shifter, producing a linear variation of the power as function of time. The signal at the output of the measurement channel is measured simultaneously. The circuit of interest is the single active MZI shown in Figure 4.9, and the measurement channel is the channel represented by E'_a.

The following periodic voltage is applied to the phase shifter:

$$V^2(t) = \lambda t + V_0^2 \; mod(V_1^2 - V_0^2) \tag{4.2}$$

where $V_1 = 30V$, as specified by Cailabs for the maximum voltage applied to a phase shifter. In this way, V_0 is adjusted until $\delta\varphi$ is a sinusoidal signal, i.e.: until s(V_1)=s(V_0), or $\delta\varphi(V_1) = \delta\varphi(V_0) mod(2\pi)$, thus obtaining $V_0 = 13.14V$, as reported in Figure 4.10.

Finally, with the previous Eq. 4.1, the constant α can be written as:

$$\alpha = \frac{R \cdot 2\pi}{V_1^2 - V_0^2} \approx 7.34 \tag{4.3}$$

hence, $\alpha \frac{30^2}{R} = 2.48\pi$. Contrarily, through the values obtained by Cailabs PIC datasheet, we have that a ΔV from $0V$ to $30V$ corresponds to a phase shift of 3π. The length of each phase shifter is $L_{PS} \approx 3mm$, which leads to an efficiency of $V_\pi L_{PS} \approx 6V \cdot cm$, for $V_\pi \approx 19\ V$.

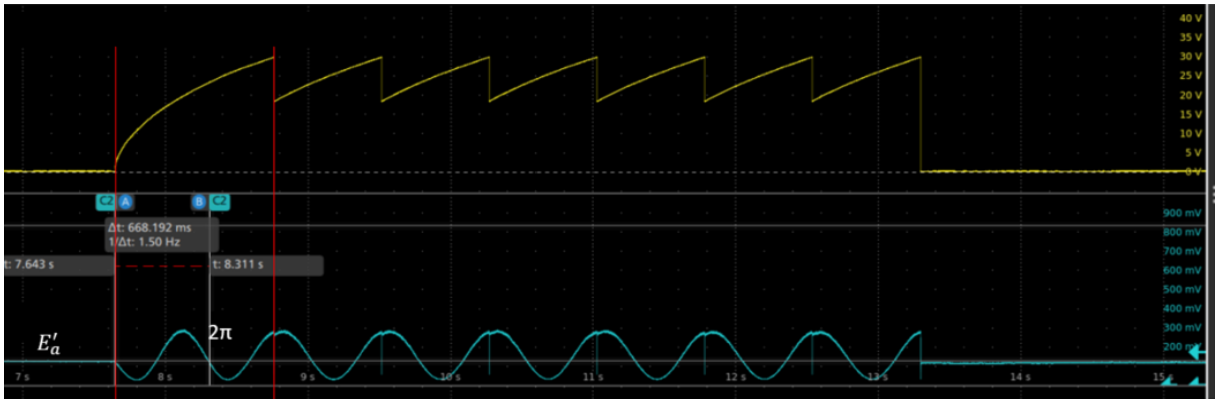

Figure 4.10: Response of the PIC (blue line) to a square root variation in applied voltage (yellow line). $0 < V < 30\ V$.

4.3.3 Time response

In order to drive the photonic integrated circuit correctly, a 12-bit digital-analog converter was developed during this thesis and reported in Figure 4.11.

It is capable of supplying an output voltage ranging from 0 to $32V$, with an associated current of 0 to $40\ mA$. Hence, considering a resistance of 850Ω and a maximum voltage applicable to the circuit of $30V$, the maximum current is $35\ mA$, which is less than the maximum current the DAC can supply. Furthermore, we want to measure now the time between sending the delivery voltage by such a DAC and its application by the PIC. As soon as the voltage is applied to a phase shifter, the PIC will heat up until it reaches the thermal equilibrium corresponding to the delivery voltage. In Figure 4.12 we present the voltage rising time measurement at phase shifter terminals (left) and the interferometric signal at the output of the active MZI (right). The descent of the latter curve can be explained by considering the output signal of each MZI, i.e. the lower part of Figure 4.10.

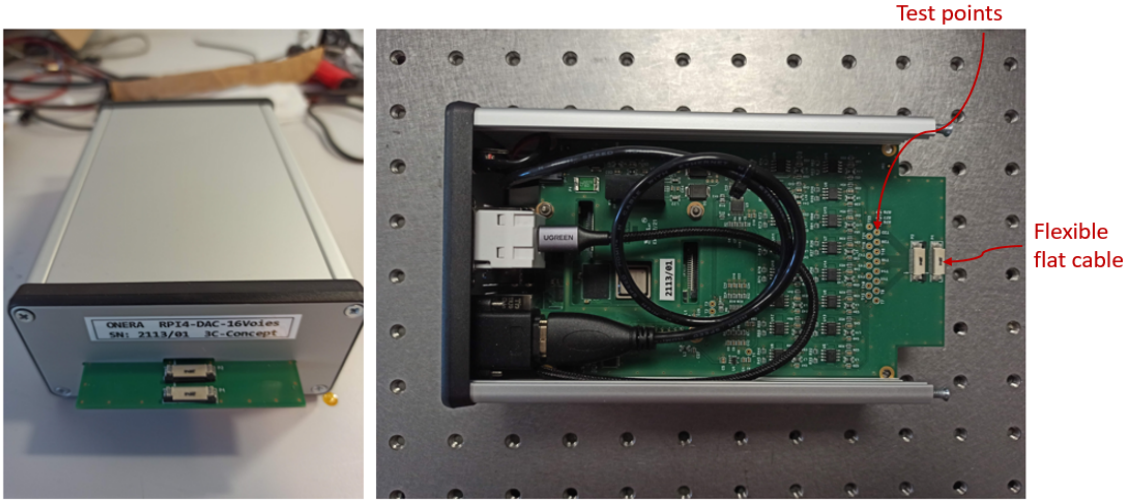

Figure 4.11: Digital-analog converter developed for the PIC control.

By applying a voltage step to a phase shifter, we move around a point of this signal. The signal on the left-hand part was obtained from the test points available on the DAC, as shown in Figure 4.11. In order to evaluate its characteristics, this signal is taken from the test points, shown in the Figure above. It should be noted that the signals are sent to the DAC through a Raspberry Pi4, directly integrated on the box shown in the Figure above.

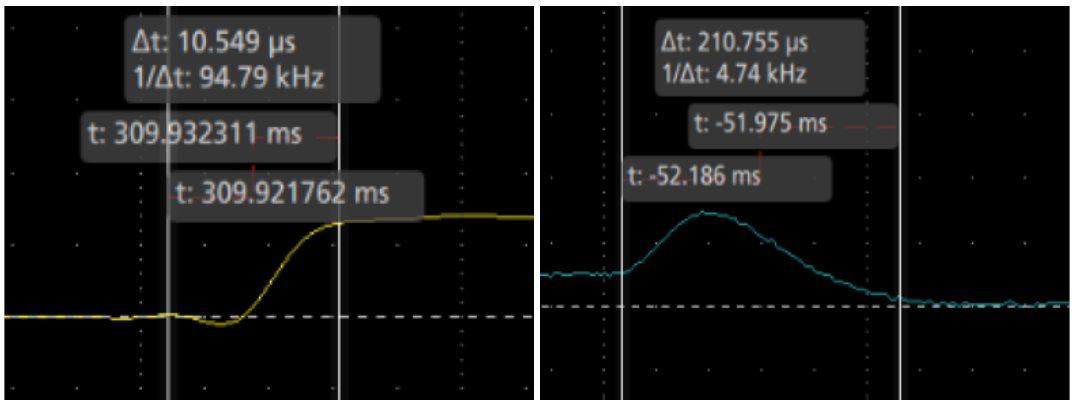

Figure 4.12: Voltage rising time for the application of a ΔV to a phase shifter from 0 to $20V$ (left), and rising time of a phase shifter after the application of the delivery voltage (right)

In this case we measure a voltage rising time in the order of tens of microseconds, $\Delta t \approx 10\ \mu s$, while a $\Delta t^{'}$ 10 times larger can be found for the PIC response time, applying a voltage equal to $\approx 20V$ from an initial value of zero. Therefore, the reported $\Delta t^{'}$ can be considered as a characteristic time response of a thermal phase shifter. Such applied voltage corresponds in an expected phase shift of $\frac{\alpha 20^2}{R} = 1.48\pi$. As one can see, the upper limit in operating frequency is given by the Raspberry (equipped with several Serial Peripheral Interface (SPI)), whose frequency is around $100\ kHz$.

4.3.4 2 π phase shift

In the following we evaluated the PS rising time ($\tau_{rise} \approx 100\mu s$) with two different approaches: as a periodic function, or square signal between $V_0(\varphi = 0)$ and $V_{2\pi}(\varphi = 2\pi)$, and as a step function of 2π.

Before considering the methods mentioned above, we assume that the phase response to a power step function can be described by an exponential term, such as:

$$\varphi(t) = \varphi_\infty(1 - e^{-t/\tau}) \tag{4.4}$$

where φ_∞ denotes the static response.
Assuming an identical amplitude on both channels, the interferometric signal of an active MZI in presence of a phase shift write:

$$\begin{aligned} s_i = |A + Ae^{j(\varphi-\varphi_0)}|^2 = \frac{|A|^2}{2}|e^{j(\varphi-\varphi_0)/2}(e^{-j(\varphi-\varphi_0)/2} + e^{j(\varphi-\varphi_0)/2})|^2 = \\ = \frac{|A|^2}{2}cos^2[(\varphi-\varphi_0)/2] \propto \frac{1}{2}[1 + cos(\varphi-\varphi_0)] \end{aligned} \tag{4.5}$$

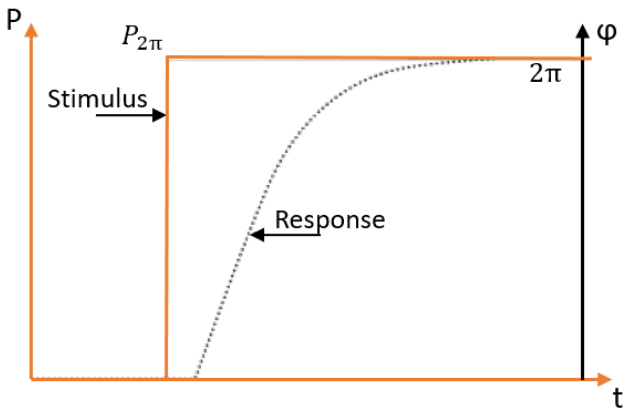

Figure 4.13: Response time of a phase shifter for a given applied power step function.

The first results on the 2π phase shift experienced by the PIC are presented. As already stated, the voltages applied to the circuit range from 0 to 30 V. Therefore, when a phase shift implies a voltages higher as well as lower to the maximum and minimum value respectively, a phase shift of the order of 2π appears, thus preserving the applied range of voltages. During this phase shift, the PIC will heat up again, with a non-negligible response time. In Figure 4.14, starting from a voltage of $0V$, a second voltage of $V_{2\pi} = 23.24V$ is applied (Section 4.3.2), which corresponds to a phase shift of 2π.

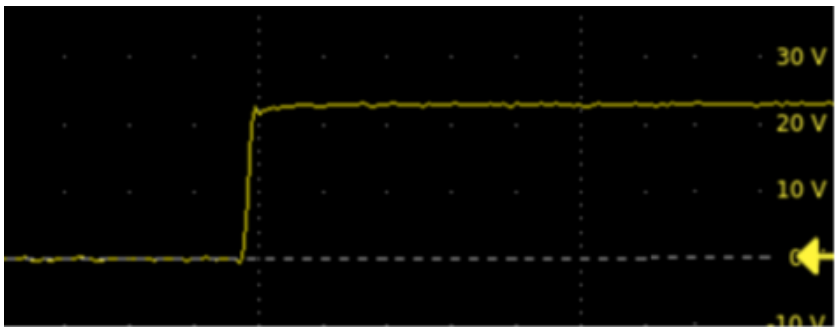

Figure 4.14: Applied voltage for a phase shift of 2π. $V_0 = 0V$ and $V_{2\pi} = 23.24V$.

The PIC response time is also reported in Figure 4.15, where the signal at the output of an arm of a MZI is presented. Following again a sinusoidal pattern, we measured the time between the application of the previous voltage, or phase shift, and the time when the circuit returns to its initial state (same value, shifted by 2π).

Another way to estimate the dynamics limited to the 2π phase shift is to study the behavior of the circuit considering a periodic signal.

Based on this, we first apply to the circuit the same square root variation reported in the top part of Figure 4.10. This applied signal leads to the previous reported sinusoidal interferometric response of the circuit, as well as when the PIC is in static regime. Note that the 2π phase shift happens at the maximum of the sinusoid. Increasing the frequency of the applied signal,

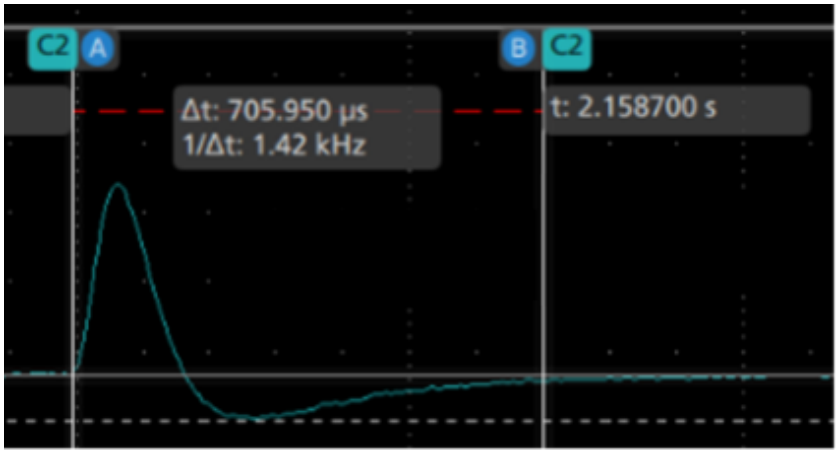

Figure 4.15: PIC response to a 2π phase shift.

the previous square root voltage changes its shape, thus becoming a square signal when the frequency reaches its maximum value. Such squared signal in turns corresponds to two voltage points which gives a phase shift of 2π, i.e.: the maximum and the minimum point of a sinusoidal signal. When the frequency is too high with respect to the response time of the PIC, the maximum cannot be reached, and the amplitude of the signal decreases. In both Figure 4.16 and Figure 4.17 the signal at the output of the PIC is reported, thus being able to evaluate its maximum frequency of $f_{max} \approx 1.7kHz$, with a rising time of $\tau_{rise} \approx 300\mu s$, for an attenuation of $\frac{15}{390} = 4\%$.

Considering now the first approach (periodic function between $V_0(\varphi = 0)$ and $V_{2\pi}(\varphi = 2\pi)$), the amplitude on s_i is reduced, achieving a value of $1 - s(\varepsilon)$, being ε a small initial offset on the previous phase response (as reported in both Figure 4.15 and Figure 4.16). As long as ε is small, it is possible to have a Taylor expansion of the signal s_i, near $s_i(0)$. Indeed, we now have that the previous interferometric signal writes: $\frac{1}{2}(1 + cos\varphi) = 1 - \frac{\varphi^2}{4}$.

Through the previous amplitude attenuation of 4%, we have $\frac{\varphi^2}{4} = 0.04$ and $\varphi = 0.16\, rad$. Finally, substituting such phase shift in Eq. 4.4 (with a maximum value of 2π), leads to: $\varphi(t) = 0.16 = 2\pi e^{-t/\tau}$, thus resulting in a rising time of $\tau = \left(ln(\frac{2\pi}{0.16})\right)^{-1} 300\ \mu s = 80\ \mu s$.

Following the second approach and considering a 2π step as input voltage signal, the interferometric signal of Figure 4.15 at $t = 0$ is found to be $s_i(t_0) \approx 0.25$. The Eq. 4.4 writes: $\varphi(\tau) = 2\pi(1 - \frac{1}{e})$, which in turns give: $\varphi(\tau) \approx 1.26\pi$. In this context, substituting again this phase shift in Eq. 4.5, we have: $s_i(t) = s_i(\varphi(t)) = \frac{1}{2}[1 + cos(\varphi(t) - \varphi_0)]$.

Indeed, assuming that the phase shift at $t = 0$ is $\varphi(t_0) = 0$, such signal s_i now writes: $s(\varphi(t_0)) = \frac{1}{2}(1 + cos(\varphi_0))$.

Through this formulation and assuming a rising signal, the phase shift $\varphi_0 = -0.71\pi$. Finally, the signal in Eq. 4.5 is given by: $s_i(\tau) = \frac{1}{2}(1 + cos(1.26 - 0.71)\pi) = 0.42$. The rising time can be found in Figure 4.15 when the signal reach the previous value of $s_i = 0.42$, thus having $\tau = 117\ \mu s$.

On the other hand, characteristic rising time of thermo-optic phase shifters on SOI platform are reported in literature by Jacques and al., ranging from $3\mu s \leqslant \tau_{rise} \leqslant 30\mu s$ [Jacques et al. (2019)].

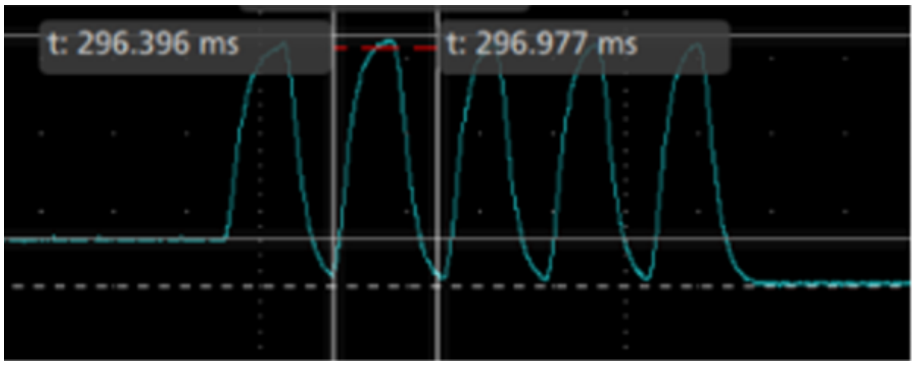

Figure 4.16: Output signal of an active MZI after the application of a squared signal as the one shown in Figure 4.14

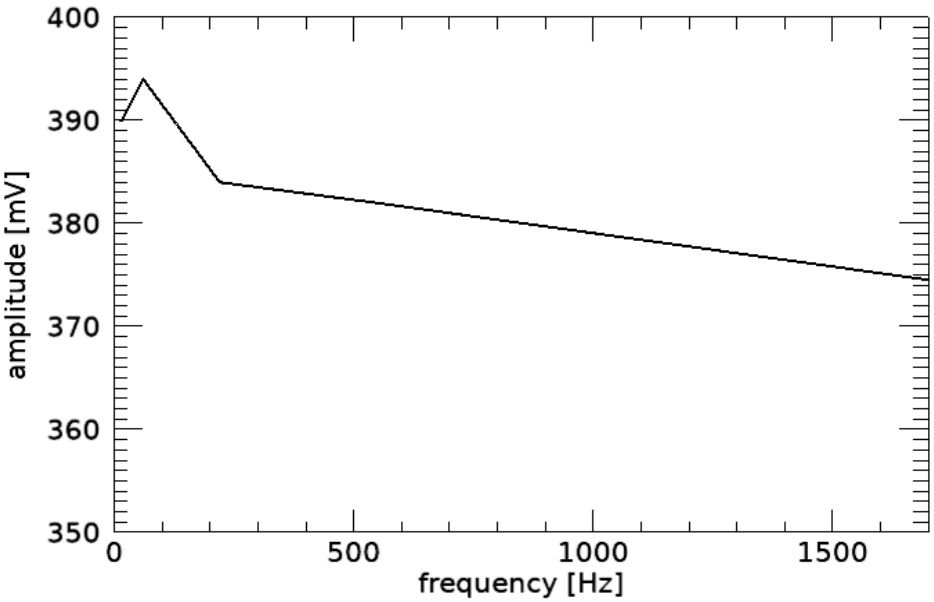

Figure 4.17: Amplitude of the output signal of an active MZI, function of the applied signal frequency.

4.3.5 Coupling effect

In order to measure the presence of a thermal coupling on the Si-based PIC, we evaluated the performance of the three-channel combiner, shown in Figure 4.18. In such circuit, the cascade of two MZI is reported, with a delay line placed at the input of one MZI in order to ensure the balance of optical paths between In_1, In_2, and In_3.

We apply a voltage on the first phase shifter of the second MZI, denoted by $\delta\varphi_3$. As one can see in Figure 4.19, both output 1 (blue line) and output 2 (red line) are concerned by the application of such voltage, even though there is no signal applied to the input of the first MZI. Given the considerable losses present in such circuits, heating of the second MZI may eventually lead to signal dissipation, such as that seen in these figures.

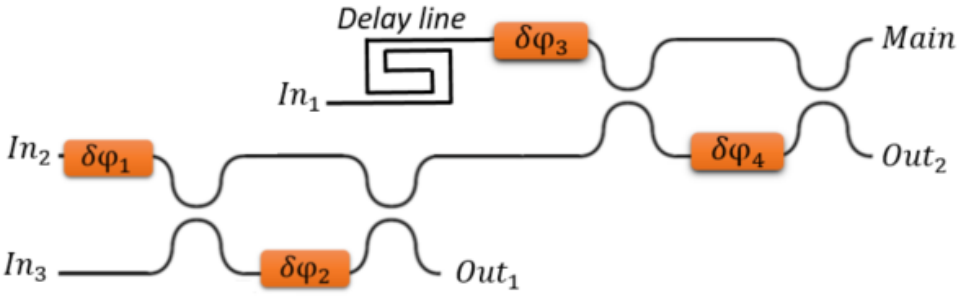

Figure 4.18: Principle of the 3-channel combiner developed by Cailabs.

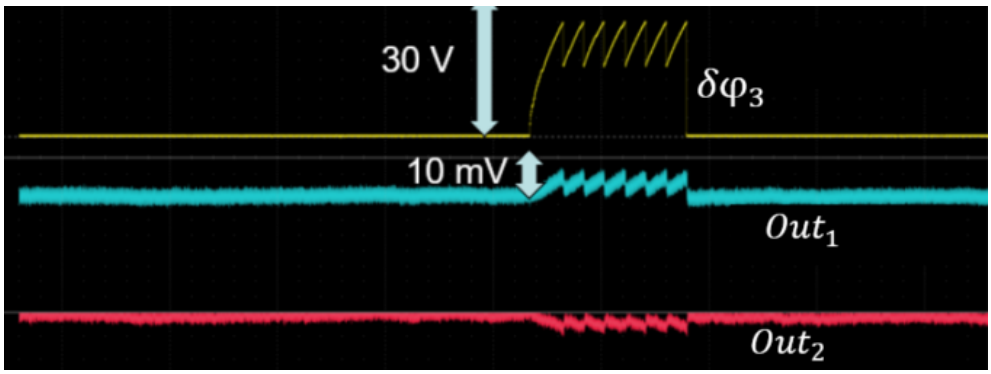

Figure 4.19: Coupling effects on a 3-channel combiner.

It is worth noting that an amplitude variation of about 10% of the maximum signal value is measured without any signal at the input of the circuit. Such signal variation is mainly due to thermal variations and vibrations to which the optical fibers are subjected, thus also causing a difference in the optical path experienced by the SMFs. In this way, even when no signal is applied, a drift in the output signal can be observed.

4.3.6 Conclusion on SiN-based PIC

In this last section, we evaluated the performance of a SiN-based photonic integrated circuit, as the one developed by Cailabs. The time response of the PIC to 2π phase shift as well as coupling effects on the PIC are studied. Indeed, we found a relatively slow time response compared to performance reported in the literature, with a rising time of $\tau_{rise} \approx 100\ \mu s$ when a 2π phase shift is applied.

It is also worth noting that characteristics rising time of the order of tens of microseconds are shown in literature, as reported by Jacques and al. [Jacques et al. (2019)], thus having $3\mu s \leqslant \tau_{rise} \leqslant 30\mu s$. Finally, with regard to coupling effects, the appearance of parasitic signals has been noted, which are likely to disrupt circuit control.

4.3.7 Signal detection analysis

In this section, we present the analysis of the measurement noise present in our experimental setup. The total available flux, as reported on the link budget, is $P = -45\,dBm$, or $P = 3.16 \cdot 10^{-8}\ W \approx 3.8 \cdot 10^{11}\ ph/s$. Even assuming a small amount of useful flux, for example 10% of the total received flux, we have $i_{signal} \approx 3.8 \cdot 10^{10}\ ph/s$.

Indeed, an important parameter characterizing our photodiodes is based on the Noise Equivalent Power (NEP). Such quantity represents the optical input power which produces an output power identical with the noise power, such that the signal-to-noise ratio is equal to 1. In this context, considering a Thorlabs InGaAs high speed photodiode (FGA01FC), a $NEP = 4.5 \times 10^{-15}\ W/\sqrt{Hz}$ is taken into account. Considering its reponsivity ($\approx 1.003\ A/W$), such NEP can be also expressed in $[A/\sqrt{Hz}]$.

Different sources of noise can be compared to the previous NEP: the thermal noise is firstly considered, thus having $i_{th} = \sqrt{\frac{4KT}{R}} \approx 1.3 \cdot 10^{-13}\ A/\sqrt{Hz}$. Furthermore, considering a dark current of $i_d = 0.05\ nA$, the noise associated with such current can be expressed as: $i_d = \sqrt{2qi_d} \approx 5 \cdot 10^{-15}\ A/\sqrt{Hz}$. As we can see, shot noise is of the same order of magnitude as NEP, while thermal noise is predominant, thus constituting the major limiting factor in our case. Indeed, a signal-to-noise ratio of ≈ 30 is obtained between the thermal noise and the NEP, i.e. a ≈ 1000 ratio in variance. As a consequence, the readout electronics for optical detectors are too noisy in this case, and a transimpedance amplifier is under development as a solution to this problem. With such amplifier and by cooling the circuit, the NEP value can be reached.

In addition, the previous NEP can also be expressed in photons per second, such as:

$$NEP = \frac{4.5 \cdot 10^{-15}}{1.3 \cdot 10^{-19}} \approx 3.4 \cdot 10^{4} \Big[\frac{ph}{s} \cdot \frac{1}{\sqrt{Hz}}\Big]$$

where $1ph/s = h\nu/s$. In this context, considering a bandwidth of $\Delta f = 10\ kHz$, the noise on our photodiodes is about $n_{PD} = NEP \cdot \sqrt{\Delta f} \approx 3.4 \cdot 10^4 \cdot 100 \approx 3.4 \cdot 10^6 [ph/s]$, i.e. considering a quantum efficiency of $\eta = 0.82$ and an exposure of $10^{-4}s$, we have ≈ 300 photoelectrons on our photodiodes. By comparing this NEP value with the noise associated with our input signal ($i_n = \sqrt{2q^2 i_{signal}} \approx 10^{-14}\ A/\sqrt{Hz}$) we can see that this value is still good but remains a limit for our case study.

From this analysis we can see that, as long as the losses of the integrated circuit remain high, as reported by Billault et al. [Billault et al. (2021)], an alternative solution for correcting the effects of atmospheric turbulence will have to be found. For this reason, in the following Chapter a sensorless approach is considered, relying on a deformable mirror and the multi-outputs of a spatial-division multiplexing device.

4.4 Conclusion

We presented in this Chapter preliminary specifications of a photonic integrated circuit for the mitigation of atmospheric turbulence effects. We introduced the design and fabrication of a lithium-niobate based PIC, realized in collaboration with the IPAG and Femto-ST research laboratories. The BeamPROP software allow us to define and simulate the correct parameters for such device and its basic elements, namely directional coupler and phase shifter. Moreover, a first developed architecture of a 8-channel device with its lithography mask is reported during this Chapter. However, due to time constraints, the encapsulation phase of this component began in October 2021. First characterizations of such PIC, including the time response of a given phase shifter and the half-wave voltage have been performed in the latter part of this thesis. An insertion loss value of about $12\,dB$ and an half-wave voltage value of about $V_\pi \approx 13\,V$ have been found, and are in agreement with what is theoretically predicted.

In the last part of this Chapter, a SiN-based PIC has been characterized in terms of time response and coupling effects, thus evaluating the performance of a single active MZI. This work was carried out in the context of two MSc internship at the ONERA, which saw Yann Lucas and François Leroux integrate the optical bench, while evaluating the performance of the PIC. Indeed, a relatively slow time response of about $100\,\mu s$ has been evaluated and compared to those found in literature, when a 2π phase shift is applied to a given phase shifter [Jacques et al. (2019)]. In this context, alternative methods must be found to handle this phase shifts. The presence of a coupling between different MZIs has been also observed, which adds to the already large losses in the circuit. Further studies on its behavior are needed to assess its performance in dynamic conditions, as well as its use in real-life conditions.

Through this study, a way forward has been mapped out on the specifications to be assigned for the development of an integrated circuit in a satellite-to-ground optical telecommunication scenario. Once again, there is no any suited technology for such an application, and different solutions still need to be analyzed in detail, following the parameters reported in this Chapter. As we already stated, this is only a first rough specification of a PIC prototype used as combiner block in a coherent combining system for the mitigation of atmospheric turbulence effects. More accurate analysis on the choice of the control algorithm and further tests on dynamic perturbations are planned in the framework of Yann Lucas's doctoral thesis, together with the development of a photonic integrated circuit with more than 8 channels while considering alternative material platforms for its construction, such as the InP already described in the last part of Chapter 1.

Conclusion

In the context of high-speed free-space optical communications, this work dealt with a satellite-to-ground optical downlink at 10° elevation. Among the main impairments that affects such links, atmospheric turbulence effects highly degrade the coupling efficiency of the incoming beam into a single-mode fiber. In this framework, a new approach, called coherent combining, represents a new solution that circumvents the main disadvantages of the most commonly used techniques for turbulence mitigation, such as AO. Within this approach, the incoming disrupted beam is firstly decomposed into a set of propagation modes associated with different waveguides, and subsequently recombined through a photonic integrated circuit. This thesis is dedicated to the study of coherent recombination for the mitigation of atmospheric turbulence effects. In particular, this work goes from the definition of the use case to the technology of the photonic circuit.

For this purpose, the first part of this thesis concerned the study of the atmospheric turbulence effects when coupling a beam in free-space with a SDM device, i.e. with a set of propagation modes. Particularly, I established an analytical approach for the average coupling efficiency of an optical perturbed wave and a set of Hermite-Gaussian modes. I derived in this case the optimum beam size for different set of modes. Furthermore, in presence of atmospheric turbulence, we presented the coupling as function of different turbulence conditions and number of modes. Such turbulence conditions are represented by the ratio between the telescope pupil diameter and the Fried parameter, D/r_0. As expected, the normalized coupling efficiency mainly depends on D/Nr_0, in which N^2 denotes the total number of modes. The performance found in this case are in good agreement with the instantaneous Strehl ratio obtained with the adaptive optics, even though a double number of degrees of freedom need to be considered due to the complex nature of the Hermite-Gaussian modes, with respect to the AO one. A tip-tilt correction has been also employed, and compared to the optimization derived with the eigenmodes approach. This study allows us to show that the contribution of tip-tilt correction is much more significant than modal optimization.

In this context, a link-budget has been closed for a realistic scenario of a LEO-to-ground link at 10° elevation. Through this analysis, I derived the coupling efficiency fluctuations as function of the number of modes. A Monte-Carlo approach confirm the same results obtained in the first part of Chapter 2. The cumulative distribution functions is also demonstrated to be function of the considered number of modes rather than the applied correction (phase and amplitude, or phase-only correction). Regarding the scenario of interest, we have seen how a telescope diameter of $D = 25\ cm$ does not mitigate correctly the fluctuations of the received beam, and a more large diameter of $D = 50\ cm$ has been analyzed.

Moreover, the temporal analysis is detailed, studying the performance of the PIC as function of the phase shift experienced. Moreover, the power spectral density has been presented when a 2π phase shift is applied to the PIC, highlighting a flat spectrum until tens of KHz. In order to accelerate the control loop, and also due to the high losses still present on the PIC development, a new sensorless AO approach is proposed. In this particular approach a SDM device is used for the mode decomposition of the collected beam. A multi-detector based control algorithm is proposed in this case in order to optimize the signal metric, increasing the convergence time of this method with respect to standard sensorless AO approaches.

For this purpose, the architecture of the numerical simulations developed is introduced. A proposal of a modulation capable to create an invertible matrix has been detailed. It is composed by a defocus and a tip-tilt aberration. The dynamic of this method represent another important parameter for the performance definition, and has been derived as function of the amplitude of the applied perturbation. In this context, two different perturbations has been considered: a tip-tilt and a defocus aberration. Applying both perturbations previously mentioned, I also studied the estimate of the phase on the DM. In the last part, I describe our laboratory bench, as well as the first results comparing the SPGD method with our multi-output approach. It is noteworthy that only 8 outputs of the MPLC device are equipped with photodiodes, and 8 modes of deformation are controlled onto the deformable mirror. With respect to the SPGD algorithm, for which 15 modulations are required to optimize the signal metric, only one modulation is needed when considering our multi-output approach, thus showing the interest of such an approach. As evidence of this interest, Yann Lucas is currently developing new control laws for this approach in the context of his doctoral thesis.

Finally, in the last part I also introduced the design of an 8-channel $LiNbO_3$ based PIC performed in collaboration with N. Courjal and G. Martin. The main elementary components of this device are detailed, along with their implementation constraints. Based on this analysis a correct geometry has been defined are presented in Chapter 3. The encapsulation of the chip is currently in progress. Furthermore, I evaluated the performance, in terms of time response and coupling effects, of a SiN based PIC developed by Cailabs company. Indeed, I found a slow time response ($\tau \approx 100\ \mu s$) with respect to the values reported in literature ($3\ \mu s \leqslant \tau \leqslant 30\ \mu s$), when a 2π phase shift is applied to the PIC [Jacques et al. (2019)]. Coupling effects has been also observed, adding additional losses to the circuit.

Perspectives

Despite the various results achieved during this work, several limitations arise which require further improvement. In this respect, the main arguments requiring further investigation are summarized below:

- **The impact of the temporal error and the noise measurement on the PIC specification**

  We have considered in this study the coupling efficiency of the coherent combining approach, composed by the MPLC + PIC, as limited only by the number of modes used for the decomposition of the received disrupted beam. We have called such limitation spatial error. On the other hand, having a large signal available, the noise measurement was considered negligible. Furthermore, since the temporal error depends on the control law employed, in our analysis has not been studied. It would be interesting to be able to observe more closely the behavior of the system with regard to these errors, addressing these points both theoretically and by developing end-to-end simulations in order to specify the required bandwidth, and thus the specifications of a PIC. This point will be addressed in Yann Lucas' thesis, which began in October 2021.

- Concerning the materials for the PIC development, **the study of new material platforms, increasing the number of channels of the circuit**

  Through the study conducted during this thesis, the specifications to be assigned for the development of an integrated circuit in a satellite-to-ground optical telecommunications scenario were defined. However, there is no any suited technology for such an application, and different solutions still need to be analyzed in detail. Further analysis may be planned in order to consider alternative material platforms for the PIC construction, also increasing the total number of channel at the input/output of this circuit. Examples of these activities involve 32-channel circuits manufactured using the silicon thick technology of VTT as part of the european Actphast project, in which ONERA is involved alongside VTT and the University of Pisa.

- **Implementation of a control law in an RTC** in order to have a system capable of being used in the on-sky demonstration

  Finally, in the last part of this thesis we have presented some experimental evaluation on the PIC performance. Nevertheless, a dedicated control law needs to be specified and implemented on a RTC in order to upgrade the device for on-sky demonstration. The objective is to carry out a feasibility study of a system with a dozen correction modes.

List of publications

Peer-reviewed article

L. Rinaldi, V. Michau, M. Boutillier, "Decomposition of turbulence perturbed field over a set of propagation modes", Optics Express (submitted).

Conference proceedings

L. Rinaldi, V. Michau, N. Védrenne, C. Petit, L. Mugnier, C. Lim, J. Montri, L. Paillier, M. Boutillier, "Sensorless adaptive optics for optical communications", Free-Space Laser Communications XXXIII, volume 11678, pages 164–169. SPIE. Photonics West, San Francisco, 6-11 March 2021.

L. Rinaldi, V. Michau, M. Boutillier, "Coupling of atmospheric perturbed optical beams with guided modes of propagation", Workshop COAT, Châtillon, December 2019.

Y. Lucas, L. Rinaldi, V. Michau, C. Petit, S. Meimon, J. Montri, L. Mugnier, N. Védrenne, T. Fusco, C. Lim, M. Boutillier, "Sensorless adaptive optics with wave modal demultiplexer", Workshop Wavefront Sensing in the VLT/ELT era VII, December 2021.

Bibliography

Bibliography

(2021). Airbus & tno, https://www.airbus.com/newsroom/press-releases/en/2021/04/airbus-and-tno-to-develop-aircraft-laser-communication-terminal.html.

Abramochkin, E. and Volostnikov, V. (1991). Beam transformations and nontransformed beams. *Optics Communications*, 83(1):123–135.

Agrawal, G. P. (2012). Fiber-optic communication systems. *John Wiley Sons*, 222.

Alonso, A., Reyes Garcia-Talavera, M., and Sodnik, Z. (2004). Performance of satellite-to-ground communications link between ARTEMIS and the Optical Ground Station. *Proceedings of SPIE - The International Society for Optical Engineering*.

Anzalchi, J., Wong, J., Verges, T., Navasquillo, O., Mengual, T., Piqueras, M. A., Prevost, E., Ravel, K., Parsons, N., Enrico, M., Bauwelink, J., Vanhoecke, M., Vannucci, A., and Tienforti, M. (2019). Towards demonstration of photonic payload for telecom satellites. In *International Conference on Space Optics — ICSO 2018*, volume 11180, page 111804T. International Society for Optics and Photonics.

Arafin, S. and Coldren, L. A. (2018). Advanced InP Photonic Integrated Circuits for Communication and Sensing. *IEEE Journal of Selected Topics in Quantum Electronics*, 24(1):1–12.

Arikawa, M. and Ito, T. (2018). Performance of mode diversity reception of a polarization-division-multiplexed signal for free-space optical communication under atmospheric turbulence. *Opt. Express, OE*, 26(22):28263–28276.

Arimoto, Y., Toyoshima, M., Toyoda, M., Takahashi, T., Shikatani, M., and Araki, K. (1995). Preliminary result on laser communication experiment using Engineering Test Satellite-VI (ETS-VI). In *Free-Space Laser Communication Technologies VII*, volume 2381, pages 151–158. International Society for Optics and Photonics.

Artaud, G., Benammar, B., Jouglet, D., Canuet, L., and Lacan, J. (2019). Impact of molecular absorption on the design of free space optical communications. In *International Conference on Space Optics — ICSO 2018*, volume 11180, pages 544–554. SPIE.

Artaud, G., Issler, J.-L., Vedrenne, N., Phung, D.-H., Toyoshima, M., Robert, C., Petit, C., Samain, E., Maurice, N., and Kolev, D. (2017). Laser communication experiments between Sota and Meo optical ground station. page 273.

Aveline, M., Sotom, M., Barbaste, R., Benazet, B., Kernec, A. L., Magnaval, J., Ginestet, P., Navasquillo, O., and Piqueras, M. A. (2017). Reconfigurable microwave photonic repeater for broadband telecom missions: concepts and technologies. In *International Conference on Space Optics — ICSO 2014*, volume 10563, page 105633M. International Society for Optics and Photonics.

Babcock, H. W. (1953). The possibility of compensating astronomical seeing. *The Publications of the Astronomical Society of the Pacific, 65:229*.

Bade, S., Denolle, B., Trunet, G., Riguet, N., Jian, P., Pinel, O., and Labroille, G. (2018). Fabrication and Characterization of a Mode-selective 45-Mode Spatial Multiplexer based on Multi-Plane Light Conversion. In *Optical Fiber Communication Conference Postdeadline Papers (2018), paper Th4B.3*, page Th4B.3. Optical Society of America.

Baets, R., Subramanian, A. Z., Clemmen, S., Kuyken, B., Bienstman, P., Le Thomas, N., Roelkens, G., Van Thourhout, D., Helin, P., and Severi, S. (2016). Silicon photonics: Silicon nitride versus silicon-on-insulator. In *2016 Optical Fiber Communications Conference and Exhibition (OFC)*, pages 1–3.

Barchers, J. D., Fried, D. L., and Link, D. J. (2002). Evaluation of the performance of Hartmann sensors in strong scintillation. *Applied Optics*, 41(6):1012–1021.

Barchers, J. D., Fried, D. L., Link, D. J., Tyler, G. A., Moretti, W., Brennan, T. J., and Fugate, R. Q. (2003). Performance of wavefront sensors in strong scintillation. In *Adaptive Optical System Technologies II*, volume 4839, pages 217–227. International Society for Optics and Photonics.

Billaud, A., Allioux, D., Laurenchet, N., Jian, P., Pinel, O., and Labroille, G. (2020). Pointing Error Compensation For Inter-Satellite Communication Using Multi-Plane Light Conversion Spatial Demultiplexer. *arXiv:2012.10247*.

Billaud, A., Gomez, F., Allioux, D., Laurenchet, N., Jian, P., Pinel, O., and Labroille, G. (2019). Optimal Coherent Beam Combining Based on Multi-Plane Light Conversion for High Throughput Optical Feeder Links. In *2019 IEEE International Conference on Space Optical Systems and Applications (ICSOS)*, pages 1–5.

Billault, V., Bourderionnet, J., Mazellier, J.-P., Leviandier, L., Feneyrou, P., Maho, A., Sotom, M., Normandin, X., Lonjaret, H., and Brignon, A. (2021). Free space optical communication receiver based on a spatial demultiplexer and a photonic integrated coherent combining circuit. *Optics Express*.

Birks, T. A., Gris-Sánchez, I., Yerolatsitis, S., Leon-Saval, S. G., and Thomson, R. R. (2015). The photonic lantern. *Advances in Optics and Photonics*, 7(2):107–167.

Boes, A., Corcoran, B., Chang, L., Bowers, J., and Mitchell, A. (2018). Status and Potential of Lithium Niobate on Insulator (LNOI) for Photonic Integrated Circuits. *Laser & Photonics Reviews*, 12(4):1700256.

Bogaerts, W. and Chrostowski, L. (2018). Silicon Photonics Circuit Design: Methods, Tools and Challenges. *Laser & Photonics Reviews*, 12(4):1700237.

Bogaerts, W., Fiers, M., and Dumon, P. (2014). Design Challenges in Silicon Photonics. *IEEE Journal of Selected Topics in Quantum Electronics*, 20(4):1–8.

Bonnefois, A. M., Conan, J.-M., Petit, C., Lim, C. B., Michau, V., Meimon, S., Perrault, P., Mendez, F., Fleury, B., Montri, J., and Védrenne, N. (2019). Adaptive optics pre-compensation for GEO feeder links: the FEEDELIO experiment. In *International Conference on Space Optics — ICSO 2018*, volume 11180, page 111802C. International Society for Optics and Photonics.

Booth, M. J. (2006). Wave front sensor-less adaptive optics: a model-based approach using sphere packings. *Optics Express*, 14(4):1339–1352.

Bourderionnet, J., Bellanger, C., Primot, J., and Brignon, A. (2011). Collective coherent phase combining of 64 fibers. *Optics Express*, 19(18):17053–17058.

Brignon, A. (2013). Coherent Laser Beam Combining | Wiley Online Books.

Bruesselbach, H., Minden, M. L., Wang, S., Jones, D. C., and Mangir, M. S. (2004). A coherent fiber-array-based laser link for atmospheric aberration mitigation and power scaling. In *Free-Space Laser Communication Technologies XVI*, volume 5338, pages 90–101. International Society for Optics and Photonics.

Brüning, R., Zhang, Y., McLaren, M., Duparré, M., and Forbes, A. (2015). Overlap relation between free-space Laguerre Gaussian modes and step-index fiber modes. *JOSA A*, 32(9):1678–1682.

Buckreuss, S. and Roth, A. (2008). Status Report on the TerraSAR-X Mission. volume 2, pages 1–4.

Bufton, J. L. (1973). Comparison of Vertical Profile Turbulence Structure with Stellar Observations. *Applied Optics*, 12(8):1785–1793.

Calvo, R. M., Allioux, D., Reeves, A., Billaud, A., Poliak, J., Pinel, O., Kelemu, H. F., Labroille, G., and Richerzhagen, M. (2020). Alternative passive fiber coupling system based on multiplane light conversion for satellite-to-ground communications. In *Free-Space Laser Communications XXXII*, volume 11272, page 112720Q. International Society for Optics and Photonics.

Calvo, R. M., Becker, P., Giggenbach, D., Moll, F., Schwarzer, M., Hinz, M., and Sodnik, Z. (2014). Transmitter diversity verification on ARTEMIS geostationary satellite. In *Free-Space Laser Communication and Atmospheric Propagation XXVI*, volume 8971, pages 24–37. SPIE.

Calvo, R. M., Poliak, J., Surof, J., Reeves, A., Richerzhagen, M., Kelemu, H. F., Barrios, R., Carrizo, C., Wolf, R., Rein, F., Dochhan, A., Saucke, K., and Luetke, W. (2019). Optical technologies for very high throughput satellite communications. In *Free-Space Laser Communications XXXI*, volume 10910, pages 189–204. SPIE.

Carrizo, C. E., Calvo, R. M., and Belmonte, A. (2018). Intensity-based adaptive optics with sequential optimization for laser communications. *Optics Express*, 26(13):16044–16053.

Chang, H., Chang, Q., Xi, J., Hou, T., Su, R., Su, R., Ma, P., Wu, J., Li, C., Jiang, M., Ma, Y., Zhou, P., and Zhou, P. (2020). First experimental demonstration of coherent beam combining of more than 100 beams. *Photonics Research*, 8(12):1943–1948.

Choudhury, D., McNicholl, D. K., Repetti, A., Gris-Sánchez, I., Li, S., Phillips, D. B., Whyte, G., Birks, T. A., Wiaux, Y., and Thomson, R. R. (2020). Computational optical imaging with a photonic lantern. *Nature Communications*, 11(1):5217.

Corrigan, M., Harris, R. J., Thomson, R. R., MacLachlan, D. G., Allington-Smith, J., Myers, R., and Morris, T. (2016). Wavefront sensing using a photonic lantern. 9909:1848–1855.

Courjal, N., Bernal, M.-P., Caspar, A., Ulliac, G., Bassignot, F., Gauthier-Manuel, L., and Suarez, M. (2018). Lithium niobate optical waveguides and microwaveguides. *Emerging Waveguide Technology (IntechOpen)*.

Cruz-Delgado, D., Alvarado-Zacarias, J. C., Cooper, M. A., Wittek, S., Dobias, C., Martinez-Mercado, J., Antonio-Lopez, J. E., Fontaine, N. K., and Amezcua-Correa, R. (2021). Photonic lantern tip/tilt detector for adaptive optics systems. *Optics Letters*, 46(13):3292–3295.

Cvetojevic, N. (2020). Starlight on a chip: astrophotonic technologies for interferometry. In *Optical and Infrared Interferometry and Imaging VII*, volume 11446, page 1144616. International Society for Optics and Photonics.

Davenport, J. J., Diab, M., Deka, P. J., Tripathi, A., Madhav, K., and Roth, M. M. (2021). Photonic lanterns: a practical guide to filament tapering. *Optical Materials Express*, 11(8):2639–2649.

Diab, M., Dinkelaker, A. N., Davenport, J., Madhav, K., and Roth, M. M. (2020). Starlight coupling through atmospheric turbulence into few-mode fibres and photonic lanterns in the presence of partial adaptive optics correction. *Monthly Notices of the Royal Astronomical Society*, 501(2):1557–1567.

Diab, M. and Minardi, S. (2019). Modal analysis using photonic lanterns coupled to arrays of waveguides. *Optics Letters*, 44(7):1718–1721.

Dikmelik, Y. and Davidson, F. M. (2005). Fiber-coupling efficiency for free-space optical communication through atmospheric turbulence. *Applied Optics*, 44(23).

Doerr, C. R. (2015). Silicon photonic integration in telecommunications. *Frontiers in Physics*.

Essiambre, R.-J. and Tkach, R. W. (2012). Capacity Trends and Limits of Optical Communication Networks. *Proceedings of the IEEE*, 100(5):1035–1055.

Fante, R. (1975). Electromagnetic beam propagation in turbulent media. *Proc. of the IEEE, 63(12):1669-1692*.

Fatemi, R., Abiri, B., Khachaturian, A., and Hajimiri, A. (2018). High sensitivity active flat optics optical phased array receiver with a two-dimensional aperture. *Optics Express*, 26(23):29983.

Fienup, J. R. (1982). Phase retrieval algorithms: a comparison. *Applied Optics*, 21(15):2758–2769.

Flatté, S. M., Wang, G.-Y., and Martin, J. (1993). Irradiance variance of optical waves through atmospheric turbulence by numerical simulation and comparison with experiment. *JOSA A*, 10(11):2363–2370.

Fried, D. L. (1966). Optical resolution through a randomly inhomogeneous medium for very long and very short exposures. *J. Opt. Soc. Am.*, 56(10):1372–1379.

Friis, H. (1946). A Note on a Simple Transmission Formula. *Proceedings of the IRE*, 34(5):254–256.

Fusco, T. and Conan, J.-M. (2004). On- and off-axis statistical behavior of adaptive-optics-corrected short-exposure Strehl ratio. *J. Opt. Soc. Am. A, JOSAA*, 21(7):1277–1289.

Geisler, D. J., Yarnall, T. M., Stevens, M. L., Schieler, C. M., Robinson, B. S., and Hamilton, S. A. (2016). Multi-aperture digital coherent combining for free-space optical communication receivers. *Optics Express*, 24(12):12661–12671.

Giggenbach, D., Wilkerson, B. L., Henniger, H., and Perlot, N. (2006). Wavelength-diversity transmission for fading mitigation in the atmospheric optical communication channel. In *Free-Space Laser Communications VI*, volume 6304, page 63041H. International Society for Optics and Photonics.

Gregory, M., Heine, F., Kämpfner, H., Meyer, R., Fields, R., and Lunde, C. (2017). TESAT laser communication terminal performance results on 5.6Gbit coherent inter satellite and satellite to ground links. In *International Conference on Space Optics — ICSO 2010*, volume 10565, page 105651F. International Society for Optics and Photonics.

Gregory, M., Troendle, D., Muehlnikel, G., Heine, F., Meyer, R., Lutzer, M., and Czichy, R. (2013). Three years coherent space to ground links: performance results and outlook for the optical ground station equipped with adaptive optics. In *Free-Space Laser Communication and Atmospheric Propagation XXV*, volume 8610, pages 17–29. SPIE.

Harris, N. C., Ma, Y., Mower, J., Baehr-Jones, T., Englund, D., Hochberg, M., and Galland, C. (2014). Efficient, Compact and Low Loss Thermo-Optic Phase Shifter in Silicon. *Optics Express*, 22(9):10487.

Hauschildt, H., Elia, C., Moeller, H. L., and Schmitt, D. (2017). ScyLight — ESA's secure and laser communication technology framework for SatCom. In *2017 IEEE International Conference on Space Optical Systems and Applications (ICSOS)*, pages 250–254.

He, M., Xu, M., Ren, Y., Jian, J., Ruan, Z., Xu, Y., Gao, S., Sun, S., Wen, X., Zhou, L., Liu, L., Guo, C., Chen, H., Yu, S., Liu, L., and Cai, X. (2019). High-performance hybrid silicon and lithium niobate Mach–Zehnder modulators for 100 Gbit s-1 and beyond. *Nature Photonics*.

Heck, M. J. R. (2017). Highly integrated optical phased arrays: photonic integrated circuits for optical beam shaping and beam steering. *Nanophotonics*, 6(1):93–107.

Heine, F., Pimentel, P. M., Rochow, C., Saucke, K., Tröndle, D., Lutzer, M., Meyer, R., Bischl, H., and Matuz, B. (2018). The European data relay system and Alphasat to T-AOGS space to ground links, status, and achievements in 2017. In *Free-Space Laser Communication and Atmospheric Propagation XXX*, volume 10524, page 105240T. International Society for Optics and Photonics.

Hemmati, H. (2009). Near-earth laser communications - chapter 2. *CRC press.*

Hiraki, T., Aihara, T., Fujii, T., Takeda, K., Kakitsuka, T., Tsuchizawa, T., and Matsuo, S. (2020). Membrane InGaAsP Mach–Zehnder Modulator Integrated With Optical Amplifier on Si Platform. *Journal of Lightwave Technology*, 38(11):3030–3036.

Hosseinnia, A. H., Atabaki, A. H., Eftekhar, A. A., and Adibi, A. (2015). High-quality silicon on silicon nitride integrated optical platform with an octave-spanning adiabatic interlayer coupler. *Optics Express*, 23(23):30297–30307.

Hu, J. and Beaulieu, N. (2005). Accurate simple closed-form approximations to Rayleigh sum distributions and densities. *IEEE Communications Letters*, 9(2):109–111.

Jacques, M., Samani, A., El-Fiky, E., Patel, D., Xing, Z., and Plant, D. V. (2019). Optimization of thermo-optic phase-shifter design and mitigation of thermal crosstalk on the SOI platform. *Optics Express*, 27(8):10456–10471.

Jahid, A., Alsharif, M. H., and Hall, T. J. (2020). A Contemporary Survey on Free Space Optical Communication: Potential, Technical Challenges, Recent Advances and Research Direction. *arXiv:2012.00155 [cs, eess, math]*. arXiv: 2012.00155.

Jono, T., Takayama, Y., Kura, N., Ohinata, K., Koyama, Y., Shiratama, K., Sodnik, Z., Demelenne, B., Bird, A., and Arai, K. (2006). OICETS on-orbit laser communication experiments. In *Free-Space Laser Communication Technologies XVIII*, volume 6105, page 610503. International Society for Optics and Photonics.

Kaushal, H. and Kaddoum, G. (2017). Optical Communication in Space: Challenges and Mitigation Techniques. *IEEE Communications Surveys Tutorials*, 19(1):57–96.

Kernec, A. L., Canuet, L., Maho, A., Sotom, M., Matter, D., and Francou, L. (2019). Optical feeder links for high throughput satellites and the H2020 VERTIGO project.

Khalighi, M. A. (2021). Survey on Free Space Optical Communication: A Communication Theory Perspective | IEEE Journals & Magazine | IEEE Xplore.

Khalighi, M.-A., Schwartz, N., Aitamer, N., and Bourennane, S. (2009). Fading Reduction by Aperture Averaging and Spatial Diversity in Optical Wireless Systems. *Journal of Optical Communications and Networking*, 1(6):580–593.

Khurgin, J. B., Stievater, T. H., Pruessner, M. W., and Rabinovich, W. S. (2015). On the origin of the second-order nonlinearity in strained Si–SiN structures. *JOSA B*, 32(12):2494–2499.

Kiasaleh, K. (2017). Wavelength diversity for PPM photon channels subject to atmospheric turbulence. In *2017 IEEE International Conference on Space Optical Systems and Applications (ICSOS)*, pages 294–298.

Kimel, I. (2021). Relations between Hermite and Laguerre Gaussian modes | IEEE Journals & Magazine | IEEE Xplore.

Kimel, I. and Elias, L. (1993). Relations between Hermite and Laguerre Gaussian modes. *IEEE Journal of Quantum Electronics*, 29(9):2562–2567.

Klein, B. J. and Degnan, J. J. (1974). Optical Antenna Gain. 1: Transmitting Antennas. *Applied Optics*, 13(9):2134–2141.

Kogelnik, H. and Li, T. (1966). Laser beams and resonators. *J. Opt. Soc. Am. A*, pages 1550–1567.

Kolmogorov, A. N. (1941). The local structure of turbulence in incompressible viscous fluid for very large reynolds number. *Cr Acad. Sci. URSS, 30:301-305*.

Kuzkov, V., Kuzkov, S., Volovyk, D., Sodnik, Z., Caramia, V., and Pukha, S. (2012). Laser Ground System for Communication Experiments with ARTEMIS.

Labroille, G., Denolle, B., Jian, P., Genevaux, P., Treps, N., and Morizur, J.-F. (2014). Efficient and mode selective spatial mode multiplexer based on multi-plane light conversion. *Opt. Express, OE*, 22(13):15599–15607.

Lao, C., Sun, J., Lu, Z., Li, J., Xu, M., He, H., Han, R., Cai, X., and Li, Y. (2020). Multi-aperture fiber coherent combining system in urban horizontal atmospheric laser link. *Optics Communications*, 466:125172.

Leijtens, X. J. M. (2010). JePPIX : the platform for InP-based photonics. *Proceedings of the 15th European Conference in Integrated Optics, ECIO 2010, April 6-9, 2010, Cambridge, United Kingdom*, pages ThG3–1/2.

Leon-Saval, S. G., Argyros, A., and Bland-Hawthorn, J. (2010). Photonic lanterns: a study of light propagation in multimode to single-mode converters. *Optics Express*, 18(8):8430–8439.

Leon-Saval, S. G., Fontaine, N. K., and Amezcua-Correa, R. (2017). Photonic lantern as mode multiplexer for multimode optical communications. *Optical Fiber Technology*, 35:46–55.

Leon-Saval, S. G., Fontaine, N. K., Salazar-Gil, J. R., Ercan, B., Ryf, R., and Bland-Hawthorn, J. (2014). Mode-selective photonic lanterns for space-division multiplexing. *Optics Express*, 22(1):1036.

Li, L., Xie, G., Yan, Y., Ren, Y., Liao, P., Zhao, Z., Ahmed, N., Wang, Z., Bao, C., Willner, A. J., Ashrafi, S., Tur, M., and Willner, A. E. (2017). Power loss mitigation of orbital-angular-momentum-multiplexed free-space optical links using nonzero radial index Laguerre–Gaussian beams. *JOSA B*, 34(1):1–6.

Li, Z. and Zhao, X. (2017). BP artificial neural network based wave front correction for sensor-less free space optics communication. *Optics Communications*, 385:219–228.

Littlejohns, C. G., Tran, Y., Du, H., Stanković, S., Yan, X., Sharp, G., Sorel, M., Webb, R., England, J., Chong, H., Gardes, F. Y., Thomson, D. J., Mashanovich, G. Z., and Reed, G. T. (2019). Rapid device prototyping using the CORNERSTONE platform (Conference

Presentation). In *Silicon Photonics XIV*, volume 10923, page 1092303. International Society for Optics and Photonics.

McGlamery, B. L. (1976). Computer Simulation Studies Of Compensation Of Turbulence Degraded Images. In *Image Processing*, volume 0074, pages 225–233. International Society for Optics and Photonics.

McManamon, P., Dorschner, T., Corkum, D., Friedman, L., Hobbs, D., Holz, M., Liberman, S., Nguyen, H., Resler, D., Sharp, R., and Watson, E. (1996). Optical phased array technology. *Proceedings of the IEEE*, 84(2):268–298.

Michau, V. and Petit, C. (2021). Optique adaptative - principe et applications.

Miller, S. A., Chang, Y.-C., Phare, C. T., Shin, M. C., Zadka, M., Roberts, S. P., Stern, B., Ji, X., Mohanty, A., Gordillo, O. A. J., Dave, U. D., and Lipson, M. (2020). Large-scale optical phased array using a low-power multi-pass silicon photonic platform. *Optica*, 7(1):3–6.

Muñoz, P., Micó, G., Bru, L. A., Pastor, D., Pérez, D., Doménech, J. D., Fernández, J., Baños, R., Gargallo, B., Alemany, R., Sánchez, A. M., Cirera, J. M., Mas, R., and Domínguez, C. (2017). Silicon Nitride Photonic Integration Platforms for Visible, Near-Infrared and Mid-Infrared Applications. *Sensors*, 17(9):2088.

Noll, R. J. (1976). Zernike polynomials and atmospheric turbulence. *Journal of the Optical Society of America*, 66(3):207.

Noordegraaf, D., Skovgaard, P. M. W., Maack, M. D., Bland-Hawthorn, J., Haynes, R., and Lægsgaard, J. (2010). Multi-mode to single-mode conversion in a 61 port Photonic Lantern. *Optics Express*, 18(5):4673–4678.

Norris, B. R. M., Wei, J., Betters, C. H., Wong, A., and Leon-Saval, S. G. (2020). An all-photonic focal-plane wavefront sensor. *Nature Communications*, 11(1).

Obukhov, A. (1949). Structure of the temperature field in a turbulent current. *Izvestiya Akademia Nauk SSSR, Series Goegraficheskaya i Geograficheskaya*.

O'Meara, T. R. (1977). The multidither principle in adaptive optics. *JOSA*, 67(3):306–315.

Paine, S. W. and Fienup, J. R. (2018). Machine learning for improved image-based wavefront sensing. *Optics Letters*, 43(6):1235–1238.

Petit, C., Védrenne, N., Velluet, M.-T., Michau, V., Artaud, G., Samain, E., and Toyoshima, M. (2016). Investigation on adaptive optics performance from propagation channel characterization with the small optical transponder. *OE*, 55(11):111611.

Piscaer, P., Soloviev, O., and Verhaegen, M. (2019). Predictive wavefront sensorless adaptive optics for time-varying aberrations. *JOSA A*, 36(11):1810–1819.

Primmerman, C. A., Price, T. R., Humphreys, R. A., Zollars, B. G., Barclay, H. T., and Herrmann, J. (1995). Atmospheric-compensation experiments in strong-scintillation conditions. *Applied Optics*, 34(12):2081–2088.

Rabiei, P., Ma, J., Khan, S., Chiles, J., and Fathpour, S. (2013). Heterogeneous lithium niobate photonics on silicon substrates. *Optics Express*, 21(21):25573.

Ragazzoni, R. (1996). Pupil plane wavefront sensing with an oscillating prism. *Journal of Modern Optics, 43:289-293*.

Rahim, A., Hermans, A., Wohlfeil, B., Petousi, D., Kuyken, B., Thourhout, D. V., and Baets, R. G. (2021). Taking silicon photonics modulators to a higher performance level: state-of-the-art and a review of new technologies. *Advanced Photonics*, 3(2):024003.

Rahim, A., Ryckeboer, E., Subramanian, A. Z., Clemmen, S., Kuyken, B., Dhakal, A., Raza, A., Hermans, A., Muneeb, M., Dhoore, S., Li, Y., Dave, U., Bienstman, P., Thomas, N. L., Roelkens, G., Thourhout, D. V., Helin, P., Severi, S., Rottenberg, X., and Baets, R. (2017). Expanding the Silicon Photonics Portfolio With Silicon Nitride Photonic Integrated Circuits. *Journal of Lightwave Technology*, 35(4):639–649.

Rahim, A., Spuesens, T., Baets, R., and Bogaerts, W. (2018). Open-Access Silicon Photonics: Current Status and Emerging Initiatives. *Proceedings of the IEEE*, 106(12):2313–2330.

Richardson, D. J. (2016). New optical fibres for high-capacity optical communications. *Philosophical Transactions of the Royal Society A: Mathematical, Physical and Engineering Sciences*, 374(2062):20140441.

Rickman, A. (2014). The commercialization of silicon photonics. *Nature Photonics*, 8(8):579–582.

Rinaldi, L., Michau, V., Védrenne, N., Petit, C., Mugnier, L. M., Lim, C., Montri, J., Paillier, L., and Boutillier, M. (2021). Sensorless adaptive optics for optical communications. In *Free-Space Laser Communications XXXIII*, volume 11678, pages 164–169. SPIE.

Roberts, L. C., Burruss, R., Roberts, J. E., Piazzolla, S., Dew, S., Truong, T., Fregoso, S., and Page, N. (2015). Performance Predictions for the Adaptive Optics System at LCRD's Ground Station 1. In *Imaging and Applied Optics 2015 (2015), paper JW4F.4*, page JW4F.4. Optical Society of America.

Roddier, F. (1981). The effects of atmospheric turbulence in optical astronomy. *Progress in Optics*, 19.

Roddier, F. (1988). Curvature sensing and compensation: a new concept in adaptive optics. *Appl. Opt. 27:1223-1225*.

Roelkens, G., Abassi, A., Cardile, P., Dave, U., de Groote, A., de Koninck, Y., Dhoore, S., Fu, X., Gassenq, A., Hattasan, N., Huang, Q., Kumari, S., Keyvaninia, S., Kuyken, B., Li, L., Mechet, P., Muneeb, M., Sanchez, D., Shao, H., Spuesens, T., Subramanian, A., Uvin, S., Tassaert, M., van Gasse, K., Verbist, J., Wang, R., Wang, Z., Zhang, J., van Campenhout, J., Yin, X., Bauwelinck, J., Morthier, G., Baets, R., and van Thourhout, D. (2015). III-V-on-Silicon Photonic Devices for Optical Communication and Sensing. *Photonics*, 2(3):969–1004.

Roeloffzen, C. G. H., Hoekman, M., Klein, E. J., Wevers, L. S., Timens, R. B., Marchenko, D., Geskus, D., Dekker, R., Alippi, A., Grootjans, R., Rees, A. v., Oldenbeuving, R. M.,

Epping, J. P., Heideman, R. G., Wörhoff, K., Leinse, A., Geuzebroek, D., Schreuder, E., Dijk, P. W. L. v., Visscher, I., Taddei, C., Fan, Y., Taballione, C., Liu, Y., Marpaung, D., Zhuang, L., Benelajla, M., and Boller, K. (2018). Low-Loss Si3N4 TriPleX Optical Waveguides: Technology and Applications Overview. *IEEE Journal of Selected Topics in Quantum Electronics*, 24(4):1–21.

Roey, J. V., Donk, J. v. d., and Lagasse, P. E. (1981). Beam-propagation method: analysis and assessment. *JOSA*, 71(7):803–810.

Rousset, G. (1993). Wavefront sensing. *In Adaptive Optics for Astronomy, Cargèse, France. ASI, Kluwer Academic Publisher*, 243.

Rousset, G., Fontanella, J., Kern, P., Gigan, P., and Rigaut, F. (1990). First diffraction-limited astronomical images with adaptive optics. *Astronomy and Astrophysics 230, 230:L29-L32*.

Ruilier, C. and Cassaing, F. (2001). Coupling of large telescopes and single-mode waveguides: application to stellar interferometry. *Journal of the Optical Society of America A*, 18(1):143.

Saab, K. (2017). Optique adaptative pour les télécommunications optiques. *Thèse de doctorat, Université de recherche Paris Sciences et Lettres*.

Saathof, R., Crowcombe, W., Kuiper, S., Pettazzi, F., Vosteen, A., van der Valk, N., Truyens, N., Breeje, R., and Ferrario, I. (2017). TNO optical communications space terminals — Current projects and future plans. In *2017 IEEE International Conference on Space Optical Systems and Applications (ICSOS)*, pages 255–259.

Schwartz, N. (2009). Précompensation des effets de la turbulence par optique adaptative : application aux liaisons optiques en espace libre. *Thèse de doctorat, Université de Nice-Sophia Antipolis*.

Shaklan, S. and Roddier, F. (1988). Coupling starlight into single-mode fiber optics. *Applied Optics*, 27:2334–2338.

Smit, M., Leijtens, X., Ambrosius, H., Bente, E., Tol, J. v. d., Smalbrugge, B., Vries, T. d., Geluk, E.-J., Bolk, J., Veldhoven, R. v., Augustin, L., Thijs, P., D'Agostino, D., Rabbani, H., Lawniczuk, K., Stopinski, S., Tahvili, S., Corradi, A., Kleijn, E., Dzibrou, D., Felicetti, M., Bitincka, E., Moskalenko, V., Zhao, J., Santos, R., Gilardi, G., Yao, W., Williams, K., Stabile, P., Kuindersma, P., Pello, J., Bhat, S., Jiao, Y., Heiss, D., Roelkens, G., Wale, M., Firth, P., Soares, F., Grote, N., Schell, M., Debregeas, H., Achouche, M., Gentner, J.-L., Bakker, A., Korthorst, T., Gallagher, D., Dabbs, A., Melloni, A., Morichetti, F., Melati, D., Wonfor, A., Penty, R., Broeke, R., Musk, B., and Robbins, D. (2014). An introduction to InP-based generic integration technology. *Semiconductor Science and Technology*, 29(8):083001.

Smit, M., Williams, K., and van der Tol, J. (2019). Past, present, and future of InP-based photonic integration. *APL Photonics*, 4(5):050901.

Tanzilli, S., de Riedmatten, H., Tittel, W., Zbinden, H., Baldi, P., de Micheli, M., Ostrowsky, D. B., and Gisin, N. (2000). Highly efficient photon-pair source using a Periodically Poled Lithium Niobate Waveguide. *arXiv:quant-ph/0012053*. arXiv: quant-ph/0012053.

Tatarski, V. (1961). Wave propagation in a turbulent medium. *Dover Publications Inc., New York*.

Tatarski, V. (1971). The effects of the turbulent atmosphere on wave propagation.

Thi Bich, M. N. and Le, N. T. (2018). Electromagnetic Field Modeling and Analysis Based on QuickField Simulator. In *2018 4th International Conference on Green Technology and Sustainable Development (GTSD)*, pages 682–686.

Thiessen, T., Grosse, P., Fonseca, J. D., Billondeau, P., Szelag, B., Jany, C., Poon, J. k. S., and Menezo, S. (2019). 30 GHz heterogeneously integrated capacitive InP-on-Si Mach–Zehnder modulators. *Optics Express*, 27(1):102.

Thomson, D., Zilkie, A., Bowers, J., Komljenovic, T., Reed, G., Vivien, L., Marris-Morini, D., Cassan, E., Virot, L., Fédéli, J.-M., Hartmann, J.-M., Schmid, J., Xu, D.-X., Boeuf, F., O'Brien, P., Mashanovich, G., and Nedeljković, M. (2016). Roadmap on silicon photonics. *Journal of Optics*, 18(7):1–20.

Thylen, L. (2006). A Moores law for photonics. In *2006 International Symposium on Biophotonics, Nanophotonics and Metamaterials*, pages 256–263.

Thylén, L. (1983). The beam propagation method: an analysis of its applicability. *Optical and Quantum Electronics*, 15(5):433–439.

Tian, Q., Lu, C., Liu, B., Zhu, L., Pan, X., Zhang, Q., Yang, L., Tian, F., and Xin, X. (2019). DNN-based aberration correction in a wavefront sensorless adaptive optics system. *Optics Express*, 27(8):10765–10776.

Toyoshima, M. (2005). Trends in satellite communications and the role of optical free-space communications [Invited]. *Journal of Optical Networking*, 4(6):300–311.

Toyoshima, M. (2021). Recent Trends in Space Laser Communications for Small Satellites and Constellations. *Journal of Lightwave Technology*, 39(3):693–699.

Toyoshima, M., Fuse, T., Kolev, D., Takenaka, H., Munemasa, Y., Iwakiri, N., Suzuki, K., Koyama, Y., Kubooka, T., Akioka, M., and Kunimori, H. (2015). Current status of research and development on space laser communications technologies and future plans in NICT. pages 1–5.

Tu, X., Song, C., Huang, T., Chen, Z., and FU, H. Y. (2019). State of the Art and Perspectives on Silicon Photonic Switches. *Micromachines*, 10:51.

Valley, G. C. (1980). Isoplanatic degradation of tilt correction and short-term imaging systems. *Applied Optics*, 19(4):574–577.

Vedrenne, N., Petit, C., Montmerle-Bonnefois, A., Lim, C. B., Conan, J.-M., Paillier, L., Velluet, M.-T., Caillault, K., Gustave, F., Durecu, A., Michau, V., Cassaing, F., Meimon, S., and Montri, J. (2021). Performance analysis of an adaptive optics based optical feeder link ground station. In *International Conference on Space Optics — ICSO 2020*, volume 11852, page 1185219. International Society for Optics and Photonics.

Vera, E., Guzmán, F., and Weinberger, C. (2021). Boosting the deep learning wavefront sensor for real-time applications [Invited]. *Applied Optics*, 60(10):B119–B124.

Vorontsov, M. A., Carhart, G. W., and Ricklin, J. C. (1997). Adaptive phase-distortion correction based on parallel gradient-descent optimization. *Optics Letters*, 22(12):907–909.

Vorontsov, M. A. and Lachinova, S. L. (2008). Laser beam projection with adaptive array of fiber collimators. I. Basic considerations for analysis. *JOSA A*, 25(8):1949–1959.

Vorontsov, M. A. and Sivokon, V. P. (1998). Stochastic parallel-gradient-descent technique for high-resolution wave-front phase-distortion correction. *JOSA A*, 15(10):2745–2758.

Wang, C., Langrock, C., Marandi, A., Jankowski, M., Zhang, M., Desiatov, B., Fejer, M. M., and Lončar, M. (2018). Ultrahigh-efficiency wavelength conversion in nanophotonic periodically poled lithium niobate waveguides. *Optica*, 5(11):1438–1441.

Weigel, P. O., Zhao, J., Fang, K., Al-Rubaye, H., Trotter, D., Hood, D., Mudrick, J., Dallo, C., Pomerene, A. T., Starbuck, A. L., DeRose, C. T., Lentine, A. L., Rebeiz, G., and Mookherjea, S. (2018). Bonded thin film lithium niobate modulator on a silicon photonics platform exceeding 100 GHz 3-dB electrical modulation bandwidth. *Optics Express*, 26(18):23728.

Weyrauch, T., Vorontsov, M. A., Gowens, J., and Bifano, T. G. (2002). Fiber coupling with adaptive optics for free-space optical communication. pages 177–184, San Diego, CA.

Williams, K. (2017). InP Integrated Photonics: State of the Art and Future Directions. In *Optical Fiber Communication Conference (2017), paper M3B.5*, page M3B.5. Optical Society of America.

Wilson, K. E. (1993). GOPEX Experiment Results.

Wilson, K. E., Leatherman, P. R., Cleis, R., Spinhirne, J., and Fugate, R. Q. (1997a). Results of the Compensated Earth–Moon–Earth Retroreflector Laser Link (CEMERLL) Experiment.

Wilson, K. E., Lesh, J. R., Araki, K., and Arimoto, Y. (1997b). Overview of the Ground-to-Orbit Lasercom Demonstration (GOLD). In *Free-Space Laser Communication Technologies IX*, volume 2990, pages 23–30. International Society for Optics and Photonics.

Wilson, K. E. and Roberts, L. C. (2014). Recent developments in adaptive optics for the lcdr optical ground station at table mountain. *Proc. International Conference on Space Optical System and Applications (ICSOS), May 7-9*.

Wright, M. W., Kovalik, J., Morris, J., Abrahamson, M., and Biswas, A. (2016). LEO-to-ground optical communications link using adaptive optics correction on the OPALS downlink. In *Free-Space Laser Communication and Atmospheric Propagation XXVIII*, volume 9739, page 973904. International Society for Optics and Photonics.

Wright, M. W., Morris, J. F., Kovalik, J. M., Andrews, K. S., Abrahamson, M. J., and Biswas, A. (2015). Adaptive optics correction into single mode fiber for a low Earth orbiting space to ground optical communication link using the OPALS downlink. *Optics Express*, 23(26):33705–33712.

Wu, H., Yan, H., and Li, X. (2010). Modal correction for fiber-coupling efficiency in free-space optical communication systems through atmospheric turbulence. *Optik*, 121(19):1789–1793.

Xu, F., Khalighi, M.-A., Causse, P., and Bourennane, S. (2008). Performance of coded time-diversity free-space optical links. In *2008 24th Biennial Symposium on Communications*, pages 146–149.

Yang, Y., Geng, C., Li, F., Huang, G., and Li, X. (2017). Multi-aperture all-fiber active coherent beam combining for free-space optical communication receivers. *Optics Express*, 25(22):27519–27532.

Zhang, B., Yuan, R., Sun, J., Cheng, J., and Alouini, M.-S. (2020a). *Free-Space Optical Communication Using Non-mode-Selective Photonic Lantern Based Coherent Receiver*.

Zhang, L., Zhang, L., Fu, X., Yang, L., and Yang, L. (2020b). Polarization-independent, lithium-niobate-on-insulator directional coupler based on a combined coupling-sections design. *Applied Optics*, 59(28):8668–8673.

Zhao, H., Pinna, S., Song, B., Megalini, L., Brunelli, S. T. , Coldren, L. A., and Klamkin, J. (2018). Indium Phosphide Photonic Integrated Circuits for Free Space Optical Links. *IEEE Journal of Selected Topics in Quantum Electronics*, 24(6):1–6.